

# REPORT DOCUMENTATION PAGE

AFRL-SR-AR-TR-04-

Public reporting burden for this collection of information is estimated to average 1 hour per response, including the time for reviewing instructions, searching existing data sources, gathering the required data, and completing and reviewing this collection of information. Send comments regarding this burden estimate or any other aspect of this burden to Department of Defense, Washington Headquarters Services, Directorate for Information Operations and Reports (0704-0188), 1215 Jefferson Davis Highway, Suite 1204, Arlington, VA 22202-4302. Respondents should be aware that notwithstanding any other provision of law, no person shall be subject to any penalty for failing to comply with a collection of information if it does not have a valid OMB control number. **PLEASE DO NOT RETURN YOUR FORM TO THE ABOVE ADDRESS.**

0417

1. REPORT DATE (DD-MM-YYYY) 01-06-2004		2. REPORT TYPE Final Technical		3. DATES COVERED (From - To) 01-01-2001 - 31-01-2004	
4. TITLE AND SUBTITLE (U) Large Eddy Simulation of the Lattice Boltzmann Equation For Turbulent Combustion <del>Simulations</del>				5a. CONTRACT NUMBER	
				5b. GRANT NUMBER F49620-01-1-0142	
				5c. PROGRAM ELEMENT NUMBER 61102F	
				5d. PROJECT NUMBER 2308	
6. AUTHOR(S)  Sharath S. Girimaji, Huidan Yu, Dazhi Yu, Li-Shi Luo				5e. TASK NUMBER BX	
				5f. WORK UNIT NUMBER	
				8. PERFORMING ORGANIZATION REPORT NUMBER	
7. PERFORMING ORGANIZATION NAME(S) AND ADDRESS(ES)  Texas A&M University College Station TX 77843					
9. SPONSORING / MONITORING AGENCY NAME(S) AND ADDRESS(ES) AFOSR/NA 4015 Wilson Boulevard Room 713 Arlington VA 22203-1954					
12. DISTRIBUTION / AVAILABILITY STATEMENT  Approved for public release; distribution is unlimited					
13. SUPPLEMENTARY NOTES					
14. ABSTRACT The Lattice Boltzmann equation (LBE) was used to perform direct numerical simulations (DNS) and large-eddy simulations (LES) of benchmark problems in turbulence, scalar mixing, and reaction. The most important contribution was the development of LBE theory for binary mixing, which can be extended in a straight-forward manner to multi-scalar mixing. Computational simulations were performed to verify that the desired diffusive effects could be achieved in classical mixing problems. It was demonstrated that the shape of the probability density functions during binary mixing from non-premixed initial conditions was captured precisely. The technique for handling reactions in the LBE context also was demonstrated. In the standard one-dimensional flame propagation problem, the burning rate was captured accurately. The third significant contribution was the adaptation of the multi-time-scale relaxation technique to LES. Several DNS and LES calculations of benchmark turbulent flows (decaying isotropic and homogeneous shear, square jet) were performed to establish the effectiveness and efficiency of LBE. The decay exponent in decaying turbulence, the equilibrium anisotropies in homogeneous turbulence, and the spread rates in square jets were calculated accurately.					
15. SUBJECT TERMS  Turbulent combustion, lattice Boltzmann method, large eddy simulation					
16. SECURITY CLASSIFICATION OF:			17. LIMITATION OF ABSTRACT  UL	18. NUMBER OF PAGES  192	19a. NAME OF RESPONSIBLE PERSON Julian M. Tishkoff
a. REPORT Unclassified	b. ABSTRACT Unclassified	c. THIS PAGE Unclassified			19b. TELEPHONE NUMBER (include area code) (703) 696-8478

20040810 025

# **ABSTRACT of Final Report of F49620-01-1-0142**

Lattice Boltzmann equation (LBE) was used to perform direct numerical simulations (DNS) and large-eddy simulations (LES) of benchmark problems in turbulence, scalar mixing and reaction. The most important contribution was the development of LBE theory for binary mixing which can be extended in a straight-forward manner to multi-scalar mixing. Computational simulations were performed to verify that the desired diffusive effects are achieved in classical mixing problems. For example, it was demonstrated that the shape of the probability density functions during binary mixing from non-premixed initial conditions were precisely captured. The technique for handling reactions in the LBE context was also demonstrated. In the standard one-dimensional flame propagation problem, the burning rate was captured accurately. The third significant contribution was the adaptation of multi-time-scale relaxation technique to LES. Several DNS and LES of benchmark turbulent flows (decaying isotropic and homogeneous shear, square jet) were performed to establish the effectiveness and efficiency of LBE. The decay exponent in decaying turbulence, the equilibrium anisotropies in homogeneous turbulence, and the spread rates in square jets were accurately calculated. In summary, a solid foundation for future LBE-LES calculations of turbulent combustion has been established.

# **ABSTRACT of Final Report of F49620-01-1-0142**

Lattice Boltzmann equation (LBE) was used to perform direct numerical simulations (DNS) and large-eddy simulations (LES) of benchmark problems in turbulence, scalar mixing and reaction. The most important contribution was the development of LBE theory for binary mixing which can be extended in a straight-forward manner to multi-scalar mixing. Computational simulations were performed to verify that the desired diffusive effects are achieved in classical mixing problems. For example, it was demonstrated that the shape of the probability density functions during binary mixing from non-premixed initial conditions were precisely captured. The technique for handling reactions in the LBE context was also demonstrated. In the standard one-dimensional flame propagation problem, the burning rate was captured accurately. The third significant contribution was the adaptation of multi-time-scale relaxation technique to LES. Several DNS and LES of benchmark turbulent flows (decaying isotropic and homogeneous shear, square jet) were performed to establish the effectiveness and efficiency of LBE. The decay exponent in decaying turbulence, the equilibrium anisotropies in homogeneous turbulence, and the spread rates in square jets were accurately calculated. In summary, a solid foundation for future LBE-LES calculations of turbulent combustion has been established.

# Lattice Boltzmann Method for LES of turbulent combustion

Sharath S. Girimaji and Li-Shi Luo

Texas A& M University and National Institute of Aerospace

AFOSR Grant: F49620-01-1-0142

## Publication List

## References

- [1] L.-S. Luo and S. S. Girimaji, *Lattice Boltzmann model for binary mixtures*, Phys. Rev. E **66**(4):035301(R) (2002).
- [2] L.-S. Luo and S. S. Girimaji, *Theory of the lattice Boltzmann model: Two-fluid model for binary mixtures*, Phys. Rev. E **67**:036302 (2003).
- [3] H. Yu, L.-S. Luo, and S. S. Girimaji, *Scalar mixing and chemical reaction simulations using lattice Boltzmann method*, Int. J. Computat. Eng. Sci. **3**(1):73–87 (2002).
- [4] D. d’Humières, I. Ginzburg, M. Krafczyk, P. Lallemand, and L.-S. Luo, *Multiple-relaxation-time lattice Boltzmann models in three-dimensions*, Philos. Trans. R. Soc. London A **360**(1792):437–451 (2002).
- [5] M. Krafczyk, J. Tölke, and L.-S. Luo, *Large-eddy simulations with a multiple-relaxation-time LBE model*, Int. J. Mod. Phys. C **17**(1/2):33–39 (2003).
- [6] P. Lallemand and L.-S. Luo, *Hybrid finite-difference thermal lattice Boltzmann equation*, Int. J. Mod. Phys. C **17**(1/2):41–47 (2003).
- [7] P. Lallemand and L.-S. Luo, *Lattice Boltzmann method for moving boundaries*, J. Computat. Phys. **184**(2):406–421 (2003).
- [8] P. Lallemand, D. d’Humières, L.-S. Luo, and R. Rubinstein, *Theory of the lattice Boltzmann method: Three-dimensional model for linear viscoelastic fluids*, Phys. Rev. E **67**:021203 (2003).
- [9] H. D. Yu, S. S. Girimaji and L.-S. Luo, *Lattice Boltzmann simulations of decaying isotropic turbulence*, submitted to Phys. Rev. E. (2003)



---

## **Personnel Supported:**

**Huidan Yu** (graduate student, to defend Ph.D thesis in Aug. 2004)

**Dr. Dazhi Yu** (summer post-doctoral support)

Few other students were supported for short times for performing specific tasks.

---

## **Contacts with Dr. Bish Ganguly of AFRL**

**My main AFRL contact was Dr. Bish Ganguly.**

**2002:** I visited with Dr. Ganguly at AFRL in Dayton in April of 2002. I was particularly interested in his plasma ignition work. I believe that an LBM-based computational scheme could be well-suited for performing important calculations in support of this work. Currently, some continuum-based physical models are being used for this purpose. While such methods may be adequate for some parameter regimes, a Boltzmann-based scheme may have a wider range of applicability. The use of stochastic chemistry schemes may be particularly appropriate for this purpose.

**2003:** I held telephone conversations with Dr. Bish Ganguly about using the Lattice Boltzmann method (LBM) turbulence in non-equilibrium flows, such as hypersonic flows. The discussion revolved around LBM's natural ability to represent non-equilibrium effects. Direct numerical simulation (DNS) of non-equilibrium effects on turbulence was the main topic of discussion. The degree and type of non-equilibrium effects as a function of Mach number was discussed. Also discussed was how the relaxation to equilibrium would differ in the engine when compared to the external flow. The presence of water vapor (as a combustion product) would substantially speed up the relaxation in the engine.

**Over the years,** I have also held several discussions with Dr. Mel Roqumore of AFRL (during Contractor meetings) about the ability of LBM to highlight important flow physics not amenable to the continuum approach. Of special interest, was the non-equilibrium transport effect which was a major subject of our discussion. Upon Dr. Ganguly's suggestion I have also held conversations with Dr. Datta Gaitonde of WPAFB regarding the computation of non-equilibrium flows.

---

**Inventions and Patents:** None at this time

---

# **Large Eddy Simulation of the Lattice Boltzmann Equation for Turbulent Combustion**

PI: Sharath S. Girimaji

Department of Aerospace Engineering, Texas A&M University,  
College Station, Texas

Co-PI: Li-Shi Luo

The National Institute of Aerospace (NIA), Hampton, Virginia

PostDoc: Dazhi Yu

Department of Aerospace Engineering, Texas A&M University  
College Station

Ph.D student: Huidan Yu

Department of Aerospace Engineering, Texas A&M University  
College Station

March 31, 2004

# Contents

<b>1</b>	<b>General Introduction</b>	<b>5</b>
1.1	Lattice Boltzmann vs. Navier-Stokes equations . . . . .	6
1.2	Objectives and accomplishments. . . . .	8
<b>2</b>	<b>Main Results and Inferences</b>	<b>11</b>
2.1	Lattice Boltzmann model for binary mixtures . . . . .	12
2.1.1	Introduction . . . . .	12
2.1.2	Kinetic theory of gas mixtures and lattice Boltzmann equation . . .	13
2.1.3	Discussion and conclusions . . . . .	15
2.2	Simple model for binary scalar mixing . . . . .	16
2.2.1	Lattice Boltzmann equation for scalar mixing . . . . .	16
2.2.2	Simulations and Conclusions . . . . .	17
2.3	Lattice Boltzmann equations for reacting flow . . . . .	20
2.3.1	Introduction . . . . .	20
2.3.2	Simulations and conclusions . . . . .	21
2.4	DNS and LES of decaying homogenous isotropic turbulence (HIT) . . . . .	23
2.4.1	Introduction . . . . .	23
2.4.2	Simulation results . . . . .	23
2.4.3	Summary and conclusions . . . . .	26
2.5	Study of homogenous turbulence shear . . . . .	29

---

2.5.1	Introduction . . . . .	29
2.5.2	Homogenous shear flow . . . . .	29
2.5.3	Homogenous turbulence subjected to time-dependent shear . . . . .	29
2.5.4	Comparison: DNS vs. RANS models . . . . .	35
2.5.5	Conclusions . . . . .	35
2.6	The LBM for axisymmetric flows in cylindrical coordinate . . . . .	36
2.6.1	Simulation and conclusions . . . . .	37
<b>3</b>	<b>Conclusions</b>	<b>41</b>
<b>4</b>	<b>Appendix</b>	<b>43</b>
<b>A</b>	<b>Background of Lattice Boltzmann Method</b>	<b>44</b>
<b>B</b>	<b>Lattice Boltzmann Model for Binary Mixtures</b>	<b>51</b>
B.1	Introduction . . . . .	52
B.2	Kinetic theory of gas mixtures . . . . .	54
B.3	The lattice Boltzmann model for binary mixture . . . . .	61
B.4	Hydrodynamics . . . . .	63
B.5	Diffusion in isothermal mixtures . . . . .	65
B.6	Short and long time behaviors . . . . .	67
B.7	Discussion and conclusions . . . . .	69
<b>C</b>	<b>Computational Assessment of Diffusivity in LBM for Binary Scalar Mixing</b>	<b>83</b>
C.1	Introduction . . . . .	83
C.2	Lattice Boltzmann model for binary scalar mixing . . . . .	84
C.2.1	Macroscopic equations of each species . . . . .	86
C.2.2	Mutual diffusivity calculation . . . . .	89

---

C.3	Non-premixed binary scalar mixing . . . . .	90
C.4	Conclusions . . . . .	92
C.5	Figures . . . . .	92
<b>D</b>	<b>Scalar Mixing and Chemical Reaction Simulations</b>	<b>97</b>
D.1	Introduction . . . . .	97
D.2	Lattice Boltzmann equation for scalar mixing . . . . .	98
D.3	Lattice Boltzmann equations for reacting flow . . . . .	100
D.4	Simulations . . . . .	103
D.4.1	Non-premixed binary scalar mixing . . . . .	103
D.4.2	Reacting flow in a 1-D channel . . . . .	106
D.5	Conclusions . . . . .	107
D.6	Figures . . . . .	112
<b>E</b>	<b>DNS and LES of Decaying Isotropic Turbulence With and Without Frame Rotation</b>	<b>114</b>
E.1	Introduction . . . . .	115
E.2	Homogeneous isotropic turbulence . . . . .	116
E.3	LBE formulation for DNS and LES of turbulence . . . . .	117
E.3.1	Lattice Boltzmann equation for DNS . . . . .	117
E.3.2	LES extension of lattice Boltzmann equation . . . . .	119
E.4	Simulation results . . . . .	121
E.4.1	LBE-DNS of decaying isotropic turbulence . . . . .	122
E.4.2	LBE-LES of decaying isotropic turbulence . . . . .	123
E.4.3	LBE-LES vs. NS-LES . . . . .	125
E.5	Summary and conclusions . . . . .	126
E.6	Figures . . . . .	126

<b>F Study of Homogenous Turbulence Shear</b>	<b>144</b>
F.1 Introduction . . . . .	144
F.2 Reynolds-stress evolution equations . . . . .	146
F.3 Results and discussions . . . . .	147
F.3.1 Homogenous shear flow . . . . .	147
F.3.2 Homogenous turbulence subjected to periodically varied shears. . .	148
F.3.3 Comparison: DNS vs. RANS models . . . . .	152
F.4 Conclusions . . . . .	152
F.5 Figures . . . . .	154
 <b>G Lattice Boltzmann Models for Axisymmetric Flows in Cylindrical Coordinate</b>	 <b>171</b>
G.1 Introduction . . . . .	171
G.2 Lattice Boltzmann model for axisymmetric flows . . . . .	172
G.2.1 Hydrodynamic equations in cylindrical coordinate system . . . . .	172
G.2.2 Lattice Boltzmann equation for vector(momentum) field . . . . .	174
G.2.3 Lattice Boltzmann equation for scalar field . . . . .	178
G.3 Evaluation simulations . . . . .	179
G.3.1 Axisymmetric flows . . . . .	180
G.4 Conclusions . . . . .	181
G.5 Figures . . . . .	182

# Chapter 1

## General Introduction

Physically accurate and computationally viable calculation procedures for turbulent combustion are required for a variety of propulsion applications ranging from improving combustor performance to estimating the concentrations of environmentally-harmful trace chemicals and strategically-crucial signature producing species precisely. Despite the vast strides in computational capabilities, direct numerical simulation (DNS) of turbulent combustion for device-size computations remains well beyond the capabilities of current computers, as well as those for the foreseeable future. It is now a widely held view that large-eddy simulation (LES), in conjunction with the probability density function (PDF) method for the subgrid scales, offers the best hope for computing practical turbulent combustion problems. The moment methods are generally unsuited for reacting flows because of the strong non-linearity introduced by the reaction-rate term. The LES-PDF technique is an attractive choice, as it combines precise simulation of the problem-dependent large-scale motion with the reasonably accurate PDF method for the universal small-scale fluctuations. While much less computationally intensive than direct numerical simulations (DNS), a clean LES simulation with the spectral cut-off well in the inertial range (as dictated by theory) still can be very expensive. Many applications of interest to the Air Force involve multi-phase flows (sprays and atomization), preferential diffusion requiring the computation of multi-

component diffusivity, and complex geometry. For these problems, the LES method can be very tedious, to the point of being computationally intractable. In the PDF methodology, advection and reaction terms appear in closed form but diffusion processes require closure modeling. Physically accurate diffusion models tend to be computationally expensive, and the simpler models can be quite inaccurate. As currently practiced, the evaluation of the reaction-rate term can take up to 80% of the computational effort per time step. Reduced chemistry models are used typically to alleviate this computational burden. The reduced chemical kinetics, while adequately capturing the slow reactions and major species, may be inaccurate for trace species that could be environmentally harmful or signature producing. Most traditional reduction techniques assume that many trace species are in partial equilibrium, leading to errors in estimation of the concentration of these species. Even in the more sophisticated reduction techniques, such as the Intrinsic Low-Dimensional Manifold (ILDM) method, the fast eigen-species are assumed to be in equilibrium, leading to less accurate estimation of these species than the slow-evolving major species. While the LES-PDF method is the best technique available currently, there is a lot of room for improvement.

In this report, we describe the early development of a new methodology for calculating turbulent combustion based on the more fundamental Boltzmann equation rather than Navier-Stokes equation. The ultimate goal of the proposed work is, in effect, a large eddy simulation of the Boltzmann equation in which the (molecular) velocity distribution function is discretized in phase space with a lattice. More succinctly, we call our approach the large eddy simulation (LES) of the lattice Boltzmann equation (LBE). This LBE-LES technique has several physical and computational advantages over the LES-PDF approach.

## 1.1 Lattice Boltzmann vs. Navier-Stokes equations

The Boltzmann equation is potentially a better hydrodynamic platform for LES calculations of turbulent combustion than is the Navier-Stokes equation. The advantages lie both in



improved physical accuracy and better computational characteristics. The physical accuracy aspects will be discussed in detail later.

**Computational advantages.** The computational philosophies of the two methods are vastly different. While the LBE method leads to very simple, explicit and frequent calculations at each node, the NS-based calculation at each node is complex (often implicit) and occurs less frequently. At first glance, it would appear that the advantage achieved by LBE due to the simplicity of the calculation would be offset by the higher frequency of computations, rendering the two methods equal. That is not to be. What sets the two methods apart is the locality of the calculations at each node. The LBE scheme leads to calculations that are not only simple but also involve only local interactions. In the NS methods, global interactions play a major role, resulting in a severe communication penalty and a marked reduction of computational speed. This difference becomes even more significant when computations are performed on multi-processor parallel platforms. The NS-based computations typically scale poorly with an increase in the number of processors. The LBE computations, on the other hand, display excellent scalability characteristics; even super-linear scaling has been observed in some very special cases. The main advantages of the LBE-based methods are:

1. LBE is better suited for large-scale, especially, parallel computing.
2. LBE is ideally suited for handling multi-phase flow with phase transition and multi-species mixtures, where multi-component diffusivity is important. Navier-Stokes solvers can be computationally too expensive for these flows.
3. LBE can handle complex geometry with relative ease. Even computations involving moving boundaries, *e.g.*, rotating turbine blades, can be handled without loss of computational speed.

In our own work, we have determined that LBM is a factor of six times faster than a commercial second-order finite difference code (FIRE) for isotropic  $64^3$  DNS simulations. We expect this factor to be larger for larger-size computations.

## 1.2 Objectives and accomplishments.

*The objective of the research is to develop the fundamentals of the Lattice-Boltzmann method to enable large-eddy simulations of turbulent combustion. Our ultimate goal is to compete with NS methods in their strength areas and provide a superior computational capability in problems that are not easily tractable by the NS method.*

The areas of focus of the completed research are:

1. Molecular mixing, especially between species of vastly different molecular weights.
2. DNS and LES of turbulence.
3. Laminar flames.
4. Chemical kinetics and their reduction.
5. Treatment of complex geometry.

During this period, important progress in the areas of molecular mixing, laminar flames, treatment of complex geometry in laminar flows, DNS/LES of turbulence in simple geometry and chemical kinetics reduction has been made. In the area of molecular mixing, we have developed, from kinetic theory, the basic LBM model for multi-component mixtures. We also demonstrated that the LBM mixing model can reproduce classical results and obtain important new results that are beyond the scope of continuum-based methods. LBM can simulate mixing and segregation with equal facility. In the area of laminar flames, we have developed computational capability that accurately calculates the burning velocity in a simple one-dimensional premixed flame. Since practical combustors are typically of

complex geometry, we have developed preliminary versions of complex boundary treatments. Reducing chemical kinetics is as important in LBM as it is in NS-based computations. For LBM, we have evaluated stochastic chemistry and deterministic chemistry methods. We have concluded that stochastic kinetics models are not yet feasible due to computational issues.

An incomplete list of refereed journal articles published from research (partly or fully) supported by this grant is given below.

1. L.-S. Luo and S. S. Girimaji, *Lattice Boltzmann model for binary mixtures*, Phys. Rev. E **66**(4):035301(R) (2002). [Addresses Theory of mixing]
2. L.-S. Luo and S. S. Girimaji, *Theory of the lattice Boltzmann model: Two-fluid model for binary mixtures*, Phys. Rev. E **67**:036302 (2003). [Addresses Theory of mixing]
3. H. Yu, L.-S. Luo, and S. S. Girimaji, *Scalar mixing and chemical reaction simulations using lattice Boltzmann method*, Int. J. Computat. Eng. Sci. **3**(1):73–87 (2002). [Addresses random mixing and chemical reaction]
4. D. d’Humières, I. Ginzburg, M. Krafczyk, P. Lallemand, and L.-S. Luo, *Multiple-relaxation-time lattice Boltzmann models in three-dimensions*, Philos. Trans. R. Soc. London A **360**(1792):437–451 (2002). [Addresses fundamental LBM issues]
5. M. Krafczyk, J. Tölke, and L.-S. Luo, *Large-eddy simulations with a multiple-relaxation-time LBE model*, Int. J. Mod. Phys. C **17**(1/2):33–39 (2003). [Addresses fundamental LES issues]
6. P. Lallemand and L.-S. Luo, *Hybrid finite-difference thermal lattice Boltzmann equation*, Int. J. Mod. Phys. C **17**(1/2):41–47 (2003). [Address heat-release physics model]
7. P. Lallemand and L.-S. Luo, *Lattice Boltzmann method for moving boundaries*, J. Computat. Phys. **184**(2):406–421 (2003). [Addresses complex moving boundary issues]

Several more papers are undergoing review or under preparation.

## Chapter 2

# Main Results and Inferences

Turbulent combustion involves three important physical processes: (i) turbulent stirring, (ii) molecular mixing, and (iii) chemical reaction. The first two constitute the process of turbulent mixing. The stirring of a scalar field (temperature, concentration, etc.) by a turbulent velocity field causes gradient steepening, leading to enhancement of molecular mixing. Since turbulence is essentially a 3-D phenomena, our LBE computation of turbulence is three-dimensional in nature. Molecular diffusion process, on the other hand, is essentially one-dimensional in nature: the diffusion is along the direction of the scalar concentration gradient which is orthogonal to the iso-scalar surface. Hence, the LBE studies of molecular mixing have been conducted in three and two dimensions. Chemical reaction is a local (zero-physical dimension) process. Hence we assess the suitability of the LBE for chemical reaction in a simple 1-D flame. In our work, we develop and test the LBE models for these processes individually. Extensive simulations have been performed leading to important results. In this Chapter, we summarize the main results and inferences.

A novel lattice Boltzmann model for binary mixing is proposed and discussed in Section 2.1 (details in Appendix B). In Section 2.2, we simplified the mixing model further and test that model in non-premixed binary scalar mixing (details in Appendix C and D). In Section 2.3, LBE is tested for one-dimensional flame propagation through a premixed mixture of

propane and air (details in Appendix D). Results from DNS and LES of turbulence in isotropic and homogeneous turbulence are presented in Section 2.4 and 2.5, respectively (details in Appendix E and F). Finally, a LBE model for axisymmetric geometry is given in Section 2.6 (details in Appendix G). Further work of LBE-LES on investigation of mixing enhancement using square jet is not presented, as it is not yet complete.

## 2.1 Lattice Boltzmann model for binary mixtures

### 2.1.1 Introduction

The present day lattice Boltzmann equation, with its high fidelity physics and computationally efficient formulation, is a viable alternative to the continuum methods for simulating fluid flows. In fact, it can be argued that for many complex problems involving multi-fluid phenomena, the physics can be captured more naturally by the Boltzmann equation-based methods rather than Navier-Stokes equation-based methods. There is a growing interest in using the lattice Boltzmann equation (1; 2; 3; 4; 5; 6; 7). However, most existing LBE models for multi-component fluids (8; 9; 10; 11; 12; 13; 14; 15; 16) tend to be somewhat heuristic and make the single-fluid assumption. The single-relaxation-time or Bhatnagar-Gross-Krook (BGK) approximation (17) is used in most existing models (10; 11; 12; 13; 14; 15; 16), restricting applicability to unity Prandtl and Schmidt numbers.

In this work, we develop a two-fluid lattice Boltzmann model that is based on kinetic theory for binary mixtures. Such a model would be capable of (i) simulating arbitrary Schmidt and Prandtl numbers, and (ii) accurately modeling the interaction between miscible and immiscible fluids. We follow a general approach within the framework of kinetic theory for developing the lattice Boltzmann models for multi-fluid mixtures. This work is a part of our ongoing effort to set the lattice Boltzmann equation on a more rigorous theoretical foundation and extend its use to more complex flows. We derive a discretized version of the continuum Boltzmann equations for binary mixtures. The extension of this methodology

to multi-fluid mixtures is relatively straight-forward.

### 2.1.2 Kinetic theory of gas mixtures and lattice Boltzmann equation

The simultaneous Boltzmann equations for a binary system are (please see Appendix B for nomenclature)

$$\partial_t f^A + \boldsymbol{\xi} \cdot \nabla f^A + \mathbf{a}_A \cdot \nabla_{\boldsymbol{\xi}} f^A = Q^{AA} + Q^{AB}, \quad (2.1a)$$

$$\partial_t f^B + \boldsymbol{\xi} \cdot \nabla f^B + \mathbf{a}_B \cdot \nabla_{\boldsymbol{\xi}} f^B = Q^{BA} + Q^{BB}, \quad (2.1b)$$

where  $Q^{AB} = Q^{BA}$  is the collision term due to the interaction among two different species A and B.

With the BGK approximation (17; 18), the collision integrals  $Q^{\sigma\varsigma}$  [ $\sigma, \varsigma \in (A, B)$ ] can be approximated by the following linearized collision terms

$$J^{\sigma\sigma} = -\frac{1}{\lambda_{\sigma}}[f^{\sigma} - f^{\sigma(0)}], \quad (2.2a)$$

$$J^{\sigma\varsigma} = -\frac{1}{\lambda_{\sigma\varsigma}}[f^{\sigma} - f^{\sigma\varsigma(0)}], \quad (2.2b)$$

where  $f^{\sigma(0)}$  and  $f^{\sigma\varsigma(0)}$  are Maxwellians

$$f^{\sigma(0)} = \frac{n_{\sigma}}{(2\pi R_{\sigma} T_{\sigma})^{D/2}} e^{-(\boldsymbol{\xi} - \mathbf{u}_{\sigma})^2 / (2R_{\sigma} T_{\sigma})}, \quad (2.3a)$$

$$f^{\sigma\varsigma(0)} = \frac{n_{\sigma}}{(2\pi R_{\sigma} T_{\sigma\varsigma})^{D/2}} e^{-(\boldsymbol{\xi} - \mathbf{u}_{\sigma\varsigma})^2 / (2R_{\sigma} T_{\sigma\varsigma})}, \quad (2.3b)$$

where  $D$  is the spatial dimension,  $R_{\sigma} = k_B / m_{\sigma}$  is the gas constant of the  $\sigma$  species,  $k_B$  is the Boltzmann constant and  $m_{\sigma}$  is the molecular mass of the  $\sigma$  species. There are three adjustable relaxation parameters in the collision terms:  $\lambda_{\sigma}$ ,  $\lambda_{\varsigma}$ , and  $\lambda_{\sigma\varsigma} = (n_{\varsigma} / n_{\sigma}) \lambda_{\varsigma\sigma}$ . The first Maxwellian  $f^{\sigma(0)}$  is characterized by the conserved variables of each individual species: the number density  $n_{\sigma}$ , the mass velocity  $\mathbf{u}_{\sigma}$ , and the temperature  $T_{\sigma}$ . The second Maxwellians  $f^{\sigma\varsigma(0)}$  and  $f^{\varsigma\sigma(0)}$  are characterized by four adjustable parameters:  $\mathbf{u}_{\sigma\varsigma}$ ,  $\mathbf{u}_{\varsigma\sigma}$ ,  $T_{\sigma\varsigma}$ , and  $T_{\varsigma\sigma}$ .

For the isothermal flows, we can derive the lattice Boltzmann equation by discretizing the model equations (2.1) following the procedure described in (4; 5) (for details, please refer to Appendix B):

$$\begin{aligned} f_{\alpha}^{\sigma}(\mathbf{x}_i + \mathbf{e}_{\alpha}\delta_t, t + \delta_t) - f_{\alpha}^{\sigma}(\mathbf{x}_i, t) \\ = J_{\alpha}^{\sigma\sigma} + J_{\alpha}^{\sigma\varsigma} - F_{\alpha}^{\sigma}\delta_t, \end{aligned} \quad (2.4)$$

where the self-collision term  $J_{\alpha}^{\sigma\sigma}$ , the cross-collision term  $J_{\alpha}^{\sigma\varsigma}$ , and the forcing term  $F_{\alpha}^{\sigma}$  are given by

$$J_{\alpha}^{\sigma\sigma} = -\frac{1}{\tau_{\sigma}} \left[ f_{\alpha}^{\sigma} - f_{\alpha}^{\sigma(0)} \right], \quad (2.5a)$$

$$J_{\alpha}^{\sigma\varsigma} = -\frac{1}{\tau_D} \frac{\rho_{\varsigma}}{\rho} \frac{f_{\alpha}^{\sigma(\text{eq})}}{R_{\sigma}T} (\mathbf{e}_{\alpha} - \mathbf{u}) \cdot (\mathbf{u}_{\sigma} - \mathbf{u}_{\varsigma}), \quad (2.5b)$$

$$F_{\alpha}^{\sigma} = -w_{\alpha}\rho_{\sigma} \frac{\mathbf{e}_{\alpha} \cdot \mathbf{a}_{\sigma}}{R_{\sigma}T}, \quad (2.5c)$$

where  $\rho_{\sigma}$  and  $\rho_{\varsigma}$ , and  $\mathbf{u}_{\sigma}$  and  $\mathbf{u}_{\varsigma}$  are the mass densities and flow velocities for species  $\sigma$  and  $\varsigma$ . They are the moments of the distribution functions:

$$\rho_{\sigma} = \sum_{\alpha} f_{\alpha}^{\sigma} = \sum_{\alpha} f_{\alpha}^{\sigma(0)}, \quad (2.6a)$$

$$\rho_{\sigma}\mathbf{u}_{\sigma} = \sum_{\alpha} f_{\alpha}^{\sigma}\mathbf{e}_{\alpha} = \sum_{\alpha} f_{\alpha}^{\sigma(0)}\mathbf{e}_{\alpha}, \quad (2.6b)$$

and  $\rho$  and  $\mathbf{u}$  are, respectively, the mass density and the barycentric velocity of the mixture:

$$\rho = \rho_{\sigma} + \rho_{\varsigma}, \quad (2.7a)$$

$$\rho\mathbf{u} = \rho_{\sigma}\mathbf{u}_{\sigma} + \rho_{\varsigma}\mathbf{u}_{\varsigma}. \quad (2.7b)$$

The collision terms  $J_{\alpha}^{\sigma\sigma}$  and  $J_{\alpha}^{\sigma\varsigma}$  are constructed in such a way to satisfy the mass and momentum conservation laws.

The equilibrium distribution function  $f_{\alpha}^{\sigma(0)}$  has the following form in general:

$$f_{\alpha}^{\sigma(0)} = \left[ 1 + \frac{1}{R_{\sigma}T} (\mathbf{e}_{\alpha} - \mathbf{u}) \cdot (\mathbf{u}_{\sigma} - \mathbf{u}) \right] f_{\alpha}^{\sigma(\text{eq})}, \quad (2.8a)$$

$$f_{\alpha}^{\sigma(\text{eq})} = w_{\alpha}\rho_{\sigma} \left[ 1 + \frac{(\mathbf{e}_{\alpha} - \mathbf{u}) \cdot \mathbf{u}}{R_{\sigma}T} + \frac{(\mathbf{e}_{\alpha} \cdot \mathbf{u})^2}{2(R_{\sigma}T)^2} \right]. \quad (2.8b)$$

where coefficients  $\{w_{\alpha}\}$  depend on the discrete velocity set  $\{\mathbf{e}_{\alpha}\}$ .



### 2.1.3 Discussion and conclusions

We have constructed a lattice Boltzmann model for binary mixtures with several important features. All the modeling issues are addressed within the framework of extended kinetic theory. The lattice Boltzmann model then is derived directly from the continuous kinetic model equations using a formal discretization procedure. The lattice model thus inherits the sound physics and mathematical rigor incumbent in kinetic theory. This rigor is in contrast to previous lattice Boltzmann models for mixtures (11; 12; 13; 14; 15; 16), which are not based directly on the fundamental physics of continuum kinetic equations. These models rely on fictitious interactions (11; 12) or heuristic free energies (13; 14; 15; 16) to produce the requisite mixing. (Many defects of the free-energy models (13; 14; 15; 16) are due to the incorrectly defined equilibria (19).) These non-physical effects present a further problem, since they are not easily amenable to mathematical analysis (19; 20). The heuristic elements of the previous lattice Boltzmann models (11; 12; 13; 14; 15; 16) have been eliminated, resulting in a physically justifiable model that is simple to compute. Further, due to the close connection to kinetic theory, the derivation of the hydrodynamic equations associated with the lattice Boltzmann model is simplified significantly and rendered mathematically more rigorous. The derivation of the hydrodynamic equations from the previous lattice models are much less rigorous (11; 12; 13; 14; 15; 16).

The second important feature of the present work is that the model is based upon a two-fluid theory of binary mixtures. The previous models (8; 9; 10; 11; 12; 13; 14; 15; 16), on the other hand, are derived from a simpler, but highly restrictive, one-fluid theory. In the single-fluid models with the BGK approximation one is constrained to use the *ad hoc* “equilibrium velocity” (11; 12)

$$\mathbf{u}^{(\text{eq})} = \frac{(\tau_\varsigma \rho_\sigma \mathbf{u}_\sigma + \tau_\sigma \rho_\varsigma \mathbf{u}_\varsigma)}{(\tau_\varsigma \rho_\sigma + \tau_\sigma \rho_\varsigma)}$$

in the equilibrium distribution function  $f_\alpha^{\sigma(0)}$  in order to satisfy the local conservation laws. As a result, the viscous relaxation process and the diffusion process are inseparable. The

analysis of these models, therefore, becomes unnecessarily tedious and cumbersome (11; 12). The models with free energies (13; 14; 15; 16) do not yield correct hydrodynamic equations (19; 20), mostly due to the incorrectly defined equilibrium distribution functions used in these models (19). Furthermore, single-fluid models cannot be applied to mixtures of species with vastly different properties. In the present two-fluid model, the diffusion behavior is decoupled from viscous relaxation. The diffusivity is determined by the parameter  $\tau_D$  and the physical properties of the mixture. The model is capable of simulating either miscible or immiscible fluids by changing the sign of  $(\tau_D - 1/2)$ .

## 2.2 Simple model for binary scalar mixing

While the binary mixing model derived in the previous Section is general and mathematically rigorous, it may be difficult to implement. In this Section, we will develop a relatively simple model for binary mixing by adding inter-particle reaction. This model is amenable to easier implementation and testing. (For nomenclature and details, please see Appendix C and D)

### 2.2.1 Lattice Boltzmann equation for scalar mixing

Let  $\sigma$  and  $\sigma'$  denote the two species of interest. The LBE for each species is

$$n_\alpha^\sigma(\vec{x} + \vec{e}_\alpha, t + 1) = n_\alpha^\sigma(\vec{x}, t) + \Omega_\alpha^\sigma(\vec{x}, t) \quad (2.9)$$

where  $n_\alpha$  is number density distribution function and the collision operator is given by

$$\Omega_\alpha^\sigma = -\frac{1}{\tau_\sigma} [n_\alpha^\sigma - n_\alpha^{\sigma(eq)}] + \frac{J_\alpha^{\sigma\sigma'}}{m^\sigma} \quad (2.10)$$

includes an additional term  $J_\alpha^{\sigma\sigma'}$  that reflects interactions between the two species.

We use the following number density equilibrium distribution function

$$n_\alpha^{\sigma(eq)} = w_\alpha n^\sigma [1 + 3(\vec{e}_\alpha \cdot \vec{u}') + \frac{9}{2}(\vec{e}_\alpha \cdot \vec{u}')^2 - \frac{1}{2}u'^2] \quad (2.11)$$

with

$$\vec{u}' = \frac{1}{\rho} \sum_{\sigma} \frac{m^{\sigma}}{\tau^{\sigma}} (n^{\sigma} \vec{u}^{\sigma}) \quad (2.12)$$

The binary interaction term is modeled as

$$J_{\alpha}^{\sigma\sigma'} = \frac{1}{\tau^{\sigma\sigma'}} n_{\alpha}^{eq} \cdot [\nabla x^{\sigma} + (x^{\sigma} - \omega^{\sigma}) \frac{\nabla \rho}{\rho}] = -J_{\alpha}^{\sigma'\sigma} \quad (2.13)$$

where  $x^{\sigma}$  and  $\omega^{\sigma}$  are molar and mass fractions of the species  $\sigma$

$$x^{\sigma} = \frac{n^{\sigma}}{n}, \quad \omega^{\sigma} = \frac{\rho^{\sigma}}{\rho}$$

and

$$n_{\alpha}^{(eq)} = w_{\alpha} n [1 + 3(\vec{e}_{\alpha} \cdot \vec{u}) + \frac{9}{2}(\vec{e}_{\alpha} \cdot \vec{u})^2 - \frac{1}{2}u^2] \quad (2.14)$$

The hydrodynamic properties of the above equations are given in Appendix C.

## 2.2.2 Simulations and Conclusions

We performed non-premixed binary scalar mixing computation in a periodic box. This problem epitomizes the molecular mixing issues encountered in a typical non-premixed combustion application. Two species (presumably fuel and oxidizer) are segregated initially and randomly distributed in the computational domain, which, in the present case, is a square box. The two species are labeled generically as black and white. A typical initial distribution is shown in Figure 2.1.

The macroscopic velocity is set everywhere to zero, corresponding to a pure diffusion problem. The initial values for the number densities are  $n^b = 1.0$ ,  $n^w = 0.0$  in region of the black species and  $n^w = 1.0$ ,  $n^b = 0.0$  in region of white species. Assuming homogeneity of the scalar field, periodic boundary conditions are used in all directions.

The first case studied is the mixing of two fluids of equal molecular weights and number densities ( $m^b = m^w = 1.0$ ), hence of equal mass density. This case is particularly interesting, as the results can be compared directly with direct numerical simulation (DNS) of the Navier-Stokes equation data of Eswaran and Pope (21). Figure 2.2(a) shows the time evolution of

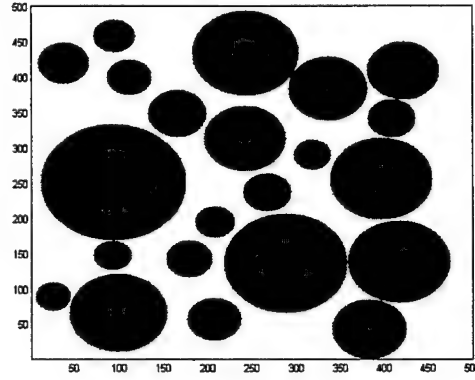


**Figure 2.1: Initial number density distribution for both equal and unequal mass cases**

the probability density function(pdf) of the scalar  $\bar{\rho}$ :

$$\bar{\rho} = \frac{\rho^b - \rho^w}{\rho^b + \rho^w}$$

The corresponding DNS(21) data are shown in Figure 2.2(b). The LBE and DNS data show excellent qualitative agreement.

In Figure 2.3, the time evolution of the root-mean-square(rms) of scalar fluctuations ( $\rho'$ ) obtained from LBE is compared with that from DNS(21). They agree quite well. We also performed the simulation for an unequal mass case( $m^b = 2.0, m^w = 1.0$ ). The detailed results are given in Appendix D.

In conclusion, we present a binary mixing model and use it to simulate scalar mixing. In the case of equal-density species mixing, well-known results from a continuum Navier-Stokes simulation are reproduced. The true advantage of the LBM can be seen from the mixing simulations of species of different molecular weights. The results appear quite encouraging. Such simulations are very difficult with continuum based methods.

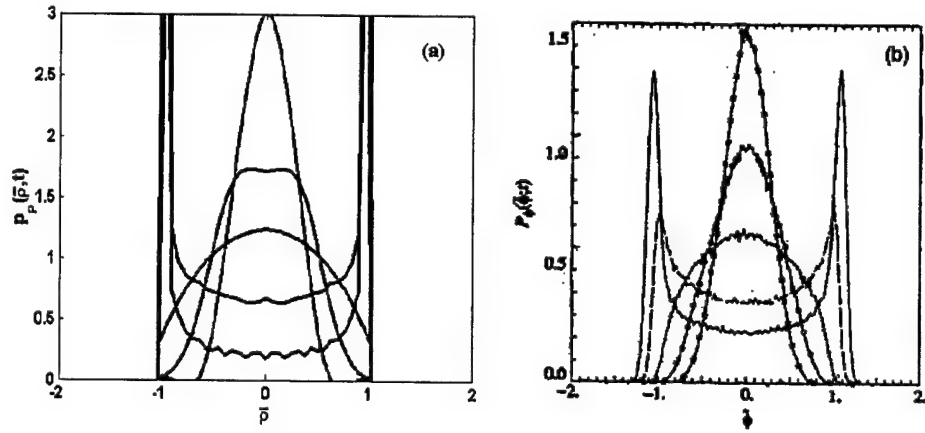


Figure 2.2: Pdf evolution of number density in equal mass case. (a)LBE; (b)DNS

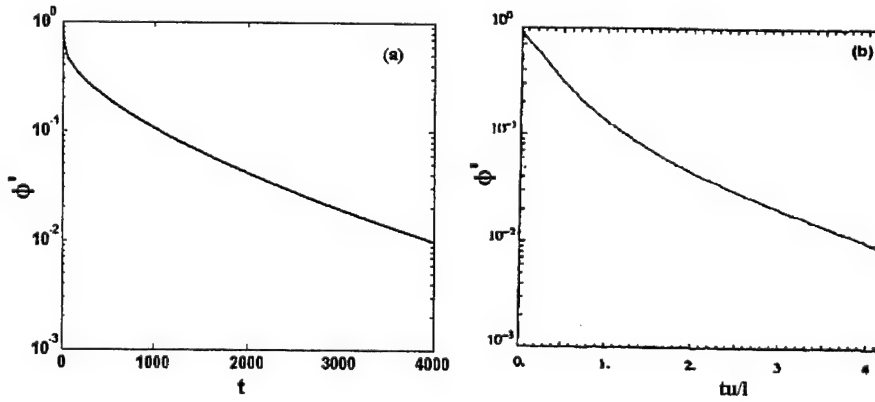


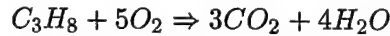
Figure 2.3: Evolution of rms scalar ( $\phi'$ ) in equal mass case. (a)LBE( $\phi' = 2\rho'$ ); (b)DNS

## 2.3 Lattice Boltzmann equations for reacting flow

### 2.3.1 Introduction

We simulate simple one-dimensional flame propagation through premixed propane and air. The problem studied is identical to that of Yamamoto(22), but the physical combustion field is slightly different. The simplifying assumptions invoked in this study are:

- There are no external forces in the field.
- The flow is incompressible.
- The chemical reaction (heat release) does not affect the flow field; the temperature and concentration fields are decoupled and solved separately.
- Nitrogen is inert.
- The transport properties are constants (not functions of temperature).
- Viscous energy dissipation and radiative heat losses are negligible.
- A simple one-step reaction is considered



and the overall reaction rate is given by

$$\omega_{ov} = \kappa_{ov} C_{C_3H_8} C_{O_2} e^{-E/RT}$$

where  $C_{C_3H_8}$ ,  $C_{O_2}$ ,  $\kappa_{ov}$  and  $E$  are the concentrations of propane and oxygen, the reaction coefficient, and the effective activation energy, respectively.

The details of modeling this problem are given in Appendix D. Here we will only present numerical results.

### 2.3.2 Simulations and conclusions

A schematic of the simulated flow is shown in Figure 2.4. For this simple case, the background flow maintains both the pressure and velocity fields uniform in space and time. A heat source is placed at a location close to the inlet to ignite the mixture. Once ignition is achieved, the heat source is removed. At subsequent time the flame propagates to the right.

In Figure 2.5 the flame position is shown as a function of time. The flame location is identified as the position with the highest reaction rate at any given time. The linear variation of flame location with time (in Figure 2.5) indicates that the flame propagates at a nearly constant rate. The burning velocity is  $S_L = 0.11m/s$ , which compares extremely well with the value obtained from experiments for a propane-air flame(23).

Figure 2.6 shows the reaction rate profile in the reaction zone as time evolves. Simulations indicate that flame behavior is sensitive to the magnitude of the heat source. The premixed reacting flow simulations produce results that are in good agreement with known data. Based on these simulations, we believe that LBM can perform adequately for more complex chemical reaction calculations.

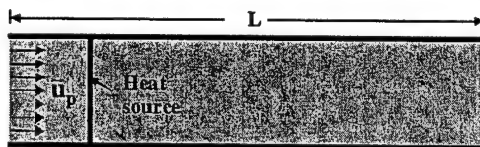


Figure 2.4: A schematic illustration of a simple 1-D reacting flow

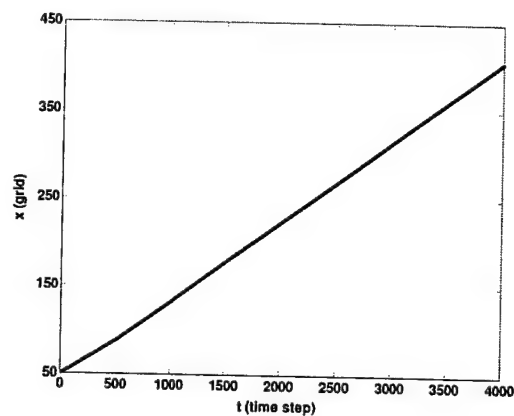


Figure 2.5: The flame position evolution with time

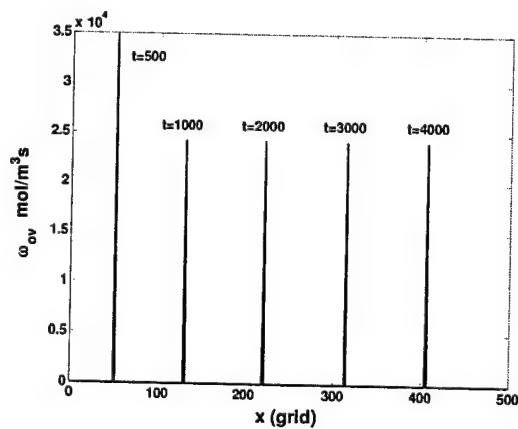


Figure 2.6: Reaction rate profiles at different times.



## 2.4 DNS and LES of decaying homogenous isotropic turbulence (HIT)

### 2.4.1 Introduction

We now examine the ability of LBM to simulate turbulence cascade which is responsible for stirring a scalar field. We perform three type of simulations: **(a) LBE-DNS of decaying HIT in inertial and rotating frame of reference.** The decay exponents for the kinetic energy  $k$  and the dissipation rate  $\varepsilon$  are computed and compared with corresponding NS-DNS results. The low wave-number scalings of the energy spectrum are studied. The effect of rotation on the kinetic energy decay is investigated. **(b) LBE-LES of decaying HIT inertial frame of reference.** We compute the kinetic energy decay, energy spectrum, and flow structures using LBE-LES. By comparing LBE-LES results with the corresponding LBE-DNS results, we observe that LBE-LES accurately captures large scale flow behavior. We find that the optimal Smagorinsky constant value for LBE-LES is smaller than the traditional value used in NS-LES approaches. **(c) LBE-LES vs. NS-LES.** We carry out a comparative study of the LBE-LES and NS-LES of decaying HIT. We show that the LBE-LES simulations preserve flow structures more accurately than the NS-LES counterpart. This accuracy is due to the fact that some history/non-local effects are inherent in the LBE subgrid closure.

### 2.4.2 Simulation results

#### LBE-DNS of decaying isotropic turbulence

The variation of decay exponent ( $n$ ) with Taylor Reynolds number ( $Re_\lambda$ ) in various simulations is shown in Fig. 2.7. The dependence of  $n$  on  $Re_\lambda$  obtained by the LBE-DNS is very similar to that observed in NS-DNS calculations (24). The values of  $n$  obtained in the present work agree well with the experimental and numerical NS-DNS data. In Figure 2.8,

we can see that the low wave-number spectra scale as  $\hat{E}(\kappa) \sim \kappa^4$  or  $\hat{E}(\kappa) \sim \kappa^2$  depending upon initial spectrum. This dependence of low-wave number scaling on the initial spectrum is in exact agreement with the results reported in (24; 25).

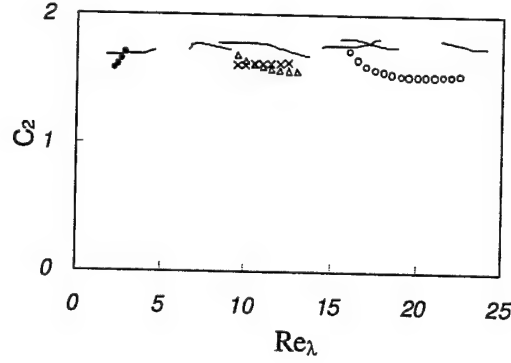


Figure 2.7: Dependence of the decay exponent  $n = 1/(C_2 - 1)$  on initial conditions and  $Re_\lambda$ . The quantity  $C_2$  is depicted in the figure in stead of  $n$ . Solid lines represent NS-DNS data from (24), and symbols correspond to the LBE-DNS results of the present work. For the  $128^3$  resolution,  $\bullet$ :  $u_{rms} = 0.0064$ ,  $k_{min} = 1$ ,  $k_{max} = 8$ , and  $\nu = 0.01$  ( $\tau = 0.53$ );  $\Delta$ :  $u_{rms} = 0.021$ ,  $k_{min} = 8$ ,  $k_{max} = 16$ , and  $\nu \approx 0.00167$  ( $\tau = 0.505$ );  $\circ$ :  $u_{rms} = 0.022$ ,  $k_{min} = 1$ ,  $k_{max} = 8$ , and  $\nu \approx 0.00167$  ( $\tau = 0.505$ ). For the  $64^3$  resolution ( $\times$ ):  $u_{rms} = 0.022$ ,  $k_{min} = 4$  and  $k_{max} = 8$ , and  $\nu \approx 0.00167$  ( $\tau = 0.505$ ).

### LBE-LES of decaying isotropic turbulence

Our first effort is to determine the appropriate Smagorinsky constant ( $C_{sm}$ ) for LBE-LES. Figure 2.9 shows that the kinetic energy decays with different Smagorinsky constant values for both  $32^3$  and  $64^3$  cases. We find that  $C_{sm} = 0.1$  is the best choice, and we shall use it in all calculations.

In Fig. 2.10, we compare the instantaneous flow structure of  $u_z(i, j, k = N/2, t')$  obtained by the LBE-LES with that by LBE-DNS. As shown in Fig. 2.10, the LBE-LES appears to capture the flow-field structure quite adequately even with a coarse resolution of  $32^3$  grid points.

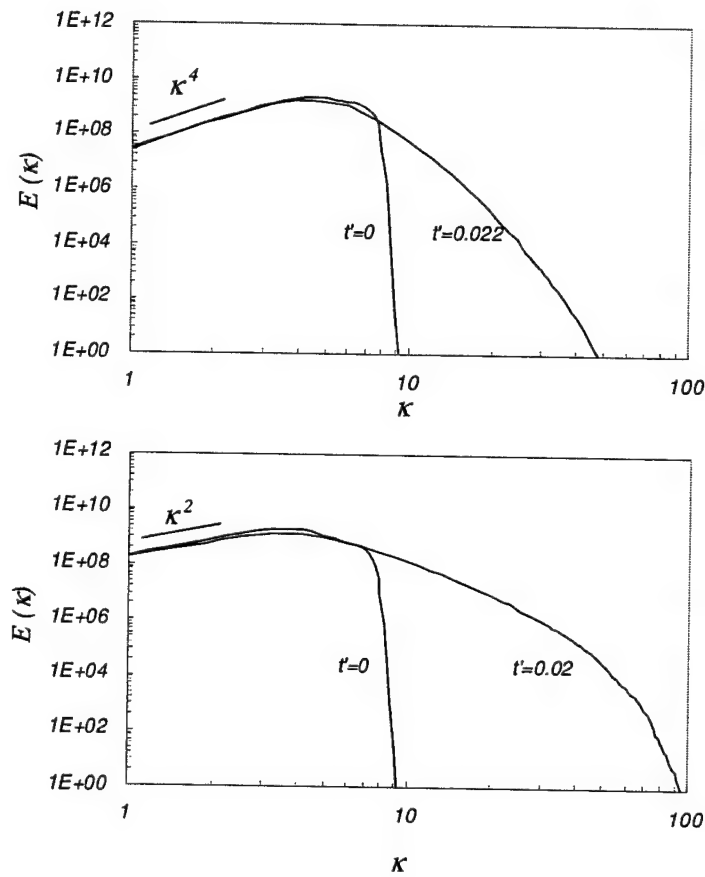


Figure 2.8: Energy spectra for two cases of  $128^3$  above with initial energy concentrating in the range of  $1 \leq \kappa \leq 8$  at  $t' = 0$  and  $t' = 0.022$  respectively. The initial energy spectra are given by  $E(\kappa) = 0.038\kappa^4 \exp(-0.14\kappa^2)$  (upper plot) and  $E(\kappa) = 0.038\kappa^2 \exp(-0.14\kappa^2)$  (bottom plot) respectively.

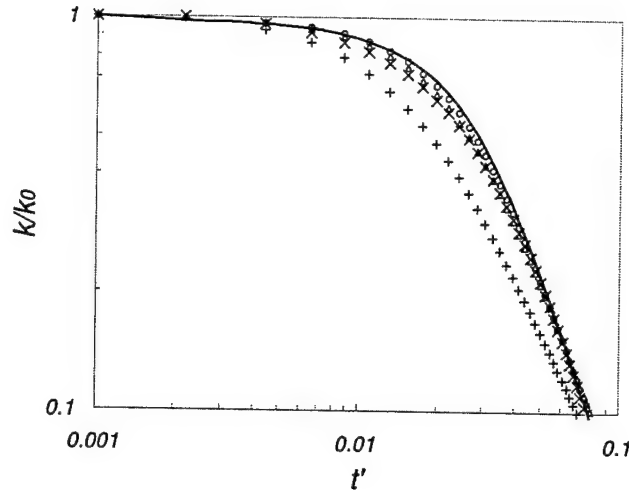


Figure 2.9: Kinetic energy decay with different  $C_{sm}$  and resolution. Solid line for LBE-DNS ( $128^3$ ) and symbols for LBE-LES ( $\circ$ :  $64^3$ ,  $C_{sm} = 0.1$ ;  $\triangle$ :  $64^3$ ,  $C_{sm} = 0.17$ ;  $\times$ :  $32^3$ ,  $C_{sm} = 0.1$ ;  $+$ :  $32^3$ ,  $C_{sm} = 0.17$ ).

### LBE-LES vs. NS-LES

We compare the LBE-LES with the NS-LES results at  $32^3$  resolution. The difference can be seen from contours of the instantaneous flow field  $u_z(i, j, k = N/2, t')$  at three different times, as shown in Fig. 2.11. By Comparing the LBE-LES results (left column) and the NS-LES results (right column) with the LBE-DNS results (center column), we observe that LBE-LES preserves the flow structure better than the corresponding NS-LES. The  $32^3$  LBE-DNS contours shown here are obtained by truncating the  $128^3$  LBE-DNS data.

### 2.4.3 Summary and conclusions

First, we conduct the direct numerical simulations by using the LBM. The well known power-law decay of the kinetic energy is reproduced. The decay exponents obtained in the LBE simulations are in good agreement with the results from experimental measurements and NS-DNS calculations. Second, we conduct a comparative study of the LBE-LES and the LBE-DNS. Comparisons of  $64^3$  and  $32^3$  LBE-LES with  $128^3$  LBE-DNS show that the

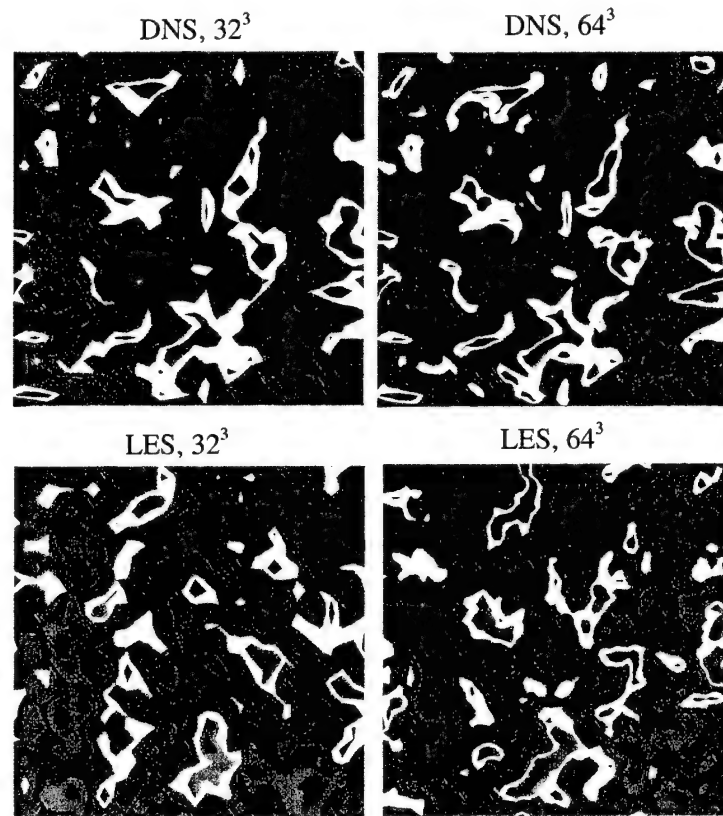


Figure 2.10: Contours of the instantaneous flow field  $u_z(i, j, k = N/2, t')$ . LBE-DNS vs. LBE-LES with different resolutions. The  $32^3$  and  $64^3$  LBE-DNS contours shown here are obtained by truncating the  $128^3$  LBE-DNS data

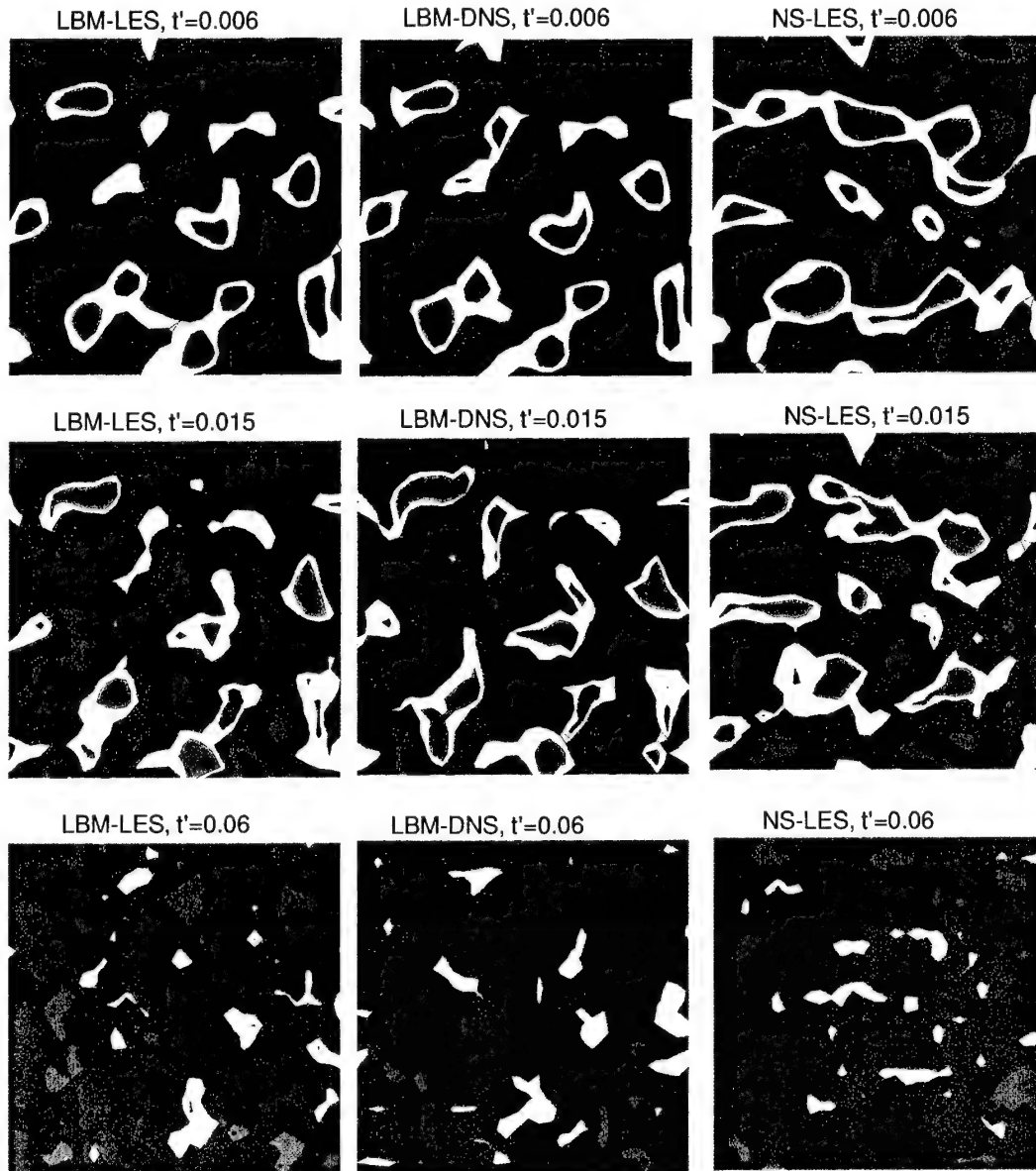


Figure 2.11: Contours of the instantaneous flow field  $u_z(i, j, k = N/2, t')$ . The LBE-LES and NS-LES with a resolution of  $32^3$  compared to the LBE-DNS with a resolution of  $128^3$  at three different times. The  $32^3$  LBE-DNS contours shown here are obtained by truncating the  $128^3$  LBE-DNS data

large scale motion is captured well by LBE-LES. Finally, we compare both the LBE-LES and NS-LES results with the corresponding DNS results. Our comparisons indicate that LBE-LES has better capability to preserve flow-field structure than NS-LES. This work further establishes the LBE method as a viable computational tool for turbulence stirring simulations.

## 2.5 Study of homogenous turbulence shear

### 2.5.1 Introduction

We will first verify the applicability of the lattice Boltzmann method (LBM) in the DNS of steady homogenous turbulence and then focus on the new physics in flows subjected to time-dependent shear. For details, please refer to Appendix F. Time-dependent shear can simulate the effect of mixing in wakes and mixing layers where flow is stirred by vortices.

### 2.5.2 Homogenous shear flow

The computational domain is shown in Fig. 2.12. An uniform  $128^3$  mesh is considered. Figure 2.13 shows the development of the normal components of anisotropy tensor ( $b_{ij}$ ). LBM agrees with the experimental data and numerical results very well (26; 27). Fig. 2.14 compares the present  $b_{12}$  (diagonal component) with the result obtained by Jacobitz et al. (28). The agreement is again very good. From the above comparisons, we conclude that DNS using LBM can recover classical results accurately.

### 2.5.3 Homogenous turbulence subjected to time-dependent shear

Here we let shear vary with time and investigate the effects of the variation on the development of turbulence. The periodic variation is meant to simulate the effect of periodic stirring.

Figures 2.15 and 2.16 show the evolution of turbulent kinetic energy for the low ( $\frac{\omega}{S}=0.5$ )

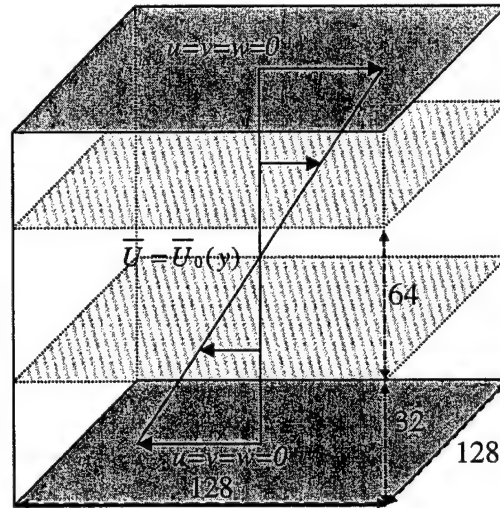
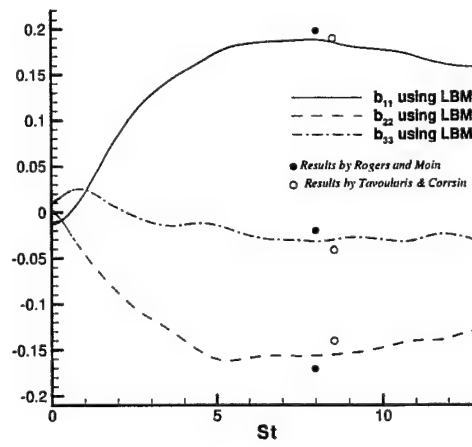


Figure 2.12: Computational domain.

Figure 2.13: The results of anisotropy tensor obtained from DNS using LBM, Navier-Stokes equations, and experiment.  $St$  is non- dimensional time



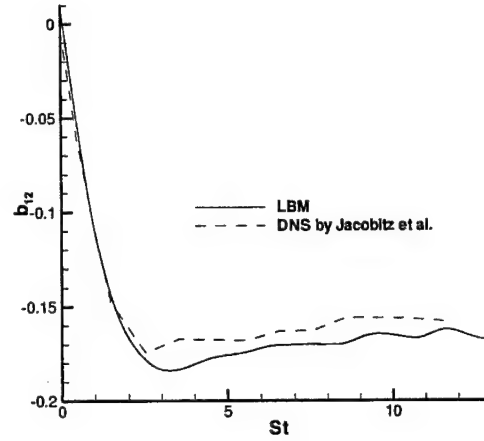


Figure 2.14: The results of anisotropy  $b_{12}$  obtained from DNS using LBM and Navier-Stokes Equations by Jacobitz et al. (28) with the initial values of  $Re_\lambda = 44.72$  and  $Sk/\varepsilon = 2.0$ .  $St$  is non- dimensional time

and high ( $\frac{\omega}{S} = 1.0$ ) frequency cases ( $S$  is the shear rate and  $\omega$  is the frequency of the variation of shear). When frequency is low, the turbulence kinetic energy  $k$  increases after an initial decay while for the high frequency case,  $k$  decreases. Thus, there exists a critical frequency at which turbulence goes from growth-mode to decay-mode. The knowledge of this physics is important for evaluating mixing enhancement strategies. More details of the analysis of this phenomenon are given in Appendix F.

The details of the development of turbulence anisotropy tensor are given in Figs. 2.17 and 2.18. In the low frequency case, the anisotropy in turbulence is fully developed. The mean values of  $b_{11}$  and  $b_{22}$  are about 0.15 and -0.1 respectively. In the high frequency case, the mean values of  $b_{11}$  and  $b_{22}$  are about zero. Thus, turbulence has no opportunity to develop as in the high frequency case.

Figures 2.19 and 2.20 show the evolution of production over dissipation ratios. There exists negative production during some period of evolution. For the low frequency case, the average value of  $P/\varepsilon$  is above one, and for the high frequency case, this value is around zero. This explains why the turbulent kinetic energy evolves differently in these cases.

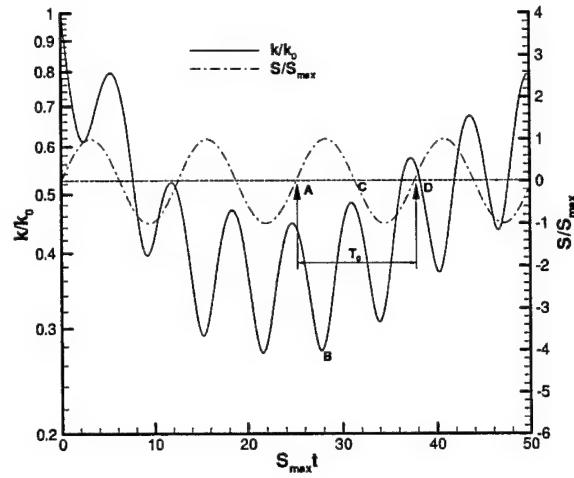


Figure 2.15: Evolution of the turbulence kinetic energy  $k$  for  $\frac{\omega}{S} = 0.5$  case.  $k_0$  is the turbulence kinetic energy at the initial stage;  $S_{max}t$  is non-dimensional time.

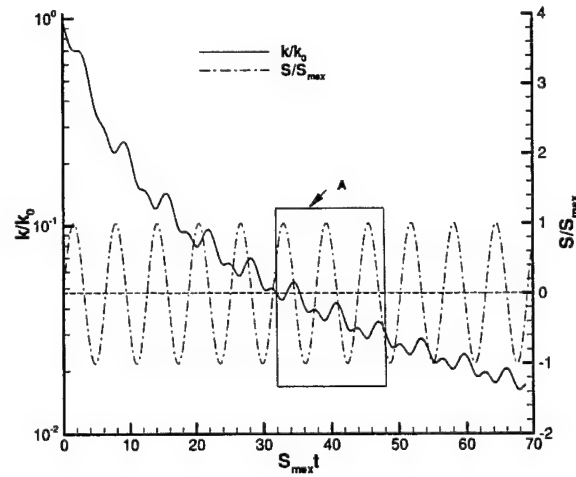


Figure 2.16: Evolution of  $k$  for  $\frac{\omega}{S} = 1.0$  case

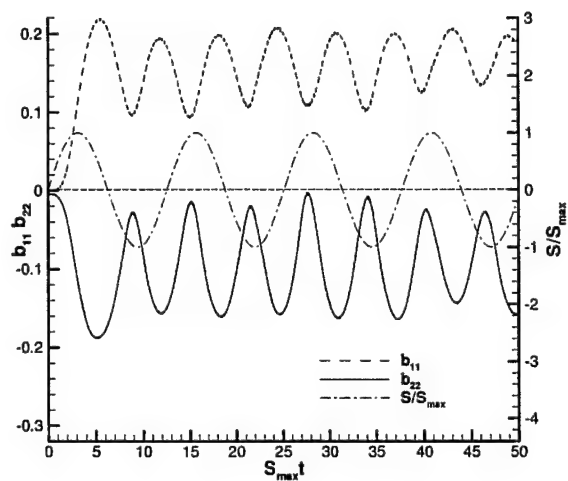


Figure 2.17: Evolution of anisotropy  $b_{11}$  and  $b_{22}$  for  $\frac{\omega}{S} = 0.5$  case

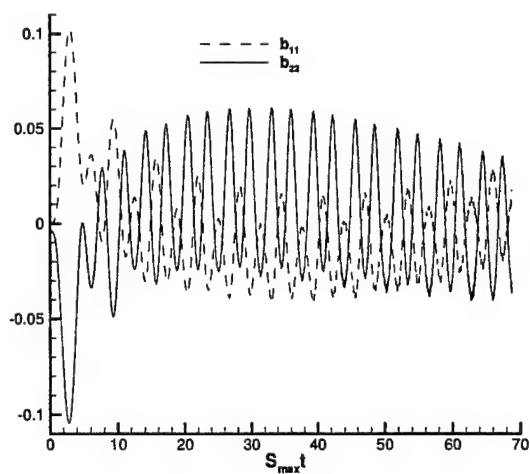


Figure 2.18: Evolution of anisotropy  $b_{11}$  and  $b_{22}$  for  $\frac{\omega}{S} = 1.0$  case

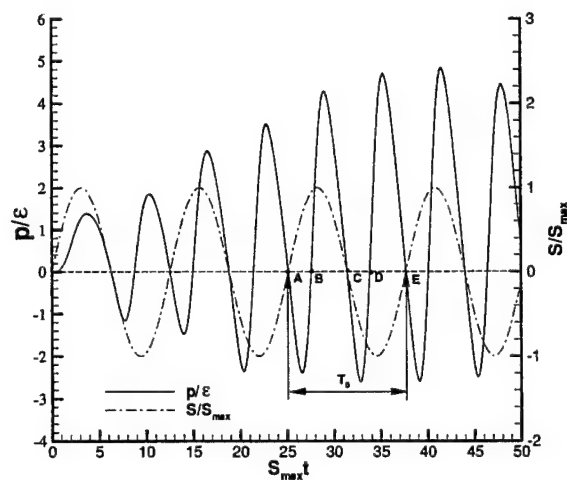


Figure 2.19: Evolution of production over dissipation ratio  $\frac{P}{\epsilon}$  for  $\frac{\omega}{\epsilon} = 0.5$  case

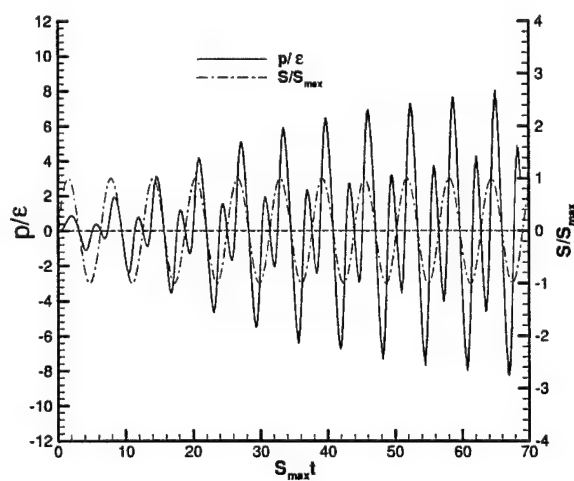


Figure 2.20: Evolution of production over dissipation ratio  $\frac{P}{\epsilon}$  for  $\frac{\omega}{\epsilon} = 1.0$  case

### 2.5.4 Comparison: DNS vs. RANS models

We compare DNS results with the Reynolds averaged Navier-Stokes (RANS) turbulence models. We use 3 different models: LRR-IP, LRR-QI, and SSG models (29). In the high frequency case, DNS and the models predict decay of  $k$ , as shown in Fig. 2.21. However the models predict much slower decay rates. In the low frequency case, the models fail to predict the growth of  $k$ , as shown in Fig. 2.22.

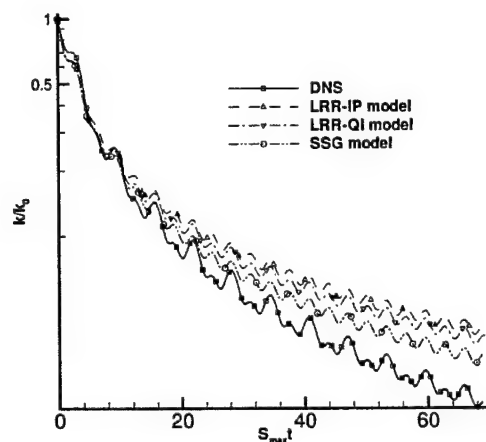


Figure 2.21: DNS vs. RANS models : kinetic energy evolution for  $\frac{\omega}{S} = 1.0$  case

### 2.5.5 Conclusions

DNS of homogenous turbulent shear flow (constant shear) is performed using the lattice Boltzmann method. DNS-LBM results agree well with DNS-NS and experimental data. In DNS of homogenous turbulence subjected to periodically varied shear, a critical frequency, which determines whether  $k$  decays or not, is found. We observe the negative production of  $k$ , which means that there is a mechanism to take kinetic energy away from turbulence. The comparisons of the results of DNS and turbulence models show that the models fail to predict much of the observed behavior.

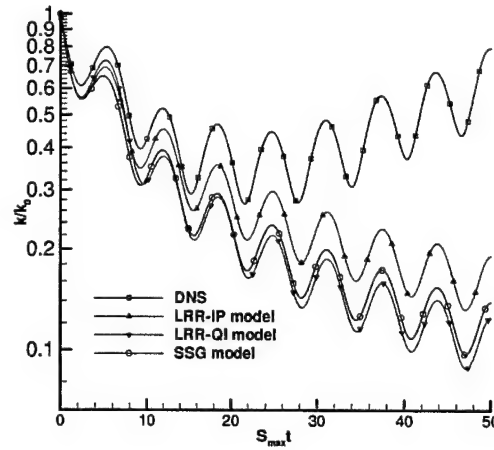


Figure 2.22: DNS vs. RANS models : kinetic energy evolution for  $\frac{\omega}{S} = 0.5$  case

## 2.6 The LBM for axisymmetric flows in cylindrical coordinate

In this Section, we extend the LBM to a cylindrical coordinate system and present lattice Boltzmann models for axisymmetric flows for both the vector(momentum) field and scalar(temperature, concentration, etc.) field. This is accomplished by inclusion of a source-like term or a body force-like term(30) in the lattice Boltzmann equations.

By introducing a body force term  $g_\alpha(\mathbf{r}, t)$  in the lattice Boltzmann equation with single-relaxation collision operator — the so-called BGK model (17)— we obtain

$$f_\alpha(\mathbf{r} + \mathbf{e}_\alpha \delta t, t + \delta t) = f_\alpha(\mathbf{r}, t) - \frac{1}{\tau} [f_\alpha - f_\alpha^{(eq)}] + \delta t g_\alpha(\mathbf{r}, t), \quad (2.15)$$

For the cylindrical system, we find that body force term  $g_\alpha$  can be expressed as

$$g_\alpha = w_\alpha s + \frac{3\rho_0}{c^2} w_\alpha \mathbf{e}_\alpha \cdot \mathbf{a} + \frac{1}{2} \frac{c^2}{3r} \frac{\partial \rho'}{\partial r} + \frac{\rho_0}{r} \mathbf{u} \cdot \nabla u_r + w_\alpha \mathbf{e}_\alpha \cdot \mathbf{a}' \quad (2.16)$$

with

$$s = -\frac{\rho_0 u_r}{r},$$

$$a_z = \frac{\nu}{r} \frac{\partial u_z}{\partial r}, \quad a_r = \frac{\nu}{r} \left( \frac{\partial u_r}{\partial r} - \frac{u_r}{r} \right),$$

$$a'_z = \delta_t \tau \frac{\partial s}{\partial z}, \quad a'_r = \delta_t \tau \frac{\partial s}{\partial r}$$

### 2.6.1 Simulation and conclusions

We verify our model using a pipe Poiseuille flow as it amenable to an exact solution. In Fig. 2.23, the flatness corresponding to  $E_2/h^2 \approx \text{constant}$  demonstrates that this model is second order in space. In the discussion,  $E_2$  is  $L_2$  norm error and  $h$  is grid size.

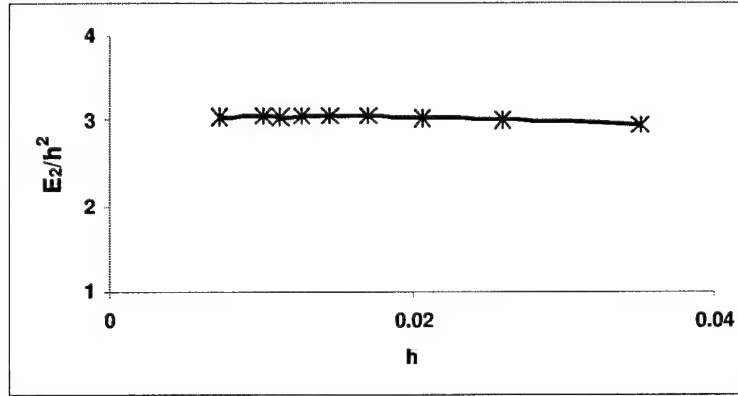


Figure 2.23: Errors between numerical and analytical solutions computed by formula G.48.  $G = 2.89351e - 05$ ,  $\tau = 1.0$

In conclusion, we present a LBM model for axisymmetric flows. The scheme has been proved to be second order accurate in space.

## Bibliography

- [1] G. R. McNamara and G. Zanetti, Use of the Boltzmann equation to simulate lattice-gas automata, *Phys. Rev. Lett.* **61**, 2332 (1988).
- [2] G. D. Doolen, ed., *Lattice Gas Methods for Partial Differential Equations* (Addison-Wesley, New York, 1990).
- [3] R. Benzi, S. Succi, and M. Vergassola, The lattice Boltzmann equation: Theory and applications, *Phys. Rep.* **222**, 145 (1992).
- [4] X. He and L.-S. Luo, A priori derivation of the lattice Boltzmann equation, *Phys. Rev. E* **55**, R6333 (1997).
- [5] X. He and L.-S. Luo, *Theory of the lattice Boltzmann method: From the Boltzmann equation to the lattice Boltzmann equation*, *Phys. Rev. E* **56**, 6811 (1997).
- [6] X. Shan and X. He, Discretization of the velocity space in the solution of the Boltzmann equation, *Phys. Rev. Lett.* **80**, 65 (1998).
- [7] D. Wolf-Gladrow, *Lattice-Gas Cellular Automata and Lattice Boltzmann Models*, Lecture Notes in Mathematics Vol. 1725 (Springer, Berlin, 2000).
- [8] A. K. Gunstensen, D. H. Rothman, S. Zaleski, and G. Zanetti, Lattice Boltzmann model of immiscible fluids, *Phys. Rev. A* **43**, 4320 (1991).
- [9] E. G. Flekkøy, Lattice Bhatnagar-Gross-Krook models for miscible fluids, *Phys. Rev. E* **47**, 4247 (1993).
- [10] D. Grunau, S. Chen, and K. Eggert, A lattice Boltzmann model for multiphase flow, *Phys. Fluids A* **5**, 2557 (1993).
- [11] X. Shan and G. Doolen, Multicomponent lattice-Boltzmann model with interparticle interaction, *J. Stat. Phys.* **81**, 379 (1995).



- [12] X. Shan and G. Doolen, Diffusion in a multicomponent lattice Boltzmann equation model, *Phys. Rev. E* **54**, 3614 (1996).
- [13] E. Orlandini, W. R. Osborn, and J. M. Yeomans, A lattice Boltzmann model of binary-fluid mixtures, *Europhys. Lett.* **32**, 463 (1995).
- [14] W. R. Osborn, E. Orlandini, M. R. Swift, J. M. Yeomans, and J. R. Banavar, Lattice Boltzmann study of hydrodynamic spinodal decomposition, *Phys. Rev. Lett.* **75**, 4031 (1995).
- [15] M. R. Swift, E. Orlandini, W. R. Osborn, and J. M. Yeomans, Lattice Boltzmann simulations of liquid-gas and binary fluid systems, *Phys. Rev. E* **54**, 5041 (1996).
- [16] A. Lamura, G. Gonnella, and J. M. Yeomans, A lattice Boltzmann model of ternary fluid mixtures, *Europhys. Lett.* **45**, 314 (1999).
- [17] P. L. Bhatnagar, E. P. Gross, and M. Krook, *A Model for Collision Processes in Gases. I. Small Amplitude Processes in Charged and Neutral One-Component Systems*, *Phys. Rev.* **94**, 511 (1954).
- [18] E. P. Gross and M. Krook, Models for Collision Processes in Gases: Small-Amplitude Oscillations of Charged Two-Component Systems, *Phys. Rev.* **102**, 593 (1956).
- [19] L.-S. Luo, Theory of the lattice Boltzmann method: Lattice Boltzmann models for nonideal gases; *Phys. Rev. E* **62**, 4982 (2000).
- [20] L.-S. Luo, Unified theory of lattice Boltzmann models for nonideal gases, *Phys. Rev. Lett.* **81**, 1618 (1998).
- [21] V. Eswaran and S.B. Pope, Direct Numerical Simulations of the Turbulent mixing of a Passive Scalar, *Physics of Fluids*, **31**, 506 (1988).
- [22] K. Yamamoto, X. He and G. D. Doolen, Simulation of Combustion Field with Lattice Boltzmann Method, accepted by *Journal Computational Physics*.

- [23] I. Yamaoka and H. Tsuji, *Twentieth Symposium(International) Combustion*, The Combustion Institute, Pittsburgh, 1883(1982).
- [24] N. N. Mansour and A. A. Wray, "Decay of isotropic turbulence at low Reynolds number," *Phys. Fluids* **6**, 808 (1994).
- [25] M.-J. Huang and A. Leonard, "Power-law decay of homogeneous turbulence at low Reynolds numbers," *Phys. Fluids* **6**, 3765 (1994).
- [26] Tavoulris S. and Corrsin S. Experiments in nearly homogenous turbulent shear flow with a uniform mean temperature gradient. Part 1. *J. Fluid Mech.* 1981;104:311.
- [27] Rogers MM, Moin P. The structure of the vorticity field in homogeneous turbulent flows. *J. Fluid Mech.*1987;176:33-66
- [28] Jacobitz FG, Sarkar S, and Van Atta CW. Direct numerical simulations of turbulence evolution in a uniformly sheared and stably stratified flow. *J. Fluid Mech.* 1997; 342:231-261.
- [29] S. B. Pope, *Turbulent Flows* (Cambridge University Press, Cambridge, 2000).
- [30] I. Halliday, L. A. Hammond, C. M. Care, K. Good, and A. Stevens, *Phys. Rev. E* **64** 011208(2001).

## Chapter 3

# Conclusions

The Lattice Boltzmann method (LBM) is an innovative computational tool for calculating complex fluid flow. This method is based on the more fundamental Boltzmann equation rather than the Navier-Stokes equation. Due to its firm founding in kinetic theory, LBM offers several key physical advantages for computing chemically reacting flow. Most importantly, it offers the possibility of modeling the processes of advection, mass transfer, and scalar and thermal transport in one single unified description. Furthermore, chemical-reaction computation at the sub-continuum level is easily amenable to LBM because of the its kinetic nature. These attributes are significant advantages over continuum-based methods, where various processes are modeled with individual, often incompatible, models. Progress made in the research under this grant clearly demonstrates the potential of this approach; however, much more needs to be done before this method can be used routinely for large scale turbulent combustion calculations. In future research, we shall continue to perform fundamental research necessary to realize that goal.

The research was performed principally at Texas A & M University with Prof. Sharath S. Girimaji as the principal investigator (PI). The National Institute of Aerospace (NIA) Hampton, Virginia, was a sub-contractor, with Dr. Li-Shi Luo as the co-PI. We also collaborated with the leading research groups in the world, as necessary, to advance LBM as

a viable computational tool for turbulent combustion.

## Chapter 4

## Appendix

## Appendix A

# Background of Lattice Boltzmann Method

Nomenclature			
$a^{(n)}$	Coefficients of $H^{(n)}$	$a^i$	Acceleration due to external force
$c_s$	Speed of sound	$e_\alpha$	Discretized particle velocity
$f$	Distribution function	$f^{(0)}$	Equilibrium distribution function
$H^{(n)}$	Hermite polynomial	$L$	Linearization operator
$Q$	Collision operator	$P_{\alpha\beta}$	Second moments of $f$
$R$	Gas constant	$T$	Temperature
$u$	Fluid velocity	$\rho$	Fluid density
$\xi$	Particle velocity	$'$	After collision state
$\lambda$	Relaxation time	$\tau$	Normalized relaxation time
$w_\alpha$	Weight function		

Historically, Lattice Boltzmann Equation was developed from lattice gas automata (1; 2; 3). However, the lattice Boltzmann equation can be directly derived from the continuous Boltzmann equation (4; 5; 6; 7), which can be written in a general form for a  $N$ -component

mixture (8):

$$\begin{aligned}
\partial_t f^i + \xi^i \cdot \nabla f^i + \mathbf{a}^i \cdot \nabla_{\xi} f^i &= \sum_{j=1}^N \int f'^i f'^j (1 + \vartheta_i f^i) (1 + \vartheta_j f^j) \\
&\quad - f^i f^j (1 + \vartheta_i f'^i) (1 + \vartheta_j f'^j) d\varphi d\xi^j \\
&= \sum_{j=1}^N Q(f^i, f^j),
\end{aligned} \tag{A.1}$$

where  $\vartheta_i = -1, 0, +1$ , for Fermi-Dirac, Maxwell-Boltzmann, and Einstein-Bose statistics;  $d\varphi = 2\pi\sigma \sin\chi d\chi$ , the quantities  $\sigma$  and  $\chi$  are the differential scattering cross-section and the angle of deflection, respectively;  $f^i = f(\mathbf{x}, \xi^i, t)$  and  $f'^i = f'(\mathbf{x}, \xi'^i, t)$  are the distributions before and after collision for the  $i$ -th species, and  $\mathbf{a}^i$  is the acceleration due to external force fields or a mean-field interaction. Derivation of LBM equations from the Boltzmann equation involves three steps that are briefly described here.

**Linearization.** For continuum systems or even neutron scattering processes, it is sufficient to use the linearized collision term  $L(g)$  to approximate the nonlinear collision term  $Q(f, f)$  as  $f = f^{(0)}(1 + g)$  and only keep linear terms in  $g$ , where  $f^{(0)}$  is the equilibrium solution, i.e.,  $Q(f^{(0)}, f^{(0)}) = 0$ . Function  $g$  can be expanded in some appropriate orthogonal basis, such as the generalized Hermite polynomials  $\{H^{(n)}\}$  (9),

$$g = \sum_{n=0}^{\infty} \frac{1}{n!} \mathbf{a}^{(n)}(\mathbf{x}, t) \cdot \mathbf{H}^{(n)}(\xi_0), \tag{A.2}$$

where  $\xi_0 := (\xi - \mathbf{u})$ ,  $a^{(0)} = 1$ ,  $a_{\alpha}^{(1)} = 0$ , and  $a_{\alpha\beta}^{(2)} = (P_{\alpha\beta}/p - \delta_{\alpha\beta})$ ,

$$P_{\alpha\beta} = \int \xi_{0\alpha} \xi_{0\beta} f d\xi, \quad p = \frac{1}{3} \int \xi_0^2 f d\xi.$$

The linearized collision term can be written in terms of  $\{H^{(n)}\}$ . For Maxwell molecules, the linearized collision operator becomes

$$L(g) = \sum_{n=0}^{\infty} \lambda_n \mathbf{a}^{(n)} \cdot \mathbf{H}^{(n)}, \quad L(H^{(n)}) = \lambda_n H^{(n)}. \tag{A.3}$$

**Reduction.** By approximating the spectrum  $\{\lambda_n\}$  of  $L$  by a finite number of distin-

guished eigenvalues, the linearized collision operator becomes

$$L_N(g) = \sum_{n=0}^N \lambda_n a^{(n)} \cdot H^{(n)} - \omega_N \sum_{n=N+1}^{\infty} a^{(n)} \cdot H^{(n)} = \sum_{n=0}^N (\lambda_n + \omega_N) a^{(n)} \cdot H^{(n)} - \omega_N g. \quad (\text{A.4})$$

By setting  $N = 0$ , the collision term is reduced to the simplest linear collision model, the celebrated Bhatnaga-Gross-Krook (BGK) model:

$$f^{(0)} L_0(g) = -\frac{1}{\lambda} [f - f^{(0)}], \quad \lambda = \frac{1}{\omega}.$$

**Discretization.** We shall only briefly describe the derivation of a lattice Boltzmann model from a continuous kinetic equation (4; 5; 6; 7). For the sake of simplicity without losing generality, we use the BGK equation for a single-component system without the forcing term and rewrite it as the following

$$D_t f = -\frac{1}{\lambda} [f - f^{(0)}], \quad D_t := \partial_t + \xi \cdot \nabla. \quad (\text{A.5})$$

Integration along characteristics followed by Taylor series expansion to first order in time leads to

$$f(x + \xi \delta_t, \xi, t + \delta_t) - f(x, \xi, t) = \frac{1}{\tau} [f(x, \xi, t) - f^{(0)}(x, \xi, t)], \quad \tau := \frac{\lambda}{\delta_t}. \quad (\text{A.6})$$

Further discretization in phase space, followed by appropriate approximation of the equilibrium distribution and low Mach number assumption leads to the current popular form of LBM. For a simple single species problem mixing, this leads to the following lattice Boltzmann equations:

$$f_\alpha(x + e_\alpha \delta_t, t + \delta_t) - f_\alpha(x, t) = -\frac{1}{\tau} (f_\alpha - f_\alpha^{(0)}), \quad (\text{A.7})$$

where  $\tau$  is the normalized relaxation time which determines the viscosity and  $f_\alpha^{(0)}$  is the discretized equilibrium distribution function:

$$f_\alpha^{(0)} = \left[ 1 + \frac{1}{RT} (e_\alpha - u) \cdot (u_\sigma - u) \right] f_\alpha^{(eq)}, \quad f_\alpha^{(eq)} = w_\alpha \rho \left[ 1 + \frac{(e_\alpha - u) \cdot u}{RT} + \frac{(e_\alpha \cdot u)^2}{2(RT)^2} \right]. \quad (\text{A.8})$$



The fluid density and flow momentum are moments of the distribution given by

$$\rho = \sum_{\alpha} f_{\alpha} = \sum_{\alpha} f_{\alpha}^{(0)}, \quad \rho u = \sum_{\alpha} e_{\alpha} f_{\alpha} = \sum_{\alpha} e_{\alpha} f_{\alpha}^{(0)}, \quad (\text{A.9})$$

In the above equations  $\{w_{\alpha}\}$  are uniquely determined by the discrete velocity set  $\{e_{\alpha}\}$ . It is important to point out that since the LBM is intrinsically multi-dimensional, there is no essential difference between two- and three-dimensional models – the only difference is the number of discrete velocities.

The most popular models of the LBM for one-component are D2Q9 and D3Q19 models for 2D and 3D, respectively, as shown in Figure A.1 and A.2.

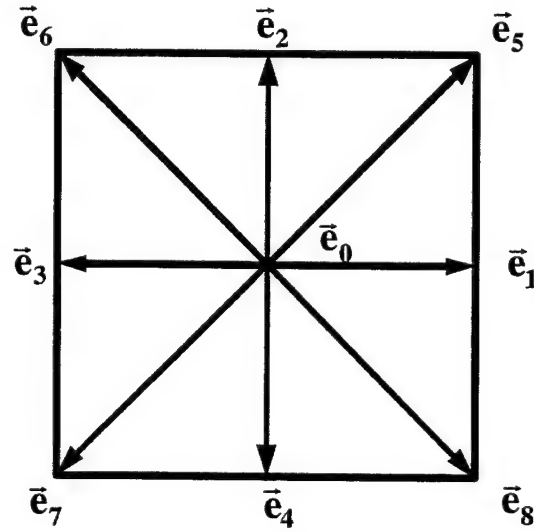


Figure A.1: D2Q9 model: 9 discrete velocities on a square lattice

Then the equilibrium distribution function for isothermal fluids is given as

$$f_{\alpha}^{(0)} = w_{\alpha} \rho \left[ 1 + 3 \frac{1}{c_s^2} (e_{\alpha} \cdot u) + \frac{1}{2c_s^4} (e_{\alpha} \cdot u)^2 - \frac{1}{c_s^2} u^2 \right] \quad (\text{A.10})$$

in which, for D2Q9 model, the discrete particle velocities  $e_{\alpha}$  and the weighting factor

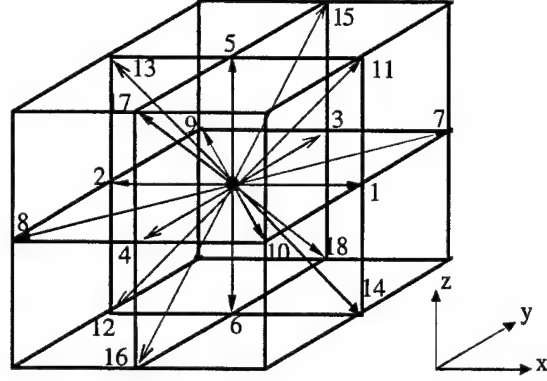


Figure A.2: D3Q19 model: 19 velocities lattice in 3D

$w_\alpha (\alpha = 0, 1, 2, \dots, 8)$  are

$$e_\alpha = \begin{cases} (0, 0), & \alpha = 0 \\ (\cos[(\alpha - 1)\pi/2], \sin[(\alpha - 1)\pi/2]), & \alpha = 1, 2, 3, 4 \\ (\cos[(\alpha - 5)\pi/2 + \pi/4], \sin[(\alpha - 5)\pi/2 + \pi/4]), & \alpha = 5, 6, 7, 8 \end{cases} \quad (\text{A.11})$$

and

$$w_\alpha = \begin{cases} 4/9, & \alpha = 0 \\ 1/9, & \alpha = 1, 2, 3, 4 \\ 1/36, & \alpha = 5, 6, 7, 8 \end{cases} \quad (\text{A.12})$$

respectively, and for D3Q19 model, the discrete particle velocities  $e_\alpha$  and the weighting factor  $w_\alpha (\alpha = 0, 1, 2, \dots, 18)$  are

$$e_\alpha = \begin{cases} (0, 0), & \alpha = 0 \\ (\pm 1, 0, 0)c, (0, \pm 1, 0)c, (0, 0, \pm 1)c, & \alpha = 1-6 \\ (\pm 1, \pm 1, 0)c, (\pm 1, 0, \pm 1)c, (\pm 1, \pm 1, 0)c, & \alpha = 7-18. \end{cases} \quad (\text{A.13})$$

and

$$w_\alpha = \begin{cases} 1/3, & \alpha = 0 \\ 1/18, & \alpha = 1, 2, \dots, 6 \\ 1/36, & \alpha = 7, 8, \dots, 18 \end{cases} \quad (\text{A.14})$$

respectively.

The sound speed is  $c_s = 1/\sqrt{3}(\delta_x/\delta_t)$  with  $\delta_x$  being the lattice constant of the underlying square lattice. The macroscopic quantities such as mass density  $\rho$  and mass velocity  $\mathbf{u}$  are given by

$$\rho = \sum_{\alpha} f_{\alpha} \quad (\text{A.15})$$

$$\rho \mathbf{u} = \sum_{\alpha} f_{\alpha} \mathbf{e}_{\alpha} \quad (\text{A.16})$$

Further points of note are: (i) By means of the Chapman-Enskog analysis (multiple scale expansion), we can derive the hydrodynamic equations for single-species fluid. (ii) This LBM formulation can be extended for multi-species systems as shown in (7). (iii) The lattice Boltzmann equation can be constructed as a fully *discrete* dynamical system without referring to the Boltzmann equation, but relying to some first principles of the kinetic theory. The LBM in this setting is called the generalized LBE method or multiple-relaxation-time (MRT) LBE (10; 11; 12; 13). Clearly the MRT-LBE is the fully discrete truncated counterpart of the linearized Boltzmann equation.

## Bibliography

- [1] U. Frisch, B. Hasslacher, Y. Pomeau, Lattice-gas automata for the navier-stokes equation, Phys. Rev. Lett. 56 (1986) 1505–1508.
- [2] S. Wolfram, Cellular automaton fluids 1: Basic theory, J. Stat. Phys. 45 (1986) 471–526.

- [3] U. Frisch, D. d'Humières, B. Hasslacher, P. Lallemand, Y. Pomeau, J.-P. Rivet, Lattice gas hydrodynamics in two and three dimensions, *Complex Systems* 1 (1987) 649–707.
- [4] X. He, L.-S. Luo, A priori derivation of the lattice boltzmann equation, *Phys. Rev. E.* 55 (1997) R6333.
- [5] X. He, L.-S. Luo, Theory of the lattice boltzmann method: From the boltzmann equation to the lattice boltzmann equation a priori derivation of the lattice boltzmann equation, *Phys. Rev. E.* 56 (1997) 6811.
- [6] L.-S. Luo, Unified theory of lattice boltzmann models for nonideal gases, *Phys. Rev. Lett.* 81 (1998) 1618–1621.
- [7] L.-S. Luo, S. S. Girimaji, Lattice boltzmann model for binary mixtures, *Phys. Rev. E.* 66 (2002) 035301.
- [8] J. O. Hirschfelder, C. F. Curtiss, R. B. Bird, *Molecular Theory of Gases and Liquids*, Wiley, New York, 1954.
- [9] H. Grad, *Handbuch der Physik*, Springer-Verlag, Berlin, 1958, pp. 205–294.
- [10] D. d'Humières, Generalized lattice boltzmann equations, *Prog. in Astro. Aero.* 159 (1992) 450–458.
- [11] P. Lallemand, L.-S. Luo, Theory of the lattice boltzmann method: Dispersion, dissipation, isotropy, galilean invariance, and stability, *Phys. Rev. E.* 61 ((6)) (2000) 6546.
- [12] D. d'Humières, I. Ginzburg, M. Krafczyk, P. Lallemand, L.-S. Luo, Multiple-relaxation-time lattice boltzmann models in three dimensions, *Phil. Trans. R. Soc. Lond. A* 220 (2002) 437–451.
- [13] P. Lallemand, L.-S. Luo, Theory of the lattice boltzmann method: Acoustic and thermal properties in two and three dimensions, *Phys. Rev. E.* 68 (2003) 036706.

## Appendix B

# Lattice Boltzmann Model for Binary Mixtures

### Nomenclature

$a$	Acceleration due to external force	$c$	Peculiar velocity of molecule
$D_{\sigma s}$	Binary-diffusion coefficient	$D_{\sigma\sigma}$	Self-diffusion coefficient
$e_\alpha$	Discretized particle velocity	$J$	Linearized collision operator
$f$	Distribution function	$f^{(0)}$	Equilibrium distribution function
$k$	Thermal conductivity	$k_B$	Boltzmann constant
$m$	Mass of molecule	$n$	Number density
$Q$	Collision operator	$p$	Pressure
$R$	Gas constant	$S_{ij}$	Strain rate
$T$	Temperature	$\Omega$	Solid angle
$u$	Fluid velocity	$\rho$	Fluid density
$\phi$	Mass concentration	$\varphi$	Molar concentration
$\xi$	Particle velocity	$'$	After collision state
$\lambda$	Relaxation time	$\tau$	Normalized relaxation time
$w_\alpha$	Weight function	$\nu$	Viscosity
$e$	Internal energy	$\delta_t$	Time step
$\mathbf{P}$	Stress tensor	$q$	Heat flux
$\mu_D, \mu_T, \mu_M, \nu'_M$			Relaxation parameters

## B.1 Introduction

In many practical flows involving pollutant dispersion, chemical processing, and combustor mixing/reaction, mass and momentum transport within multispecies fluids plays an important role. For these flows, it can be difficult to construct continuum-based models from first principles. Further, these flows typically involve complex geometry and/or multiple phases making computation with continuum-based models quite complicated. Therefore, for these flows, there is a growing interest in using the lattice Boltzmann equation (1; 2; 3; 4; 5; 6; 7).

In general, for computing fluid flow of any type, the lattice Boltzmann equation (LBE) (1; 2; 3; 4; 5; 6; 7) offers several computational advantages over continuum-based methods while retaining the flow physics intact. Although the origins of the modern lattice Boltzmann equation (LBE) can be traced back to lattice-gas automata (8; 9; 10), the new LBE models are free of some well-known defects associated with their predecessors. Recent works have unequivocally established that the lattice Boltzmann equation is in fact connected to kinetic theory (4; 5; 6) and completely consistent with the fundamental conservation principles governing fluid flow (11; 12; 13). In these Appendix, *a priori* derivation of the lattice Boltzmann equation from the parent continuous Boltzmann equation is developed (4; 5; 6). The Navier-Stokes equation also has its basis in the Boltzmann equation — the former can be derived from the latter through the Chapman-Enskog analysis (14). That very same Chapman-Enskog analysis can be used to show that the lattice Boltzmann methodology can be applied to solve any conservation law of the continuous Boltzmann equation including the Navier-Stokes equations. It has also been proved that the lattice Boltzmann equation tantamount to an explicit finite difference scheme of the Navier-Stokes equations with second order spatial accuracy and first order temporal accuracy with a non-zero compressibility (11; 12; 13). The present day lattice Boltzmann equation, with its high-fidelity physics and computation-efficient formulation, is a viable alternative to the continuum methods for simulating fluid flows. In fact, it can be argued that for many complex problems involving

multi-fluid phenomena, the physics can be more naturally captured by the Boltzmann-equation based methods rather than Navier-Stokes equation based methods. Recently LBE method has been extended to multiphase flows (15; 16; 17; 18) and multicomponent flows (19; 20; 21; 22; 23; 24; 25; 26; 27; 28; 29; 30; 31), flows through porous media (32; 33), and particulate suspensions in fluids (34; 35; 36; 37). Most existing LBE models for multicomponent fluids (19; 20; 21; 22; 23; 24; 25; 26; 27) tend to be somewhat heuristic and make the single-fluid assumption. The single-relaxation-time or Bhatnagar-Gross-Krook (BGK) approximation (38) is used in most existing models (21; 22; 23; 24; 25; 26; 27) restricting applicability to unity Prandtl and Schmidt numbers.

A rigorous mathematical development of multi-fluid lattice Boltzmann equation for multicomponent fluids is still in its infancy and such is the object of the present work. As a first step, in this work we develop a two-fluid lattice Boltzmann model which is based on kinetic theory for binary mixtures. Such a model would be capable of (i) simulating arbitrary Schmidt and Prandtl numbers, and (ii) accurately modeling the interaction between miscible and immiscible fluids. We follow a general approach within the framework of kinetic theory for developing the lattice Boltzmann models for multi-fluid mixtures. This work is a part of our ongoing effort to set the lattice Boltzmann equation on a more rigorous theoretical foundation and extend its use to more complex flows. We derive a discretized version of the continuum Boltzmann equations for binary mixtures. The extension of this methodology to multi-fluid mixtures is relatively straight-forward.

Kinetic theory of gas mixtures has received much attention in literature (14; 39; 40; 41; 42; 43; 44; 45; 47; 46; 48; 49; 50; 51). Many of the kinetic models for gas mixtures are based on the linearized Boltzmann equation (38; 52; 53), especially the single-relaxation-time model due to Bhatnagar, Gross, and Krook — the celebrated BGK model (38). The kinetic-theory mixtures model employed in this work was proposed by Sirrovich (43) which is also linear in nature.

This document is a detailed follow-up to our previous work published as a Rapid Com-

munications in PRE (31) and it is organized as follows. Section B.2 provides a brief review for some of the existing kinetic models of mixtures that form the theoretical basis of the present work. Section B.3 contains the derivation of the lattice Boltzmann model for binary mixtures from the corresponding continuous Boltzmann equations. In Sec. B.4, the hydrodynamic equations of the lattice Boltzmann model are determined. Section B.5 contains the derivation of the diffusion force and the mutual diffusion coefficient in the lattice Boltzmann model, and the diffusion-advection equations for the mass and molar concentrations of the system. Section B.6 discusses the short and long time behaviors of the model. Section B.7 concludes the Appendix with a summary of the present work and possible directions of future work. The three appendixes contain the details of: B.A.1 the iterative procedure to solve the Boltzmann equation; B.A.2 the discretized equilibrium distribution function; and, B.A.3 the Chapman-Enskog analysis of the lattice Boltzmann model for binary mixtures.

## B.2 Kinetic theory of gas mixtures

Following a procedure similar to the derivation of the Boltzmann equation for a pure system of single species, one can derive  $N$  simultaneous equations for a system of  $N$  species by reducing the appropriate Liouville equation. For the sake of simplicity without loss of generality, we shall only discuss the Boltzmann equations for a binary system here. The simultaneous Boltzmann equations for a binary system are

$$\partial_t f^A + \xi \cdot \nabla f^A + \mathbf{a}_A \cdot \nabla_\xi f^A = Q^{AA} + Q^{AB}, \quad (\text{B.1a})$$

$$\partial_t f^B + \xi \cdot \nabla f^B + \mathbf{a}_B \cdot \nabla_\xi f^B = Q^{BA} + Q^{BB}, \quad (\text{B.1b})$$

where  $Q^{AB} = Q^{BA}$  is the collision term due to the interaction among two different species A and B. Obviously, for an  $N$ -component system, there will be  $N$  such equations, each containing  $N$  collision terms on the right hand side. In general, the collision term is

$$Q^{AB} = \int d\xi_B d\Omega \sigma_{AB} \|\xi_B - \xi_A\| [f'^A f'^B - f^A f^B] \quad (\text{B.2})$$



where  $\sigma_{AB}$  is the differential cross section of A-B collision, and  $\Omega$  is the solid angle, and  $f'^A$  ( $f'^B$ ) and  $f^A$  ( $f^B$ ) denote the post-collision and pre-collision state of the particle A (B), respectively. Obviously, the equations for a system of multiple species are much more formidable to analyze than the comparable Boltzmann equation for a pure system of single species. The first modeling objective is to find a suitable approximation for the collision term given by Eq. (B.2) that would substantially simplify computation without compromising the essential physics.

The justified approximation of the collision terms must rely on our clear understanding of the underlying physical system. In a system of multiple species, there are a number of competing equilibration processes occurring simultaneously. The approach to equilibrium in the system can be roughly divided into two stages. First of all, each individual species equilibrates within itself so that its local distribution function approaches a local Maxwellian distribution. This process of individual equilibration is also referred to as Maxwellization. In the second stage, the entire system equilibrates so that the velocity and temperature differences among different species vanishes eventually. There are many different time scales in the equilibrating process of a multicomponent system. In addition, the Maxwellization itself can take place in many scenarios depending on the molecular weights and mass fractions of the participating species. Consider two mixtures, each consisting of a light and heavy gas. In Mixture 1, the total mass of each species is the same, implying smaller number density for the heavier gas. In Mixture 2, the number densities of the two species is the same, implying the mass density (or mass fraction) of the heavier species is larger. In Mixture 1, the Maxwellization of light species is mostly due to self-collision whereas the equilibration of the heavier species is predominantly due to cross collisions. This is due to the fact that the number of molecules of heavy species available for collisions is small. In Mixture 2, where the number densities of the two species are comparable, Maxwellization of both species involves self and cross collisions. When the process of Maxwellization is complete, the stress of the corresponding species becomes isotropic, or equivalently the heat conduction relaxes.

Therefore, the scale on which the stress becomes isotropic or the heat conduction relaxes is a suitable measure of Maxwellization.

The equilibration among different species can also take place in several different manners. Velocity and temperature differences may equilibrate on the same temporal scale (as in Mixture 1 above) or on vastly different scales (as in Mixture 2). In addition, these equilibrating processes need not to occur sequentially but also concurrently with the Maxwellization.

There is a significant amount of literature on gas mixtures within the framework of kinetic theory (14; 39; 40; 41; 42; 43; 44; 45; 47; 46; 48; 49; 50; 51). In the Chapman-Enskog analysis for a simple gas, one assumes a clear separation of scales in space and time, that is, to distinguish the spatial and temporal scales which are much larger than the mean free path or mean free time. An analogy for a mixture becomes difficult because of multiplicity of length scales. In the classic work of Chapman and Cowling (14), the full Boltzmann equations (with integral collision terms) for a binary mixture are analyzed under the assumptions that all scales are roughly of the same order, or equivalently, that the phenomenon to be examined is smooth with respect to all collisional scales. Determination of the various transport coefficients — viscosities, diffusivities, thermal diffusivities and conductivity — was the main objective of that work. However, no attempt was made to describe the dynamics of the evolution.

Direct analysis or computation of the Boltzmann equation is not generally feasible. This is due to the difficulty involved in evaluating the complex integral collision operators. To make further progress one can follow one of two approaches. The first, Grad's moment method, is to obtain the non-normal solutions of the Boltzmann equation (i.e., the solutions beyond the hydrodynamic or conserved variables) (54). Closure modeling would then be required to express the unclosed moments in terms of the closed moments. And the second is to derive simplified model equations from the Boltzmann equation which are more manageable to solve. Many model equations are influenced by Maxwell's approach to solving the Boltzmann equation by making extensive use of the properties of the Maxwell molecule (55)

and the linearized Boltzmann equation. The simplest model equations for a binary mixture is that by Gross and Krook (41), which is an extension of the single-relaxation-time model for a pure system — the celebrated BGK model (38).

With the BGK approximation (38; 41), the collision integrals  $Q^{\sigma\varsigma}$  [ $\sigma, \varsigma \in (A, B)$ ] can be approximated by following linearized collision terms

$$J^{\sigma\sigma} = -\frac{1}{\lambda_\sigma} [f^\sigma - f^{\sigma(0)}], \quad (\text{B.3a})$$

$$J^{\sigma\varsigma} = -\frac{1}{\lambda_{\sigma\varsigma}} [f^\sigma - f^{\sigma\varsigma(0)}], \quad (\text{B.3b})$$

where  $f^{\sigma(0)}$  and  $f^{\sigma\varsigma(0)}$  are Maxwellians

$$f^{\sigma(0)} = \frac{n_\sigma}{(2\pi R_\sigma T_\sigma)^{D/2}} e^{-(\xi - \mathbf{u}_\sigma)^2 / (2R_\sigma T_\sigma)}, \quad (\text{B.4a})$$

$$f^{\sigma\varsigma(0)} = \frac{n_\sigma}{(2\pi R_\sigma T_{\sigma\varsigma})^{D/2}} e^{-(\xi - \mathbf{u}_{\sigma\varsigma})^2 / (2R_\sigma T_{\sigma\varsigma})}, \quad (\text{B.4b})$$

where  $D$  is the spatial dimension,  $R_\sigma = k_B/m_\sigma$  is the gas constant of the  $\sigma$  species,  $k_B$  is the Boltzmann constant and  $m_\sigma$  is the molecular mass of the  $\sigma$  species. There are three adjustable relaxation parameters in the collision terms:  $\lambda_\sigma$ ,  $\lambda_\varsigma$ , and  $\lambda_{\sigma\varsigma} = (n_\varsigma/n_\sigma)\lambda_{\varsigma\sigma}$ . The first Maxwellian  $f^{\sigma(0)}$  is characterized by the conserved variables of each individual species: the number density  $n_\sigma$ , the mass velocity  $\mathbf{u}_\sigma$ , and the temperature  $T_\sigma$ ; while the second Maxwellian  $f^{\sigma\varsigma(0)}$  and  $f^{\varsigma\sigma(0)}$  is characterized by four adjustable parameters:  $\mathbf{u}_{\sigma\varsigma}$ ,  $\mathbf{u}_{\varsigma\sigma}$ ,  $T_{\sigma\varsigma}$ , and  $T_{\varsigma\sigma}$ . There are several considerations in determining these arbitrary parameters: simplicity of the resulting theory, accuracy of approximation, and ease of computation. Cross-collisional terms will be symmetric only if one takes  $\mathbf{u}_{\sigma\varsigma} = \mathbf{u}_{\varsigma\sigma} = \mathbf{u}$  and  $T_{\sigma\varsigma} = T_{\varsigma\sigma} = T$ , where  $\mathbf{u}$  and  $T$  are the velocity and temperature of the mixture. This is essential in preserving a similarity to irreversible thermodynamics, especially the Onsager relation (56). On the other hand, fewer terms in the expansion of  $f^\sigma$  about  $f^{\sigma\varsigma(0)}$  would be needed in many cases if one chooses  $\mathbf{u}_{\sigma\varsigma} = \mathbf{u}_\sigma$  and  $T_{\sigma\varsigma} = T_\sigma$ , i.e.,  $f^{\sigma\varsigma(0)} = f^{\sigma(0)}$ . One salient difference between using  $\mathbf{u}$  and  $T$  of the mixture in the Maxwellian  $f^{\sigma\varsigma(0)}$  as opposed to using  $\mathbf{u}_\sigma$  and  $T_\sigma$  for the species is that the former choice leads to a single-fluid theory,

i.e., a set of hydrodynamic equations for the mixture, while the latter leads to a two-fluid theory (43; 49), i.e., two sets of hydrodynamic equations for the species. Obviously, in the cases where the properties between the two species are vastly different, the two-fluid theory is preferred (56).

The cross-collision term  $J^{\sigma\varsigma}$  can be better approximated by expanding  $f^\sigma$  around the Maxwellian (43)

$$J^{\sigma\varsigma} = -\frac{f^{\sigma(0)}}{n_\sigma k_B T_\sigma} \left[ \mu_D \mathbf{c}_\sigma \cdot (\mathbf{u}_\sigma - \mathbf{u}_\varsigma) + \mu_T \frac{3}{2} \left( \frac{c_\sigma^2}{2R_\sigma T_\sigma} - 1 \right) (T_\sigma - T_\varsigma) - M_{\sigma\varsigma} \left( \frac{c_\sigma^2}{2R_\sigma T_\sigma} - 1 \right) (\mathbf{u}_\sigma - \mathbf{u}_\varsigma)^2 \right], \quad (\text{B.5})$$

where  $\mathbf{c}_\sigma = (\boldsymbol{\xi} - \mathbf{u}_\sigma)$  is the peculiar (or thermal) velocity of the  $\sigma$  species, and

$$M_{\sigma\varsigma} = \mu_m \frac{\rho_\sigma \rho_\varsigma}{\rho} \left[ \frac{1}{\rho_\sigma} + \mu'_m \frac{(n_\sigma - n_\varsigma)}{n_\sigma n_\varsigma (m_\sigma + m_\varsigma)} \right], \quad (\text{B.6})$$

and  $\mu_D$ ,  $\mu_T$ ,  $\mu_m$ ,  $\mu'_m$  are positive and at most functions of density and temperature (43), the physical significance of these parameters are to be discussed next.

We now consider the following model equations for a binary mixture due to Sirovich (43):

$$\partial_t f^\sigma + \boldsymbol{\xi} \cdot \nabla f^\sigma + \mathbf{a}_\sigma \cdot \nabla_{\boldsymbol{\xi}} f^\sigma = J^{\sigma\sigma} + J^{\sigma\varsigma}, \quad (\text{B.7})$$

where the self-collision term  $J^{\sigma\sigma}$  is approximated with the BGK model of Eq. (B.3a), and the cross-collision term  $J^{\sigma\varsigma}$  is given by Eq. (B.5). When the external force is not present ( $\mathbf{a}_\sigma = \mathbf{0}$ ), and if  $\mu_D$ ,  $\mu_T$ ,  $\mu_m$ ,  $\mu'_m$  are considered as constants (for the sake of simplicity) we can immediately obtain the following moment equations from the above equations

$$\partial_t (\mathbf{u}_\sigma - \mathbf{u}_\varsigma) = -\mu_D \left( \frac{1}{\rho_\sigma} + \frac{1}{\rho_\varsigma} \right) (\mathbf{u}_\sigma - \mathbf{u}_\varsigma), \quad (\text{B.8a})$$

$$\begin{aligned} \partial_t (T_\sigma - T_\varsigma) &= -\mu_T \frac{1}{k_B} \left( \frac{1}{n_\sigma} + \frac{1}{n_\varsigma} \right) (T_\sigma - T_\varsigma) \\ &\quad + \frac{2}{3k_B} \left( \frac{M_{\sigma\varsigma}}{n_\sigma} - \frac{M_{\varsigma\sigma}}{n_\varsigma} \right) (\mathbf{u}_\sigma - \mathbf{u}_\varsigma)^2. \end{aligned} \quad (\text{B.8b})$$

The above equations describe the exponential decay of the velocity and temperature differences for the two species, as discussed in the earlier remarks regarding the processes of Maxwellianization and equilibration in the mixture. The physical significance of the parameters  $\mu_D$ ,  $\mu_T$ ,  $\mu_m$ , and  $\mu'_m$  become apparent in the above equations — these parameters determine the relaxation rates in the Maxwellization processes.

Solving Eqs. (B.7) by means of iteration (cf. Ref. (43) or Appendix B.A.1), one first obtains

$$\mathbf{u}_\sigma = \mathbf{u}_\varsigma = \mathbf{u}, \quad (\text{B.9a})$$

$$T_\sigma = T_\varsigma = T, \quad (\text{B.9b})$$

$$\begin{aligned} f^{\sigma(0)} &= f^{\sigma\varsigma(0)}(n_\sigma, \mathbf{u}, T) \\ &= \frac{n_\sigma}{(2\pi R_\sigma T)^{D/2}} \exp \left[ -\frac{(\boldsymbol{\xi} - \mathbf{u})^2}{2R_\sigma T} \right]. \end{aligned} \quad (\text{B.9c})$$

Substituting the above results into the left-hand side of Eqs. (B.7), one has the following equation for the second-order solution of  $f^\sigma$  (43):

$$\begin{aligned} &f^{\sigma\varsigma(0)}(n_\sigma, \mathbf{u}, T) \left[ \frac{n}{n_\sigma} \mathbf{c}_\sigma \cdot \mathbf{d}_\sigma + \left( \frac{c_{\sigma i} c_{\sigma j}}{R_\sigma T} - \delta_{ij} \right) \cdot S_{ij} \right. \\ &\quad \left. + \left( \frac{c_\sigma^2}{2R_\sigma T} - \frac{5}{2} \right) \mathbf{c}_\sigma \cdot \nabla \ln T \right] \\ &= -\frac{1}{\lambda_\sigma} [f^\sigma - f^{\sigma(0)}] - \frac{f^{\sigma(0)}}{n_\sigma k_B T_\sigma} \left[ \mu_D \mathbf{c}_\sigma \cdot (\mathbf{u}_\sigma - \mathbf{u}_\varsigma) \right. \\ &\quad \left. + \mu_T \left( \frac{c_\sigma^2}{3R_\sigma T_\sigma} - 1 \right) (T_\sigma - T_\varsigma) \right. \\ &\quad \left. - M_{\sigma\varsigma} \left( \frac{c_\sigma^2}{3R_\sigma T_\sigma} - 1 \right) (\mathbf{u}_\sigma - \mathbf{u}_\varsigma)^2 \right], \end{aligned} \quad (\text{B.10})$$

where  $\mathbf{c}_\sigma = (\boldsymbol{\xi} - \mathbf{u}_\sigma)$ , and the diffusion force  $\mathbf{d}_\sigma$  and the rate-of-shear tensor  $S_{ij}$  are given

by

$$\begin{aligned} \mathbf{d}_\sigma &= \nabla \left( \frac{n_\sigma}{n} \right) + \frac{n_\sigma n_\zeta}{n\rho} (m_\zeta - m_\sigma) \nabla \ln p \\ &\quad - \frac{\rho_\sigma \rho_\zeta}{\rho p} (\mathbf{a}_\sigma - \mathbf{a}_\zeta), \\ &= -\mathbf{d}_\zeta, \end{aligned} \quad (\text{B.11a})$$

$$S_{ij} = \frac{1}{2} \left( \partial_i u_j + \partial_j u_i - \frac{2}{3} \nabla \cdot \mathbf{u} \delta_{ij} \right), \quad (\text{B.11b})$$

and  $p = nk_B T$  is the total pressure of the mixture. From the above solution of  $f^\sigma$ , one can compute for the relative velocity  $(\mathbf{u}_\sigma - \mathbf{u}_\zeta)$ , the temperature difference  $(T_\sigma - T_\zeta)$ , the (traceless) stress tensor  $p_{ij}$ , and the heat flux  $\mathbf{q}$  (43):

$$(\mathbf{u}_\sigma - \mathbf{u}_\zeta) = -\frac{nk_B T}{\mu_D} \mathbf{d}'_\sigma = -\frac{n^2}{n_\sigma n_\zeta} D_{\sigma\zeta} \mathbf{d}'_\sigma, \quad (\text{B.12a})$$

$$(T_\sigma - T_\zeta) = \frac{\mu_D \mu'_m}{\mu_T} \frac{m_\sigma m_\zeta (n_\sigma - n_\zeta)}{\rho (m_\sigma + m_\zeta)} (\mathbf{u}_\sigma - \mathbf{u}_\zeta)^2, \quad (\text{B.12b})$$

$$\begin{aligned} p_{ij} &= -2k_B T \left( \frac{n_\sigma}{\lambda_\sigma} + \frac{n_\zeta}{\lambda_\zeta} \right) S_{ij} - \frac{2\mu_D}{\rho} \left( \frac{\rho_\zeta}{\lambda_\sigma} + \frac{\rho_\sigma}{\lambda_\zeta} \right) \\ &\quad \times \left[ (\mathbf{u}_\sigma - \mathbf{u}_\zeta)_i (\mathbf{u}_\sigma - \mathbf{u}_\zeta)_j - \frac{1}{3} (\mathbf{u}_\sigma - \mathbf{u}_\zeta)^2 \delta_{ij} \right], \end{aligned} \quad (\text{B.12c})$$

$$\begin{aligned} \mathbf{q} &= \frac{5}{2} k_B T [n_\sigma (\mathbf{u}_\sigma - \mathbf{u}) + n_\zeta (\mathbf{u}_\zeta - \mathbf{u})] \\ &\quad - \frac{5}{2} k_B T \left( \frac{\rho_\sigma}{\lambda_\sigma} + \frac{\rho_\zeta}{\lambda_\zeta} \right) k_B \nabla T, \end{aligned} \quad (\text{B.12d})$$

where the diffusion force

$$\begin{aligned} \mathbf{d}'_\sigma &= \nabla \left( \frac{n_\sigma}{n} \right) + \frac{T_\sigma}{T} \frac{n_\sigma n_\zeta}{n\rho} (m_\zeta - m_\sigma) \nabla \ln p \\ &\quad - \frac{\rho_\sigma \rho_\zeta}{\rho p} (\mathbf{a}_\sigma - \mathbf{a}_\zeta), \end{aligned} \quad (\text{B.13a})$$

and the binary diffusion coefficient (53) of the model

$$D_{\sigma\zeta} = \frac{n_\sigma n_\zeta k_B T}{n \mu_D}. \quad (\text{B.14})$$

The self-diffusion coefficient  $D_{\sigma\sigma}$  is a special case of the above formula when  $n = n_\zeta = n_\sigma$ .

The viscosity  $\nu$  and thermal conductivity  $\kappa$  can also be read from the above formulas for

$p_{ij}$  and  $q$  as the following

$$\nu = k_B T \left( \frac{n_\sigma}{\lambda_\sigma} + \frac{n_\varsigma}{\lambda_\varsigma} \right), \quad (\text{B.15a})$$

$$\kappa = \frac{5}{2} k_B^2 T \left( \frac{\rho_\sigma}{\lambda_\sigma} + \frac{\rho_\varsigma}{\lambda_\varsigma} \right). \quad (\text{B.15b})$$

The above transport coefficients are determined by the parameters  $\lambda_\sigma$  and  $\mu_D$ ,  $\mu_T$ ,  $\mu_m$ , and  $\mu'_m$ :  $\lambda_\sigma$  determines the viscosity and the thermal conductivity of the  $\sigma$  species and the combination of  $\lambda_\sigma$ 's determines that of the mixture;  $\mu_D$  determines the diffusion coefficients in the model; and  $\mu_D \mu'_m / \mu_T$  determines the diffusion of the temperature difference due to velocity difference.

Two salient features of the model described by Eqs. (B.7) should be addressed. First, the cross-collision term  $J^{\sigma\varsigma}$  of Eq. (B.5) is exact for the Maxwell molecules obeying the inverse fifth-power interaction potential. Equations (B.7), therefore, can be considered to be a model for the Maxwell gas (43). One immediate consequence of this approximation is that the diffusion force of Eq. (B.12a) does not contain a thermal diffusion term, as it should. Second, the BGK approximation of the self-collision term  $J^{\sigma\sigma}$  of Eq. (B.3a) imposes the limitation of a unity Prandtl number. However both these limitations of the model can be overcome by using the linearized Boltzmann equation (57; 58; 59) with multiple relaxation times and a nonlinear approximation of the collision terms (43; 49; 60).

### B.3 The lattice Boltzmann model for binary mixture

We shall construct a lattice Boltzmann model for binary mixtures based on the model given by Eqs. (B.7). In the present work we only consider the isothermal case such that  $T_\sigma = T_\varsigma = T_{\sigma\varsigma} = T = \text{const.}$  Consequently, we can also ignore the terms related to thermal effects in  $J^{\sigma\varsigma}$  of Eq. (B.5) by setting  $\mu_T = \mu_m = \mu'_m = 0$ , i.e.,

$$J^{\sigma\varsigma} = -\frac{1}{\tau_D} \frac{\rho_\varsigma}{\rho} \frac{f^{\sigma(0)}}{R_\sigma T} (\boldsymbol{\xi} - \mathbf{u}) \cdot (\mathbf{u}_\sigma - \mathbf{u}_\varsigma), \quad (\text{B.16})$$

where the equilibrium function  $f^{\sigma(0)}$  for the  $\sigma$  species is chosen to be the Maxwellian equilibrium distribution depending on the mass velocity of the  $\sigma$  species  $\mathbf{u}_\sigma$  as the following

$$f^{\sigma(0)} = \frac{\rho_\sigma}{(2\pi R_\sigma T)^{D/2}} \exp \left[ -\frac{(\boldsymbol{\xi} - \mathbf{u}_\sigma)^2}{2R_\sigma T} \right]. \quad (\text{B.17})$$

Note that from hereafter  $f^{\sigma(0)}$  and  $f^\sigma$  are the single particle mass density distribution functions, as opposed to the single particle number density distribution functions. We can derive the lattice Boltzmann equation by discretizing the model equations (B.7), following the procedure described in (4; 5):

$$\begin{aligned} f_\alpha^\sigma(\mathbf{x}_i + \mathbf{e}_\alpha \delta_t, t + \delta_t) - f_\alpha^\sigma(\mathbf{x}_i, t) \\ = J_\alpha^{\sigma\sigma} + J_\alpha^{\sigma\varsigma} - F_\alpha^\sigma \delta_t, \end{aligned} \quad (\text{B.18})$$

where the self-collision term  $J_\alpha^{\sigma\sigma}$ , the cross-collision term  $J_\alpha^{\sigma\varsigma}$ , and the forcing term  $F_\alpha^\sigma$  are given by

$$J_\alpha^{\sigma\sigma} = -\frac{1}{\tau_\sigma} \left[ f_\alpha^\sigma - f_\alpha^{\sigma(0)} \right], \quad (\text{B.19a})$$

$$J_\alpha^{\sigma\varsigma} = -\frac{1}{\tau_D} \frac{\rho_\varsigma}{\rho} \frac{f^{\sigma(\text{eq})}}{R_\sigma T} (\mathbf{e}_\alpha - \mathbf{u}) \cdot (\mathbf{u}_\sigma - \mathbf{u}_\varsigma), \quad (\text{B.19b})$$

$$F_\alpha^\sigma = -w_\alpha \rho_\sigma \frac{\mathbf{e}_\alpha \cdot \boldsymbol{\alpha}_\sigma}{R_\sigma T}, \quad (\text{B.19c})$$

where  $\rho_\sigma$  and  $\rho_\varsigma$ , and  $\mathbf{u}_\sigma$  and  $\mathbf{u}_\varsigma$  are the mass densities and flow velocities for species  $\sigma$  and  $\varsigma$ , they are the moments of the distribution functions:

$$\rho_\sigma = \sum_\alpha f_\alpha^\sigma = \sum_\alpha f_\alpha^{\sigma(0)}, \quad (\text{B.20a})$$

$$\rho_\sigma \mathbf{u}_\sigma = \sum_\alpha f_\alpha^\sigma \mathbf{e}_\alpha = \sum_\alpha f_\alpha^{\sigma(0)} \mathbf{e}_\alpha, \quad (\text{B.20b})$$

and  $\rho$  and  $\mathbf{u}$  are respectively the mass density and the barycentric velocity of the mixture:

$$\rho = \rho_\sigma + \rho_\varsigma, \quad (\text{B.21a})$$

$$\rho \mathbf{u} = \rho_\sigma \mathbf{u}_\sigma + \rho_\varsigma \mathbf{u}_\varsigma. \quad (\text{B.21b})$$



The collision terms  $J_\alpha^{\sigma\sigma}$  and  $J_\alpha^{\sigma\varsigma}$  are constructed in such a way to respect the mass and momentum conservation laws. (The derivation of the forcing term  $F_\alpha^\sigma$  is given in Refs. (17; 18).)

The equilibrium distribution function  $f_\alpha^{\sigma(0)}$  has the following form in general (cf. Appendix B.A.2):

$$f_\alpha^{\sigma(0)} = \left[ 1 + \frac{1}{R_\sigma T} (\mathbf{e}_\alpha - \mathbf{u}) \cdot (\mathbf{u}_\sigma - \mathbf{u}) \right] f_\alpha^{\sigma(\text{eq})}, \quad (\text{B.22a})$$

$$f_\alpha^{\sigma(\text{eq})} = w_\alpha \rho_\sigma \left[ 1 + \frac{(\mathbf{e}_\alpha - \mathbf{u}) \cdot \mathbf{u}}{R_\sigma T} + \frac{(\mathbf{e}_\alpha \cdot \mathbf{u})^2}{2(R_\sigma T)^2} \right]. \quad (\text{B.22b})$$

where coefficients  $\{w_\alpha\}$  depend on the discrete velocity set  $\{\mathbf{e}_\alpha\}$ . For the sake of concreteness and simplicity without losing generality, we shall restrict ourselves to a nine-velocity model on a two-dimensional square lattice (D2Q9 model). In this case,

$$w_\alpha = \begin{cases} 4/9, & \alpha = 0 \\ 1/9, & \alpha = 1 - 4 \\ 1/36, & \alpha = 5 - 8. \end{cases} \quad (\text{B.23})$$

## B.4 Hydrodynamics

The left-hand side of Eq. (B.18) can be expanded in a Taylor series in  $\delta_t$  (up to second order in  $\delta_t$ ) and the equation can be rewritten as:

$$\delta_t D_\alpha f_\alpha^\sigma + \frac{1}{2} \delta_t^2 D_\alpha^2 f_\alpha^\sigma = J_\alpha^{\sigma\sigma} + J_\alpha^{\sigma\varsigma} - F_\alpha^\sigma \delta_t, \quad (\text{B.24})$$

where  $D_\alpha = \partial_t + \mathbf{e}_\alpha \cdot \nabla$ . Obviously,

$$\sum_\alpha J_\alpha^{\sigma\sigma} = \sum_\alpha J_\alpha^{\varsigma\sigma} = \sum_\alpha F_\alpha^\sigma = 0, \quad (\text{B.25a})$$

$$\sum_\alpha J_\alpha^{\sigma\sigma} \mathbf{e}_\alpha = 0, \quad (\text{B.25b})$$

$$\sum_\alpha J_\alpha^{\varsigma\sigma} \mathbf{e}_\alpha = -\frac{1}{\tau_D} \frac{\rho_\sigma \rho_\varsigma}{\rho} (\mathbf{u}_\sigma - \mathbf{u}_\varsigma), \quad (\text{B.25c})$$

$$\sum_\alpha F_\alpha^\sigma \mathbf{e}_\alpha = -\rho_\sigma \mathbf{a}_\sigma. \quad (\text{B.25d})$$

By means of the Chapman-Enskog analysis (multiple-scale expansion), we can derive the hydrodynamic equations for the mixture from Eq. (B.24) (see details in Appendix B.A.3 ).

The mass conservation laws for each species and the mixture can be derived immediately from Eq. (B.24):

$$\partial_t \rho_\sigma + \nabla \cdot (\rho_\sigma \mathbf{u}_\sigma) = \frac{1}{2} \nabla \cdot \left[ \frac{\rho_\sigma \rho_\varsigma}{\tau_D \rho} (\mathbf{u}_\sigma - \mathbf{u}_\varsigma) \right], \quad (\text{B.26})$$

$$\partial_t \rho + \nabla \cdot (\rho \mathbf{u}) = 0. \quad (\text{B.27})$$

Note that the mass conservation does not hold for each individual species at the Navier-Stokes level, although it does at the Euler level. However, the mass conservation law does apply to the mixture as a whole. The right hand side of Eq. (B.26) reflects the mass flux due to diffusion.

We can also derive the Euler equation for each species:

$$\begin{aligned} \rho_\sigma \partial_{t_0} \mathbf{u}_\sigma + \rho_\sigma \mathbf{u}_\sigma \cdot \nabla \mathbf{u}_\sigma &= -\nabla p^\sigma \\ &+ \rho_\sigma \mathbf{a}_\sigma - \frac{1}{\tau_D \delta_t} \frac{\rho_\sigma \rho_\varsigma}{\rho} (\mathbf{u}_\sigma - \mathbf{u}_\varsigma), \end{aligned} \quad (\text{B.28})$$

where  $p^\sigma = n_\sigma k_B T = \rho_\sigma R_\sigma T$  is the partial pressure of the  $\sigma$  species, and the Navier-Stokes equation:

$$\begin{aligned} \rho_\sigma \partial_t \mathbf{u}_\sigma + \rho_\sigma \mathbf{u}_\sigma \cdot \nabla \mathbf{u}_\sigma &= -\nabla p^\sigma + \rho_\sigma \nu_\sigma \nabla^2 \mathbf{u}_\sigma \\ &+ \rho_\sigma \mathbf{a}_\sigma - \frac{1}{\tau_D \delta_t} \frac{\rho_\sigma \rho_\varsigma}{\rho} (\mathbf{u}_\sigma - \mathbf{u}_\varsigma), \end{aligned} \quad (\text{B.29})$$

where the viscosity of the  $\sigma$  species is

$$\nu_\sigma = R_\sigma T \left( \tau_\sigma - \frac{1}{2} \right) \delta_t. \quad (\text{B.30})$$

Eq. (B.29) is consistent with the results in Ref. (49).

## B.5 Diffusion in isothermal mixtures

The difference between the two Navier-Stokes equations for individual species ( $\sigma$  and  $\varsigma$ ) leads to the following equation:

$$\begin{aligned} \frac{1}{\tau_D \delta_t} (\mathbf{u}_\sigma - \mathbf{u}_\varsigma) = & -\frac{\rho p}{\rho_\sigma \rho_\varsigma} \mathbf{d}_\sigma \\ & - \left\{ \partial_t \delta \mathbf{u} + \nabla \cdot (\bar{\mathbf{u}} \delta \mathbf{u}) + \nabla^2 (\nu_\sigma \mathbf{u}_\sigma - \nu_\varsigma \mathbf{u}_\varsigma) \right\}, \end{aligned} \quad (\text{B.31})$$

where  $\delta \mathbf{u} = (\mathbf{u}_\sigma - \mathbf{u}_\varsigma)$ ,  $\bar{\mathbf{u}} = \frac{1}{2}(\mathbf{u}_\sigma + \mathbf{u}_\varsigma)$ ,  $\nabla \cdot (\bar{\mathbf{u}} \delta \mathbf{u}) = \bar{\mathbf{u}} \cdot \nabla \delta \mathbf{u} + \delta \mathbf{u} \cdot \nabla \bar{\mathbf{u}}$ , and the diffusion force

$$\begin{aligned} \mathbf{d}_\sigma &= \frac{\rho_\sigma \rho_\varsigma}{\rho p} \left[ \left( \frac{1}{\rho_\sigma} \nabla p_\sigma - \frac{1}{\rho_\varsigma} \nabla p_\varsigma \right) - (\mathbf{a}_\sigma - \mathbf{a}_\varsigma) \right] \\ &= \nabla \left( \frac{n_\sigma}{n} \right) + \left( \frac{n_\sigma}{n} - \frac{\rho_\sigma}{\rho} \right) \nabla \ln p \\ &\quad + \frac{\rho_\sigma \rho_\varsigma}{\rho p} (\mathbf{a}_\varsigma - \mathbf{a}_\sigma) \\ &= \nabla \left( \frac{n_\sigma}{n} \right) + \frac{n_\sigma n_\varsigma}{n \rho} (m_\varsigma - m_\sigma) \nabla \ln p \\ &\quad + \frac{\rho_\sigma \rho_\varsigma}{\rho p} (\mathbf{a}_\varsigma - \mathbf{a}_\sigma) \\ &= -\mathbf{d}_\varsigma, \end{aligned} \quad (\text{B.32})$$

where  $p = nk_B T$  is the total pressure of the mixture, and the total number density  $n$  is

$$n = n_\sigma + n_\varsigma = \frac{\rho_\sigma}{m_\sigma} + \frac{\rho_\varsigma}{m_\varsigma}. \quad (\text{B.33})$$

The diffusion force includes the effects due to the molar concentration gradient  $\nabla(n_\sigma/n)$ , the total pressure gradient and the particle mass difference  $(m_\sigma - m_\varsigma) \nabla \ln p$ , and the external force  $(\mathbf{a}_\sigma - \mathbf{a}_\varsigma)$ .

It has already been assumed in the derivation of the two-fluid equations that derivatives are slowly varying on the time scale of Maxwellization (49). Therefore the terms inside the curly brackets Eq. (B.31) can be neglected in the diffusion time scale. Thus, to the leading order, we have

$$(\mathbf{u}_\sigma - \mathbf{u}_\varsigma) = -\tau_D \delta_t \frac{\rho p}{\rho_\sigma \rho_\varsigma} \mathbf{d}_\sigma. \quad (\text{B.34})$$

Also, by definition (53, Eq. (6.5-7a)), we have

$$(\mathbf{u}_\sigma - \mathbf{u}_\zeta) = -\frac{n^2}{n_\sigma n_\zeta} D_{\sigma\zeta} \mathbf{d}_\sigma, \quad (\text{B.35})$$

thus the mutual diffusion coefficient in the mixture is

$$D_{\sigma\zeta} = \frac{\rho k_B T}{n m_\sigma m_\zeta} \tau_D \delta_t. \quad (\text{B.36})$$

Note that the difference between the above formula and Eq. (B.14) is due to the difference of a factor  $\rho_\sigma \rho_\zeta / \rho$  between  $J_\alpha^{\sigma\zeta}$  of Eq. (B.19b) and  $J^{\sigma\zeta}$  of Eq. (B.5), i.e.,

$$\tau_D \delta_t = \frac{\rho_\sigma \rho_\zeta}{\rho} \frac{1}{\mu_D}.$$

The mass flux of the  $\sigma$  species, by definition, is

$$\mathbf{j}_\sigma = \rho_\sigma (\mathbf{u}_\sigma - \mathbf{u}) = -\tau_D \delta_t p \mathbf{d}_\sigma,$$

where we have used the identity that  $\rho(\mathbf{u}_\sigma - \mathbf{u}) = \rho_\zeta(\mathbf{u}_\sigma - \mathbf{u}_\zeta)$ . The continuity equation (B.26) for the  $\sigma$  species can be written as

$$D_t \rho_\sigma + \rho_\sigma \nabla \cdot \mathbf{u} + \nabla \cdot \mathbf{j}_\sigma = -\frac{1}{2} \delta_t \nabla \cdot (p \mathbf{d}_\sigma), \quad (\text{B.37})$$

where  $D_t = (\partial_t + \mathbf{u} \cdot \nabla)$ . By assuming the incompressibility of the fluid (i.e.,  $\nabla \cdot \mathbf{u} = 0$ ), we obtain the following advection-diffusion equation for an isothermal mixture

$$\partial_t \rho_\sigma + \mathbf{u} \cdot \nabla \rho_\sigma = \nabla \cdot \tau_D^* \delta_t p \mathbf{d}_\sigma, \quad \tau_D^* \equiv \left( \tau_D - \frac{1}{2} \right). \quad (\text{B.38})$$

Similar to the Hénion correction for the viscosity (61), the diffusivity is modified by the second-order discrete effect:

$$D_{\sigma\zeta}^* = \frac{\rho k_B T}{n m_\sigma m_\zeta} \left( \tau_D - \frac{1}{2} \right) \delta_t = \frac{\rho k_B T}{n m_\sigma m_\zeta} \tau_D^* \delta_t. \quad (\text{B.39})$$

Obviously, the self-diffusion coefficient in the lattice Boltzmann model for the  $\sigma$  species is

$$D_{\sigma\sigma}^* = \frac{k_B T}{m_\sigma} \tau_D^* \delta_t. \quad (\text{B.40})$$

The mass concentration  $\phi$  and molar concentration  $\varphi$  (dimensionless order parameters) are defined as

$$\phi = \frac{(\rho_\sigma - \rho_\varsigma)}{(\rho_\sigma + \rho_\varsigma)}, \quad \varphi = \frac{(n_\sigma - n_\varsigma)}{(n_\sigma + n_\varsigma)}, \quad (\text{B.41})$$

and they related to each other

$$\phi = \frac{(m_\sigma - m_\varsigma) + (m_\sigma + m_\varsigma)\varphi}{(m_\sigma + m_\varsigma) + (m_\sigma - m_\varsigma)\varphi}, \quad (\text{B.42a})$$

$$\varphi = \frac{(m_\varsigma - m_\sigma) + (m_\varsigma + m_\sigma)\phi}{(m_\varsigma + m_\sigma) + (m_\varsigma - m_\sigma)\phi}. \quad (\text{B.42b})$$

The diffusion force can be written in terms of  $\phi$  and  $\varphi$ :

$$\mathbf{d}_\sigma = \frac{1}{2} \left[ \nabla \varphi + (\varphi - \phi) \nabla \ln p + \frac{\rho(1 - \phi^2)}{2p} (\mathbf{a}_\varsigma - \mathbf{a}_\sigma) \right].$$

The nonlinear diffusion-advection equations satisfied by  $\phi$  and  $\varphi$  can be derived from Eq. (B.38):

$$\partial_t \phi + \mathbf{u} \cdot \nabla \phi = \frac{1}{\rho} \nabla \cdot (D_\phi^* \nabla \phi + \mathbf{F}), \quad (\text{B.43a})$$

$$\partial_t \varphi + \mathbf{u} \cdot \nabla \varphi = \frac{A}{n} \nabla \cdot (D_\varphi^* \nabla \varphi + \mathbf{F}), \quad (\text{B.43b})$$

where

$$D_\phi^* = \frac{p\tau_D^* \delta_t}{m_\sigma m_\varsigma} \left( \frac{\rho}{n} \right)^2 = \frac{k_B T}{m_\sigma m_\varsigma} \frac{\rho^2}{n} \tau_D^* \delta_t, \quad (\text{B.44a})$$

$$D_\varphi^* = p\tau_D^* \delta_t, \quad (\text{B.44b})$$

$$\mathbf{F} = \left[ (\varphi - \phi) \nabla p + \frac{1}{2} \rho(1 - \phi^2) (\mathbf{a}_\varsigma - \mathbf{a}_\sigma) \right] \tau_D^* \delta_t, \quad (\text{B.44c})$$

$$A = \frac{1}{2} \left[ \frac{(1 - \varphi)}{m_\sigma} + \frac{(1 + \varphi)}{m_\varsigma} \right]. \quad (\text{B.44d})$$

Obviously, when  $m_\sigma = m_\varsigma$ ,  $\varphi = \phi$ , and then Eq. (B.43a) and Eq. (B.43b) become identical.

## B.6 Short and long time behaviors

As discussed in Sec. B.2, short and long time behaviors of a binary mixture involve different Maxwellization and equilibration processes. This is reflected in the macroscopic equations

derived in preceding sections. In an initial stage (short time), the diffusion velocity ( $\mathbf{u}_\sigma - \mathbf{u}_\zeta$ ) is significant, thus the system is described  $2(D + 1)$  equations, i.e., two sets of mass and momentum conservation laws for each species given by Eqs. (B.26) and (B.29). As the system equilibrates so that the diffusion velocity ( $\mathbf{u}_\sigma - \mathbf{u}_\zeta$ ) is diminishing, the physics is then described by  $(D + 2)$  equations: the continuity equation of the mixture, Eq. (B.27), the Navier-Stokes equation for the barycentric velocity of the mixture  $\mathbf{u}$ , and the diffusion-advection equation for the mass [Eq. (B.43a)] or molar [Eq. (B.43b)] concentrations. Only in very late stage of equilibration, the concentration behaves more or less as a passive scalar.

The Navier-Stokes equation for  $\mathbf{u}$  is

$$\rho \partial_t \mathbf{u} + \rho \mathbf{u} \cdot \nabla \mathbf{u} = -\nabla p + \nabla \cdot \Pi + \rho \mathbf{a}, \quad (\text{B.45})$$

where  $p = k_B T(n_\sigma + n_\zeta)$ ,  $\rho \mathbf{a} = \rho_\sigma \mathbf{a}_\sigma + \rho_\zeta \mathbf{a}_\zeta$ , and

$$\begin{aligned} \Pi &= \sum_\sigma \rho_\sigma \nu_\sigma [(\nabla \mathbf{u}_\sigma) + (\nabla \mathbf{u}_\sigma)^\dagger] \\ &\approx (\rho_\sigma \nu_\sigma + \rho_\zeta \nu_\zeta) [(\nabla \mathbf{u}) + (\nabla \mathbf{u})^\dagger]. \end{aligned} \quad (\text{B.46})$$

In the derivation of Eq. (B.45), we ignore two terms: one is  $(\tau_D D_{\sigma\zeta}^* n / R_\sigma T n_\sigma n_\zeta) \nabla (p d_\sigma)^2$ , and the other is in proportion of  $\mathbf{u}(\mathbf{u}_\sigma - \mathbf{u}_\zeta)$  due to  $J_\alpha^{\sigma\zeta}$  [cf. Eq. (B.58)]. These terms are negligible when the mixture is more or less homogeneous. Also, when the diffusion velocity ( $\mathbf{u}_\sigma - \mathbf{u}_\zeta$ ) vanishes, the approximation in Eq. (B.46) becomes exact.

Some remarks to place the present work in perspective are in order. Unlike most existing lattice Boltzmann models for binary mixtures (22; 23; 24; 25; 26; 27), the mutual and self diffusion coefficients of the present model are independent of the viscosity. (We note that an existing model proposed by Flekkøy (20) already has this feature.) The diffusion coefficients depend on the relaxation parameter  $\tau_D$  and relevant physical properties of the mixture, such as the molecular masses of each species  $m_\sigma$  and  $m_\zeta$ , etc. The present model is therefore capable of incorporating more general physics. In addition, the present model can simulate both miscible and immiscible binary mixtures by changing the sign of  $(\tau_D - 1/2)$ , i.e., for

positive  $(\tau_D - 1/2)$ , the mixture is miscible, and for negative  $(\tau_D - 1/2)$ , the mixture is immiscible. We have performed numerical simulations to verify that: (a) the diffusion coefficient  $D_{\sigma\zeta}^*$  depends on  $\tau_D$  as given by Eq. (B.39) and it is independent of  $\tau_\sigma$  and  $\tau_\zeta$ ; and (b) when  $(\tau_D - 1/2) < 0$ , spinodal decomposition or separation (anti-diffusion) between different species in the mixture occurs. (The details of the numerical results will be reported elsewhere.)

## B.7 Discussion and conclusions

We have constructed a lattice Boltzmann model for binary mixtures with several important features. All the modeling issues are addressed at the continuum level within the framework of extended kinetic theory. The lattice Boltzmann model is then directly derived from the continuous kinetic model equations using a formal discretization procedure. The lattice model thus inherits the sound physics and mathematical rigor incumbent in kinetic theory. This is in contrast to previous lattice Boltzmann models for mixtures (22; 23; 24; 25; 26; 27), which are not directly based on the fundamental physics of continuum kinetic equations. These models rely on fictitious interactions (22; 23) or heuristic free energies (24; 25; 26; 27) to produce the requisite mixing. (Many defects of the free-energy models (24; 25; 26; 27) are due to the incorrectly defined equilibria (18).) These non-physical effects present a further problem since they are not easily amenable to mathematical analysis (17; 18). The heuristic elements of the previous lattice Boltzmann models (22; 23; 24; 25; 26; 27) have been eliminated, resulting in a physically justifiable model that is simple to compute. Further, due to the close connection to kinetic theory, the derivation of the hydrodynamic equations associated with the lattice Boltzmann model is significantly simplified and rendered mathematically more rigorous. The derivation of the hydrodynamic equations from the previous lattice models are much less rigorous (22; 23; 24; 25; 26; 27).

The second important feature of the present work is that the model is based upon a two-

fluid theory of binary mixtures. The previous models (19; 20; 21; 22; 23; 24; 25; 26; 27; 51), on the other hand, are derived from a simpler, but highly restrictive, one-fluid theory. In the single-fluid models with BGK approximation one is constrained to use the *ad hoc* “equilibrium velocity” (22; 23; 51)

$$\mathbf{u}^{(\text{eq})} = \frac{(\tau_\varsigma \rho_\sigma \mathbf{u}_\sigma + \tau_\sigma \rho_\varsigma \mathbf{u}_\varsigma)}{(\tau_\varsigma \rho_\sigma + \tau_\sigma \rho_\varsigma)}$$

in the equilibrium distribution function  $f_\alpha^{\sigma(0)}$  in order to satisfy the local conservation laws. As a result, the viscous relaxation process and the diffusion process are inseparable. The analysis of these models therefore becomes unnecessarily tedious and cumbersome (22; 23). The models with free energies (24; 25; 26; 27) do not yield correct hydrodynamic equations (17; 18), mostly due to the incorrectly defined equilibrium distribution functions used in these models (18; 62). Furthermore, single-fluid models cannot be applied to mixtures of species with vastly different properties. In the present two-fluid model, the diffusion behavior is decoupled from viscous relaxation. The diffusivity is determined by the parameter  $\tau_D$  and the physical properties of the mixture. The model is capable of simulating either miscible or immiscible fluids by changing the sign of  $(\tau_D - 1/2)$ .

The proposed LBE model for binary mixtures simulates diffusion by considering a mutual interaction term leading to the diffusion velocity  $(\mathbf{u}_\sigma - \mathbf{u}_\varsigma)$  which is directly related to the diffusion driving force in binary mixtures. The diffusion velocity  $(\mathbf{u}_\sigma - \mathbf{u}_\varsigma)$  is of the first order in the density gradient  $\nabla\rho$ . This suggests that the proposed model, however, does not include any higher order terms of the density gradient. This in turn implies that the proposed model does not have a surface tension, which is related to the density gradient square  $|\nabla\rho|^2$ . To include the effect due surface tension, the terms related to  $|\nabla\rho|^2$  must be explicitly considered.

To further improve the proposed lattice Boltzmann model for binary mixing, efforts are currently underway are: (a) development of a multiple-relaxation-time model for the self-collision term (57; 58; 59) that will significantly enhance the numerical stability of the



scheme (58; 59); (b) consideration of models with surface tension; (c) inclusion of thermal diffusion effects which may be important in combustion applications; and, (d) development of a model for non-Maxwellian molecules. It should be noted that all the existing lattice Boltzmann models are only applicable to the Maxwell molecules as a direct consequence of the linearization of the Boltzmann equation. This limitation can be overcome by either using a different expansion of the distribution function, or by including the non-Maxwellian effects in the collision terms.

## Appendix

### B.A.1 Iterative Solution of the Boltzmann Equation

We present a short description of the iterative procedure (43) to solve the Boltzmann equation

$$D_t f = Q[f] \quad (\text{B.47})$$

where  $D_t = \partial_t + \xi \cdot \nabla$  and  $Q[f]$  is the collision term. The  $(n+1)$ -th iteration solution  $f^{(n+1)}$  is obtained from the  $n$ -th iteration solution  $f^{(n)}$  by solving the equation

$$Q[f^{(n+1)}] = D_t f^{(n)}, \quad (\text{B.48})$$

subject to the following conservation constraints

$$\int d\xi f^{(n+1)} \begin{bmatrix} 1 \\ \xi \\ \xi^2 \end{bmatrix} = \int d\xi f^{(0)} \begin{bmatrix} 1 \\ \xi \\ \xi^2 \end{bmatrix}, \quad (\text{B.49})$$

where  $f^{(0)} = f^{(0)}(\rho^{(n+1)}, \mathbf{u}^{(n+1)}, T^{(n+1)})$  is the equilibrium distribution function which depends on the hydrodynamical moments  $\rho$ ,  $\mathbf{u}$ , and  $T$  computed from  $f^{(n+1)}$ . Following the Chapman-Enskog procedure, the temporal derivatives are removed by using the conserva-

tion equations:

$$\begin{aligned}\partial_t \rho^{(n+1)} &= -\nabla \cdot (\rho \mathbf{u}), \\ \partial_t \mathbf{u}^{(n+1)} &= -\mathbf{u} \cdot \nabla \mathbf{u} + \mathbf{a} - \frac{1}{\rho} \nabla \cdot \mathbf{P}^{(n)}, \\ \partial_t e^{(n+1)} &= -\nabla \cdot (e \mathbf{u}) + \rho \mathbf{a} \cdot \mathbf{u} - \nabla \cdot \mathbf{q}^{(n)} + \mathbf{P}^{(n)} : \nabla \mathbf{u},\end{aligned}$$

where  $e$  is the internal energy and  $e = \frac{D}{2} n k_B T$  for ideal gases, and  $\mathbf{P}$  and  $\mathbf{q}$  are the stress tensor and the heat flux, respectively. On right hand side of the above equations, the hydrodynamical moments  $\rho$ ,  $\mathbf{u}$ , and  $e$  are computed from the  $(n+1)$ -th iteration solution  $f^{(n+1)}$  but their superscript  $(n+1)$  are omitted since they are conserved quantities. On the other hand, the stress tensor  $\mathbf{P}$  and the heat flux  $\mathbf{q}$ , which are not conserved, are denoted with the superscript  $n$  as they are obtained from the solution of the previous iteration  $f^{(n)}$ .

In general, the iterative procedure described above is expected to converge more rapidly than a procedure of successive approximation, such as the Chapman-Enskog procedure for the Boltzmann equation. The reason is that in the iterative procedure the (nonlinear) integral equation must be solved at each step as given by Eq. (B.48), whereas in the Chapman-Enskog procedure the integral equation is only solved at the initial step and at all approximation of higher order only the linearized integral equation is solved.

### B.A.2 The equilibrium distribution function

We consider the equilibrium distribution function of Eq. (B.17) for  $\sigma$  species based on its mass velocity  $\mathbf{u}_\sigma$ . The distribution function can be written in terms of the mixture velocity  $\mathbf{u}$  as follows:

$$\begin{aligned}& \exp \left[ -\frac{1}{2} \frac{(\boldsymbol{\xi} - \mathbf{u}_\sigma)^2}{R_\sigma T} \right] \\ &= \exp \left[ -\frac{1}{2} \frac{(\boldsymbol{\xi} - \mathbf{u})^2}{R_\sigma T} \right] \exp \left[ \frac{(\boldsymbol{\xi} - \mathbf{u}) \cdot (\mathbf{u} - \mathbf{u}_\sigma)}{R_\sigma T} \right] \\ & \quad \times \exp \left[ -\frac{1}{2} \frac{(\mathbf{u} - \mathbf{u}_\sigma)^2}{R_\sigma T} \right].\end{aligned}\tag{B.50}$$

With the procedure described in (4; 5),  $f_{\alpha}^{\sigma(\text{eq})}$  of Eq. (B.22b) is the second order Taylor expansion of the first exponential in the right-hand side of the above equality. Because the velocity difference  $(\mathbf{u} - \mathbf{u}_{\sigma})$  is considered to be a small quantity (49), the second exponential in the right-hand side of the above equality can be approximated by its first order Taylor expansion:

$$\exp[\beta_{\sigma}(\boldsymbol{\xi} - \mathbf{u}) \cdot (\mathbf{u} - \mathbf{u}_{\sigma})] \approx 1 + \beta_{\sigma}(\boldsymbol{\xi} - \mathbf{u}) \cdot (\mathbf{u}_{\sigma} - \mathbf{u}), \quad (\text{B.51})$$

where  $\beta_{\sigma} = 1/R_{\sigma}T$ . Since the velocity difference  $(\mathbf{u} - \mathbf{u}_{\sigma})$  is small, the third exponential in the right-hand side which depends on  $(\mathbf{u} - \mathbf{u}_{\sigma})^2$  can be neglected in a first-order approximation. It should be noted that this term affects the temperature difference [cf. Eqs. (B.8b) and (B.12b)], and must be included if thermal diffusion is important. For the case of isothermal mixing considered here the simplifications yield the final result of the equilibrium distribution function for  $f_{\sigma}^{\sigma(0)}$  given by Eq. (B.22a) after the velocity space  $\boldsymbol{\xi}$  is properly discretized (4; 5).

### B.A.3 Chapman-Enskog Analysis

In the Chapman-Enskog expansion, we introduce a small parameter  $\varepsilon$  (which is the Knudsen number), and

$$f_{\alpha}^{\sigma} = f_{\alpha}^{\sigma(0)} + \varepsilon f_{\alpha}^{\sigma(1)} + \dots, \quad (\text{B.52a})$$

$$\partial_t = \varepsilon \partial_{t_0} + \varepsilon^2 \partial_{t_1} + \dots, \quad (\text{B.52b})$$

$$\nabla \rightarrow \varepsilon \nabla. \quad (\text{B.52c})$$

The left hand side of Eq. (B.18) is expanded in a Taylor series in  $\delta_t$  up to 2nd order first, and then is substituted with the expansions of  $\varepsilon$ :

$$\begin{aligned}
 & f_\alpha^\sigma(\mathbf{x}_i + \mathbf{e}_\alpha \delta_t, t + \delta_t) - f_\alpha^\sigma(\mathbf{x}_i, t) \\
 = & \varepsilon \delta_t D_\alpha f_\alpha^\sigma + \frac{1}{2} \varepsilon^2 \delta_t^2 D_\alpha D_\alpha f_\alpha^\sigma + \dots \\
 = & \varepsilon \delta_t D_\alpha^{(0)} f_\alpha^{\sigma(0)} \\
 & + \varepsilon^2 \delta_t \left( \partial_{t_1} f_\alpha^{\sigma(0)} + D_\alpha^{(0)} f_\alpha^{\sigma(1)} + \frac{1}{2} \delta_t D_\alpha^{(0)} D_\alpha^{(0)} f_\alpha^{\sigma(0)} \right) \\
 & + \dots
 \end{aligned}$$

where Eqs. (B.52) have been substituted, and

$$D_\alpha \equiv \partial_t + \mathbf{e}_\alpha \cdot \nabla, \quad \text{and} \quad D_\alpha^{(0)} \equiv \partial_{t_0} + \mathbf{e}_\alpha \cdot \nabla.$$

The first few equations of a set of successive equations in the order of  $\varepsilon$  obtained from the lattice Boltzmann equation (B.18) are:

$$\varepsilon^0: f_\alpha^{\sigma(0)} = f_\alpha^{\sigma(\text{eq})} \left[ 1 + \frac{(\mathbf{e}_\alpha - \mathbf{u}) \cdot (\mathbf{u}_\sigma - \mathbf{u})}{R_\sigma T} \right], \quad (\text{B.53a})$$

$$\varepsilon^1: \delta_t D_\alpha^{(0)} f_\alpha^{\sigma(0)} = -\frac{1}{\tau_\sigma} f_\alpha^{\sigma(1)} + J_\alpha^{\sigma\zeta} - \delta_t F_\alpha, \quad (\text{B.53b})$$

$$\begin{aligned}
 \varepsilon^2: \delta_t \left( \partial_{t_1} f_\alpha^{\sigma(0)} + D_\alpha^{(0)} f_\alpha^{\sigma(1)} + \frac{1}{2} \delta_t D_\alpha^{(0)} D_\alpha^{(0)} f_\alpha^{\sigma(0)} \right) \\
 = -\frac{1}{\tau_\sigma} f_\alpha^{\sigma(2)}. \quad (\text{B.53c})
 \end{aligned}$$

In the Chapman-Enskog analysis, it is assumed that the mutual interaction term  $J_\alpha^{\sigma\zeta}$  as well as the forcing term  $F_\alpha$  are of the first order in  $\varepsilon$  (17; 18; 63; 64).

The first few moments of the equilibrium distribution function  $f_\alpha^{\sigma(0)}$  can be easily com-

puted:

$$\sum_{\alpha} f_{\alpha}^{\sigma(0)} = \rho_{\sigma}, \quad (\text{B.54a})$$

$$\sum_{\alpha} f_{\alpha}^{\sigma(0)} \mathbf{e}_{\alpha} = \rho_{\sigma} \mathbf{u}_{\sigma}, \quad (\text{B.54b})$$

$$\begin{aligned} \sum_{\alpha} f_{\alpha}^{\sigma(0)} e_{\alpha i} e_{\alpha j} &= R_{\sigma} T \rho_{\sigma} \delta_{ij} + \rho_{\sigma} u_i u_j \\ &+ \rho_{\sigma} \left[ (u_{\sigma} - u)_i u_j + (u_{\sigma} - u)_j u_i - \frac{u_i u_j \mathbf{u} \cdot (\mathbf{u}_{\sigma} - \mathbf{u})}{R_{\sigma} T} \right] \\ &\approx R_{\sigma} T \rho_{\sigma} \delta_{ij} + \rho_{\sigma} u_i u_j, \end{aligned} \quad (\text{B.54c})$$

$$\begin{aligned} \sum_{\alpha} f_{\alpha}^{\sigma(0)} e_{\alpha i} e_{\alpha j} e_{\alpha k} &= R_{\sigma} T \rho_{\sigma} \Delta_{ijkl} u_l \left[ 1 - \frac{\mathbf{u} \cdot (\mathbf{u}_{\sigma} - \mathbf{u})}{R_{\sigma} T} \right] \\ &+ R_{\sigma} T \rho_{\sigma} \Delta_{ijkl} (u_{\sigma} - u)_l + \dots \\ &\approx R_{\sigma} T \rho_{\sigma} (\delta_{ij} u_{\sigma k} + \delta_{jk} u_{\sigma i} + \delta_{ki} u_{\sigma j}), \end{aligned} \quad (\text{B.54d})$$

where  $e_{\alpha i}$  is the  $i$ -th Cartesian component of the vector  $\mathbf{e}_{\alpha}$  and

$$\Delta_{ijkl} = \delta_{ij} \delta_{kl} + \delta_{ik} \delta_{jl} + \delta_{il} \delta_{jk}.$$

In the second and third order moments of  $f_{\alpha}^{\sigma(0)}$  in Eq. (B.54c) and (B.54d), respectively, the terms involving products of the velocity and the velocity difference are neglected.

With the substitution of Eq. (B.53b), Eq. (B.53c) becomes:

$$\begin{aligned} \delta_t \left[ \partial_{t_1} f_{\alpha}^{\sigma(0)} + D_{\alpha}^{(0)} f_{\alpha}^{\sigma(1)} + \frac{1}{2} D_{\alpha}^{(0)} (J_{\alpha}^{\sigma\zeta} - \delta_t F_{\alpha}) \right] \\ = \frac{1}{\tau_{\sigma}} \left[ \delta_t D_{\alpha}^{(0)} f_{\alpha}^{\sigma(1)} - f_{\alpha}^{\sigma(2)} \right]. \end{aligned} \quad (\text{B.55})$$

Therefore the second order (in  $\varepsilon$ ) equation for the mass conservation is

$$\partial_{t_1} \rho_{\sigma} = \frac{1}{2} \nabla \cdot \left[ \frac{1}{\tau_D} \frac{\rho_{\sigma} \rho_{\zeta}}{\rho} (\mathbf{u}_{\sigma} - \mathbf{u}_{\zeta}) \right] = -\frac{1}{2} \delta_t \nabla \cdot \mathbf{p} \mathbf{d}_{\sigma}, \quad (\text{B.56})$$

where the spatial variation of the external force is neglected because it is canceled out by properly setting the velocity change due to the external forcing to  $\delta \mathbf{u} = \frac{1}{2} \mathbf{a} \delta_t$  in the equilibrium distribution function (63; 64).

By construction of the forcing term  $F_\alpha$  [given by Eq. (B.19c)], we have

$$\sum_{\alpha} F_{\alpha} e_{\alpha i} e_{\alpha j} = 0. \quad (\text{B.57})$$

Therefore the forcing term has no contribution to the pressure tensor. However, the partial pressure tensor for each individual species is affected by the cross-interaction term  $J_{\alpha}^{\sigma\varsigma}$  because

$$\begin{aligned} \sum_{\alpha} J_{\alpha}^{\sigma\varsigma} e_{\alpha i} e_{\alpha j} &= -\frac{1}{\tau_D} \frac{\rho_{\sigma} \rho_{\varsigma}}{\rho} \\ &\times \left[ (u_i \delta u_j + u_j \delta u_i) - \frac{1}{R_{\sigma} T} u_i u_j \mathbf{u} \cdot \delta \mathbf{u} \right], \end{aligned} \quad (\text{B.58})$$

where  $\delta \mathbf{u} \equiv (\mathbf{u}_{\sigma} - \mathbf{u}_{\varsigma})$ , and  $\delta u_i \equiv (u_{\sigma i} - u_{\varsigma i})$ . The effect due to  $J_{\alpha}^{\sigma\varsigma}$  is of higher order in  $\mathbf{u}$  and  $\mathbf{u}_{\sigma}$ , and thus can be neglected in the pressure. Consequently, the partial pressure tensor can be approximated as the following:

$$\begin{aligned} P_{ij}^{\sigma(1)} &= \sum_{\alpha} f_{\alpha}^{\sigma(1)} e_{\alpha i} e_{\alpha j} = -\tau_{\sigma} \delta_t \sum_{\alpha} D_{\alpha}^{(0)} f_{\alpha}^{\sigma(0)} e_{\alpha i} e_{\alpha j} \\ &= -\tau_{\sigma} \delta_t \left[ \partial_{t_0} \sum_{\alpha} f_{\alpha}^{\sigma(0)} e_{\alpha i} e_{\alpha j} + \sum_{\alpha} \nabla \cdot \mathbf{e}_{\alpha} f_{\alpha}^{\sigma(0)} e_{\alpha i} e_{\alpha j} \right] \\ &= -\tau_{\sigma} \delta_t [\partial_{t_0} (R_{\sigma} T \rho_{\sigma} \delta_{ij} + \rho_{\sigma} u_i u_j) + R_{\sigma} T (\partial_j \rho_{\sigma} u_{\sigma i} + \partial_i \rho_{\sigma} u_{\sigma j} + \delta_{ij} \nabla \cdot \rho_{\sigma} \mathbf{u}_{\sigma})] + \dots \\ &= -\tau_{\sigma} \delta_t [R_{\sigma} T (\partial_{t_0} \rho_{\sigma} + \nabla \cdot \rho_{\sigma} \mathbf{u}_{\sigma}) \delta_{ij} + \partial_{t_0} (\rho_{\sigma} u_i u_j) + R_{\sigma} T (\partial_j \rho_{\sigma} u_{\sigma i} + \partial_i \rho_{\sigma} u_{\sigma j})] + \dots \\ &\approx -\tau_{\sigma} \delta_t R_{\sigma} T (\partial_j \rho_{\sigma} u_{\sigma i} + \partial_i \rho_{\sigma} u_{\sigma j}), \end{aligned} \quad (\text{B.59})$$

where the terms smaller than  $O(M^2)$  ( $M$  is the Mach number) are dropped as usual (65).

Therefore,

$$\partial_j P_{ij}^{\sigma(1)} \approx -\tau_{\sigma} \delta_t R_{\sigma} T \rho_{\sigma} \nabla^2 u_{\sigma i}. \quad (\text{B.60})$$

## Bibliography

- [1] G. R. McNamara and G. Zanetti, Use of the Boltzmann equation to simulate lattice-gas automata, *Phys. Rev. Lett.* **61**, 2332 (1988).

- [2] G. D. Doolen, ed., *Lattice Gas Methods for Partial Differential Equations* (Addison-Wesley, New York, 1990).
- [3] R. Benzi, S. Succi, and M. Vergassola, The lattice Boltzmann equation: Theory and applications, *Phys. Rep.* **222**, 145 (1992).
- [4] X. He and L.-S. Luo, A priori derivation of the lattice Boltzmann equation, *Phys. Rev. E* **55**, R6333 (1997).
- [5] X. He and L.-S. Luo, *Theory of the lattice Boltzmann method: From the Boltzmann equation to the lattice Boltzmann equation*, *Phys. Rev. E* **56**, 6811 (1997).
- [6] X. Shan and X. He, Discretization of the velocity space in the solution of the Boltzmann equation, *Phys. Rev. Lett.* **80**, 65 (1998).
- [7] D. Wolf-Gladrow, *Lattice-Gas Cellular Automata and Lattice Boltzmann Models*, Lecture Notes in Mathematics Vol. 1725 (Springer, Berlin, 2000).
- [8] U. Frisch, B. Hasslacher, and Y. Pomeau, *Phys. Rev. Lett.* **56**, 1505 (1986).
- [9] S. Wolfram, *J. Stat. Phys.* **45**, 471 (1986).
- [10] U. Frisch, D. d'Humières, B. Hasslacher, P. Lallemand, Y. Pomeau, and J.-P. Rivet, Lattice Gas Hydrodynamics in two and three dimensions, *Complex Syst.* **1**, 649 (1987).
- [11] M. Junk and A. Klar, Discretizations for the incompressible Navier-Stokes equations based on the lattice Boltzmann method, *SIAM J. Sci. Comput.* **22**, 1 (2000).
- [12] M. Junk, A finite difference interpretation of the lattice Boltzmann method, *Numer. Meth. Part. Diff. Eq.* **17**, 383 (2001).
- [13] M. Junk, A. Klar, and L.-S. Luo, (unpublished).
- [14] S. Chapman and T. G. Cowling, *The Mathematical Theory of Non-Uniform Gases*, 3rd ed. (Cambridge University Press, Cambridge, 1970).

- [15] X. Shan and H. Chen, Phys. Rev. E **47**, 1815 (1993).
- [16] X. Shan and H. Chen, Phys. Rev. E **49**, 2941 (1994).
- [17] L.-S. Luo, Unified theory of lattice Boltzmann models for nonideal gases, Phys. Rev. Lett. **81**, 1618 (1998).
- [18] L.-S. Luo, Theory of the lattice Boltzmann method: Lattice Boltzmann models for nonideal gases; Phys. Rev. E **62**, 4982 (2000).
- [19] A. K. Gunstensen, D. H. Rothman, S. Zaleski, and G. Zanetti, Lattice Boltzmann model of immiscible fluids, Phys. Rev. A **43**, 4320 (1991).
- [20] E. G. Flekkøy, Lattice Bhatnagar-Gross-Krook models for miscible fluids, Phys. Rev. E **47**, 4247 (1993).
- [21] D. Grunau, S. Chen, and K. Eggert, A lattice Boltzmann model for multiphase flow, Phys. Fluids A **5**, 2557 (1993).
- [22] X. Shan and G. Doolen, Multicomponent lattice-Boltzmann model with interparticle interaction, J. Stat. Phys. **81**, 379 (1995).
- [23] X. Shan and G. Doolen, Diffusion in a multicomponent lattice Boltzmann equation model, Phys. Rev. E **54**, 3614 (1996).
- [24] E. Orlandini, W. R. Osborn, and J. M. Yeomans, A lattice Boltzmann model of binary-fluid mixtures, Europhys. Lett. **32**, 463 (1995).
- [25] W. R. Osborn, E. Orlandini, M. R. Swift, J. M. Yeomans, and J. R. Banavar, Lattice Boltzmann study of hydrodynamic spinodal decomposition, Phys. Rev. Lett. **75**, 4031 (1995).
- [26] M. R. Swift, E. Orlandini, W. R. Osborn, and J. M. Yeomans, Lattice Boltzmann simulations of liquid-gas and binary fluid systems, Phys. Rev. E **54**, 5041 (1996).



- [27] A. Lamura, G. Gonnella, and J. M. Yeomans, A lattice Boltzmann model of ternary fluid mixtures, *Europhys. Lett.* **45**, 314 (1999).
- [28] V. M. Kendon, J.-C. Desplat, P. Bladon, and M. E. Cates, 3D Spinodal Decomposition in the Inertial Regime, *Phys. Rev. Lett.* **83**, 576 (1999).
- [29] V. M. Kendon, M. E. Cates, I. Pagonabarraga, J.-C. Desplat, and P. Bladon, Inertial effects in three-dimensional spinodal decomposition of a symmetric binary fluid mixture: a lattice Boltzmann study *J. Fluid Mech.* **440**, 147 (2001).
- [30] H. Yu, L.-S. Luo, and S. S. Girimaji, *Int. J. Computat. Eng. Sci.* **3**, 73 (2002).
- [31] L.-S. Luo and S. S. Girimaji, *Phys. Rev. E* **66**, 035301(R) (2002).
- [32] N. S. Martys and H. Chen, *Phys. Rev. E* **53**, 743 (1996).
- [33] S. Chen and G. Doolen, Lattice Boltzmann method for fluid flows, *Annu. Rev. Fluid Mech.* **30**, 329 (1998).
- [34] A. J. C. Ladd, Numerical simulation of particular suspensions via a discretized Boltzmann equation, Part 1. Theoretical foundation, *J. Fluid Mech.* **271**, 285 (1994); *ibid* **271**, 311 (1994).
- [35] D. Qi, Lattice-Boltzmann simulations of particles in non-zero-Reynolds number flows, *J. Fluid Mech.* **385**, 41 (1999).
- [36] D. Qi and L.-S. Luo, *Phys. Fluids* **14**, 4440 (2002).
- [37] D. Qi and L.-S. Luo, to appear in *J. Fluid Mech.* (2002).
- [38] P. L. Bhatnagar, E. P Gross, and M. Krook, *A Model for Collision Processes in Gases. I. Small Amplitude Processes in Charged and Neutral One-Component Systems*, *Phys. Rev.* **94**, 511 (1954).

- [39] C. F. Curtiss and J. O. Hirschfelder, Transport properties of multicomponent gas mixtures, *J. Chem. Phys.* **17**, 550 (1949).
- [40] I. Kolodner, On the application of the Boltzmann equations to the theory of gas mixtures, PhD thesis, New York University, New York (1950).
- [41] E. P. Gross and M. Krook, Models for Collision Processes in Gases: Small-Amplitude Oscillations of Charged Two-Component Systems, *Phys. Rev.* **102**, 593 (1956).
- [42] E. P. Gross and E. A. Jackson, Kinetic Models and the Linearized Boltzmann Equation, *Phys. Fluids* **2**, 432 (1959).
- [43] L. Sirovich, Kinetic Modeling of Gas Mixtures, *Phys. Fluids* **5**, 908 (1962).
- [44] T. F. Morse, Energy and momentum exchange between Nonequipartition gases, *Phys. Fluids* **6**, 1420 (1963).
- [45] B. B. Hamel, Kinetic Models for Binary Mixtures, *Phys. Fluids* **8**, 418 (1965).
- [46] B. B. Hamel, Two-fluid hydrodynamic equations for a neutral, disparate-mass, binary mixtures, *Phys. Fluids* **9**, 12 (1966).
- [47] L. Sirovich, Mixtures of Maxwell molecules, *Phys. Fluids* **9**, 2323 (1966).
- [48] S. Ziering and M. Sheinblatt, Kinetic theory of diffusion in rarefied gases, *Phys. Fluids* **9**, 1674 (1966).
- [49] E. Goldman and L. Sirovich, Equations for gas mixtures, *Phys. Fluids* **10**, 1928 (1967).
- [50] J. M. Greene, Improved Bhatnagar-Gross-Krook model of electron-ion collisions, *Phys. Fluids* **16**, 2022 (1973).
- [51] V. Sofonea and R. F. Sekerka, BGK models for diffusion in isothermal binary fluid systems, *Physica A* **299**, 494 (2001).

- [52] S. Harris, *An Introduction to the Theory of the Boltzmann Equation* (Holt, Rinehart and Winston, New York, 1971).
- [53] J. H. Ferziger and H. G. Kaper, *Mathematical Theory of Transport Processes in Gases* (Elsevier, New York, 1972).
- [54] H. Grad, Principles of the kinetic theory of gases, in *Handbuch der Physik*, edited by S. Flügge (Springer, Berlin, 1958), Vol. XII, pp. 205–294.
- [55] J. C. Maxwell, On the dynamical theory of gases, *Phil. Trans.* **157**, 26 (1866).
- [56] H. Grad, Theory of Rarefied Gases, in *Rarefied Gas Dynamics*, ed. by F. Devienne (Pergamon, London, 1960), pp. 100–138.
- [57] D. d’Humières, *Generalized lattice-Boltzmann equations*, in *Rarefied Gas Dynamics: Theory and Simulations*, eds B.D. Shizgal and D.P. Weaver, *Progress in Astronautics and Aeronautics, Prog. Astronaut. Aeronaut.* **159**, 450 (1992).
- [58] P. Lallemand and L.-S. Luo, *Theory of the lattice Boltzmann method: Dispersion, dissipation, isotropy, Galilean invariance, and stability*, *Phys. Rev. E* **61**, 6546 (2000).
- [59] D. d’Humières, I. Ginzburg, M. Krafczyk, P. Lallemand, and L.-S. Luo, *Multiple-Relaxation-Time Lattice Boltzmann Models in Three Dimensions*, *Phil. Trans. R. Soc. Lond., Ser. A* **360**, 437 (2002).
- [60] J. L. Lebowitz, H. L. Frisch, and E. Helfand, *Nonequilibrium distribution functions in a fluid*, *Phys. Fluids* **3**, 325 (1960).
- [61] M. Hénon, *Viscosity of a lattice gas*, *Complex Syst.* **1**, 763 (1987). pp. 763–789
- [62] X. He and G. D. Doolen, *Thermodynamic foundations of kinetic theory and lattice Boltzmann models for multiphase flows*, *J. Stat. Phys.* **107**, 309 (2002).

- [63] I. Ginzbourg and P. M. Adler, Boundary flow condition analysis for the three-dimensional lattice Boltzmann model, *J. Phys. II France* **4**, 191 (1994).
- [64] Z. Guo, C. Zheng, and B. Shi, Discrete lattice effects on the forcing term in the lattice Boltzmann method, *Phys. Rev. E* **65**, 046308 (2002).
- [65] X. He and L.-S. Luo, Lattice Boltzmann model for the incompressible Navier-Stokes equation, *J. Stat. Phys.* **88**, 927 (1997).

## Appendix C

# Computational Assessment of Diffusivity in LBM for Binary Scalar Mixing

Nomenclature			
$c_s$	Speed of sound	$e_\alpha$	Discretized particle velocity
$c$	Lattice constant	$D$	Diffusion coefficient
$F$	Interaction force	$G_f$	Interaction strength coefficient
$n_\alpha$	Number density distribution function	$n^{(0)}$	Equilibrium distribution function
$m$	Mass of molecule	$n$	Number density
$n^*$	Number density scalar	$p$	Pressure
$\vec{u}$	Fluid velocity	$\rho$	Fluid density
$\delta_t$	Time step	$\delta_x$	Grid size
$w_\alpha$	Weight function	$\tau$	Normalized relaxation time

### C.1 Introduction

In Appendix B, a LBE model for binary mixing was developed directly from multi-component Boltzmann Equation. In this Appendix we will develop a relatively simple model by adding

inter-particle reaction. This model has a simple interaction term and is easy to be implemented.

The remainder of this Appendix is organized as follows. In section C.2, the lattice Boltzmann model for binary scalar mixing is presented. Macroscopic governing equations for each species are derived. Numerical evaluations are presented in Section C.3. Finally we conclude in Section C.4 with a brief discussion.

## C.2 Lattice Boltzmann model for binary scalar mixing

In a two-species field, The evolution of number density function  $n_\alpha^\sigma(\vec{x}, t)$  (e.g.  $\sigma = 1, 2$ ) for each species can be described by the lattice Boltzmann equation

$$n_\alpha^\sigma(\vec{x} + \vec{e}_\alpha \delta t, t + \delta t) - n_\alpha^\sigma(\vec{x}, t) = -\frac{1}{\tau^\sigma} [n_\alpha^\sigma(\vec{x}, t) - n_\alpha^{\sigma(eq)}(\vec{x}, t)] \quad (C.1)$$

where  $\tau^\sigma$  is the relaxation time of species  $\sigma$ ;  $\{\vec{e}_\alpha; \alpha = 0, 1, \dots, b\}$  is the discrete velocity set. For the sake of concreteness and simplicity without losing generality, we shall restrict our derivation to a nine-velocity model on a two-dimensional square lattice (D2Q9 model). We choose the equilibrium distribution functions as

$$n_\alpha^{\sigma(eq)} = N_\alpha(n, \vec{u}^{\sigma(eq)}) = w_\alpha n \left[ 1 + \frac{3(\vec{e}_\alpha \cdot \vec{u}^{\sigma(eq)})}{c^2} + \frac{9(\vec{e}_\alpha \cdot \vec{u}^{\sigma(eq)})^2}{2c^4} - \frac{3(u^{\sigma(eq)})^2}{2c^2} \right] \quad (C.2)$$

where  $\vec{u}^{\sigma(eq)}$  is a equilibrium velocity which is determined by the distribution functions and interaction between two species. The sound speed of this model is  $c_s = c/\sqrt{3}$ , where  $c = \delta x/\delta t = 1$  is the lattice constant. The discrete particle velocities  $\vec{e}_\alpha$  and the weighting factors  $w_\alpha$  of this model are

$$\vec{e}_\alpha = \begin{cases} 0, & \alpha = 0 \\ (\cos(\frac{(\alpha-1)\pi}{2})c, \sin(\frac{(\alpha-1)\pi}{2}))c, & \alpha = 1-4 \\ (\cos(\frac{(\alpha-5)\pi}{2} + \frac{\pi}{4})c, \sin(\frac{(\alpha-5)\pi}{2} + \frac{\pi}{4}))c, & \alpha = 5-8 \end{cases}$$

and

$$w_\alpha = \begin{cases} 4/9, & \alpha = 0 \\ 1/9, & \alpha = 1-4 \\ 1/36, & \alpha = 5-8 \end{cases}$$

The number density, mass density, velocity of the  $\sigma$ -species and the number density, the mass density and velocity of the mixture are calculated by

$$n^\sigma = \sum_\alpha n_\alpha^\sigma \quad (\text{C.3})$$

$$\rho^\sigma = m^\sigma n^\sigma = m^\sigma \sum_\alpha n_\alpha^\sigma \quad (\text{C.4})$$

$$\vec{u}^\sigma = \frac{1}{n^\sigma} \sum_\alpha n_\alpha^\sigma \vec{e}_\alpha \quad (\text{C.5})$$

$$n = \sum_\sigma n^\sigma \quad (\text{C.6})$$

$$\rho = \sum_\sigma \rho^\sigma \quad (\text{C.7})$$

$$\vec{u} = \frac{1}{\rho} \sum_\sigma \rho^\sigma \vec{u}^\sigma \quad (\text{C.8})$$

respectively.

In the absence of interaction forces between species, we assume that the velocities  $\vec{u}^{\sigma(eq)}$  of two species are all equal to a common velocity  $\vec{u}'$ . Since in this case the total momentum of particles of all species should be conserved by collision operator at each lattice site, it follows directly from Eq (C.1) that

$$\vec{u}^{\sigma(eq)} = \vec{u}' = \frac{\sum_\sigma \rho^\sigma \vec{u}^\sigma / \tau^\sigma}{\sum_\sigma \rho^\sigma / \tau^\sigma}$$

Next, we introduce interaction force between two species

$$\vec{F}^\sigma = c_s^2 n G_f [\nabla \chi^\sigma + (\chi^\sigma - \omega^\sigma) \frac{\nabla \rho}{\rho}] \quad (\text{C.9})$$

Where  $G_f$  is a factor which determines the strength of interaction;  $\chi^\sigma = n^\sigma/n$  is number density ratio; and  $\omega^\sigma = \rho^\sigma/\rho$  is mass density ratio. To incorporate this momentum change in the dynamics of the distribution functions, one can simply define

$$\rho^\sigma \vec{u}^{\sigma(eq)} = \rho^\sigma \vec{u}' + \tau^\sigma \vec{F}^\sigma \quad (\text{C.10})$$

By summing Eq.(C.1) over all directions and multiplying Eq.(C.1) by  $\vec{e}_\alpha$  and  $m^\sigma$  and summing over all the nine directions and two species, we can obtain a mass-conservation relation for each species and momentum-conservation relation for the mixture respectively. These relations are

$$\sum_\alpha n_\alpha^\sigma(\vec{x} + \vec{e}_\alpha, t+1) - \sum_\alpha n_\alpha^\sigma(\vec{x}, t) = 0 \quad (\text{C.11})$$

$$\sum_\sigma m^\sigma \sum_\alpha n_\alpha^\sigma(\vec{x} + \vec{e}_\alpha, t+1) - \sum_\sigma m^\sigma \sum_\alpha n_\alpha^\sigma(\vec{x}, t) = \sum_\sigma \vec{F}^\sigma = 0 \quad (\text{C.12})$$

### C.2.1 Macroscopic equations of each species

Following the algorithm by Xianwen Shan and Gary Doolen (5; 6), we define the macroscopic velocity of the whole fluid  $\vec{u}$  as the average of the momentum values of species  $\sigma$  before and after collision summed over two species. The momentum of species  $\sigma$  before collision

$$m^\sigma \sum_\alpha n_\alpha^\sigma \vec{e}_\alpha = m^\sigma n^\sigma \vec{u}^\sigma = \rho^\sigma \vec{u}^\sigma \quad (\text{C.13})$$

while the momentum after collision

$$(1 - \frac{1}{\tau^\sigma}) m^\sigma \sum_\alpha n_\alpha^\sigma \vec{e}_\alpha + \frac{m^\sigma}{\tau^\sigma} \sum_\alpha n_\alpha^{\sigma(eq)} \vec{e}_\alpha = \rho^\sigma \vec{u}^\sigma - \frac{\rho^\sigma}{\tau^\sigma} \vec{u}^\sigma + \frac{m^\sigma}{\tau^\sigma} n^\sigma n^{\sigma(eq)} \vec{u}^{\sigma(eq)} \quad (\text{C.14})$$



so that

$$\rho \vec{u} = \frac{1}{2} \sum_{\sigma} (\rho^{\sigma} \vec{u}^{\sigma} + \rho^{\sigma} \vec{u}^{\sigma} - \frac{\rho^{\sigma}}{\tau^{\sigma}} \vec{u}^{\sigma} + \frac{m^{\sigma}}{\tau^{\sigma}} n^{\sigma} n^{\sigma} \vec{u}^{\sigma(eq)}) = \rho^{\sigma} \vec{u}^{\sigma} + \frac{1}{2} \vec{F}^{\sigma} \quad (\text{C.15})$$

by noticing Eq.(C.10).

In the Chapman-Enskog expansion, we introduce a small parameter  $\epsilon$  (which is the Knudsen number), and

$$n_{\alpha}^{\sigma} = n_{\alpha}^{\sigma(0)} + \epsilon n_{\alpha}^{\sigma(1)} + \dots, \quad \partial_t = \epsilon \partial_{t0} + \epsilon^2 \partial_{t1} + \dots \quad \nabla \rightarrow \epsilon \nabla \quad (\text{C.16})$$

Expanding the left-hand side of Eq.(C.1) in a Taylor series up to the 2nd order in time, we get

$$(\partial_t + \vec{e}_{\alpha} \cdot \nabla) n_{\alpha}^{\sigma} + \frac{1}{2} (\partial_t + \vec{e}_{\alpha} \cdot \nabla)^2 n_{\alpha}^{\sigma} = - \frac{[n_{\alpha}^{\sigma}(\vec{x}, t) - (n_{\alpha}^{\sigma(eq)})(\vec{x}, t)]}{\tau^{\sigma}} \quad (\text{C.17})$$

Since now the collision operator depends upon the spatial derivatives of particle number, we chose the leading order distribution functions to be the equilibrium distribution about the fluid velocity  $\vec{u}$ , namely,  $n_{\alpha}^{\sigma(0)} = N_{\alpha}(n^{\sigma}, \vec{u})$ , to obtain a set of macroscopic equations in terms of the correct fluid variables without changing the conservation relations. The lattice Boltzmann equation is then satisfied at the next order when terms that depend on spatial derivatives are included. Since

$$\sum_{\alpha} n_{\alpha}^{\sigma(0)} = n^{\sigma}, \quad \sum_{\sigma} m^{\sigma} \sum_{\alpha} n_{\alpha}^{\sigma(0)} \vec{e}_{\alpha} = \rho \vec{u} \quad (\text{C.18})$$

we get

$$\sum_{\alpha} n_{\alpha}^{\sigma(1)} = n^{\sigma}, \quad \sum_{\sigma} m^{\sigma} \sum_{\alpha} n_{\alpha}^{\sigma(1)} \vec{e}_{\alpha} = -\frac{1}{2} \sum_{\sigma} \vec{F}^{\sigma} \quad (\text{C.19})$$

Expanding the left-hand side of Eq.(C.17) by (C.16), we have

$$\begin{aligned} & n_{\alpha}^{\sigma}(\vec{x} + \vec{e}_{\alpha}, t + 1) - n_{\alpha}^{\sigma}(\vec{x}, t) \\ & \simeq \epsilon [(\partial_{t0} + \vec{e}_{\alpha} \cdot \nabla) n_{\alpha}^{\sigma(0)}] + \epsilon^2 [(\partial_{t0} + \vec{e}_{\alpha} \cdot \nabla) n_{\alpha}^{\sigma(1)} + \partial_{t1} n_{\alpha}^{\sigma(0)} + \frac{1}{2} (\partial_{t0} + \vec{e}_{\alpha} \cdot \nabla)^2 n_{\alpha}^{\sigma(0)}] \quad (\text{C.20}) \end{aligned}$$

Substituting above equation into the conversation relations (C.11) and (C.12) and collecting the first order of  $\epsilon$ , the following equations are obtained

$$\partial_{t0}\rho^\sigma + \nabla \cdot (\rho^\sigma \vec{u}) = 0, \quad \sigma = 1, 2 \quad (\text{C.21})$$

$$\partial_{t0}(\rho \vec{u}) + c_s^2 \nabla \rho \vec{\nabla} \cdot \rho \vec{u} \vec{u} = \sum_\sigma \vec{F}^\sigma \quad (\text{C.22})$$

Using Eqs.(C.21), we rewrite Eq.(C.22) in the form

$$(\partial_{t0} + \vec{u} \cdot \nabla) \vec{u} = -\frac{1}{\rho} \nabla P \quad (\text{C.23})$$

where  $P$  is the pressure given by

$$P = c_s^2 \rho + \sum_\sigma \vec{F}^\sigma \quad (\text{C.24})$$

The terms of the 2nd order of  $\epsilon$  in the expansion of the mass-conversation relation yield the following equation for each species

$$\partial_{t1}\rho^\sigma + m^\sigma \nabla \cdot \sum_\alpha n_\alpha^{\sigma(1)} \vec{e}_\alpha + \frac{m^\sigma}{2} \nabla \cdot (\partial_{t0} \sum_\alpha n_\alpha^{\sigma(0)} \vec{e}_\alpha + \nabla \cdot \sum_\alpha n_\alpha^{\sigma(0)} \vec{e}_\alpha \vec{e}_\alpha) = 0 \quad (\text{C.25})$$

Noticing Eq.(C.21), we can evaluate the third term of Eq.(C.25)

$$m^\sigma (\partial_{t0} \sum_\alpha n_\alpha^{\sigma(0)} \vec{e}_\alpha + \nabla \cdot \sum_\alpha n_\alpha^{\sigma(0)} \vec{e}_\alpha \vec{e}_\alpha) = -\omega^\sigma \nabla p + c_s^2 \nabla \rho^\sigma \quad (\text{C.26})$$

To calculate the 2nd term of Eq.(C.25), we substitute the expansions of Eqs.(C.16) into the lattice Boltzmann equation (C.1) and obtain

$$\partial_{t0} \sum_\alpha n_\alpha^{\sigma(0)} \vec{e}_\alpha + \nabla \cdot \sum_\alpha n_\alpha^{\sigma(0)} \vec{e}_\alpha \vec{e}_\alpha = -\frac{1}{\tau^\sigma} [\rho^\sigma (\vec{u} - \vec{u}') + \sum_\alpha m^\sigma n_\alpha^{\sigma(1)} \vec{e}_\alpha] + \vec{F}^\sigma \quad (\text{C.27})$$

which when multiplied by  $\tau^\sigma$  and summed over all the components, becomes

$$\rho(\vec{u} - \vec{u}') = \sum_{\sigma} \tau^{\sigma} \vec{F}^{\sigma} + \frac{1}{2} \sum_{\sigma} \vec{F}^{\sigma} + \sum_{\sigma} \tau^{\sigma} \omega^{\sigma} \nabla p - c_s^2 \sum_{\sigma} \tau^{\sigma} \nabla \rho^{\sigma} \quad (\text{C.28})$$

$\sum_{\alpha} m^{\sigma} n_{\alpha}^{\sigma(1)} \vec{e}_{\alpha}$  can then be solved by substituting Eqs. (C.28) and (C.26) into Eq. (C.27). Combining Eq. (C.25) with the first order equation (C.21), we obtain the following equation at the second order

$$\begin{aligned} \frac{\partial \rho^{\sigma}}{\partial t} + \nabla \cdot (\rho^{\sigma} \vec{u}) = & -\tau^{\sigma} \nabla \cdot \vec{F}^{\sigma} + (\tau^{\sigma} - \frac{1}{2}) \nabla \cdot [c_s^2 \nabla \rho^{\sigma} - \omega^{\sigma} \nabla p] + \nabla \cdot \omega^{\sigma} [\sum_k (\tau^k + \frac{1}{2}) \vec{F}^k \\ & + \nabla p \sum_k \tau^k \omega^k - c_s^2 \sum_k \tau^k \nabla \rho^k] \end{aligned} \quad (\text{C.29})$$

When summed over two species, the equation above becomes the continuity equation of the whole fluid at the 2nd order

$$\frac{\partial \rho}{\partial t} + \nabla \cdot (\rho \vec{u}) = 0 \quad (\text{C.30})$$

### C.2.2 Mutual diffusivity calculation

The species of a fluid mixture will be diffused into each other if the mean velocities of the species differ. The local velocity of the fluid mixture can be defined in several different ways: by averaging the velocities of the constituents by mass, mole, or volume(11). The diffusion velocities are then defined relative to this local velocity. Mathematically, all the averaging methods are equally useful in describing the diffusion of the constituents. Following the treatment presented by Chapman and Cowling(12), we use the mass fluxes of the species in our calculation. Here again, since the momentum of each species changes at each collision, we must average mass fluxes before and after collisions to get the overall mass flux

$$\rho^{\sigma} \vec{u}^{\sigma} = \frac{m^{\sigma}}{2} [\sum_{\alpha} n_{\alpha}^{\sigma} \vec{e}_{\alpha} + (1 - \frac{1}{\tau^{\sigma}}) \sum_{\alpha} n_{\alpha}^{\sigma} \vec{e}_{\alpha} + \frac{1}{\tau^{\sigma}} \sum_{\alpha} n_{\alpha}^{\sigma(eq)} \vec{e}_{\alpha}] \quad (\text{C.31})$$

By applying the same Chapman-Enskog technique above, after straightforward manipulations(5; 6), the relative mass flux of species  $\sigma$  is obtained

$$\rho^{\sigma} (\vec{u} - \vec{u}^{\sigma}) = -\tau^{\sigma} \vec{F}^{\sigma} + (\tau^{\sigma} - \frac{1}{2}) [c_s^2 \nabla \rho^{\sigma} - \omega^{\sigma} \nabla p] + \omega^{\sigma} [\sum_k (\tau^k + \frac{1}{2}) \vec{F}^k$$

$$+\nabla p \sum_k \tau^k \omega^k - c_s^2 \sum_k \tau^k \nabla \rho^k] \quad (\text{C.32})$$

The relative velocity  $\vec{u}^\sigma - \vec{u}$  is the mass-averaged diffusion velocity of species  $\sigma$  with respect to  $\vec{u}$ , which indicates the motion of species  $\sigma$ . Noticing that the right-hand side terms of Eq.(C.29) are exactly what the divergence operator acts on in the right-hand side of above equation, we can simply rewrite Eq.(C.29) as the continuity equation of species  $\sigma$

$$\frac{\partial \rho^\sigma}{\partial t} + \nabla \cdot (\rho^\sigma \vec{u}^\sigma) = 0 \quad (\text{C.33})$$

which demonstrates that each species satisfies its own continuity equation at 2nd order. Following the convention in the diffusion literature, we define the mass flux of species  $\sigma$  as  $\vec{j}^\sigma = \rho^\sigma (\vec{u} - \vec{u}^\sigma)$ . As a result, Eq.(C.29) can be simply expressed as

$$(\partial_t + \vec{u} \cdot \nabla) \rho^\sigma + \nabla \cdot \vec{u} = -\nabla \cdot \vec{j}^\sigma \quad (\text{C.34})$$

By assuming the incompressibility of the fluid (i.e.  $\nabla \cdot \vec{u} = 0$ ) and setting same molecular mass ( $m^\sigma = m$ ) and relaxation time ( $\tau^\sigma = \tau$ ), we obtain the following advection-diffusion equation

$$(\partial_t + \vec{u} \cdot \nabla) \rho^\sigma = -\nabla \cdot c_s^2 \rho (\tau n G_f - \tau + \frac{1}{2}) \nabla \chi^\sigma \quad (\text{C.35})$$

The diffusion coefficient in the mixture is

$$D = -c_s^2 \rho (\tau n G_f - \tau + \frac{1}{2}) \quad (\text{C.36})$$

### C.3 Non-premixed binary scalar mixing

In all simulations in this Appendix, we suppose that two species have the same relaxation time for simplicity and periodic boundary conditions are used in both directions.

We first compute the mutual diffusivity in a binary mixture by measuring the decay of a sinusoidal concentration wave with small amplitude. The simulation was carried out on a  $128 \times 3$  rectangular lattice. Initially, we assume that both species have a same particle density  $n^b = n^w = 0.5$  at each grid in the whole field. A perturbation particle density wave

$\tilde{n}(x) = 0.01 \sin(2\pi x/128)$  is introduced into black species, i.e.  $n^b(x, 0) = 0.5 + \tilde{n}(x)$ . Two runs with  $\tau = 1.0$  and  $\tau = 2.0$  are performed.

Analytical solutions are calculated from Eq. (C.36). Fig. C.1 exhibits that numerical computations(dots) are in excellent agreement with the analytical predictions(lines).

Secondly, we study the binary scalar mixing in a square lattice. Two species labeled black(b) and white(w) are initially segregated and randomly distributed in the computational domain as shown in Figure C.2.

Initially, the macroscopic velocity is set to zero everywhere in the domain corresponding to a pure diffusion problem. The particle densities of both species are  $n^b = 1.0$ ,  $n^w = 0.0$  in the region of the black species and  $n^w = 1.0$ ,  $n^b = 0.0$  in the region of white species.

It should be reiterated here that this model permits the simulation of scalar mixing between species of equal or unequal mass molecular weights. The mixing characteristics of both cases have been reported in the paper (10). From the time evolution of the probability density function(PDF) of number density scalar  $n^* = \frac{n^b - n^w}{n^b + n^w}$ , we have captured the changes of the PDF shape from the initial double-delta shape to, finally, a Gaussian-like distribution, which is in excellent qualitative agreement with DNS data. Here we further test the numerical accuracy of the model for equal-mass case. We focus on comparisons of the time evolutions of PDF of scalar  $n^*$  with different interaction strength (diffusivity) and different resolutions to see how the mixing is affected by these parameters. Three snapshots of PDF shape are taken in each run.

Fig. C.3 shows the time evolutions of PDF of  $n^*$  with different interaction strengths in  $128^2$ ,  $256^2$  and  $512^2$  respectively. Lines correspond to  $G_f = 0.002(D = 0.166)$  and symbols to  $G_f = 0.125(D = 0.125)$ . Three time instants are picked up: initial double-delta shape(dashed-dot line and  $\diamond$ ), intermediate uniform distribution (solid line and  $\Delta$ ), and final Gaussian-like shape (dashed line and  $*$ ). Time instants corresponding to initial, intermediate and final have been normalized by a dimensionless constant  $s = Dt/N$  where  $N$  denotes the length of the computation domain. In each resolution, PDF shape match

very well at each corresponding mixing stage, which demonstrates that the mixing process is well captured. From the resolution perspective,  $512^2$  grid performs the best as expected.

## C.4 Conclusions

We have presented a LBM model for binary scalar mixing flows. Macroscopic equations governing the flows are derived in details by the Chapman-Enskog technique.

Simulations of the mixing model yield encouraging results: (i).The well known results of PDF evolution from continuum Navier-Stokes simulation in equal mass case are reproduced and unequal mass case generated right mixing physics which is difficult to handle with continuum based numerical method. (presented in our previous paper(10)); (ii).Mutual diffusivity are calculated analytically and confirmed by simulations; (iii).Mixing characteristics are well captured in different resolutions.

These simulations demonstrate that the presented LBM models are practical and reliable. From this work, more complicated flow simulation for combustion can be expected.

## C.5 Figures

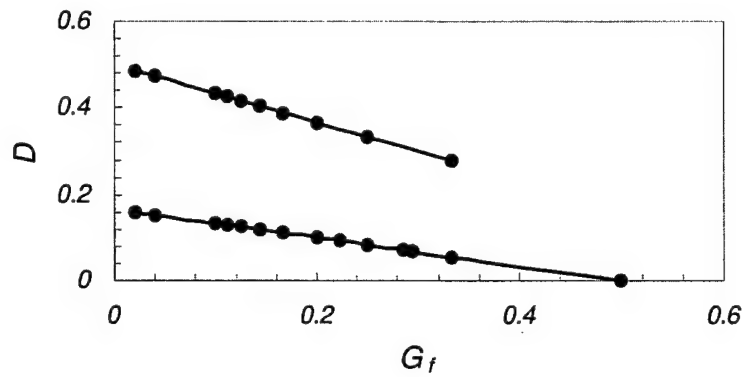


Figure C.1: Mutual diffusivity  $D$  vs. interaction strength  $G_f$  for given  $\tau s$  ( $\tau = 1.0$  upper and  $\tau = 2.0$  down). Lines: analytical prediction from Eq.(C.36); Symbols: LBM computation.

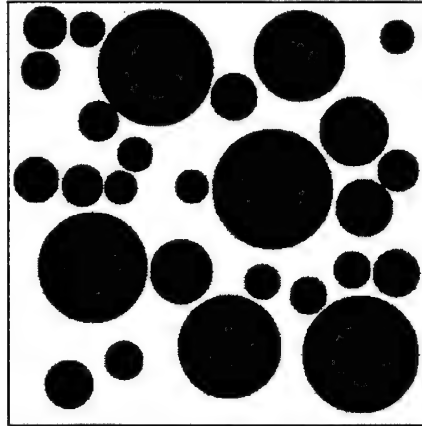


Figure C.2: A typical initial number density distribution of two species colored with black and white.  $n^b = 1.0$ ,  $n^w = 0.0$  in region of the black species and  $n^w = 1.0$ ,  $n^b = 0.0$  in region of white species. The average number density of both is nearly the same

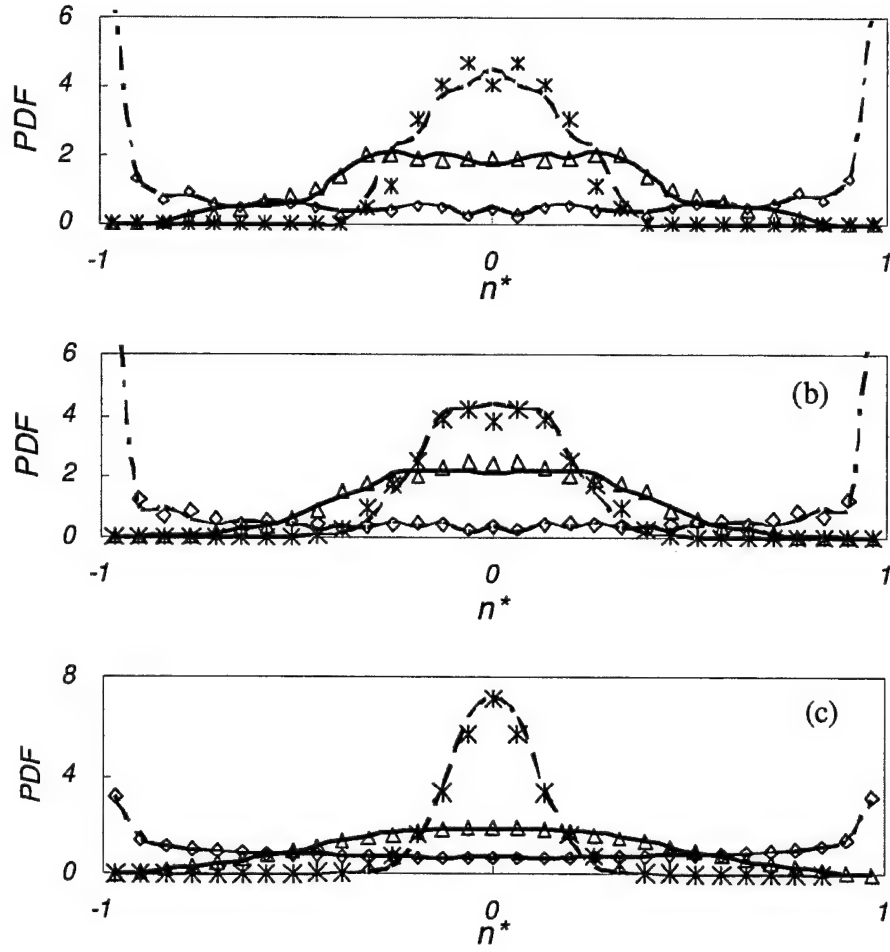


Figure C.3: Evolutions of the scalar PDF of  $n^*$ . (a).  $128^2$ , (b).  $256^2$ , (c).  $512^2$ . Lines:  $G_f = 0.002$  ( $D = 0.166$ ) and symbols:  $G_f = 0.125$  ( $D = 0.125$ ). Three normalized time stages: initial(dashed-dot lines), intermediate(solid lines) and final(dashed lines)



## Bibliography

- [1] H. Chen, S. Chen, and H. W. Matthaeus, Phys. Rev. A **45**, R5339 (1992).
- [2] Y. Qian, D. d'Humières, and P. Lallemand, Europhys. Lett. **17**(6), 479 (1992).
- [3] X. Shan and H. Chen, Lattice Boltzmann Model for Simulating Flows with Multiple Phases and Components Phys. Rev. E. **47**, 1815 (1993).
- [4] X. Shan and H. Chen, Simulation of Nonideal Gases and Liquid-gas Phase Transitions by the Lattice Boltzmann Equation Phys. Rev. E. **49**, 1815 (1994).
- [5] X. Shan and G. Doolen, Multicomponent Lattice-Boltzmann Model with Interparticle Interaction J. Stat. Phys. **81**, 379 (1995).
- [6] X. Shan and G. Doolen, Diffusion in a multicomponent Lattice Boltzmann Equation Model Phys. Rev. E. **54**, 3614 (1995).
- [7] H. Yu and K. Zhao, A New Lattice Boltzmann Model for Two-Phase Fluid Chin. Phys. Lett. **16**, 271 (1999).
- [8] L.-S. Luo and S. S. Girimaji, Lattice Boltzmann model for binary mixtures, Phys. Rev. E. **66**, 035301(R) (2002).
- [9] L.-S. Luo and S. S. Girimaji, Theory of the lattice Boltzmann method: Two-fluid model for binary mixtures, Phys. Rev. E. **67**, 036302(R) (2003).
- [10] H. Yu, L.-S. Luo, and S. S. Girimaji, Scalar Mixing and Chemical Reaction Simulations Using Lattice Boltzmann Method, Int. J. Computat. Eng. Sci. **3**, 73 (2002).
- [11] R. B. Bird, W. E. Stewart, and E. N. Lightfoot, *Transport Phenomena* (Wiley, New York, 1960)
- [12] S. Chapman and T. G. Cowling, *The Mathematical Theory of Non-Uniform Gases*(3rd ed.) (Cambridge University Press, London, 1970)

- [13] P. L. Bhatnagar, E. P. Gross, and M. Krook, Phys. Rev. **94**, 511 (1954).
- [14] X. He and L.-S. Luo, J. Stat. Phys. **88**, 927 (1997).
- [15] Dieter Wolf-Gladrow, J Stat. Phys. **79**, 1023 (1995)
- [16] L.-S Luo, Theory of the lattice Boltzmann method: Lattice Boltzmann models for nonideal gases Phys. Rev. E **62**, 4982 (2000).

## Appendix D

# Scalar Mixing and Chemical Reaction Simulations

Nomenclature			
$J$	Collision operator between two spices	$e_\alpha$	Discretized particle velocity
$n_\alpha$	Number density distribution function	$n^{(eq)}$	Equilibrium distribution function
$m$	Mass of molecule	$n$	Number density
$\vec{u}$	Fluid velocity	$\rho$	Fluid density
$\delta_t$	Time step	$\delta_x$	Grid size
$w_\alpha$	Weight function	$\Omega$	Collision operator
$x^\sigma$	Molar fraction for spice $\sigma$	$\omega^\sigma$	Mass fraction for spice $\sigma$
$C$	Concentration	$\kappa_{ov}$	Reaction coefficient
$E$	Effective activation energy	$M$	Mass weight
$R$	Universal gas constant	$S_L$	Burning velocity
$T$	Temperature	$Y$	Mass ratio

### D.1 Introduction

With few notable exceptions, the LBM has been so far used mostly for single-component, inert and isothermal flows. In this Appendix, we simulate scalar mixing in a multi-component

flow and a chemical reacting flow using the lattice Boltzmann computational approach. At the continuum level, the mixing example considered appears as a pure diffusion problem without any advection velocities. However, at the mesoscopic level, each of the components is associated with non-zero velocities. Hence, the problem considered is truly more significant than simple passive scalar mixing. Due to the kinetic nature of the LBE scheme, the extension of this method to cases with non-trivial macroscopic velocity field is straight forward. The second problem considered is one-dimensional flame propagation in a well-stirred homogeneous mixture of propane and air. The flame speed calculated using the LBM is in good agreement with experimental data. This problem is very similar to the one solved by Yamamoto(4) but with a slightly different physical field. The overall results are encouraging and establish the feasibility of the LBM as a viable computational approach for simulating mixing and reaction.

The remainder of the Appendix is organized as follows. In Section D.2, the lattice Boltzmann equations used in the simulations are presented. The results from the mixing and reacting simulations are presented in Section D.4. We conclude in Section D.5 with a brief discussion. Details of the physical parameters used in the reacting flow simulation are presented in Appendix D.A.1

## D.2 Lattice Boltzmann equation for scalar mixing

For the sake of simplicity without losing generality, we adopt D2Q9 model, as shown in Figure A.1. Consider a multi-species field:  $n_\alpha^\sigma$  denotes the number density distribution function of a particular species  $\sigma$  with discrete velocity  $\vec{e}_\alpha$ ,  $\sigma = 1, 2, 3, \dots$ . The number density and molecular weight of species  $\sigma$  are given respectively by  $n^\sigma$  and  $m^\sigma$ . Then mass density of the  $\sigma$ -species is given as

$$\rho^\sigma = m^\sigma n^\sigma = m^\sigma \sum_{\alpha} n_{\alpha}^{\sigma} \quad (\text{D.1})$$

Number density, mass density and velocity of the mixture are

$$n = \sum_{\sigma} n^{\sigma} \quad (\text{D.2})$$

$$\rho = \sum_{\sigma} \rho^{\sigma} \quad (\text{D.3})$$

and

$$\vec{u} = \frac{1}{\rho} \sum_{\sigma} (m^{\sigma} \sum_{\alpha} n_{\alpha}^{\sigma} \vec{e}_{\alpha}) \quad (\text{D.4})$$

respectively.

For the sake of concreteness and simplicity without losing generality, we construct a LBE for binary mixture with  $\delta_x = \delta_t = 1$ . Let  $\sigma$  and  $\sigma'$  denote the two species of interest. The LBE for each species is

$$n_{\alpha}^{\sigma}(\vec{x} + \vec{e}_{\alpha}, t + 1) = n_{\alpha}^{\sigma}(\vec{x}, t) + \Omega_{\alpha}^{\sigma}(\vec{x}, t) \quad (\text{D.5})$$

where the collision operator

$$\Omega_{\alpha}^{\sigma} = -\frac{1}{\tau^{\sigma}} [n_{\alpha}^{\sigma} - n_{\alpha}^{\sigma(eq)}] + \frac{J_{\alpha}^{\sigma\sigma'}}{m^{\sigma}} \quad (\text{D.6})$$

includes an additional term  $J_{\alpha}^{\sigma\sigma'}$  which reflects interactions between two species.

We use the following number density equilibrium distribution function

$$n_{\alpha}^{\sigma(eq)} = w_{\alpha} n^{\sigma} [1 + 3(\vec{e}_{\alpha} \cdot \vec{u}') + \frac{9}{2}(\vec{e}_{\alpha} \cdot \vec{u}')^2 - \frac{1}{2}u'^2] \quad (\text{D.7})$$

with

$$\vec{u}' = \frac{1}{\rho} \sum_{\sigma} \frac{m^{\sigma}}{\tau^{\sigma}} (n^{\sigma} \vec{u}^{\sigma}) \quad (\text{D.8})$$

The binary interaction term is modeled as(3)

$$J_{\alpha}^{\sigma\sigma'} = \frac{1}{\tau^{\sigma\sigma'}} n_{\alpha}^{eq} \cdot [\nabla x^{\sigma} + (x^{\sigma} - \omega^{\sigma}) \frac{\nabla \rho}{\rho}] = -J_{\alpha}^{\sigma'\sigma} \quad (\text{D.9})$$

where  $x^{\sigma}$  and  $\omega^{\sigma}$  are molar and mass fractions of the species  $\sigma$

$$x^{\sigma} = \frac{n^{\sigma}}{n}, \quad \omega^{\sigma} = \frac{\rho^{\sigma}}{\rho}$$

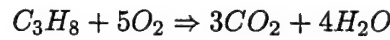
and

$$n_{\alpha}^{(eq)} = w_{\alpha} n [1 + 3(\vec{e}_{\alpha} \cdot \vec{u}) + \frac{9}{2}(\vec{e}_{\alpha} \cdot \vec{u})^2 - \frac{1}{2}u^2] \quad (\text{D.10})$$

### D.3 Lattice Boltzmann equations for reacting flow

Here we simulate simple one-dimensional flame propagation through a premixed mixture of propane and air. The problem studied is identical to that of Yamamoto(4) but the physical combustion field is slightly different. The simplifying assumptions invoked in this study are now listed:

- No external forces in the field and the flow is incompressible.
- The chemical reaction (heat release) does not affect the flow field; temperature and concentration fields are decoupled and solved separately.
- Nitrogen is inert.
- The transport properties are constants (not functions of temperature).
- Viscous energy dissipation and radiative heat losses are negligible.
- Simple one step reaction is considered



and the over-all reaction rate is given by

$$\omega_{ov} = \kappa_{ov} C_{C_3H_8} C_{O_2} e^{-E/RT}$$

where  $C_{C_3H_8}$ ,  $C_{O_2}$ ,  $\kappa_{ov}$  and  $E$  are concentrations of fuel propane and oxygen, reaction coefficient and effective activation energy respectively.

In a reacting flow, the state of the fluid at any given point in space and time can be completely specified in terms of fluid velocity, composition vector (either in terms of mass fraction or concentration) and temperature. We will need to develop the LBE for all these variables. For generating a background flow, the conventional LBM substeps of collision(relaxation) and streaming (convection) are used. However for the temperature and

concentration fields, there is an extra substep between collision and streaming substeps to account for reaction. This is identical to the time-splitting approach used in continuum methods for chemically reacting flows.

**Flow field.** The background flow-field is obtained using the following stencil for partial pressure

$$p_\alpha(\vec{x} + \vec{e}_\alpha, t + 1) = p_\alpha(\vec{x}, t) - \frac{1}{\tau_p} [p_\alpha(\vec{x}, t) - p_\alpha^{eq}(\vec{x}, t)] \quad (D.11)$$

where

$$p_\alpha^{eq} = w_\alpha p [1 + 3(\vec{e}_\alpha \cdot \vec{u}) + \frac{9}{2}(\vec{e}_\alpha \cdot \vec{u})^2 - \frac{3}{2}u^2] \quad (D.12)$$

The total pressure  $p (= \rho c_s^2)$  and the fluid velocity are calculated using

$$p = \sum_\alpha p_\alpha$$

$$\vec{u} = \frac{1}{p} \sum_\alpha \vec{e}_\alpha p_\alpha$$

This is the velocity used for determining the equilibrium distribution functions in temperature and concentration fields.

**Temperature and concentration fields.** For temperature ( $T$  is normalized by  $T_c = E/R$ ) and concentration (mass ratio  $Y^i, i = C_3H_8, O_2, CO_2$  and  $H_2O$ ) fields, there is an extra computational substep, reaction, besides conventional computational substeps of collision and advection.

- COLLISION

$$\tilde{T}_\alpha(\vec{x}, t) = T_\alpha(\vec{x}, t) - \frac{1}{\tau_T} [T_\alpha(\vec{x}, t) - T_\alpha^{(eq)}(\vec{x}, t)] \quad (D.13)$$

$$\tilde{Y}_\alpha^i(\vec{x}, t) = Y_\alpha^i(\vec{x}, t) - \frac{1}{\tau_{Y^i}} [Y_\alpha^i(\vec{x}, t) - Y_\alpha^{i(eq)}(\vec{x}, t)] \quad (D.14)$$

where

$$T_\alpha^{(eq)} = w_\alpha T [1 + 3(\vec{e}_\alpha \cdot \vec{u}) + \frac{9}{2}(\vec{e}_\alpha \cdot \vec{u})^2 - \frac{3}{2}u^2] \quad (D.15)$$

$$Y_\alpha^{i(eq)} = w_\alpha Y^i [1 + 3(\vec{e}_\alpha \cdot \vec{u}) + \frac{9}{2}(\vec{e}_\alpha \cdot \vec{u})^2 - \frac{3}{2}u^2] \quad (D.16)$$

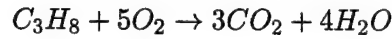
and

$$T = \sum_{\alpha} T_{\alpha}, \quad Y^i = \sum_{\alpha} Y_{\alpha}^i$$

Relaxation time-constant  $\tau_T$  is determined by thermal diffusivity and  $\tau_{Y^i}$ 's are determined by the diffusivity of corresponding species.

- REACTION

*Reaction equation*



$$\omega_{ov} = \kappa_{ov} \tilde{C}_{C_3H_8} \tilde{C}_{O_2} e^{-1/\tilde{T}}$$

*Concentrations*

$$\tilde{C}_i = \rho \tilde{Y}_i / M_i$$

*Reaction terms*

$$Q_{Y^i} = \lambda_i \frac{M_i t_0}{\rho} \omega_{ov}$$

$$Q_T = \frac{Q t_0}{\rho c_p T_c} \omega_{ov}$$

where

$$\tilde{Y}^i = \sum_{\alpha} \tilde{Y}_{\alpha}^i, \quad \tilde{T} = \sum_{\alpha} \tilde{T}_{\alpha}$$

In the above equations, the stoichiometric coefficients ( $\lambda$ 's) for the various species are:

$\lambda_{C_3H_8} = -1$ ,  $\lambda_{O_2} = -5$ ,  $\lambda_{CO_2} = 3$ ,  $\lambda_{H_2O} = 4$  and all physical parameters are listed in Appendix A.

- STREAMING

$$T_{\alpha}(\vec{x} + \vec{e}_{\alpha}, t + 1) = \tilde{T}_{\alpha}(\vec{x}, t) + w_{\alpha} Q_T$$

$$Y_{\alpha}^i(\vec{x} + \vec{e}_{\alpha}, t + 1) = \tilde{Y}_{\alpha}^i(\vec{x}, t) + w_{\alpha} Q_{Y^i}$$



## D.4 Simulations

As mentioned in the introduction, the primary objective of this work is to investigate the ability of the LBM to simulate scalar mixing, chemical reaction and ultimately turbulent combustion. Working towards this end, we perform simulations of two unit problems: one to establish the mixing characteristics and another to demonstrate the chemical reaction scheme.

### D.4.1 Non-premixed binary scalar mixing

This problem epitomizes the scalar mixing issues encountered in a typical non-premixed combustion application. Two species (presumably fuel and oxidizer) are initially segregated and randomly distributed in the computational domain which in the present case is a square box. Mesh size is set  $500 \times 500$ . The two species are generically labeled as black and white. A typical initial distribution is shown in Figure D.1.

The macroscopic velocity is set everywhere to zero corresponding to a pure diffusion problem. It should be reiterated here that the mesoscopic velocities are non-zero. The initial values for the number densities are  $n^b = 1.0$ ,  $n^w = 0.0$  in region of the black species and  $n^w = 1.0$ ,  $n^b = 0.0$  in region of white species. Simulations are performed for two different sets of relaxation time scales:  $\tau^b = \tau^w = 1.0$  and  $\tau^{bw} = \tau^{wb} = 30.0$ . Citing homogeneity of the scalar field, periodic boundary conditions are used in all directions.

To discretize  $\nabla x^\sigma$  and  $\nabla \rho$  in the binary interaction term in Equation D.9, we use central difference operator. Taylor series expansion of each of  $f(\vec{x} + \vec{e}_i)$  terms to the second order leads the following stencil of  $\partial_{x_1}$  and  $\partial_{x_2}$ :

$$\partial_{x_1} = \frac{1}{12} \begin{bmatrix} -1 & 0 & 1 \\ -4 & 0 & 4 \\ -1 & 0 & 1 \end{bmatrix}, \quad \partial_{x_2} = \frac{1}{12} \begin{bmatrix} 1 & 4 & 1 \\ 0 & 0 & 0 \\ -1 & -4 & -1 \end{bmatrix} \quad (\text{D.17})$$

That is

$$\partial_{x_1} f(\vec{x}) \approx \frac{1}{12} [4f(\vec{x} + \vec{e}_1) + f(\vec{x} + \vec{e}_5) + f(\vec{x} + \vec{e}_8) - f(\vec{x} + \vec{e}_6) - 4f(\vec{x} + \vec{e}_3) - f(\vec{x} + \vec{e}_7)] \quad (\text{D.18})$$

$$\partial_{x_2} f(\vec{x}) \approx \frac{1}{12} [4f(\vec{x} + \vec{e}_2) + f(\vec{x} + \vec{e}_5) + f(\vec{x} + \vec{e}_6) - f(\vec{x} + \vec{e}_7) - 4f(\vec{x} + \vec{e}_4) - f(\vec{x} + \vec{e}_8)] \quad (\text{D.19})$$

in which  $f$  can be  $x^\sigma$  and  $\rho^\sigma$ .

The lattice Boltzmann methodology permits simulation of mixing between species of equal or unequal number and mass densities with equal facility. However, in continuum based methods, mixing between species of unequal mass densities is not straight-forward. This represents a fundamental advantage of the LBM over continuum-based methods.

**Equal mass case**( $m^b = m^w = 1.0$ ). The first case studied is mixing of two fluids of equal molecular weights and number densities, hence of equal mass density. This case is particularly interesting as the results can be directly compared with directed numerical simulation(DNS) of Navier-stokes equation data of Eswaran and Pope (5). In this case, the number density and mass density are equivalent since the molecular weight of the two species are identical.

Figure D.2(a) shows the time evolution of the probability density function(pdf) of scalar  $\bar{\rho}$ :

$$\bar{\rho} = \frac{\rho^b - \rho^w}{\rho^b + \rho^w}$$

The corresponding DNS(5) data is shown in Figure D.2(b). The LBE and DNS data show excellent qualitative agreement. In particular, the change of the pdf shape from the initial double-delta shape through a nearly uniform distribution to, finally, a Gaussian-like distribution is well captured by the LBE results. It deserves mention here that many other mixing models do not, even qualitatively, capture the form of pdf during evolution.

In Figure D.3, the time evolution of the root-mean-square(rms) of scalar fluctuations ( $\rho'$ ) obtained from LBE is compared with that from DNS(5):

$$\rho' = \sqrt{\langle (\rho^b - \langle \rho^b \rangle)^2 \rangle} \quad (\text{D.20})$$

where  $\langle \dots \rangle$  implies volume-averaged value. The relaxation time-constant has been chosen to yield the best agreement. For the optimal time-constant, the agreement is again excellent. In ongoing work, we attempt to accurately characterize the relationship between the time-constant and diffusion coefficient(3). Here, it suffices to say that given the right time-constant, the LBE captures the DNS behavior well, qualitatively and quantitatively.

**Unequal mass case**( $m^b = 2.0, m^w = 1.0$ ). The unequal mass case is particularly interesting since it represents a more practical problem, mixing between species of unequal mass densities. In this case, the initial distribution of black and white species is similar to the equal mass case. Thus the average number density of black and white species are identical. However, the molecular weight of the black species is twice that of the white species. Hence, the macroscopic mass density of the black species is twice that of the white species. The precise definition of the mass density used here is

$$\overline{\rho^\sigma} = \frac{\rho^\sigma - \rho^{\sigma'}}{\rho^\sigma + \rho^{\sigma'}} = \frac{m^\sigma n^\sigma - m^{\sigma'} n^{\sigma'}}{m^\sigma n^\sigma + m^{\sigma'} n^{\sigma'}}$$

and the particle number density is

$$\overline{n^\sigma} = \frac{n^\sigma - n^{\sigma'}}{n^\sigma + n^{\sigma'}}$$

In the unequal molecular weight case, mass density and number density are two independent entities. The evolution of both these quantities are investigated. In Figure D.4, the mass density evolution is given for both species. The mass density goes from an initial double-delta shape to a Gaussian-like shape centered around the global average of the respective density. The final pdf shape for each species is clearly not symmetric. This is easily understood since the overall average density of the black species is twice that of the white species.

In Figure D.5, the number density evolution is shown. Since the average number density is identical for both species, the final pdf distribution is symmetric about the mean value for each species. However, the intermediate forms of the pdf are quite nonsymmetric, demonstrating that the mixing process in this case is quite different from the equal-mass

case even if the final distributions are similar. A detailed study of the physics of mixing between species of unequal mass-densities will be undertaken later.

#### D.4.2 Reacting flow in a 1-D channel

In this example, we study the ability of LBM to simulate chemical reaction. The simplest non-trivial case when reaction can be studied without the complicating effects of mixing is the case of 1-D flame propagation through a homogeneous premixed mixture.

Schematic of the flow simulated is shown in Figure D.6. For this simple case, the background flow generated from Eq.(D.11) maintains both the pressure and velocity fields uniform in space and time. A heat source is placed at a location close to the inlet to ignite the mixture. Once ignition is achieved, the heat source is removed. At subsequent times the flame propagates to the right. Initial conditions are set as following:

The values of pressure and velocity are set at  $p = 1$ ,  $u_x = u_{in} = 0.1$ ,  $u_y = 0.0$ . Both fields are maintained uniform at all times in this simple case. The temperature is set at  $T = 300^0 K$  everywhere except at  $x = 50$  where a heat source is placed with  $T_{source} = 1500^0 K$  to ignite the mixture. The hot spot is removed after the mixture ignites. The mass ratio of nitrogen is  $Y_{N_2} = 0.7375$ . The well-premixed mixture consists of propane and oxygen with the mass ratios of  $Y_{C_3H_8} = 0.2252$ ,  $Y_{O_2} = 0.0373$ . The mass fractions of the products are initially set to zero:  $Y_{CO_2} = Y_{H_2O} = 0.0$ .

Periodic boundary conditions are used at the top and bottom boundaries and the fully developed boundary condition is applied at the outlet. At the inlet, the initial conditions are maintained.

In Figure D.7, the flame position is shown as a function of time. The flame location is identified as the position with the highest reaction rate at any given time. The linear variation of flame location with time (in Figure D.7) indicates that the flame propagates at a nearly constant rate. This flame speed can be easily estimated from knowing the flame position at initial( $t_i = 0$ ;  $x_{fl} = 50$ ) and final( $t_f = 4000$ ;  $x_{fl} = 406$ ) times. The flame speed

thus calculated is

$$v_f = \frac{x_{fl}(t_f) - x_{fl}(t_i)}{t_f - t_i} = \frac{406 - 50}{4000 - 0} = 0.0089$$

in lattice units. Knowing the flame speed, the burning velocity can be easily determined:

$$S_L = u_{in} - v_f$$

In the above,  $u_{in}$  is the reactant velocity at the inlet (which is maintained uniform throughout the flow-field). The burning velocity thus obtained will be in lattice units. This can be converted into metric units as follows:

$$S_L = \frac{u_{in} - v_f}{u_{in}} \cdot u_p \quad (D.21)$$

The resulting burning velocity is  $S_L = 0.11 \text{ m/s}$  which compares extremely well with the value obtained from experiments for a propane-air flame(6).

Figure D.8 shows that the reaction rate profile in the reaction zone as time evolves. Simulations indicate that flame behavior is sensitive to the magnitude of the heat source.

## D.5 Conclusions

In this Appendix, we simulate scalar mixing and chemical reacting flows using LBM. In the case of equal-density species mixing, well known results from continuum Navier-stokes simulation are reproduced. The true advantage of the LBM can be seen from the mixing simulations of species of different molecular weights. The results appear quite encouraging. Such simulations are very difficult with continuum based methods. The premixed reacting flow simulations also produce results that are in good agreement with known data. Based on these simulations, we conclude that LBM can perform adequately for more complicated turbulent combustion simulations.

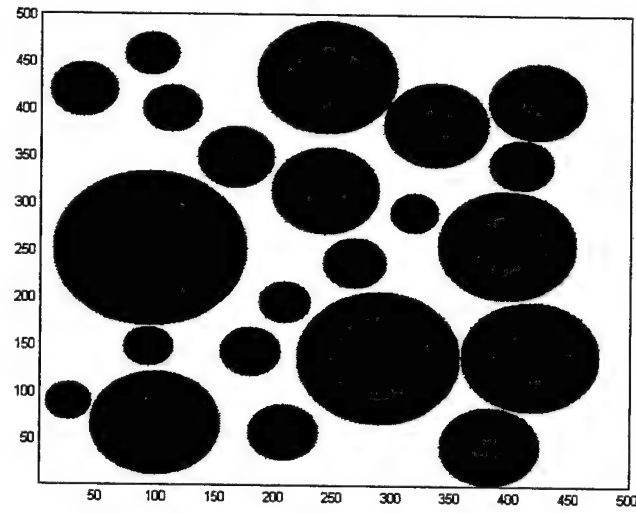


Figure D.1: Initial number density distribution for both equal and unequal mass cases

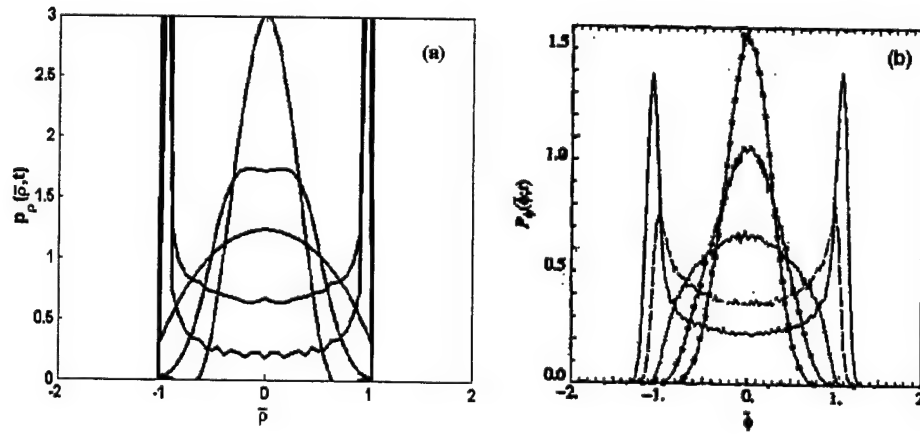


Figure D.2: Pdf evolution of number density in equal mass case. (a)LBE; (b)DNS

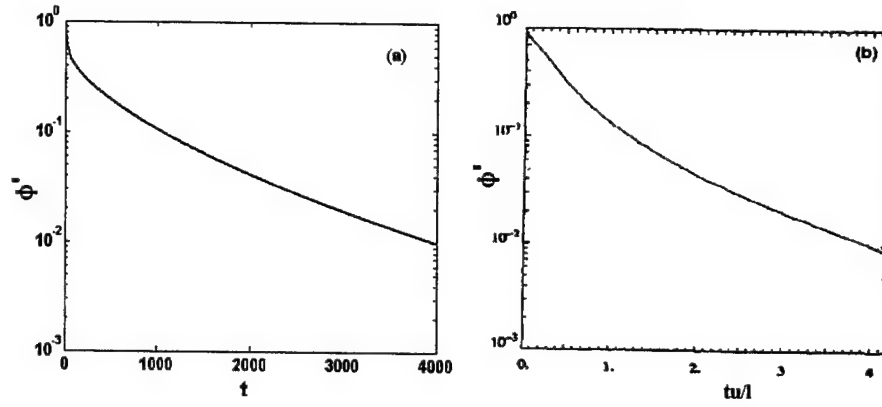


Figure D.3: Evolution of rms scalar ( $\phi'$ ) in equal mass case. (a)LBE( $\phi' = 2\rho'$ ); (b)DNS

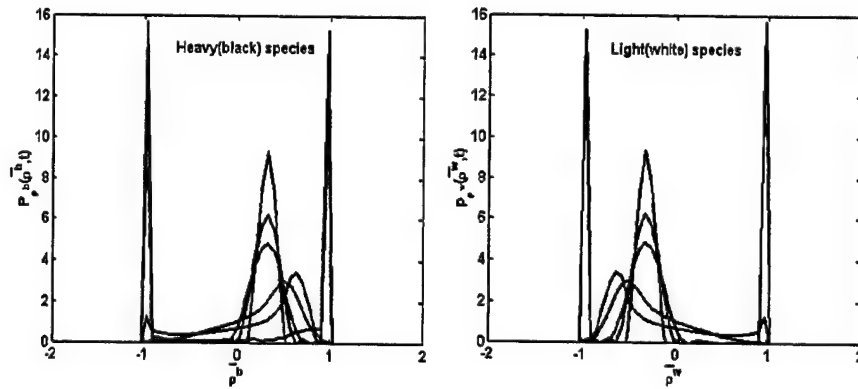


Figure D.4: Pdf evolution of mass density in unequal mass case( $m^b : m^w = 2 : 1$ )

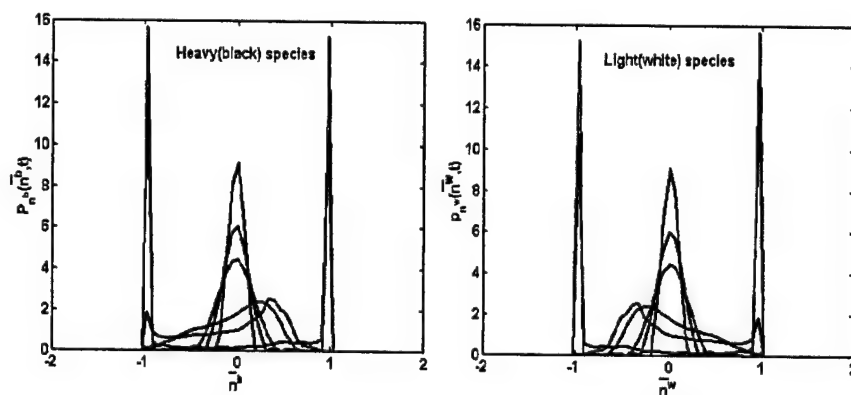


Figure D.5: Pdf evolution of number density in unequal mass case( $m^b : m^w = 2 : 1$ )

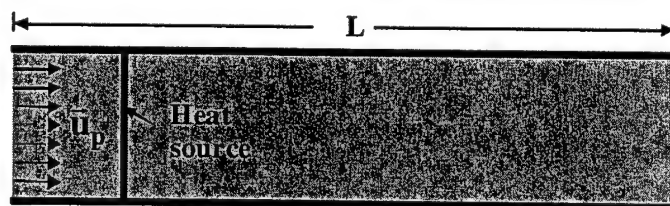


Figure D.6: A schematic illustration of a simple 1-D reacting flow



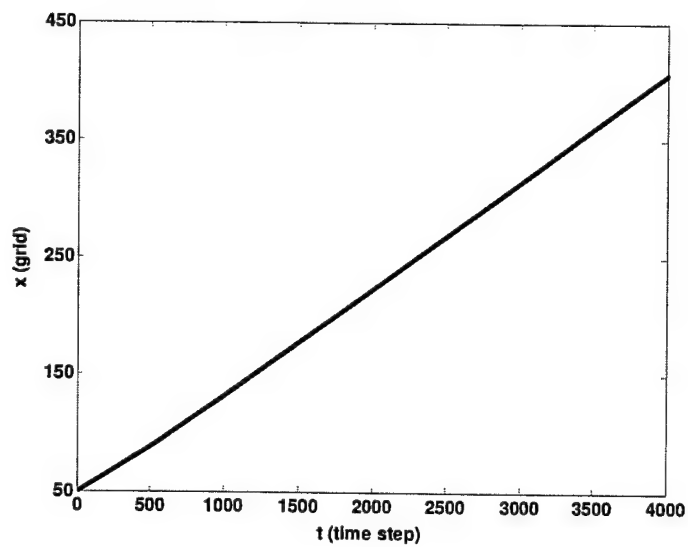


Figure D.7: The flame position evolution with time

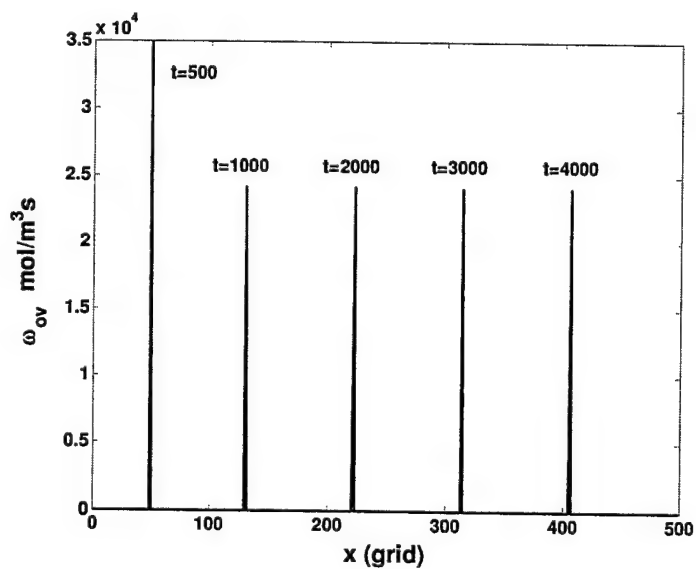


Figure D.8: Reaction rate profiles at different times.

## D.6 Figures

### Appendix D.A.1: Physical parameters used in the reacting flow simulation

- Reaction coefficient  $\kappa_{ov} = 9.9 \times 10^7 [m^3 \cdot mol^{-1} \cdot s^{-1}]$
- Universal gas constant  $R = 8.315 [J \cdot mol^{-1} \cdot K^{-1}]$
- Effective activation energy  $E = 30 [kcal \cdot mol^{-1}] = 1.26 \times 10^5 [J \cdot mol^{-1}]$
- Heat of overall reaction  $Q = 2.05 \times 10^6 [J \cdot mol^{-1}]$
- Density of pre-mixed mixture  $\rho = 1.2 [kg \cdot m^{-3}]$
- Heat capacity  $c_p = 29.1 [J \cdot mol^{-1} \cdot K^{-1}] = 10^3 [J \cdot kg^{-1} \cdot K^{-1}]$
- Kinetic viscosity  $\nu = 1.6 \times 10^{-5} [m^2 \cdot s^{-1}]$
- Thermal diffusivity  $\kappa = 2.2 \times 10^{-5} [m^2 \cdot s^{-1}]$
- Diffusivities

$$D_{C_3H_8} = 1.1 \times 10^{-5} [m^2 \cdot s^{-1}], \quad D_{O_2} = 2.1 \times 10^{-5} [m^2 \cdot s^{-1}]$$

$$D_{CO_2} = 1.6 \times 10^{-5} [m^2 \cdot s^{-1}], \quad D_{H_2O} = 2.2 \times 10^{-5} [m^2 \cdot s^{-1}]$$

- Mass weight

$$M_{C_3H_8} = 4.4 \times 10^{-2} [kg/mol], \quad M_{O_2} = 3.2 \times 10^{-2} [kg/mol]$$

$$M_{CO_2} = 4.4 \times 10^{-2} [kg/mol], \quad M_{H_2O} = 1.8 \times 10^{-2} [kg/mol]$$

- Equivalent ratio

$$\phi = \frac{Y_{C_3H_8}/Y_{O_2}}{0.276} = 0.6$$

- Length of the 1-D channel  $L = 16.7 [mm]$
- Physical velocity  $u_p = 1.0 [m \cdot s^{-1}]$

## Bibliography

- [1] Y. H. Qian, D. d'Humières and P. Lallemand, Lattice BGK Model for Navier-Stokes Equation, *Europhysics Letters*, **17**(6):479(1992).
- [2] H. Chen, S. Chen and H.W. Matthaeus, Recovery of the Navier-Stokes Equation Using a Lattice Boltzmann Method, *Physical Review A*, **15**:R5339(1992).
- [3] L.-S. Luo, H. D. Yu and S. Girimaji, Binary Mixing Simulations Using Lattice Boltzmann Method, being prepared.
- [4] K. Yamamoto, X. He and G. D. Doolen, Simulation of Combustion Field with Lattice Boltzmann Method, accepted by *Journal Computational Physics*.
- [5] V. Eswaran and S.B. Pope, Direct Numerical Simulations of the Turbulent mixing of a Passive Scalar, *Physics of Fluids*, **31**,506(1988).
- [6] I. Yamaoka and H. Tsuji, *Twentieth Symposium(International) Combustion*, The Combustion Institute, Pittsburgh, 1883(1982).

## Appendix E

# DNS and LES of Decaying Isotropic Turbulence With and Without Frame Rotation

### Nomenclature

$C_{sm}$	Smagorinsky constant	$\mathbf{a}$	Coriolis acceleration
$c_s$	Speed of sound	$\mathbf{e}_\alpha$	Discretized particle velocity
$f$	Distribution function	$f^{(eq)}$	Equilibrium distribution function
$\mathbf{u}$	Fluid velocity	$\rho$	Fluid density
$\nu$	Viscosity	$S_{ij}$	Strain rate
$\delta_t$	Time step	$\delta_x$	Grid size
$\tau$	Normalized relaxation time	$w_\alpha$	Weight function
$\Omega$	Angular velocity	$n$	Decay exponential
$\kappa$	Wave number	$k$	Turbulent kinetic energy
$\varepsilon$	Dissipation rate	$\lambda$	Taylor microscale length
$Re_\lambda$	Taylor microscale Reynolds number	$t'$	Normalized time ( $t\varepsilon_0/k_0$ )

## E.1 Introduction

In this Appendix, we explore the application of LBM to turbulence. In an effort to evaluate the capability of the LBM in turbulence, we perform direct numerical simulation (DNS) and large-eddy simulation (LES) of decaying homogenous isotropic turbulence (HIT) in both inertial and rotating frames of reference. Decaying HIT is an important benchmark problem in the field of DNS and LES of turbulence. In fact, the first attempt at DNS with incompressible Navier-Stokes equation involved this problem (1). Since then several numerical investigations of decaying HIT have been carried out, including some recent NS studies on decay exponents and low wave-number spectral scaling (2; 3; 4; 5). Some preliminary studies of three-dimensional (3D) decaying HIT using LBE have also been performed (6; 7; 8), but these investigations stop well short of quantitative comparisons with the well established classical results.

The objective of the present Appendix is to perform a comprehensive investigation of decaying HIT with LBE-DNS and LBE-LES to establish the suitability of the LBM for turbulence applications. For this purpose, we perform three type of simulations: **(a) LBE-DNS of decaying HIT in inertial and rotating frame of reference.** The decay exponent for the kinetic energy  $k$  and the dissipation rate  $\epsilon$  are computed and compared with corresponding NS-DNS results. The low wave-number scalings of the energy spectrum are studied. The effect of rotation on the kinetic energy decay is investigated. **(b) LBE-LES of decaying HIT inertial frame of reference.** We compute kinetic energy decay, energy spectrum and flow structures using LBE-LES. By comparing LBE-LES results with the corresponding LBE-DNS results, we observe that LBE-LES accurately captures large scale flow behavior. We find that the optimal Smagorinsky constant value for LBE-LES is smaller than the traditional value used in NS-LES approaches. **(c) LBE-LES vs. NS-LES.** We carry out a comparative study of the LBE-LES and NS-LES of decaying HIT. We show that the LBE-LES simulations preserve flow structures more accurately than the NS-LES counterpart.

This is due to the fact that some history/non-local effects are inherent in the LBE subgrid closure.

The remainder of this Appendix is organized as follows. Section E.2 briefly reviews relevant background on decaying HIT. Section E.3 gives a concise introduction to the LBM equations for DNS and LES. We present our results in Section E.4 and conclude in Section E.5.

## E.2 Homogeneous isotropic turbulence

The energy spectrum  $\hat{E}(\kappa, t)$  in decaying HIT evolves as

$$\partial_t \hat{E}(\kappa, t) = -\hat{T}(\kappa, t) - 2\nu\kappa^2 \hat{E}(\kappa, t), \quad (\text{E.1})$$

where  $\kappa$  is the wave-number and  $\nu$  is the kinematic viscosity, and  $\hat{T}(\kappa, t)$  represents the nonlinear energy transfer between modes (cf. Eq. (6.162) in (9)). The kinetic energy  $k$  and dissipation rate  $\varepsilon$  of turbulence are given, respectively, by

$$k = \int \hat{E}(\kappa) d\kappa, \quad \text{and} \quad \varepsilon = 2\nu \int \kappa^2 \hat{E}(\kappa) d\kappa.$$

It has been long observed that, after a short initial transient period of time, the kinetic energy  $k$  and dissipation rate  $\varepsilon$  exhibit power-law decay (9)

$$\frac{k(t)}{k_0} \sim \left(\frac{t}{t_0}\right)^n, \quad \frac{\varepsilon(t)}{\varepsilon_0} \sim \left(\frac{t}{t_0}\right)^{-(n+1)}, \quad (\text{E.2})$$

where  $k_0$  and  $\varepsilon_0$  are the values of  $k$  and  $\varepsilon$  at the reference time  $t_0 = nk_0/\varepsilon_0$ . Isotropic turbulence is typically characterized by the Taylor-microscale Reynolds number

$$\text{Re}_\lambda = \frac{u_{\text{rms}}\lambda}{\nu} = \sqrt{\frac{20}{3\nu\varepsilon}} k, \quad (\text{E.3})$$

where  $\lambda = \sqrt{15\nu u_{\text{rms}}^2/\varepsilon}$  is the transverse Taylor-microscale length and  $u_{\text{rms}} = \sqrt{2k/3}$  is the root mean square (rms) of the velocity field  $\mathbf{u}$ .

Equation (E.1) admits a continuous class of invariant solutions in the limit of  $\text{Re} \rightarrow \infty$  (10). At the large  $\text{Re}$ ,  $\hat{E}(\kappa, t)$  at the low wave-number behaves as  $\lim_{\kappa \rightarrow 0} \hat{E}(\kappa) \sim \kappa^\sigma$ , where

$\sigma$  is a time-independent constant (e.g. (11)). For inviscid fluids, if Loitsyansky's integral (12) is an invariant, then  $\sigma = 4$  and  $n = 10/7$  (13); if Birkhoff's integral (14) is an invariant, then  $\sigma = 2$  and  $n = 6/5$  (15). It has been recently shown that time-invariant integral length scale  $l$  corresponds to  $\sigma = \infty$  and  $n = 2$  and time-invariant Reynolds number corresponds to  $\sigma = 1$  and  $n = 1$  (16). Furthermore, the conservation of energy, angular momentum, and helicity lead to  $\sigma = 2, 7$ , and  $1$ , in the limit of  $\text{Re} \rightarrow \infty$ , respectively. The energy conservation of inviscid fluid uniquely determines the invariant solution of Eq. (E.1), i.e.,  $\sigma = 2$ , in accordance with Birkhoff's invariant (14). Despite the apparent simplicity of the decaying HIT problem, the relevant flow invariant, asymptotic decay exponent and the low wave-number scaling are strong functions of the initial spectrum and Reynolds number. There is still no clear consensus on whether the angular momentum or energy is the correct invariant. It is also not clear what the conditions are under which the invariance of either quantity can be observed. Consequently, various results have been reported (2; 3; 10; 17).

We perform detailed comparisons with established data qualitatively and quantitatively on the following important items: (i) energy decay exponent  $n$ , (ii) low wave-number scaling of the spectra, (iii) flow structure, and (iv) effect of rotation on kinetic energy decay.

## E.3 LBE formulation for DNS and LES of turbulence

### E.3.1 Lattice Boltzmann equation for DNS

The LBE with single-relaxation-time approximation due to Bhatnagar, Gross, and Krook (BGK) (18) for the collision operator is (19; 20)

$$f_\alpha(\mathbf{x} + \mathbf{e}_\alpha \delta_t, t + \delta_t) = f_\alpha(\mathbf{x}, t) - \frac{1}{\tau} \left[ f_\alpha - f_\alpha^{(\text{eq})} \right] + F_\alpha, \quad (\text{E.4})$$

where  $f_\alpha$  is the density distribution function with discrete velocity  $\mathbf{e}_\alpha$  along the  $\alpha$ th direction,  $f_\alpha^{(\text{eq})}$  is the equilibrium distribution function, and  $\tau$  is the relaxation time due to the fluid particle collision determining the viscosity  $\nu$  of the modeled fluid. In what follows, we

use the LBE model with 19 velocities in three dimensions, i.e., the D3Q19 model shown in Fig. A.2.

The discrete velocities are:

$$\mathbf{e}_\alpha = \begin{cases} (0, 0), & \alpha = 0 \\ (\pm 1, 0, 0)c, (0, \pm 1, 0)c, (0, 0, \pm 1)c, & \alpha = 1-6 \\ (\pm 1, \pm 1, 0)c, (\pm 1, 0, \pm 1)c, (\pm 1, \pm 1, 0)c, & \alpha = 7-18. \end{cases} \quad (\text{E.5})$$

The equilibria for incompressible flow (21) are

$$f_\alpha^{(\text{eq})} = w_\alpha \left\{ \delta\rho + \rho_0 \left[ \frac{3\mathbf{e}_\alpha \cdot \mathbf{u}}{c^2} + \frac{9(\mathbf{e}_\alpha \cdot \mathbf{u})^2}{2c^4} - \frac{3u^2}{2c^2} \right] \right\}, \quad (\text{E.6})$$

where  $\delta\rho$  is the density fluctuation, and  $\rho_0$  is the constant mean density in the system which is usually set to 1, and  $c = \delta_x/\delta_t = 1$  in lattice units (i.e.  $\delta_t = \delta_x$ ). The sound speed of the model is  $c_s = c/\sqrt{3}$ . The total density is  $\rho = \rho_0 + \delta\rho$ . The weighting factors  $w_\alpha$  for the D3Q19 model are  $w_0 = 1/3$ ,  $w_{1-6} = 1/18$ , and  $w_{7-18} = 1/36$ . The mass and momentum conservations are strictly enforced:

$$\delta\rho = \sum_\alpha f_\alpha = \sum_\alpha f_\alpha^{(\text{eq})}, \quad (\text{E.7a})$$

$$\rho_0 \mathbf{u} = \sum_\alpha \mathbf{e}_\alpha f_\alpha = \sum_\alpha \mathbf{e}_\alpha f_\alpha^{(\text{eq})}. \quad (\text{E.7b})$$

For athermal fluids, the forcing term  $F_\alpha$  is (22)

$$F_\alpha = -3w_\alpha\rho_0 \frac{\mathbf{e}_\alpha \cdot \mathbf{a}}{c^2} \delta_t, \quad (\text{E.8})$$

where  $\mathbf{a}$  is the acceleration due to external force. In our simulations, only for rotating case, we consider the Coriolis force, i.e.,  $\mathbf{a} = -2\boldsymbol{\Omega} \times \mathbf{u}$ , where  $\boldsymbol{\Omega}$  is the angular velocity of the frame of reference.

The hydrodynamic equations derived from Eq. (E.4) via the Chapman-Enskog analysis are

$$\partial_t \rho + \nabla \cdot \rho \mathbf{u} = 0, \quad (\text{E.9a})$$

$$\partial_t \mathbf{u} + \mathbf{u} \cdot \nabla \mathbf{u} = -\nabla p + \nu \nabla^2 \mathbf{u} + \mathbf{a}, \quad (\text{E.9b})$$



where  $p = c_s^2 \rho / \rho_0$  and the kinematic viscosity  $\nu$  has the following relation with the relaxation time

$$\nu = \frac{1}{3} \left( \tau - \frac{1}{2} \right) c \delta_x. \quad (\text{E.10})$$

It is important to note that in LBE the strain rate tensor  $S_{ij}$  can be obtained directly from the second-order moment of the nonequilibrium distribution function as

$$S_{ij} = -\frac{1}{2\rho_0 c_s^2 \tau} \sum_{\alpha} e_{\alpha i} e_{\alpha j} \left[ f_{\alpha} - f_{\alpha}^{(\text{eq})} \right], \quad (\text{E.11})$$

so that the dissipation rate is computed as  $\varepsilon = 2\nu \sum_{i,j} S_{ij} S_{ij}$ .

### E.3.2 LES extension of lattice Boltzmann equation

For the LES, high wave number Fourier components of the density distribution function are filtered and the resolved-scale distribution function is separated from the unresolved part. The filtered form of the LBE for LES is modeled as(23):

$$\bar{f}_{\alpha}(\mathbf{x} + \mathbf{e}_{\alpha} \delta_t, t + \delta_t) = \bar{f}_{\alpha}(\mathbf{x}, t) - \frac{1}{\tau^*} [\bar{f}_{\alpha} - \bar{f}_{\alpha}^{(\text{eq})}] + F_{\alpha}, \quad (\text{E.12})$$

where  $\bar{f}_{\alpha}$  and  $\bar{f}_{\alpha}^{(\text{eq})}$  represent the distribution function and the equilibrium function of the resolved scales respectively. The effect of the unresolved scale motion is modeled through an effective collision  $\tau_t$  which has been included in the LES effective relaxation time  $\tau^*$  in Eq. (E.12). The LES effective viscosity  $\nu^*$  is then obtained from

$$\nu^* = \nu + \nu_t = \frac{1}{3} \left( \tau^* - \frac{1}{2} \right) c \delta_x, \quad (\text{E.13})$$

with  $\nu_t$  denoting turbulent viscosity usually called eddy viscosity.

To evaluate the fidelity of the LBE-LES simulations, we use the Smagorinsky model (9; 24) for the small unresolved scale motion. In the Smagorinsky model, the eddy viscosity  $\nu_t$  is calculated from the filtered strain rate tensor  $\bar{S}_{ij} = (\partial_j \bar{u}_i + \partial_i \bar{u}_j)/2$  and a filter length

scale  $\delta_x$  as follows:

$$\nu_t = (C_{sm}\delta_x)^2 \bar{S}, \quad (\text{E.14a})$$

$$\bar{S} = \sqrt{2 \sum_{i,j} \bar{S}_{ij} \bar{S}_{ij}}, \quad (\text{E.14b})$$

where  $\bar{S}$  is the characteristic filtered rate of strain and  $C_{sm}$  is the Smagorinsky constant. With  $C_{sm}$  and  $\delta_x$  given,  $\tau_t$  can be obtained from Eq (E.11) (23):

$$\tau_t = \frac{1}{2} \left( \sqrt{\tau^2 + 18\sqrt{2}(\rho_0 c^2)^{-1} C_{sm}^2 \delta_x \bar{S}} - \tau \right). \quad (\text{E.15})$$

As shown in Eq. (E.11), the filtered strain rate tensor  $\bar{S}_{ij}$  can be computed from the second-order moment of the filtered nonequilibrium distribution function directly. In Eq. (E.15), the filtered strain rate  $\bar{S}$  which is used to determine  $\nu_t$  is current in time. Because the time step in the LBE simulations is relatively small in physical units, we can also use the value of  $\bar{S}$  of the previous time step and compute  $\nu_t$  ( $\nu_t = c_s^2 \tau_t \delta_t$ ) according to Eq. (E.14a) instead of Eq. (E.15). We will evaluate both these options. Furthermore, it is possible to use finite difference approximation for  $\bar{S}$ . We will also investigate this option.

It is important to point out the salient difference between the LBE-LES and the NS-LES. In the NS-LES, the eddy viscosity is evaluated and then used to determine the evolution of the flow fields in the next time step. In the LBE-LES, the eddy viscosity affects the relaxation process of the flow fields as well as other nonhydrodynamic variables (higher order fluxes). The relaxation process, as described by Eq. (E.12), does not force the flow fields to immediately attain the expected state specified by the equilibrium distributions. This preserves more spatio-temporal memory effects in the LBE-LES which are absent in the NS-LES counterpart. Some preliminary tests using the LBE-LES have yield encouraging results (23; 25; 26; 27). In this work we will compare the LBE-LES and NS-LES in the fundamental problem of HIT.

In all the results presented in this Appendix, we use the single-relaxation-time LBE obtained from BGK model for the collision operator. Preliminary computations of LBE-DNS in inertial frame using Multiple-relaxation-time(MRT) lattice Boltzmann model show

no distinguishable difference in the results obtained. We will investigate the use of MRT for LBE-DNS in rotational frame and LBE-LES in the future work.

## E.4 Simulation results

All numerical simulations are conducted in a three-dimensional periodic cube with various resolutions:  $N^3$ . The initial incompressible homogeneous isotropic velocity field is generated in spectral space with the following energy spectrum in a prescribed range  $\kappa_{\min} \leq \kappa \leq \kappa_{\max}$  (For further details, see the on-line article: T. Miyauchi and T. Ishizu, "Direct numerical simulation of HIT decay of passive scalar fluctuation," available at <http://cfd.me.umist.ac.uk/ercofold/database/test48/test48.html>):

$$\hat{E}(\kappa, 0) = \begin{cases} 0.038\kappa^m \exp(-0.14\kappa^2), & \kappa \in [\kappa_{\min}, \kappa_{\max}], \\ 0, & \kappa \notin [\kappa_{\min}, \kappa_{\max}], \end{cases} \quad (\text{E.16})$$

with random phase and then transferred to physical space. In the above,  $m$  is set to 4 or 2 for different simulations.

The initial density fluctuation  $\delta\rho$  (or the pressure  $p$ ) can be consistently obtained by an iteration procedure. It is important to stress that the preparation of the initial data is crucial in the LBE-DNS simulations of HIT. The pressure obtained by solving the Poisson equation from the initial velocity  $\mathbf{u}_0$  is inconsistent and insufficient to initialize the LBE simulation. It is inconsistent because LBE is intrinsically compressible thus the Poisson equation is not satisfied exactly. It is insufficient because LBE initial data consists of more than the hydrodynamic variables and the nonhydrodynamic variables cannot be specified by solving hydrodynamic equations. By consistently constructing the initial data for the LBE simulation, we are able to minimize the error due to initialization and the difference between the LBE and pseudo-spectral simulations (8).

### E.4.1 LBE-DNS of decaying isotropic turbulence

We first present the results from LBE-DNS of decaying HIT in the inertial frame at two resolutions:  $64^3$  and  $128^3$ . All initial spectra are given by Eq. E.16 in which  $m$  is set to 4 unless indicated otherwise.

Figure E.1 shows the evolutions of the normalized kinetic energy  $k/k_0$  and the normalized dissipation rate  $\varepsilon/\varepsilon_0$  with respect to normalized time  $t' = t\varepsilon_0/k_0$  for the cases of  $128^3$  and  $64^3$ . The parameters for both cases are  $u_{\text{rms}} = 0.023$  and  $\nu \approx 0.0017$  ( $\tau = 0.505$ ). In the case of  $64^3$ , the initial energy spectrum is non-zero in the range  $4 \leq \kappa \leq 8$ , resulting in  $\text{Re}_\lambda \approx 53$ . For the case of  $128^3$ , the initial energy spectrum is non-zero in the range  $1 \leq \kappa \leq 8$ , resulting in  $\text{Re}_\lambda \approx 119$ . In the absence of production, kinetic energy decays monotonically in time, whereas at early stages the dissipation rate increases. This increase in  $\varepsilon/\varepsilon_0$  is completely consistent with known turbulence physics (explained further below) and the same phenomenon is also seen in NS-DNS results. Following this period of increasing dissipation, both the kinetic energy and dissipation decay monotonically. The decay exponent  $n$  of the kinetic energy in these low  $\text{Re}_\lambda$  simulations varies in time. Furthermore,  $\text{Re}_\lambda$  itself is a function of time as the turbulence decays. The variation of  $n$  vs.  $\text{Re}_\lambda$  in various simulations are shown in Fig. E.2. The dependence of  $n$  on  $\text{Re}_\lambda$  obtained by the LBE-DNS is very similar to that observed in NS-DNS calculations (3). The values of  $n$  obtained in the present work agree well with the experimental and numerical NS-DNS data.

In Figure E.3, the left plot shows the compensated energy spectra  $[\hat{E}(\kappa, t)/\kappa^4]$  of the above  $128^3$  simulation at early times during which cascade is the dominant process. Initially, the spectrum (dashed line) is narrow and soon the energy spreads to higher wave numbers (smaller scales) due to the nonlinear cascade process. This phenomena leads to the increase of the dissipation rate in physical space, as shown in Fig. E.1. This fact, in itself, is significant since advection (the source of nonlinearity) is handled very differently in LBE. At this stage, the spectrum scales as  $\hat{E}(\kappa, t') \sim \kappa^4$  at small  $\kappa$ . The right plot shows another  $128^3$  simulation which has the same rms of the initial velocity field and  $\nu$  as the left case

but the non-zero energy is concentrated in the range of  $8 \leq \kappa \leq 16$ , resulting in  $Re_\lambda \approx 67$ . In spite of the different range of initial energy, the spectrum still scales as  $\hat{E}(\kappa, t') \sim \kappa^4$ .

Next we show results from a set of simulations in which the initial spectrum is also given by Eq. E.16 but with  $m = 2$ . In Figure E.4, the compensated spectrum  $\hat{E}(\kappa)/\kappa^2$  is shown at various times. It is seen that the spectrum now scales as  $\kappa^2$ . In summary, as shown in Figure E.5, the low wave-number spectra scale as  $\hat{E}(\kappa) \sim \kappa^4$  if  $m = 4$  (left plot) and  $\hat{E}(\kappa) \sim \kappa^2$  if  $m = 2$  (right plot). This dependence of low-wave number scaling on initial spectrum is in exact agreement with the results reported in (2; 3)

**Rotating Reference Frame.** LBE-DNS of decaying HIT in a rotating frame is also performed. Without loss of generality, we assume that the frame of reference rotates about the  $z$ -axis with the angular velocity  $\Omega = (0, 0, \omega)$ . The Rossby number is defined as  $Ro = \kappa_p u_{rms}/\omega$ , where  $\kappa_p$  characterizes the energy containing wave number at  $t = 0$ . Here, we use  $\kappa_p = (\kappa_{max} - \kappa_{min})/2$ .

The effects of rotation are scale dependent and they are enhanced by increasing the rotation rate  $\omega$  (decreasing  $Ro$ ). In general, it has been well understood that rotation slows down the cascade and delays the approach to equipartition (28; 29). These features are captured in Figs. E.6 and E.7. Figure E.6 shows the evolution of kinetic energy at various Rossby numbers in a simulation with  $128^3$  resolution. The initial energy spectrum is non-zero in the range of  $1 \leq \kappa \leq 8$ . As expected, the energy decay slows down with decreasing Rossby number (or increasing rate of rotation). Closer examination of the spectra (Fig. E.7) shows the tendency to maintain more energy at the small wave numbers (large scales) when the system rotates. The faster the system rotates (smaller Rossby number), the more prominent is this tendency.

#### E.4.2 LBE-LES of decaying isotropic turbulence

In the previous section, it was clearly demonstrated that the LBE method is an accurate DNS tool for turbulence. It is also important to assess the ability of LBE in the LES context.

In this work, we conduct LES of decaying HIT without rotation. Investigation of the LES of decaying HIT with rotation will be presented in the near future.

In order to perform close comparisons with DNS results, we perform LES with the initial large-scales identical to that of  $128^3$  LBE-DNS case (corresponding to the results presented in Fig. E.1). Thus the initial flow fields obtained in the LBE-DNS are appropriately truncated in spectral space to yield the initial fields for the LBE-LES for  $32^3$  and  $64^3$  resolutions. In other words, the initial LBE-LES field is obtained by filtering out all wave numbers above 16 for  $32^3$  and 32 for  $64^3$ .

**Calibration of  $C_{sm}$ .** Our first exercise is to determine the appropriate Smagorinsky constant for LBE-LES. Figure E.8 shows the energy spectra at some specific time instant with different Smagorinsky constant values for both  $32^3$  and  $64^3$  cases. The instantaneous LES spectra with resolutions  $32^3$  and  $64^3$  are compared against DNS spectrum at the same time. In general,  $64^3$  performs better than  $32^3$  although at small  $\kappa$  (large scale) region both  $32^3$  and  $64^3$  spectra agree well with the DNS spectrum. The comparison of the kinetic energy decay from the same runs is shown in Fig. E.9. From both figures, we find that  $C_{sm} = 0.1$  yields better results than the typical value of  $C_{sm} = 0.17$  used in the NS-LES(9). The need for a reduced  $C_{sm}$  in LBE-LES compared with the NS-LES value can be explained as follows.

In the lattice Boltzmann equation there are nonhydrodynamic variables which are higher order fluxes ( $\partial_i^n u_j, n > 1$ ). These higher order fluxes could lead to a higher effective viscosity and other nonlinear effects. Thus a smaller  $C_{sm}$  value in LBE-LES is adequate to achieve the same effect as a larger  $C_{sm}$  in NS-LES. In Fig. E.10, we compare the instantaneous flow structure of  $u_z(i, j, k = N/2, t')$  obtained by the LBE-LES with that by LBE-DNS. As shown in Fig. E.10, the LBE-LES appears to capture the flow-field structure quite adequately even with a coarse resolution of  $32^3$ . In all subsequent calculations, we use  $C_{sm} = 0.1$ .

**Other methods of  $\bar{S}$  computation.** In all the above calculations, we determine

$\bar{S}$ (in the express of  $\nu_t$ ) from the second moment of nonequilibrium distribution functions at the current time-step. We now investigate the other options for determining  $\bar{S}$  which may provide some computational advantages.

First, we test two different ways to compute the strain rate tensor: (i) from the second moment of nonequilibrium distribution functions as given in Eq. E.11 and (ii) by finite-difference approximation of derivatives  $\bar{S}_{ij} = (\partial_j \bar{u}_i + \partial_i \bar{u}_j)/2$ . In Figure E.11, we compare the kinetic energy evolution from both computations with LBE-DNS result at two resolutions. In the  $32^3$  case(left plot), it is seen that the computation using finite-difference approximation quickly diverges while computation from nonequilibrium distribution function moment captures the DNS result. In the  $64^3$  case(right plot), since the resolution is high enough, both computations yield good results. Next, we test two different ways of computing strain rate  $\bar{S}$  from the second moment of nonequilibrium distribution functions. In the implicit method,  $\bar{S}$  of the current time-step is used to yield Eq. E.15 for  $\nu_t$ . In the explicit approach,  $\bar{S}$  from previous time-step is used (as in Eq. E.14a). Figure E.12 depicts the contours of the instantaneous flow structure of  $u_z(i, j, k = N/2, t')$  obtained from LBE-LES ( $32^3$ ) by using the two formulae to compute  $\nu_t$ . The velocity fields obtained with the two formulae are almost identical, as shown in Fig. E.12; the  $L^2$ -norm difference between the two velocity fields is less than 0.02%. Therefore, we verify that the eddy viscosity can be computed by either Eq. (E.15) or Eq. (E.14a) without significant effect on the flow fields.

### E.4.3 LBE-LES vs. NS-LES

We further compare the LBE-LES with the NS-LES results at  $32^3$  resolution and the results are shown in Figs. E.13 – E.15. The initial velocity fields for LBE-LES and NS-LES calculation are nearly identical. From Fig. E.13 and E.14, it is seen that the kinetic energy and spectra computed from LBE-LES are somewhat closer to the DNS results than those calculated from NS-LES. The difference can be seen more clearly from contours of the instantaneous flow field  $u_z(i, j, k = N/2, t')$  at three different times as shown in Fig. E.15.

By Comparing the LBE-LES results (left column) and the NS-LES results (right column) with the LBE-DNS results (center column), we observe that LBE-LES preserves the flow structure better than the corresponding NS-LES. The  $32^3$  LBE-DNS contours shown here are obtained by truncating the  $128^3$  LBE-DNS data.

## E.5 Summary and conclusions

In this Appendix we perform DNS and LES of the classical decaying HIT problem with and without reference frame rotation using the LBM. Three categories of simulations have been performed. First we conduct the direct numerical simulations by using the LBM. Well known power-law decay of the kinetic energy is reproduced. The decay exponents obtained in the LBE simulations are in good agreement with the results from experimental measurements and NS-DNS calculations. The low-wavenumber energy spectrum scaling depends on initial conditions. Both  $\kappa^4$  and  $\kappa^2$  scaling are obtained from appropriate initial conditions consistent with (2; 3). The effect of rotation on turbulence, which is to suppress the spectral cascade, is also well captured.

Second, we conduct a comparative study of the LBE-LES and the LBE-DNS. Comparisons between  $64^3$ ,  $32^3$  LBE-LES and  $128^3$  LBE-DNS show that the large scale motion is well captured by LBE-LES. A smaller Smagorinsky constant,  $C_{sm} = 0.1$ , is demonstrated to achieve better performance in LBE-LES. By choosing appropriate Smagorinsky constant, even  $32^3$  can adequately capture large scale motions. Finally we compare both the LBE-LES and NS-LES with the corresponding DNS results. Our comparisons indicate that LBE-LES has better capability to preserve flow-field structure than NS-LES. This work further establishes the LBM as a viable computational tool for turbulence simulations.

## E.6 Figures



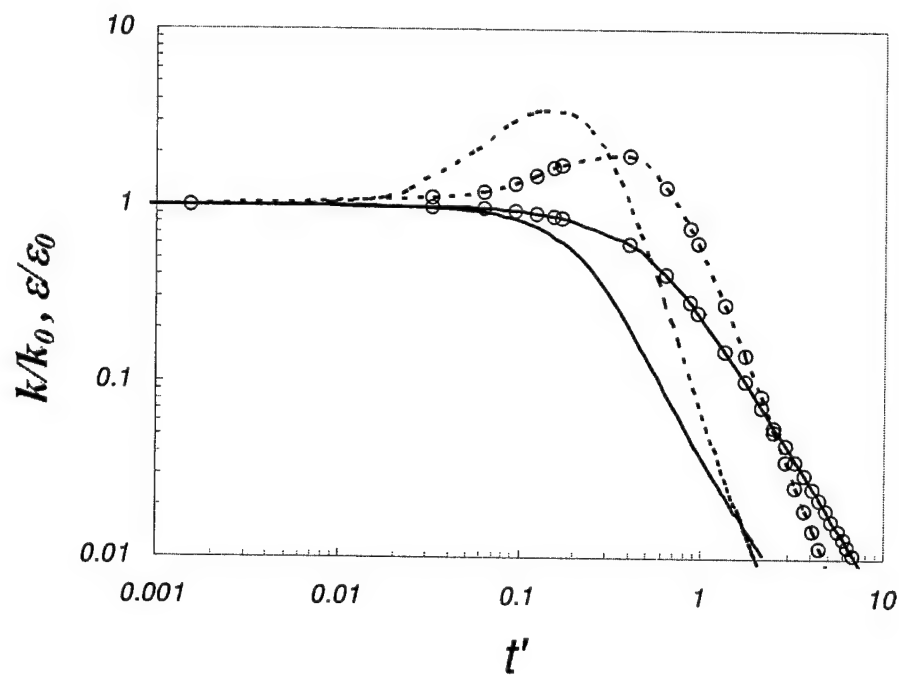


Figure E.1: Time evolution of the normalized kinetic energy  $k/k_0$  (solid lines) and normalized dissipation rate  $\varepsilon/\varepsilon_0$  (dashed lines) for  $64^3$  (lines and symbols) and  $128^3$  (lines only) by using LBE-DNS.

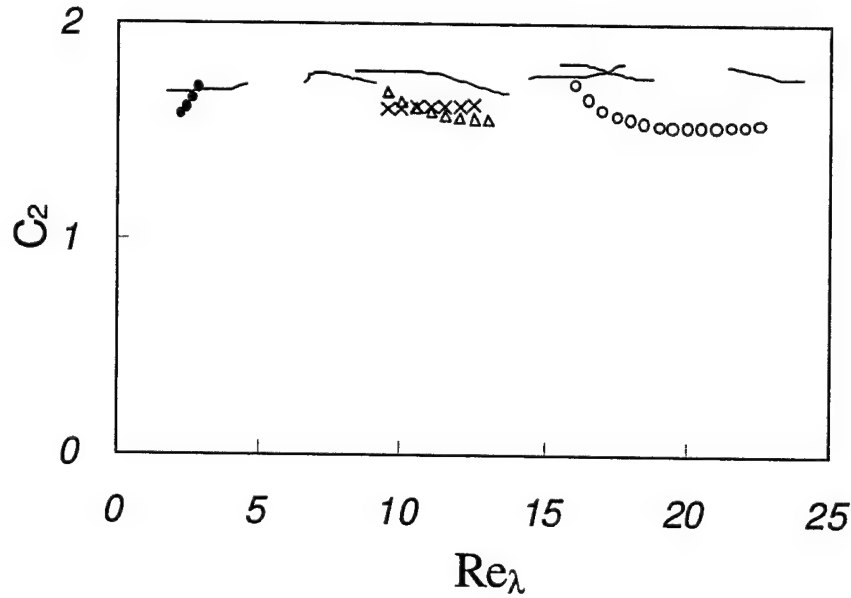


Figure E.2: Dependence of the decay exponent  $n = 1/(C_2 - 1)$  on initial conditions and  $\text{Re}_\lambda$ . The quantity  $C_2$  is depicted in the figure in stead of  $n$ . Solid lines represent NS-DNS data from (3) and symbols correspond to the LBE-DNS results of the present work. For the  $128^3$  resolution,  $\bullet$ :  $u_{\text{rms}} = 0.0064$ ,  $k_{\text{min}} = 1$ ,  $k_{\text{max}} = 8$ , and  $\nu = 0.01$  ( $\tau = 0.53$ );  $\triangle$ :  $u_{\text{rms}} = 0.021$ ,  $k_{\text{min}} = 8$ ,  $k_{\text{max}} = 16$ , and  $\nu \approx 0.00167$  ( $\tau = 0.505$ );  $\circ$ :  $u_{\text{rms}} = 0.022$ ,  $k_{\text{min}} = 1$ ,  $k_{\text{max}} = 8$ , and  $\nu \approx 0.00167$  ( $\tau = 0.505$ ). For the  $64^3$  resolution ( $\times$ ):  $u_{\text{rms}} = 0.022$ ,  $k_{\text{min}} = 4$  and  $k_{\text{max}} = 8$ , and  $\nu \approx 0.00167$  ( $\tau = 0.505$ ).

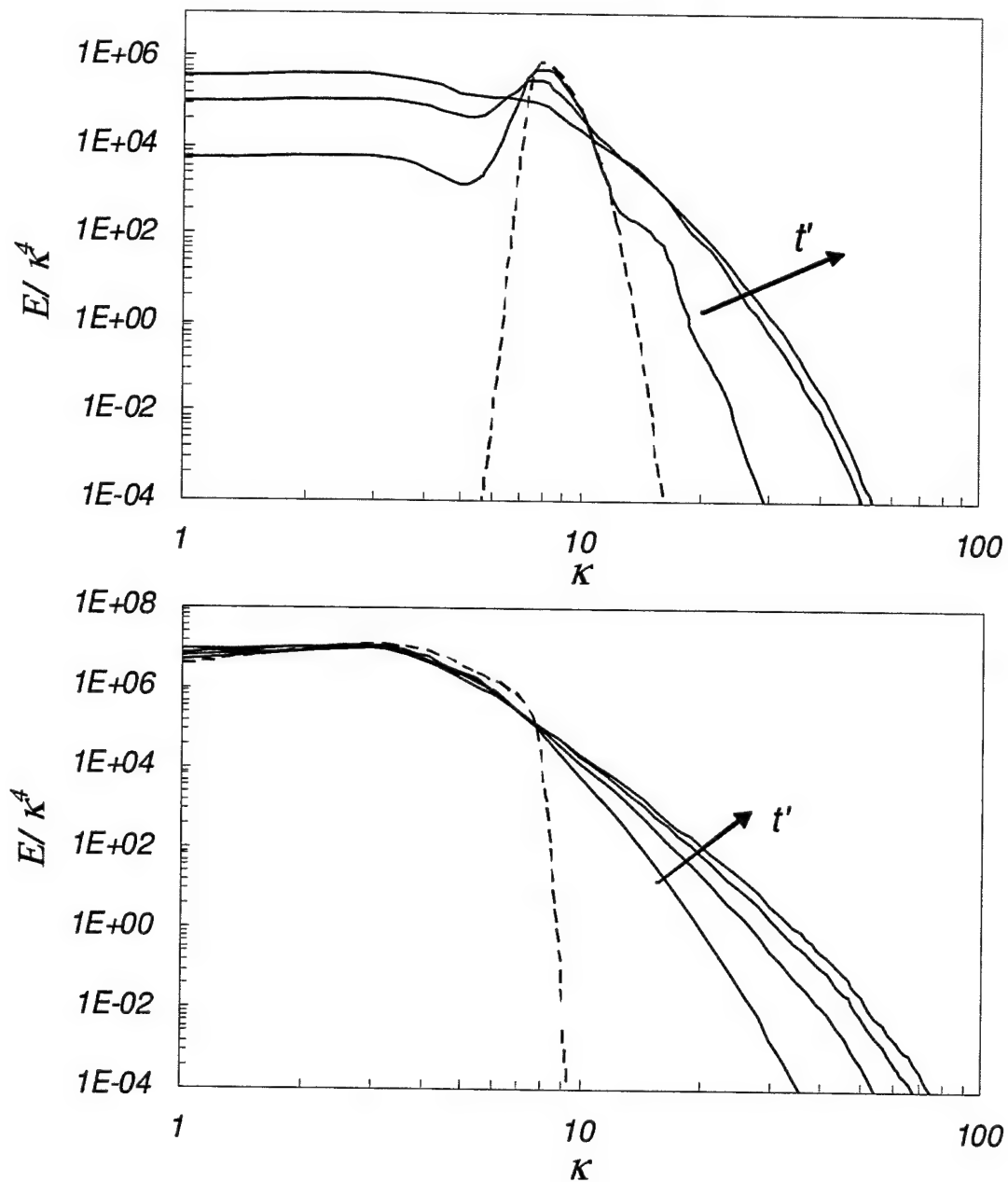


Figure E.3: Compensated energy spectra for two cases of  $128^3$  at early times,  $t' = 0.022, 0.044, 0.066,$  and  $0.088$ (left) and  $t' = 0.0022, 0.022,$  and  $0.088$ (right). The dashed lines represent the initial spectra given by Eq. (E.16) with  $m = 4$ . The spectra scale as  $\hat{E}(\kappa, t') \sim \kappa^4$  at small  $\kappa$

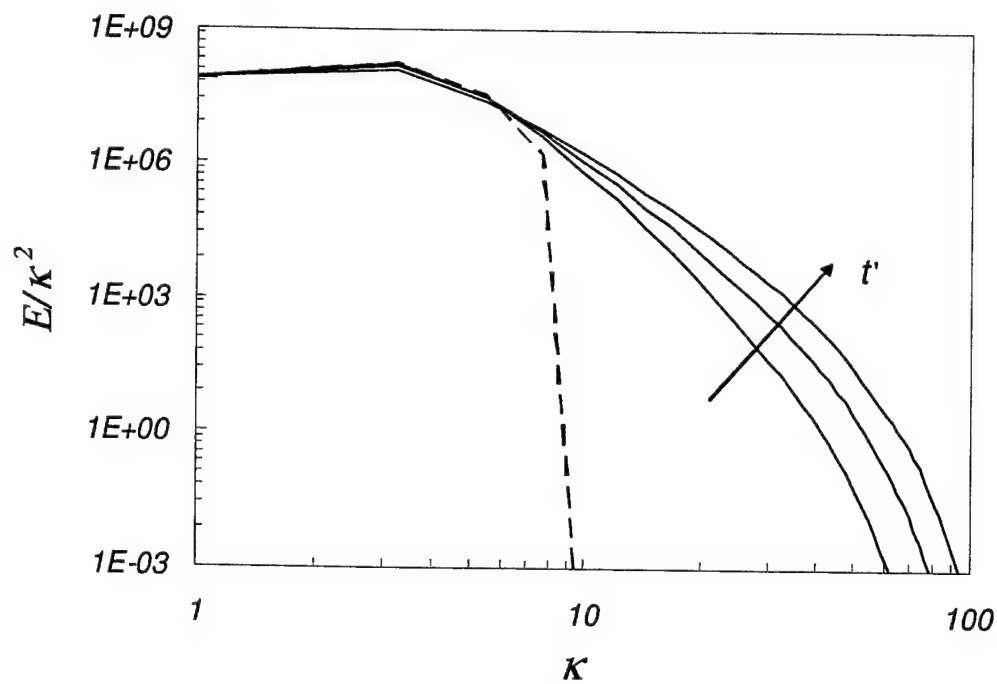


Figure E.4: Compensated energy spectra for a  $128^3$  simulation ( $u_{\text{rms}} = 0.023$ ,  $\nu \approx 0.0017$  ( $\tau = 0.505$ ), and  $Re_\lambda \approx 141$ ), at early times,  $t' = 0.011, 0.017, 0.027$ . The dashed lines represent the initial spectra given by Eq. (E.16) with  $m = 2$ . The spectra scale as  $\hat{E}(\kappa, t') \sim \kappa^2$  at small  $\kappa$ .

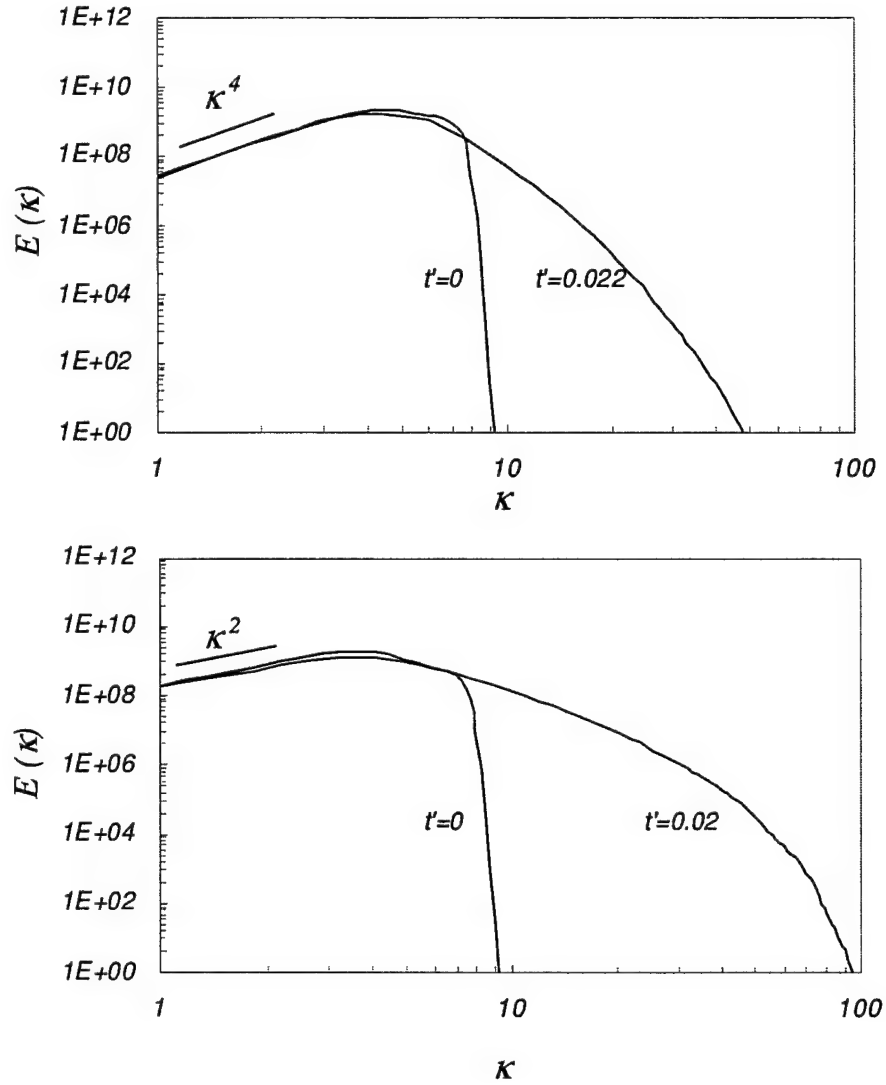


Figure E.5: Energy spectra for two cases of  $128^3$  above with initial energy concentrating in the range of  $1 \leq \kappa \leq 8$  at  $t' = 0$  and  $t' = 0.022$  respectively. The initial energy spectra are given by  $E(\kappa) = 0.038\kappa^4 \exp(-0.14\kappa^2)$  (upper plot) and  $E(\kappa) = 0.038\kappa^2 \exp(-0.14\kappa^2)$  (bottom plot) respectively.

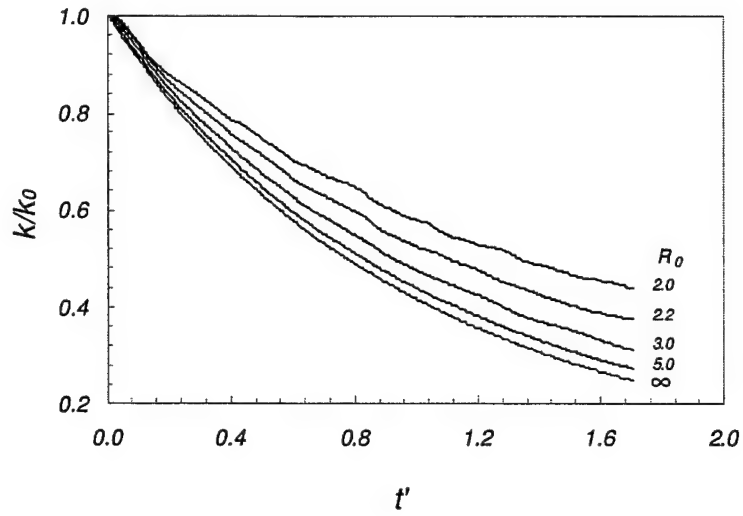


Figure E.6: Kinetic energy decay in  $128^3$  LBE-DNS with different Rossby number  $Ro$ .

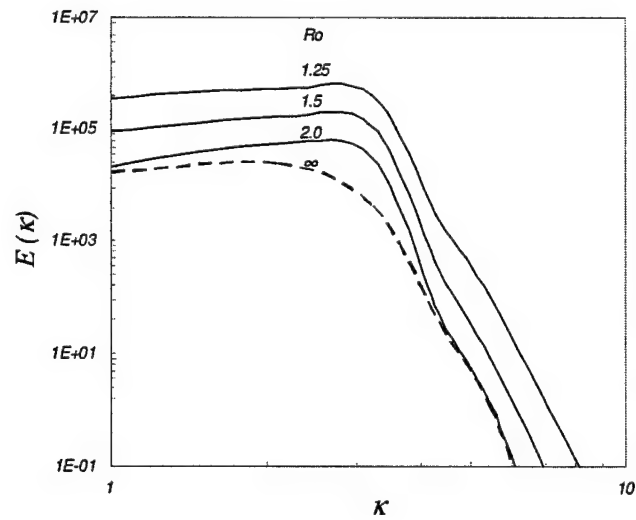


Figure E.7: Energy spectra at  $t' = 10.5$  with different Rossby number  $Ro$  for  $64^3$  case:  $u_{\text{rms}} = 0.023$ ,  $k_{\text{min}} = 1$ ,  $k_{\text{max}} = 4$ , and  $\nu = 0.01$  ( $\tau = 0.53$ ). The dashed line is the inertial case ( $\Omega = 0$  or  $Ro = \infty$ ).

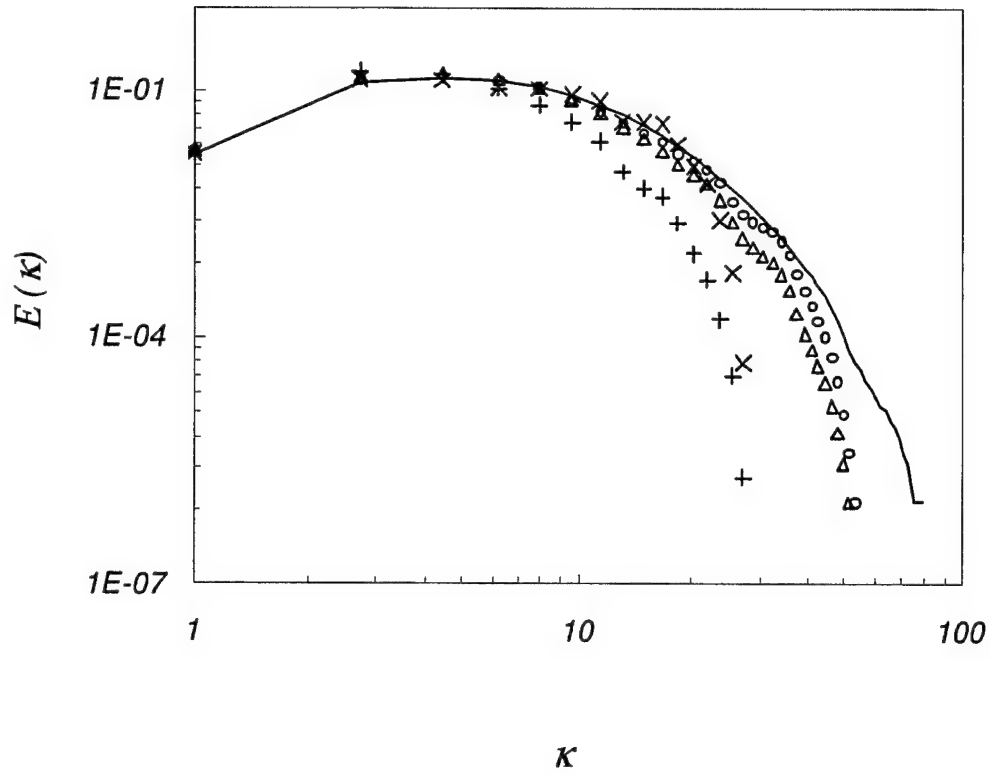


Figure E.8: Energy spectra at  $t' = 0.04796$  with different  $C_{sm}$  and resolution. Solid line for LBE-DNS ( $128^3$ ) and symbols for LBE-LES ( $\circ$ :  $64^3$ ,  $C_{sm} = 0.1$ ;  $\triangle$ :  $64^3$ ,  $C_{sm} = 0.17$ ;  $\times$ :  $32^3$ ,  $C_{sm} = 0.1$ ;  $+$ :  $32^3$ ,  $C_{sm} = 0.17$ ).

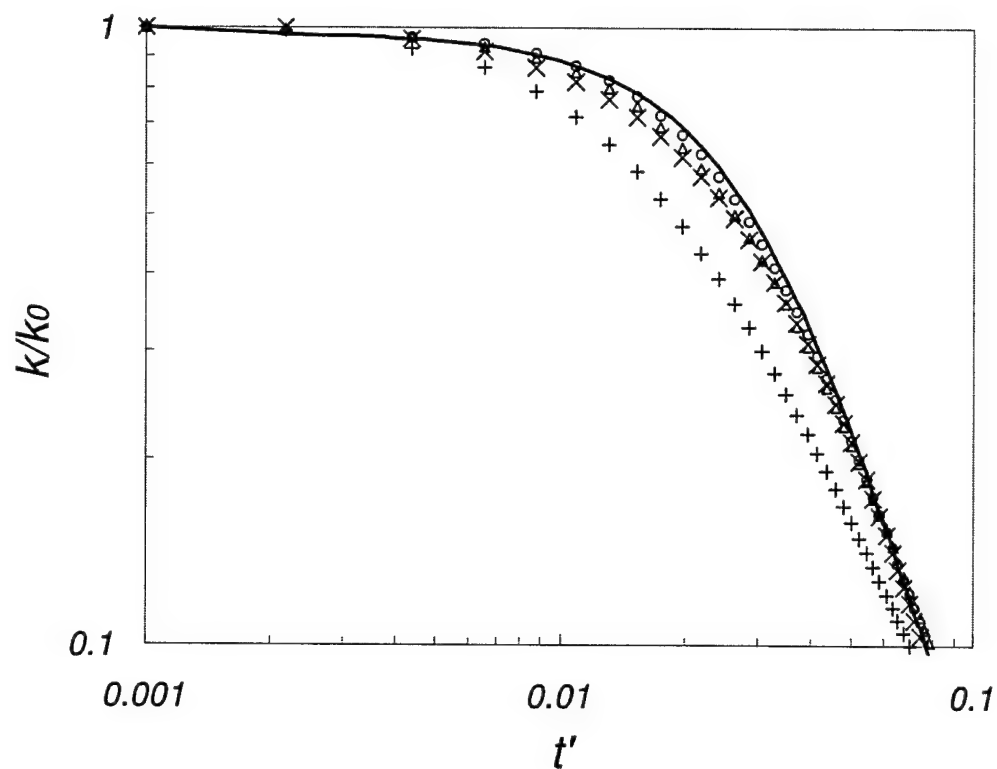


Figure E.9: Kinetic energy decay with different  $C_{sm}$  and resolution. Solid line for LBE-DNS ( $128^3$ ) and symbols for LBE-LES ( $\circ$ :  $64^3$ ,  $C_{sm} = 0.1$ ;  $\triangle$ :  $64^3$ ,  $C_{sm} = 0.17$ ;  $\times$ :  $32^3$ ,  $C_{sm} = 0.1$ ;  $+$ :  $32^3$ ,  $C_{sm} = 0.17$ ).



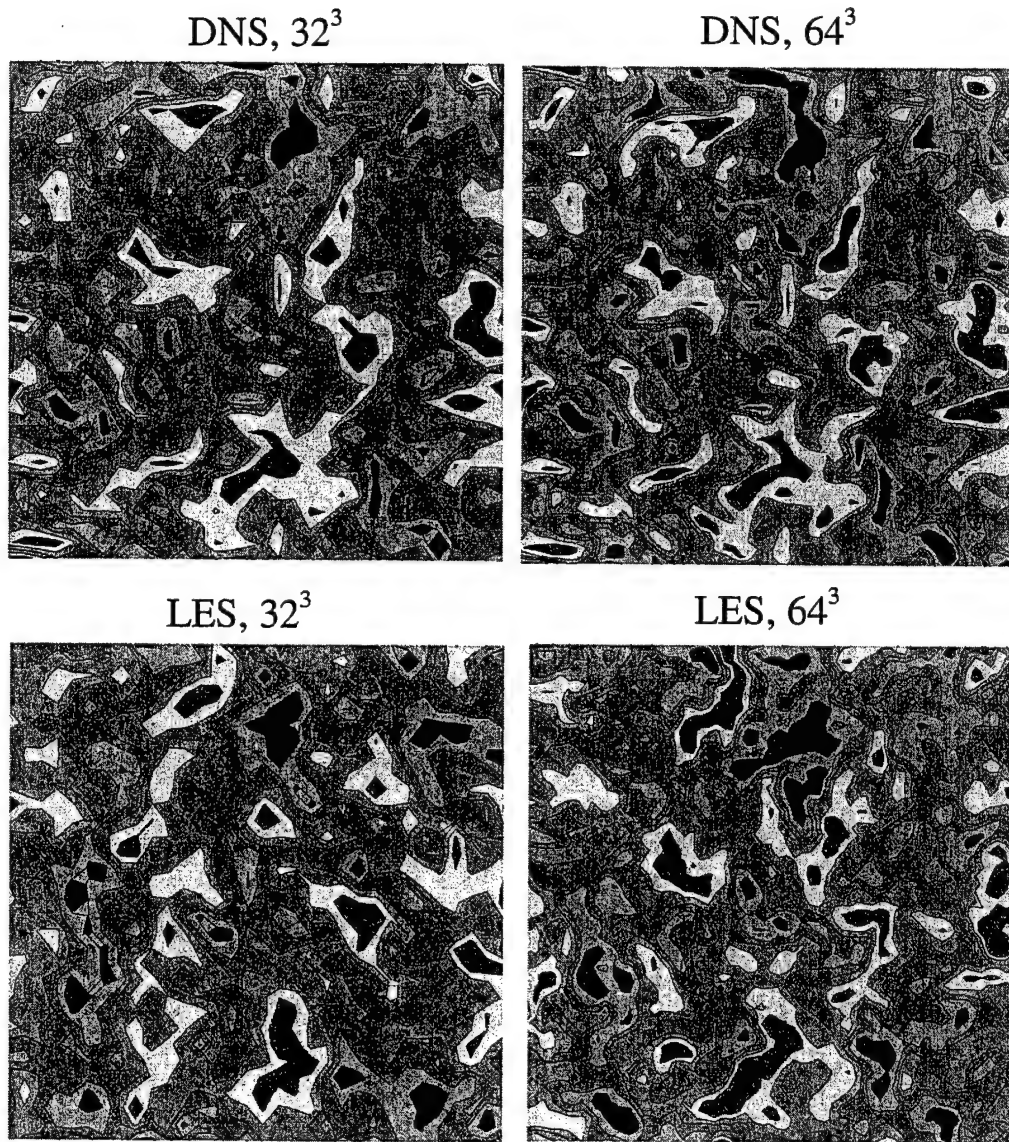


Figure E.10: Contours of the instantaneous flow field  $u_z(i, j, k = N/2, t')$ . LBE-DNS vs. LBE-LES with different resolutions. The  $32^3$  and  $64^3$  LBE-DNS contours shown here are obtained by truncating the  $128^3$  LBE-DNS data

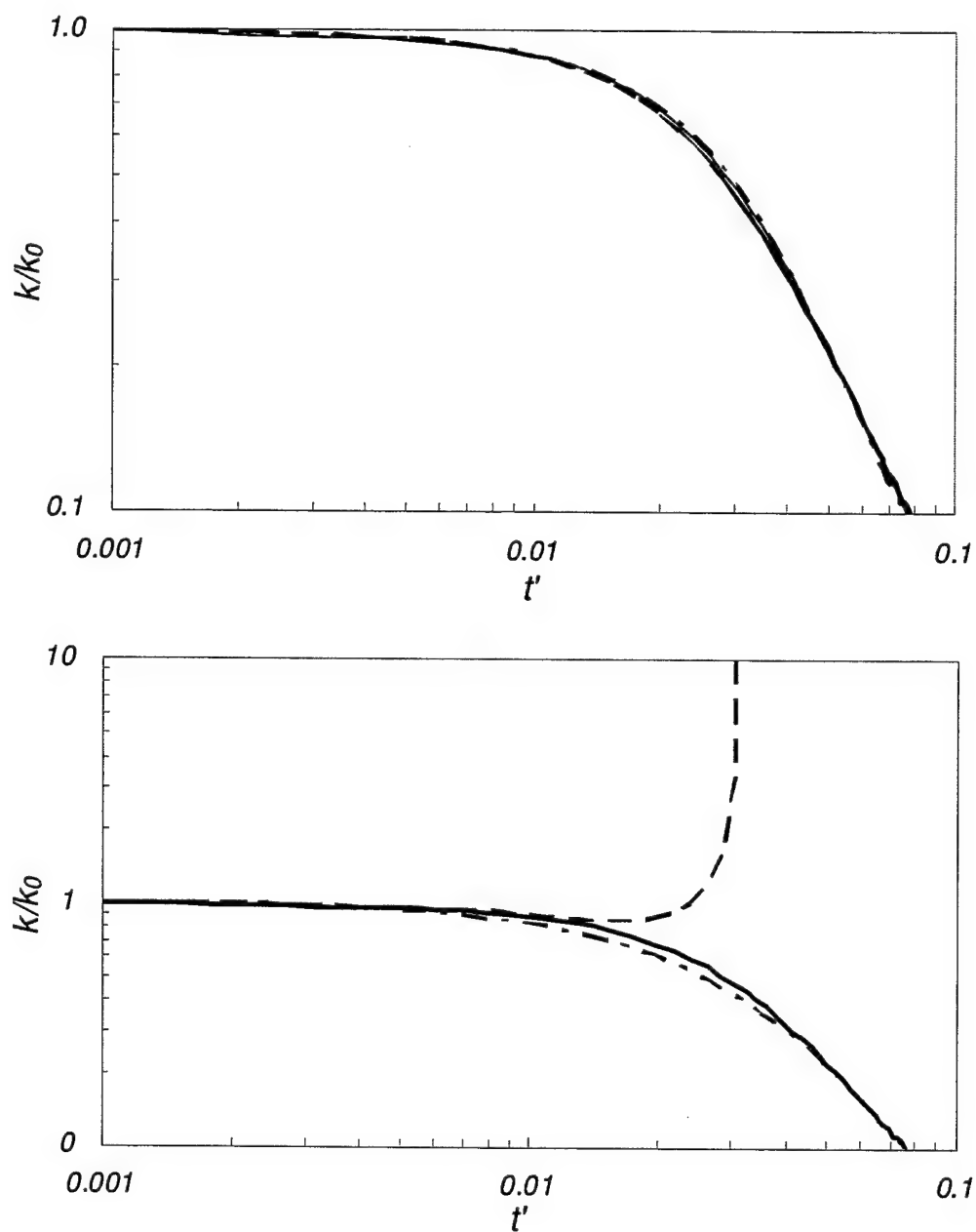


Figure E.11:  $32^3$  (upper plot) and  $64^3$  (bottom plot) kinetic energy decays of LBE-LES with different ways to compute strain rates vs. LBE-DNS. Solid lines: LBE-DNS; Dashed lines: LBE-LES, strain rate computed by finite difference; Dashed-dot lines: LBE-LES, strain rate computed by nonequilibrium distribution functions.

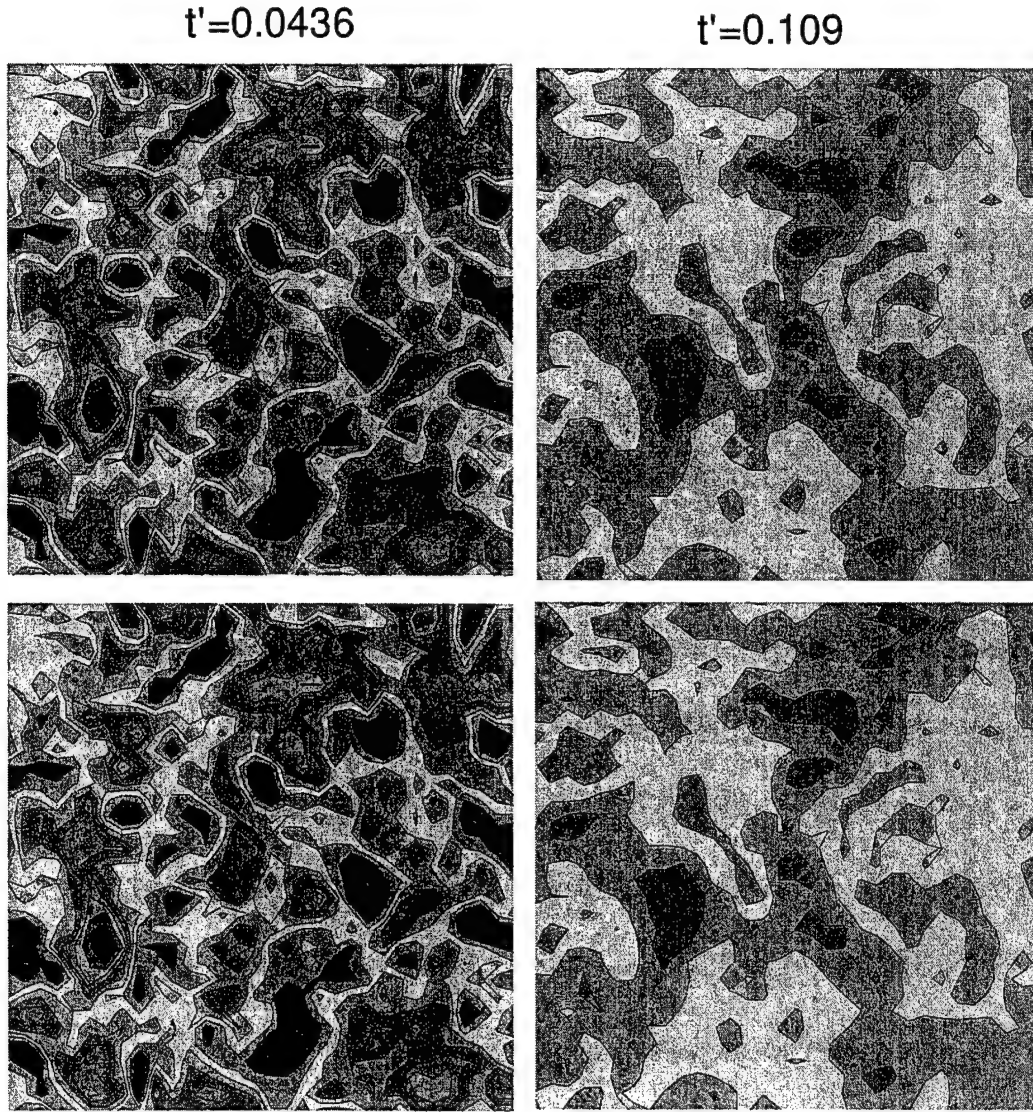


Figure E.12: Contours of the instantaneous flow field  $u_z(i, j, k = N/2, t')$  obtained by LBE-LES with a resolution of  $32^3$  and two different formulae for  $\nu_t$  in two different times. Top row:  $\nu_t$  is computed according to Eq. (E.15) and bottom row:  $\nu_t$  is computed according to Eq. (E.14a) with one time step lagging in  $\bar{S}$ .

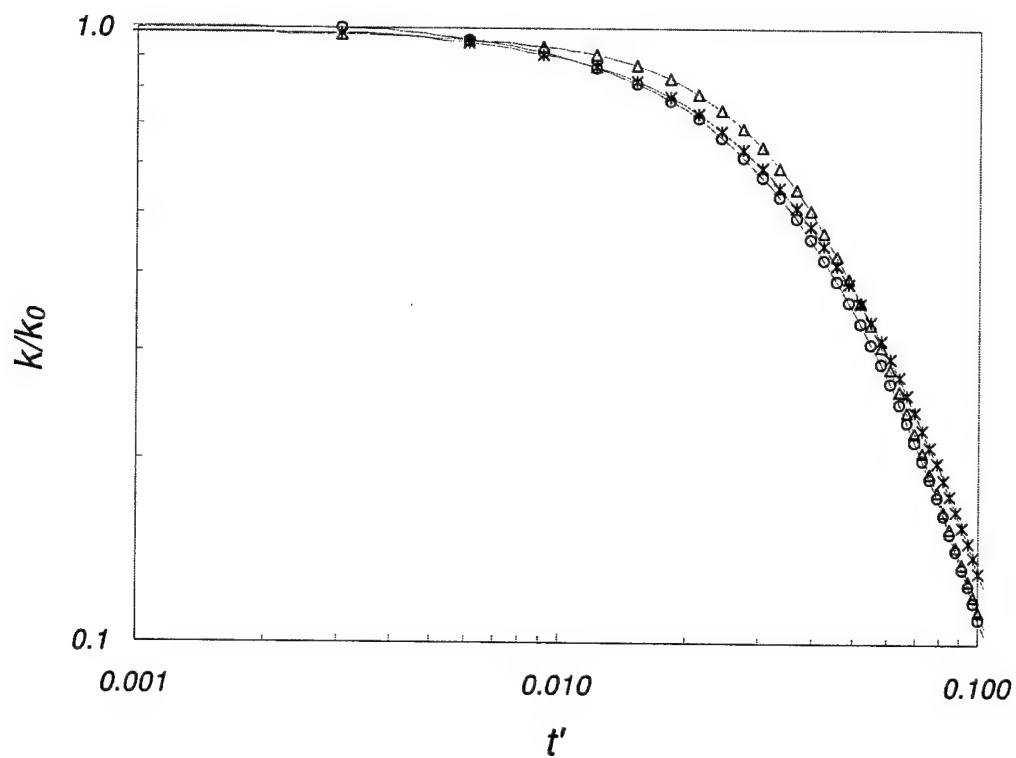


Figure E.13: Comparison of kinetic energy decay of  $32^3$  LBE-LES( $\circ$ ),  $32^3$  NS-LES( $*$ ) and  $128^3$  LBE-DNS( $\triangle$ ).

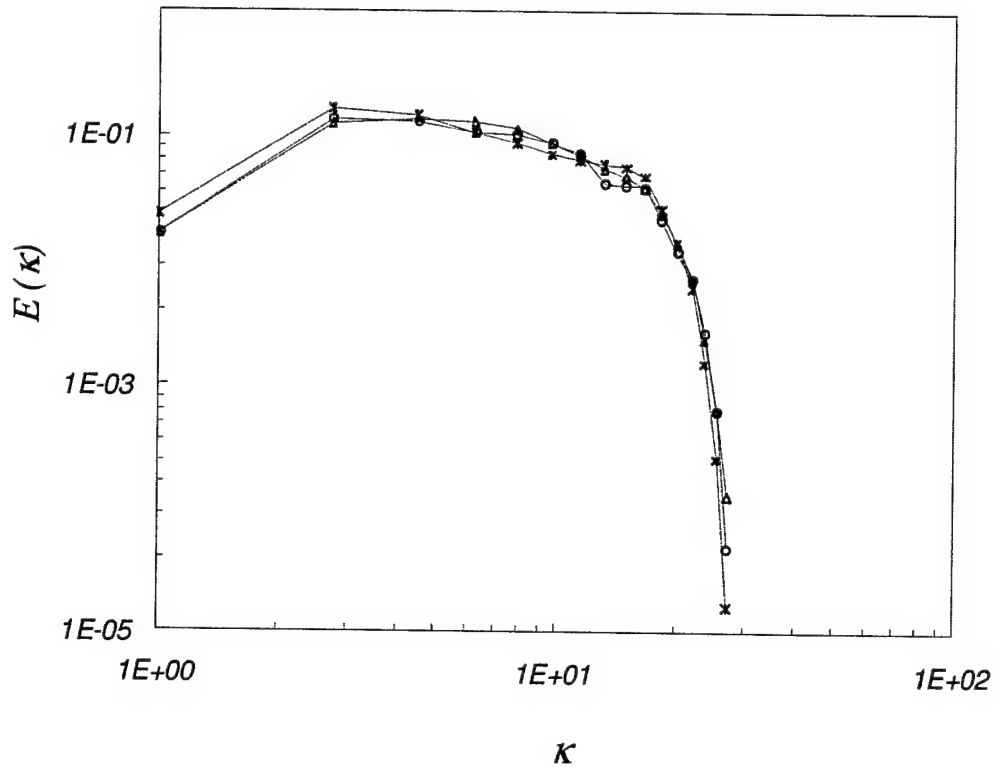


Figure E.14: Comparison of the energy spectra at  $t' = 0.06079$  of  $32^3$  LBE-LES( $\circ$ ),  $32^3$  NS-LES( $*$ ) and  $128^3$  LBE-DNS( $\Delta$ ).

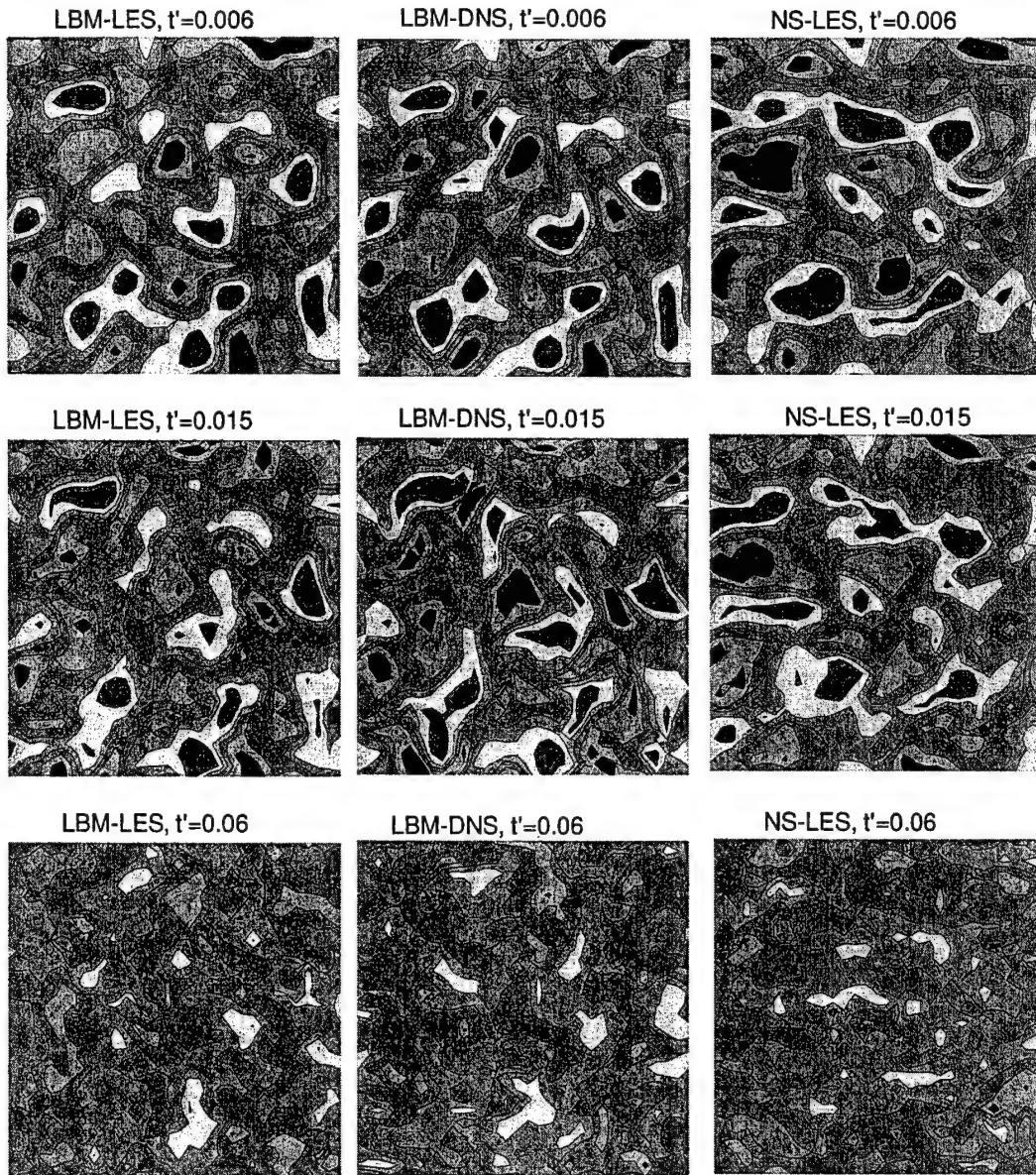


Figure E.15: Contours of the instantaneous flow field  $u_z(i, j, k = N/2, t')$ . The LBE-LES and NS-LES with a resolution of  $32^3$  compared to the LBE-DNS with a resolution of  $128^3$  at three different times. The  $32^3$  LBE-DNS contours shown here are obtained by truncating the  $128^3$  LBE-DNS data

## Bibliography

- [1] S. A. Orszag and G. S. Patterson, "Numerical simulation of three-dimensional homogeneous isotropic turbulence," *Phys. Rev. Lett.* **28**, 76 (1972).
- [2] M.-J. Huang and A. Leonard, "Power-law decay of homogeneous turbulence at low Reynolds numbers," *Phys. Fluids* **6**, 3765 (1994).
- [3] N. N. Mansour and A. A. Wray, "Decay of isotropic turbulence at low Reynolds number," *Phys. Fluids* **6**, 808 (1994).
- [4] R. Samtaney, D. I. Pullin, and B. Kosović, "Direct numerical simulation of decaying compressible turbulence and shocklet statistics," *Phys. Fluids* **13**, 1415 (2001).
- [5] S. Ossia and M. Lesieur, "Energy backscatter in large-eddy simulations of three-dimensional incompressible isotropic turbulence," *J. Turbulence* **1**, 10 (2000).
- [6] S. Chen, Z. Wang, X. Shan, and G. D. Doolen, "Lattice Boltzmann computational fluid dynamics in three dimensions," *J. Stat. Phys.* **68**, 397 (1992).
- [7] R. Benzi, M.V. Struglia, and R. Tripiccone, "Extended self-similarity in numerical simulations of three-dimensional anisotropic turbulence," *Phys. Rev. E* **53**, R5565–R5568 (1996).
- [8] L.-S. Luo, L.-P. Wang, and D. Qi, "Applications of the lattice Boltzmann method to complex and turbulent flows," in *High Performance Scientific and Engineering Computing*, edited by M. Breuer, F. Durst, and C. Zenger, Lecture Notes in Computer Science and Engineering Vol. 21 (Springer, Berlin, 2002), p. 123.
- [9] S. B. Pope, *Turbulent Flows* (Cambridge University Press, Cambridge, 2000).
- [10] M. S. Mohamed and J. C. LaRue, "The decay power law in grid-generated turbulence," *J. Fluid Mech.* **219**, 195 (1990).

- [11] J. C. Rotta, *Turbulente Strömungen* (Teubner, Stuttgart, 1972).
- [12] L. G. Loitsyansky, "Some basic laws for isotopic turbulent flows," Moscow Centr. Aero. Hydrodyn. Inst. Rep. No. 440 (1939). [NACA Tech. Memo. 1079 (1939)].
- [13] A. N. Kolmogorov, "Decay of isotropic turbulence in incompressible viscous fluids," Dokl. Akad. Nauk SSSR **31**, 299 (1941).
- [14] G. Birkhoff, "Fourier synthesis of homogeneous turbulence," Comm. Pure. Appl. Math. **7**, 19 (1954).
- [15] P. G. Saffman, "The large-scale structure of homogeneous turbulence," J. Fluid Mech. **27**, 581 (1967).
- [16] M. Oberlack, "On the decay exponent of isotropic turbulence," Proc. Appl. Math. Mech. **1**, 294 (2002).
- [17] M. R. Smith, R. J. Donnelly, N. Goldenfeld, and W. F. Vinen, "Decay of vorticity in homogeneous turbulence," Phys. Rev. Lett. **71**, 2583 (1993).
- [18] P. L. Bhatnagar, E. P. Gross, and M. Krook, "A model for collision processes in gases. I. Small amplitude processes in charged and neutral one-component systems," Phys. Rev. **94**, 511 (1954).
- [19] H. Chen, S. Chen and H.W. Matthaeus, Recovery of the Navier-Stokes Equation Using a Lattice Boltzmann Method, Physical Review A, **15**:R5339(1992).
- [20] Y. H. Qian, D. d'Humières and P. Lallemand, Lattice BGK Model for Navier-Stokes Equation, Europhysics Letters, **17**(6):479(1992).
- [21] X. He and L.-S. Luo, "Lattice Boltzmann model for the incompressible Navier-Stokes equation," J. Stat. Phys. **88**, 927 (1997).



- [22] L.-S. Luo, "Theory of the lattice Boltzmann method: Lattice Boltzmann models for nonideal gases," *Phys. Rev. E* **62**, 4982 (2000).
- [23] S. Hou, J. Sterling, S. Chen, and G. D. Doolen, "A lattice Boltzmann subgrid model for high Reynolds number flows," in *Pattern Formation and Lattice Gas Automata*, Fields Inst. Comm. **6**, edited by A. T. Lawniczak and R. Kapral (AMS, Providence, 1996), pp. 151–166.
- [24] J. Smagorinsky, "General circulation experiments with the primitive equations: I. The basic equations," *Mon. Weather Rev.* **91**, 99 (1963).
- [25] J. J. Derksen and H. E. A. Van den Akker, "Simulation of vortex core precession in a reverse-flow cyclone," *AIChE J.* **46**, 1317 (2000).
- [26] M. Krafczyk, "Gitter-Boltzmann-Methoden: Von der Theorie zur Anwendung," *Habilitation Thesis*, Tech. Univ. Munich (2001).
- [27] M. Krafczyk, J. Tölke, and L.-S. Luo, "Large-eddy simulations with a multiple-relaxation-time LBE model," *Int. J. Mod. Phys. B* **17**, 33 (2003).
- [28] Y. Yamazaki, Y. Kaneda, and R. Rubinsten, "Dynamics of inviscid truncated model of rotating turbulence," *J. Phys. Soc. Japan* **71**, 81 (2002).
- [29] J. Bardina, J. H. Ferziger, "Effect of rotation on isotropic turbulence: computation and modelling," *J. Fluid Mech.* **154**, 321 (1985).

## Appendix F

# Study of Homogenous Turbulence Shear

Nomenclature			
$b_{ij}$	Anisotropy tensor	$\langle u_i u_j \rangle$	Reynolds stress
$P_{ij}$	Production tensor	$R_{ij}$	Pressure-strain tensor
$\varepsilon$	Dissipation rate	$k$	Turbulent kinetic energy
$\varepsilon_{ij}$	Dissipation tensor	$Re_\lambda$	Taylor microscope Reynolds number
$P$	Production of $k$	$\omega$	Frequency of shear
$S$	Shear rate	$Sk/\varepsilon$	Normalized shear rate
$c_s$	Speed of sound	$e_\alpha$	Discretized particle velocity
$f$	Distribution function	$f^{(eq)}$	Equilibrium distribution function
$u$	Fluid velocity	$\rho$	Fluid density
$\delta_t$	Time step	$\delta_x$	Grid size
$\tau$	Normalized relaxation time	$w_\alpha$	Weight function
$\nu$	Viscosity		

### F.1 Introduction

In Appendix E, we have studied decay isotropic turbulence in inertial and rotational frame. As a part of our effort to perform LBM-DNS of turbulence, we will investigate the homoge-

nous shear turbulence in this Appendix.

Homogenous shear flow has been extensively studied by experiments and numerical simulations. Rose (1), Champagne Harris and Corrsin (2), Tavoularis and Corrsin (3; 4) studied homogenous shear turbulence in tunnel to investigate the local isotropy of small scales. The issue of local isotropy was also addressed numerically by Pumir and Shraiman (5) and Pumir (6). Rogers and Moin examined the structure of the vorticity in homogenous shear flows (7). They confirmed the presence of hairpin vortices in homogeneous shear flow. Lee et al (8) compared the structure of turbulence under high shear rate in shear flow with that in turbulent channel flow and found many dynamical features in the two flows to be similar. Kida and Tanaka (9) discussed the regeneration cycle of the streamwise vortices in a homogeneous shear flow. Jacobitz et al. (10) studied uniformly sheared and stably stratified flows. They found that the turbulence evolution depends strongly on the initial value of the Taylor microscale Reynolds number and the initial value of the normalized shear number  $Sk/\varepsilon$  in both cases. Most of the above simulations used the pseudo-spectral method of the solution of Navier-Stokes equations (11).

In this Appendix, we will first verify the reliability of LBM in the DNS of homogenous turbulence and then focus on the new physics in homogenous turbulence flow subjected to periodically varied shear. This Appendix is structured as follows. The Reynolds stress evolution equations are given in Section F.2. In Section F.3, firstly, the classical results (3; 4; 7) are used to verify the viability of LBM in DNS of homogenous turbulent shear (constant shear). Secondly, results of LBM-DNS of homogenous turbulence subjected to periodically shear are presented and the new physics in this flow are discussed. Finally, we compare the DNS results with the results obtained by Reynolds average Navier-stokes (RANS) turbulence models in the periodically varied shear cases. These analysis provide some new knowledge for developing models in turbulence subject to unsteady forcing. A brief conclusion is presented in Section F.4.

## F.2 Reynolds-stress evolution equations

The Reynolds-stress evolution equation can be written as

$$\frac{\bar{D}}{\bar{D}t} \langle u_i u_j \rangle + \frac{\partial}{\partial x_k} T_{kij} = P_{ij} + R_{ij} - \varepsilon_{ij}, \quad (\text{F.1})$$

where the turbulent transport of Reynolds-stress ( $T_{kij}$ ) can be decomposed as

$$T_{kij} = T_{kij}^{(u)} + T_{kij}^{(p)} + T_{kij}^{(v)}.$$

In the above,

$$T_{kij}^{(u)} \equiv \langle u_i u_j u_k \rangle, \quad T_{kij}^{(v)} \equiv -\nu \frac{\partial \langle u_i u_j \rangle}{\partial x_k}, \quad T_{kij}^{(p)} \equiv \frac{1}{\rho} \langle u_i p' \rangle \delta_{jk} + \frac{1}{\rho} \langle u_j p' \rangle \delta_{ik}.$$

Further, production, pressure redistribution, and dissipation are respectively:

$$P_{ij} \equiv -\langle u_i u_k \rangle \frac{\partial \langle U_j \rangle}{\partial x_k} - \langle u_j u_k \rangle \frac{\partial \langle U_i \rangle}{\partial x_k}, \quad (\text{F.2})$$

$$R_{ij} \equiv -\left\langle \frac{p'}{\rho} \left( \frac{\partial u_i}{\partial x_j} + \frac{\partial u_j}{\partial x_i} \right) \right\rangle, \quad (\text{F.3})$$

$$\varepsilon_{ij} \equiv 2\nu \left\langle \frac{\partial u_i}{\partial x_k} \frac{\partial u_j}{\partial x_k} \right\rangle. \quad (\text{F.4})$$

where  $\langle \rangle$  represents the mean of the fluctuating variables;  $U$  is fluid velocity;  $u$  and  $p'$  are fluctuating velocity and pressure; and  $\rho$  is the fluid density.

In homogenous turbulence, the evolution equation simplifies to

$$\frac{\partial}{\partial t} \langle u_i u_j \rangle = P_{ij} + R_{ij} - \varepsilon_{ij}. \quad (\text{F.5})$$

In our simulation, the shear is only applied in the flow along y-direction. For pertinent components of Reynolds stress in this homogenous turbulence shear flow, we get

$$\frac{\partial}{\partial t} \langle u_1 u_1 \rangle = -\langle u_1 u_2 \rangle \frac{\partial \langle U_1 \rangle}{\partial x_2} - \left\langle 2 \frac{p'}{\rho} \frac{\partial u_1}{\partial x_1} \right\rangle - 2\nu \left\langle \frac{\partial u_1}{\partial x_k} \frac{\partial u_1}{\partial x_k} \right\rangle, \quad (\text{F.6})$$

$$\frac{\partial}{\partial t} \langle u_2 u_2 \rangle = -\left\langle 2 \frac{p'}{\rho} \frac{\partial u_2}{\partial x_2} \right\rangle - 2\nu \left\langle \frac{\partial u_2}{\partial x_k} \frac{\partial u_2}{\partial x_k} \right\rangle, \quad (\text{F.7})$$

$$\frac{\partial}{\partial t} \langle u_3 u_3 \rangle = - \left\langle 2 \frac{p'}{\rho} \frac{\partial u_3}{\partial x_3} \right\rangle - 2\nu \left\langle \frac{\partial u_3}{\partial x_k} \frac{\partial u_3}{\partial x_k} \right\rangle, \quad (\text{F.8})$$

$$\frac{\partial}{\partial t} \langle u_1 u_2 \rangle = - \langle u_2 u_2 \rangle \frac{\partial \langle U_1 \rangle}{\partial x_2} - \left\langle \frac{p'}{\rho} \left( \frac{\partial u_1}{\partial x_2} + \frac{\partial u_2}{\partial x_1} \right) \right\rangle - 2\nu \left\langle \frac{\partial u_1}{\partial x_k} \frac{\partial u_2}{\partial x_k} \right\rangle. \quad (\text{F.9})$$

In studying homogenous turbulence shear, it is more common to present results in the anisotropy tensor which is defined as  $b_{ij} \equiv \frac{\langle u_i u_j \rangle}{\langle u_i u_i \rangle} - \frac{1}{3} \delta_{ij}$ .

## F.3 Results and discussions

### F.3.1 Homogenous shear flow

As mentioned in introduction, homogenous turbulent shear has been extensively studied. In this section, we will use this flow as a benchmark to verify the applicability of LBM in DNS of turbulence. The computational domain is shown in Fig. F.1. The mesh is uniform and has the resolution of  $128^3$ . In x- and z-directions, periodical boundary condition is used; Non-slip condition is used at upper and lower walls. Usually, bounce back scheme is used at the wall. However, to avoid the instability in computation, we use the equilibrium distribution function in the present simulations. For more details of discussion of boundary condition in LBM, please see reference (13). In the simulation, 19-bit (D3Q19) model is used because of its advantages in matters of stability and efficiency. Initial velocity filed is given by isotropic turbulence. Uniform mean velocity gradient  $S = \frac{\partial \bar{U}}{\partial y}$  is imposed on the isotropic turbulence by adding linear mean velocity profile along y-direction at initial stage. To maintain the linear mean velocity profile, the lower and upper walls move with a constant speed of  $\bar{U}$  in opposite direction along x-axis. At initial stage, normalized shear  $Sk/\varepsilon$  is 3.3, and Taylor microscale Reynolds number  $Re_\lambda$  is 33.  $Re_\lambda = 2k\lambda/\nu$  represents the Reynolds number based on the Taylor microscale. Statistical quantities of turbulence are obtained by spatial averaging over the inner  $128 \times 64 \times 128$  region in computational domain to avoid the wall effects. The most important inference has been made from the studies of Tavoularis and Corrsion (3; 4) and Rogers and Moin (7) is that the homogenous turbulence reaches

an asymptotic stage after initial transition. At this asymptotic stage, when normalized by the imposed shear rate  $S$  and the kinetic energy  $k(t)$ , the statistics become independent of time (12).

Figure F.2 shows the development of anisotropy tensor obtained from the present calculations as well as previous investigations. It is difficult to compare present results with those obtained by NS solver at early stage because of difference in initial conditions. At the asymptotic stage, it can be seen that LBM recovers the experimental and numerical results very well. Fig. F.3 compares present  $b_{12}$  with the results obtained by Jacobitz et al. (10). As is clearly seen, the agreement is again good. Fig. F.4 shows the development of normalized shear and the production over dissipation ratio ( $P/\epsilon$ ). We see that after initial period, normalized shear and  $P/\epsilon$  almost maintain constant values which are 3.8 for normalized shear and 1.2 for  $P/\epsilon$ . As shown by Jacobitz et al (10), these values are depended on the initial shear and  $Re_\lambda$ .

From the above results, we can conclude that the LBM is an effective tool for simulating turbulence.

### F.3.2 Homogenous turbulence subjected to periodically varied shears.

In the previous case, shear was constant which is the classical problem. Here we let shear vary with time and investigate the effects of the variation on the development of turbulence. In simulations, all the conditions are kept the same as those in the constant shear case except that non-penetration condition is used at upper and low boundaries. Further, shear is varied with time according to  $\frac{\partial \bar{U}}{\partial y} \sin(\omega t)$ , where  $\frac{\partial \bar{U}}{\partial y}$  equals to the one in constant shear case. The variation of shear is enforced by adding body force in the lattice Boltzmann Equation (14),

$$f_\alpha(x_i + e_\alpha \delta t, t + \delta t) - f_\alpha(x_i, t) = -\frac{1}{\tau} [f_\alpha(x_i, t) - f_\alpha^{(eq)}(x_i, t)] + \delta t F_\alpha$$

where  $F_\alpha = (1 - \frac{1}{2\tau}) w_\alpha \left[ \frac{e_{\alpha x} - u}{c_s^2} + \frac{e_{\alpha y} u}{c_s^2} e_\alpha \right] \cdot F$ ,  $F = \bar{U}(y) \omega \cos(\omega t) \cdot \vec{i}$ , and  $\vec{i}$  is the unit vector along x-direction. Frequency of the variation of shear ( $\omega$ ) is determined based on the

magnitude of  $S$ . In simulations, two different ratios of  $\omega$  to  $S$  are used which are  $\frac{\omega}{S}=1$  and 0.5, respectively.

Figures F.5 and F.6 show the evolution of turbulent kinetic energy for the low frequency case ( $\frac{\omega}{S}=0.5$ ) and high frequency case ( $\frac{\omega}{S}=1.0$ ), respectively. Three important observations are made in these flows. First, there exists a critical frequency at which turbulence changes from growth model to decay mode. As can be clearly seen that, in low frequency case,  $k$  increases, while in high frequency case,  $k$  decays. The second phenomenon is that the frequency of the variation of  $k$  is twice as that of shear in both cases. The third phenomenon is that in high frequency case, the variation of  $k$  is not as that in the low frequency case. In low frequency case, the variation of  $k$  can be described by a single frequency function. In high frequency case,  $k$  has two peaks with different magnitudes during a period of shear. These phenomena will be explained in following discussions by analyzing the variation of shear and  $b_{12}$  because these two terms determine the production of turbulence.

We will first look at the low frequency case. The variation of shear and  $b_{12}$  are shown in Fig. F.7. Just before time A, the shear is negative and  $b_{12}$  is positive. Thus production for  $k$  is positive. After time A, shear becomes positive while  $b_{12}$  still maintains positive from time A to B. Thus, negative production is generated for  $k$  from time A to B as shown in Fig. F.8 and is reflected also in the rapid decay of  $k$  in the same period of time in Fig. F.5. After shear taking effect,  $b_{12}$  rapidly decreases and becomes negative. Then production turns to be positive from time B to C in Fig. F.8 and is reflected also in the growth of  $k$  in same time in Fig. F.5. In the constant shear case, after reaching its largest magnitude,  $b_{12}$  will almost be maintained at that value. In Fig. F.7, we can see that  $b_{12}$  has possibly reached the maximum value because the magnitude of  $b_{12}$  has reached around 0.2 (compared with 0.18 in constant shear case) and it does not vary too much for a long time. We will refer that maximum value of  $b_{12}$  as saturation value.

In Fig. F.8, from time A to B, the turbulence is adjusting to mean flow and  $P/\varepsilon$  is negative. The largest negative  $P/\varepsilon$  happens somewhere between time A and B. It can be

seen in Fig. F.7 that shear and  $b_{12}$  are relative small in period AB. So the magnitude of negative  $P/\varepsilon$  is small. From time B to C, Turbulence has adjusted to mean flow and  $P/\varepsilon$  is positive. Shown in Fig. F.7, Concurrence of large shear and  $b_{12}$  produces larger positive  $P/\varepsilon$  during time BC. The ratio of period AB to BC is about 2:3, so turbulence stays in positive production much longer than it is in negative production.

Figures F.9 shows the variation of  $b_{12}$  when frequency is high. The difference between high and low frequency cases is obvious. The first is the asymmetry of  $b_{12}$  to x-axis in the high frequency case: the magnitude of positive  $b_{12}$  is much smaller than that of negative  $b_{12}$ . This is caused by the initial moving direction of shear and the difference of frequency. In our simulation, the shear turns to positive first. Thus  $b_{12}$  becomes negative first and may reach largest negative value. When shear becomes negative,  $b_{12}$  needs to be turned to positive. However, there is no enough time for  $b_{12}$  to fully attain the largest positive value. Thus, the asymmetry of  $b_{12}$  is generated. As shown in Fig. F.9, the asymmetry of  $b_{12}$  diminishes with time. The second difference between high frequency and low frequency cases is the relative position of shear and  $b_{12}$ . Examining in one period in Fig. F.7 and F.9b, it can be seen that, from time A to C, the relative positions of shear and  $b_{12}$  are same for both cases. This relation gives a small negative production first then follows a large positive production. However from time C to E, the difference appears. In the high frequency case period CD is much longer and period DE is much shorter than they are in low frequency case. This relation generates a large negative production during time CD and small positive production during time DE in high frequency case. This also explains the two different peaks in the variation of  $k$  in Fig. F.6a. For high frequency case, the negative and positive production will offset each other and produce no net effect in the development of turbulence.

It can be seen that magnitude of  $P/\varepsilon$  increases with time in Fig. F.10 for high frequency case. This is primarily due to the decrease of  $\varepsilon$ . The Mean value of  $P/\varepsilon$  is just above zero and much less than 1. From fig. F.10, we can see that the decay of turbulence in high



frequency is not caused by the small magnitude of  $P/\varepsilon$ . It is caused by large negative  $P/\varepsilon$ . Negative production means turbulence transfers its kinetic energy into mean flow. The mechanism of this phenomenon will be investigated in details in future works.

The details of development of turbulence anisotropy tensor are given in Figs. F.11 and F.12. In low frequency case, anisotropy in turbulence has been well developed. The mean values of  $b_{11}$  and  $b_{22}$  are about 0.15 and -0.1 respectively. In high frequency case, mean values of anisotropy  $b_{11}$  and  $b_{22}$  are about 0. Thus, turbulence has no opportunity to develop in high frequency case.

To gain more insight of evolution of turbulence, We investigate the terms in the Reynolds-stress equation (Eqs. F.6-F.9). Figs.F.13-F.14 show the comparison of time derivative of Reynolds-stress. We use two ways to obtain those values. One is from the right hand side of Reynolds-stress evolution equation (Eqs. F.6-F.9) and the other is from the finite difference operation on Reynolds-stress:

$$\frac{d\langle u_i u_j \rangle}{dt} = \frac{\langle u_i u_j(t + dt) \rangle - \langle u_i u_j(t - dt) \rangle}{2\delta t}$$

The results from two different methods agree very well. This guarantees that each term in the Reynolds-stress equation budget is reliable.

Figure.F.15 shows the different terms in Reynolds stress equation for  $\langle u_1 u_2 \rangle$  (Eq. F.9). The pressure redistribution and dissipation always counter the effect of production. The magnitude of dissipation is smaller than those of production and redistribution. Fig. 18 shows the budget of  $\langle u_1 u_1 \rangle$ . Pressure redistribution almost always counters the effect of production except when production is close to zero. In the earlier stage, magnitude of dissipation is comparable to those of production and redistribution. In the later stage, it is very small. In the Reynolds equations for  $\langle u_2 u_2 \rangle$  and  $\langle u_3 u_3 \rangle$ , the production is zero. The periodic variation of dissipation is relatively small. Pressure redistribution plays a key role in determining the variation of kinetic energy as shown in Figs. F.17 and F.18. In Fig. F.19, the variations of pressure -strain are shown. It can be seen that pressure redistribution

terms  $R_{11}$  and  $R_{22}$  evolve much similarly, while phase of  $R_{33}$  is almost 180 degree different from those of  $R_{11}$  and  $R_{22}$ . This means that both  $R_{11}$  and  $R_{22}$  will transfer turbulence kinetic energy from  $\langle u_1 u_1 \rangle$  and  $\langle u_2 u_2 \rangle$  to  $\langle u_3 u_3 \rangle$ . This is different from wall turbulence flow. In the wall flow,  $R_{22}$  will help to maintain turbulence energy in  $\langle u_2 u_2 \rangle$ . As is well known, the net effect of pressure redistribution is zero which is verified in Fig. F.19.

### F.3.3 Comparison: DNS vs. RANS models

In this Section, we compare DNS results with those obtained by solving Reynolds averaged Navier-Stokes equations (RANS) with turbulence models. Here, we use three different models which are LRR-IP, LRR-QI, and SSG models (12). In the high frequency case, DNS and models predict decay of  $k$  as shown in Fig. F.20. But models predict slow decay rate. In low frequency case, models fail to predict growth of  $k$  as shown in Fig. F.21. Comparisons of results of  $b_{12}$  are given in Figs. F.22 and F.23. The agreement is somewhat better. This is to be expected as  $b_{12}$  evolution is dominated by shear. However, in both cases, model yields smaller variations of  $b_{12}$  than DNS. In the low frequency case,  $b_{12}$  does not reach the same saturation values as in DNS. In high frequency case, models predict very large values of  $b_{11}$ . In low frequency case, SSG model gives the closest result to that of DNS for  $b_{11}$ .

## F.4 Conclusions

DNS of homogenous turbulence subjected to constant shear is performed using Lattice Boltzmann method. The results agree very well with classical results obtained by using Navier-Stokes equations. Suitability of lattice Boltzmann method for DNS of turbulence has been thus verified. In DNS of homogenous turbulence subjected to periodically varied shear, a critical frequency, which determines whether  $k$  decays or not, is found. It seems that  $b_{12}$  reaching a saturation value is a necessary condition in order to maintain turbulence. We observe negative production for  $k$  which means there is a mechanism to take kinetic energy

away from turbulence and transfer it to mean flow. The details of this mechanism need to be studied further. The comparisons of results of DNS and turbulence models show that models fail to predict the critical frequency. In terms of anisotropy of turbulence, models perform a little better.

## F.5 Figures

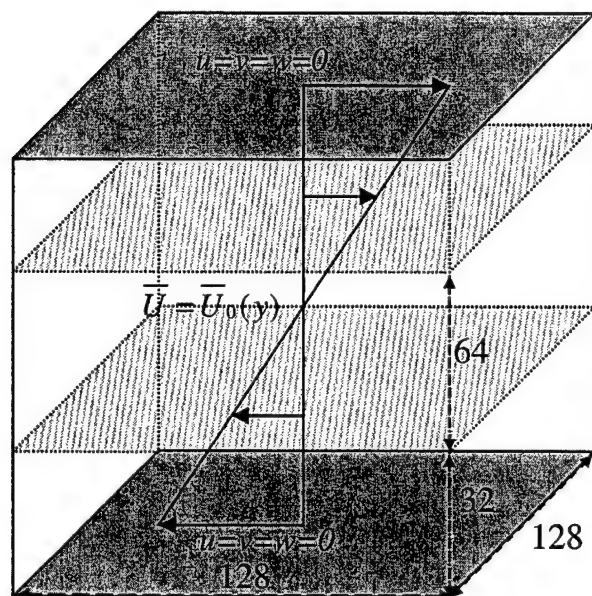


Figure F.1: Computational domain.

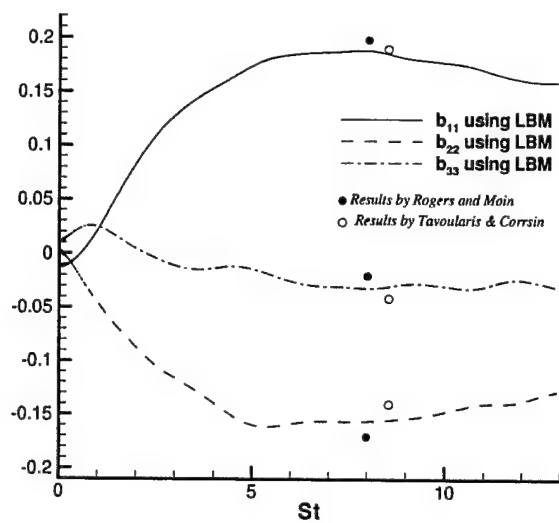


Figure F.2: The results of anisotropic tensor obtained from DNS using LBM, Navier-Stokes equations.

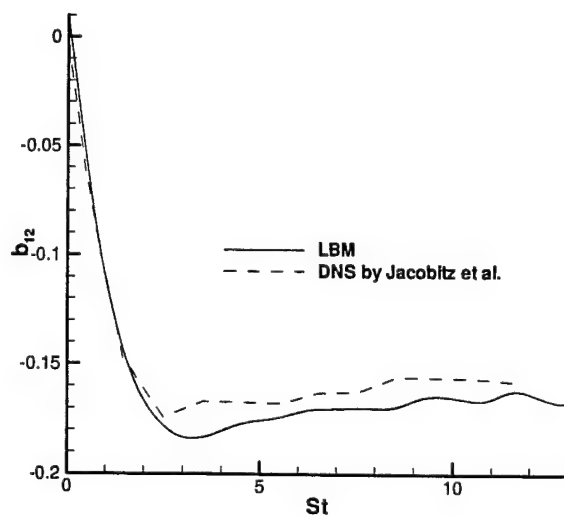


Figure F.3: The results of  $b_{12}$  obtained from DNS using LBM and Navier-Stokes Equations by Jacobitz et al. (10) with the initial values of  $Re_\lambda = 44.72$  and  $SK/\varepsilon = 2.0$ .

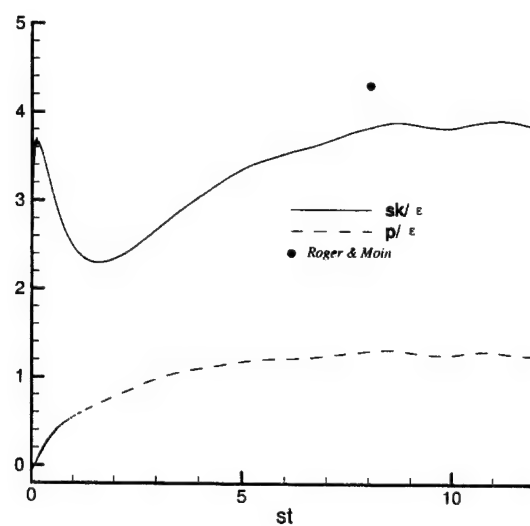


Figure F.4: Dimensionless shear rate and production over dissipation ratio by DNS using LBM. Solid circle is the value of shear obtained in the DNS by Rogers and Moin (7).

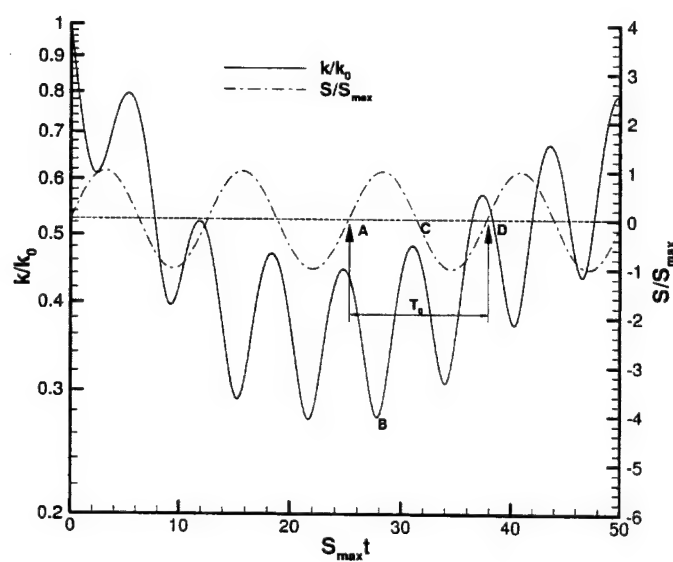
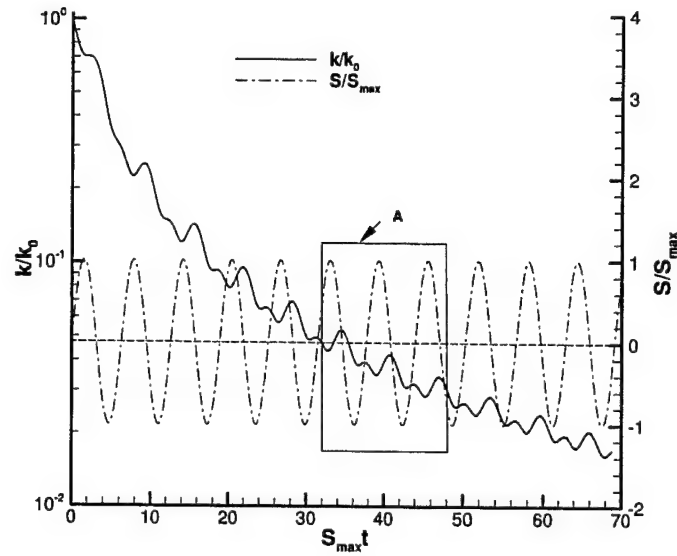
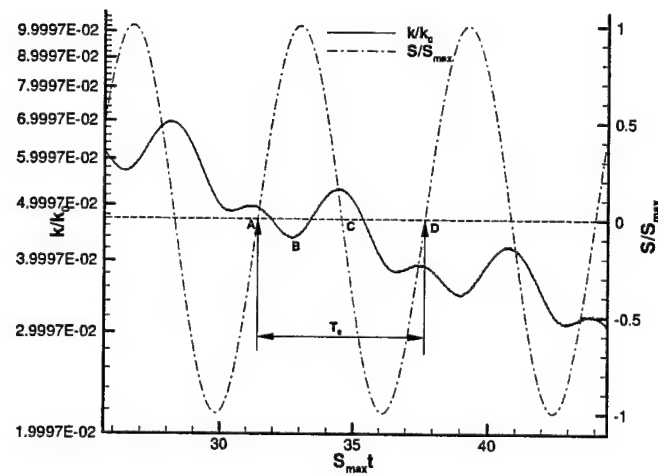


Figure F.5: Evolution of  $k$  for  $\frac{\omega}{5} = 0.5$  case



(a)



(b)

Figure F.6: (a) Evolution of  $k$  for  $\frac{\omega}{S} = 1.0$  case; (b) Amplification of area A in the Fig. F.6a

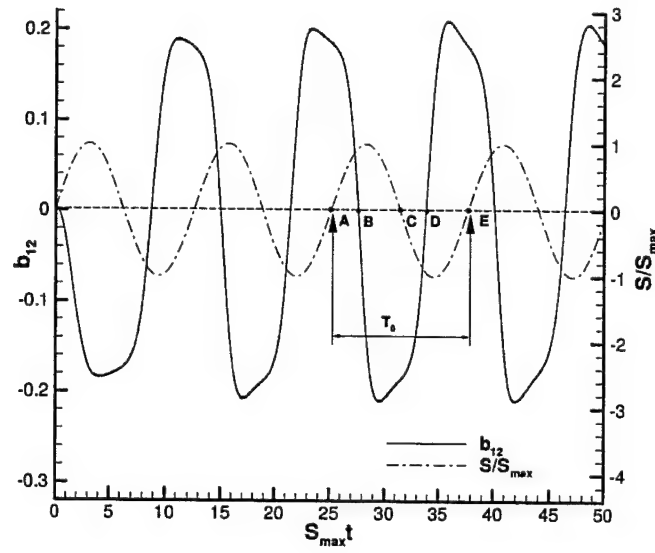


Figure F.7: Evolution of  $b_{12}$  for  $\frac{\varepsilon}{g} = 0.5$  case

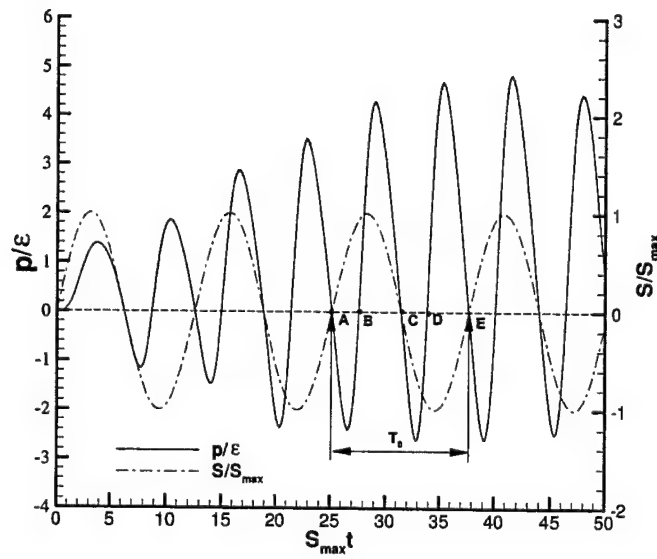


Figure F.8: Evolution of production over dissipation ratio  $\frac{P}{\varepsilon}$  for  $\frac{\varepsilon}{g} = 0.5$  case



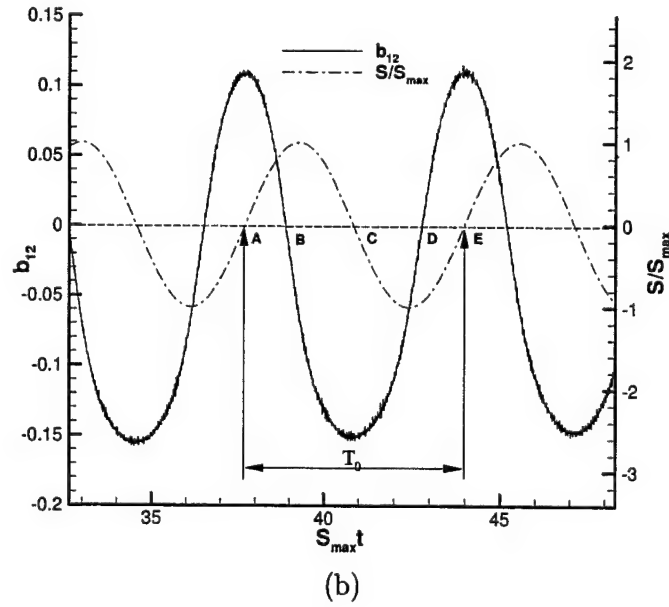
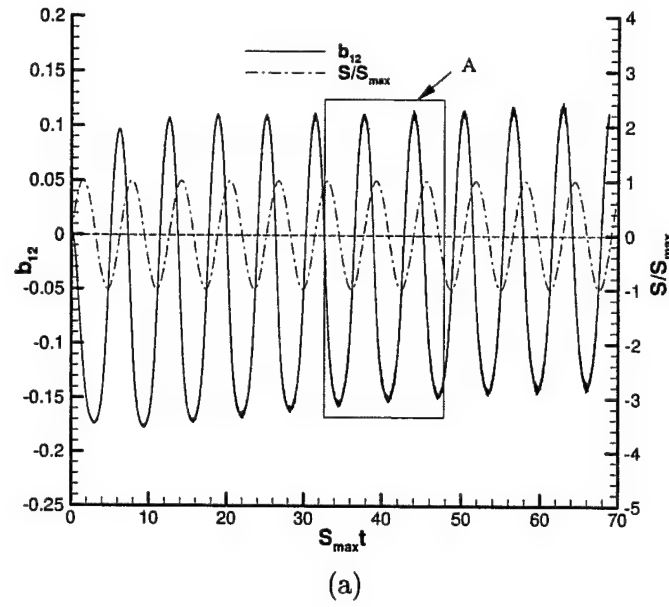


Figure F.9: (a) Evolution of  $b_{12}$  for  $\frac{\omega}{S} = 1.0$  case. (b) Amplification of area A in the Fig. F.9a

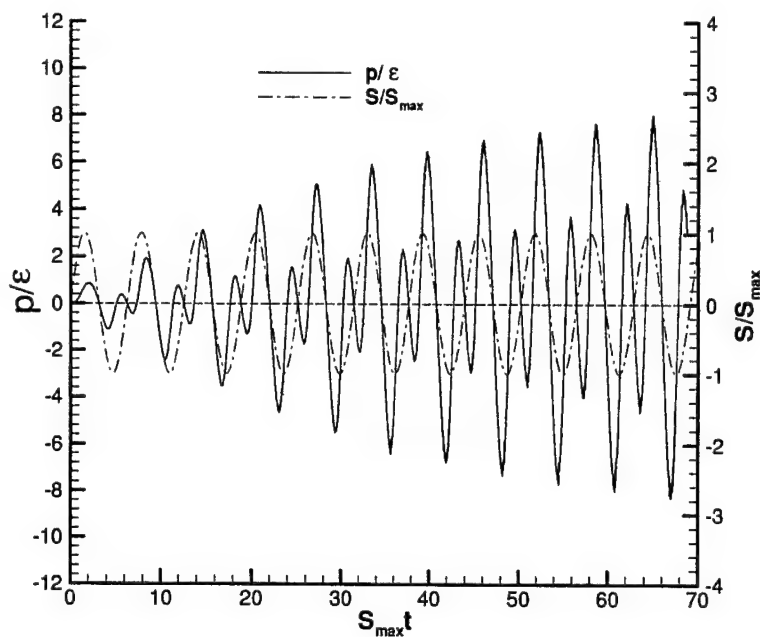


Figure F.10: Evolution of production over dissipation ratio  $\frac{P}{\varepsilon}$  for  $\frac{\omega}{\varepsilon} = 1.0$  case

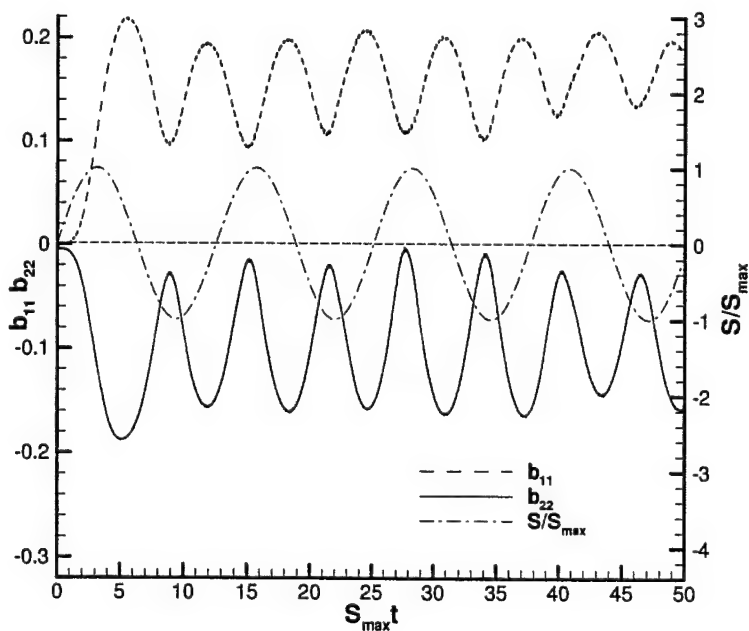


Figure F.11: Evolution of  $b_{11}$  and  $b_{22}$  for  $\frac{\omega}{\varepsilon} = 0.5$  case

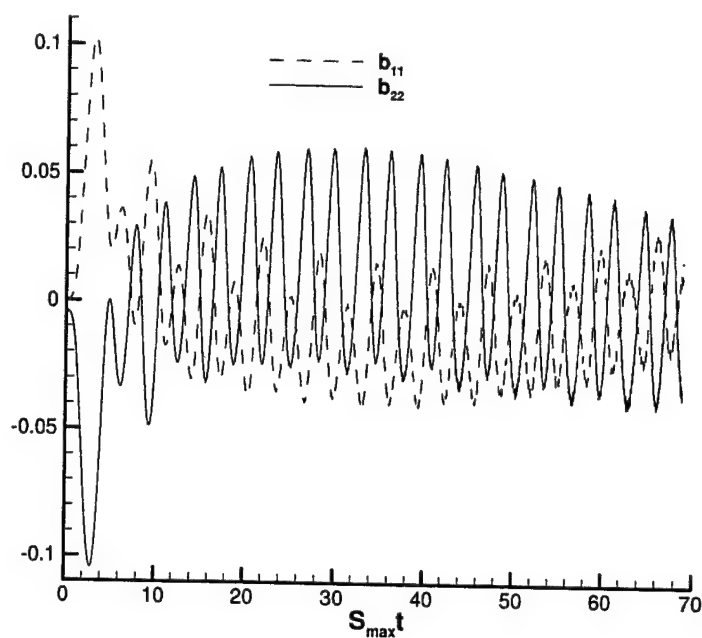


Figure F.12: Evolution of  $b_{11}$  and  $b_{22}$  for  $\frac{\omega}{S} = 1.0$  case

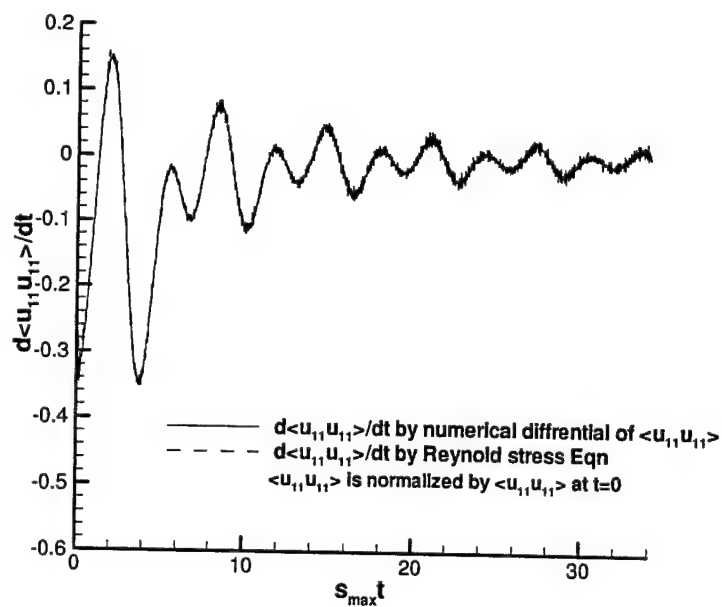


Figure F.13: Comparison of time derivative of  $\langle u_1 u_1 \rangle$  for  $\frac{\omega}{S} = 1.0$  case

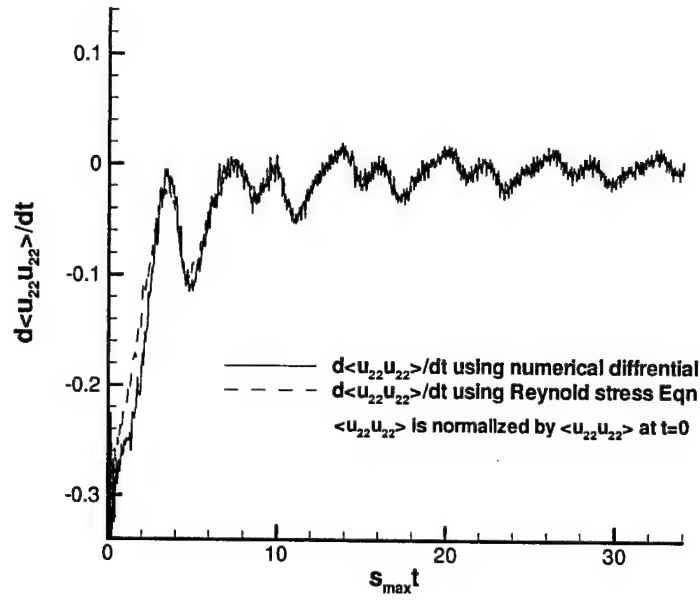


Figure F.14: Comparison of time derivative of  $\langle u_2 u_2 \rangle$  for  $\frac{\omega}{S} = 1.0$  case

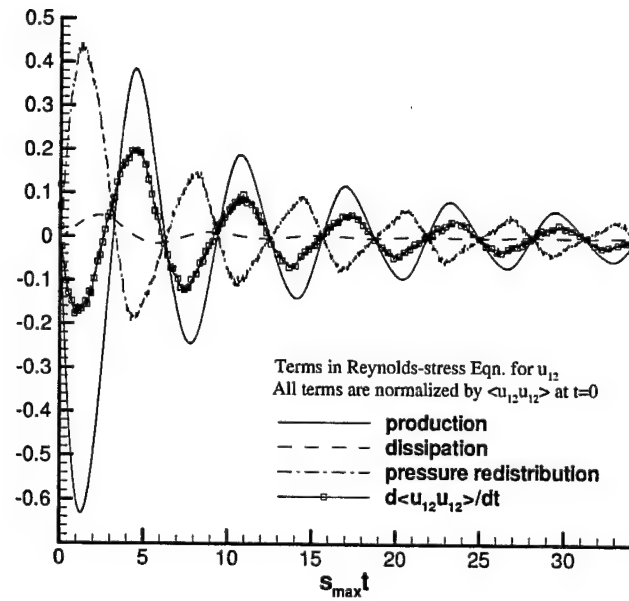
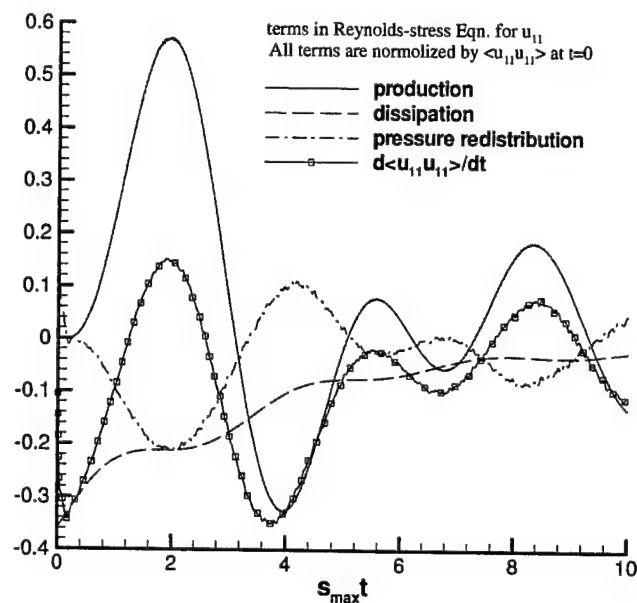
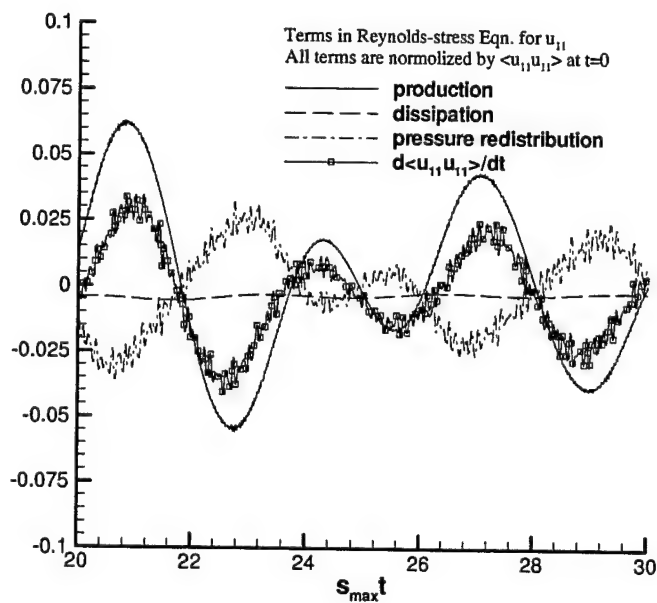


Figure F.15: Variations of terms in Reynolds-stress equation for  $\langle u_1 u_2 \rangle$  for  $\frac{\omega}{S} = 1.0$  case



(a)



(b)

Figure F.16: (a) Variations of terms in Reynolds-stress equation for  $\langle u_1 u_1 \rangle$  at earlier stage for  $\frac{\omega}{S} = 1.0$  case; (b) Variations of terms in Reynolds-stress Equation for  $\langle u_1 u_1 \rangle$  at later stage for  $\frac{\omega}{S} = 1.0$  case

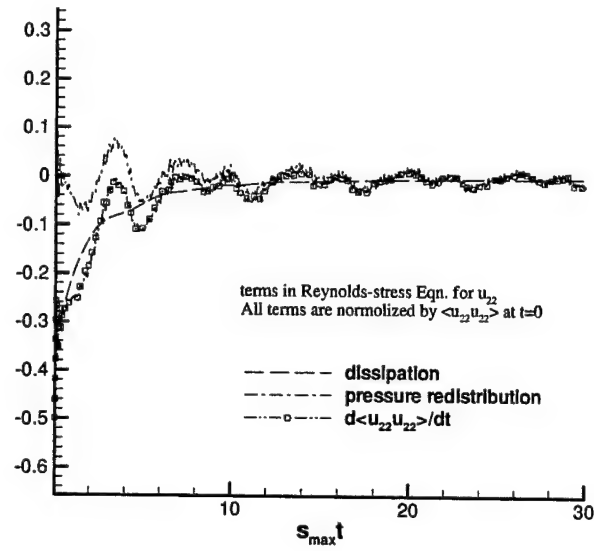


Figure F.17: Variations of terms in Reynolds-stress equation for  $\langle u_2 u_2 \rangle$  at later stage for  $\frac{\varepsilon}{S} = 1.0$  case

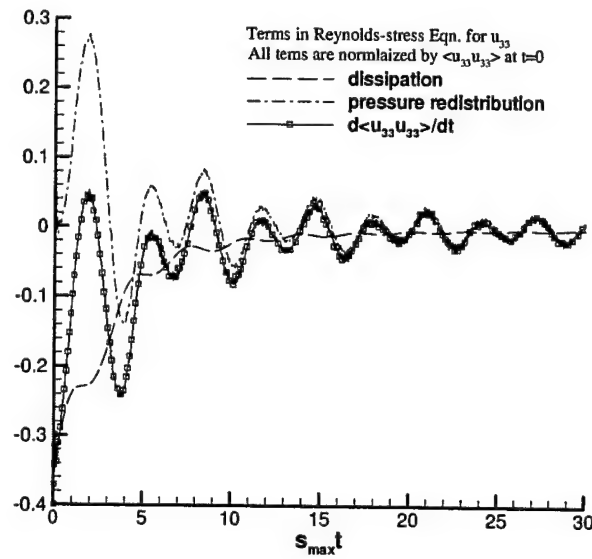


Figure F.18: Variations of terms in Reynolds-stress equation for  $\langle u_3 u_3 \rangle$  at later stage for  $\frac{\varepsilon}{S} = 1.0$  case

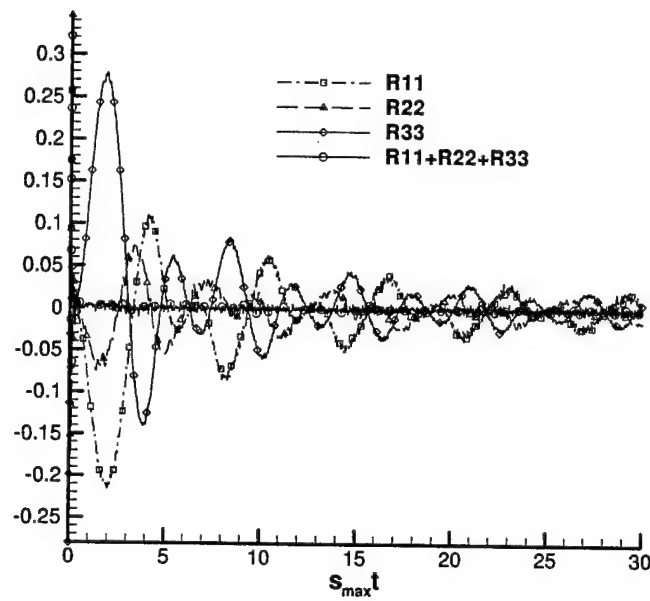


Figure F.19: The variations of pressure redistributions for  $\frac{\omega}{S} = 1.0$  case

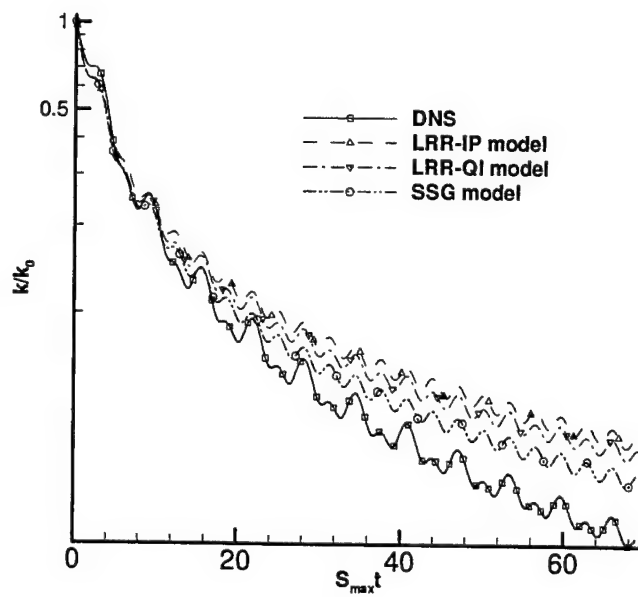


Figure F.20: Comparison of  $k$  obtained by DNS and Reynolds averaged Navier-Stokes turbulence models for  $\frac{\omega}{S} = 1.0$  case

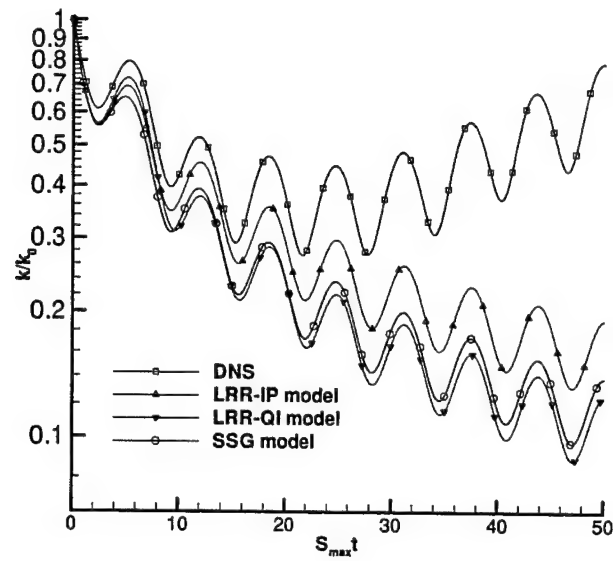


Figure F.21: Comparison of  $k$  obtained by DNS and Reynolds averaged Navier-Stokes turbulence models for  $\frac{\omega}{S} = 0.5$  case

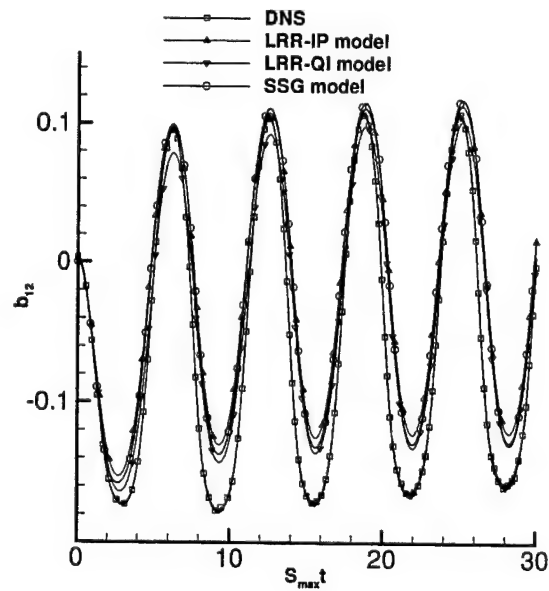


Figure F.22: Comparison of  $b_{12}$  obtained by DNS and Reynolds averaged Navier-Stokes turbulence models for  $\frac{\omega}{S} = 1.0$  case



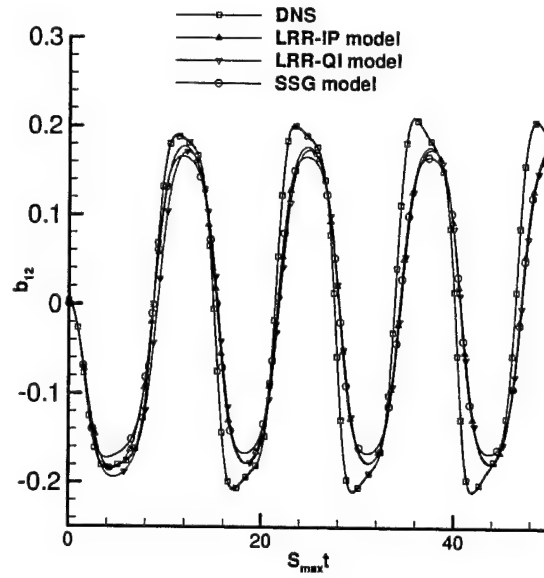


Figure F.23: Comparison of  $b_{12}$  obtained by DNS and Reynolds averaged Navier-Stokes turbulence models for  $\frac{U}{\gamma} = 0.5$  case

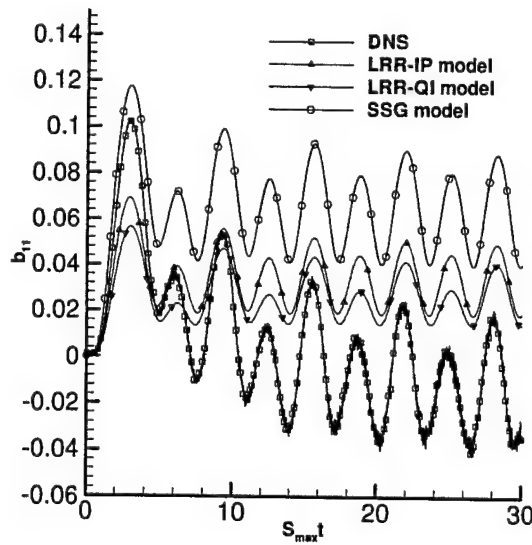


Figure F.24: Comparison of  $b_{11}$  obtained by DNS and Reynolds averaged Navier-Stokes turbulence models for  $\frac{U}{\gamma} = 1.0$  case

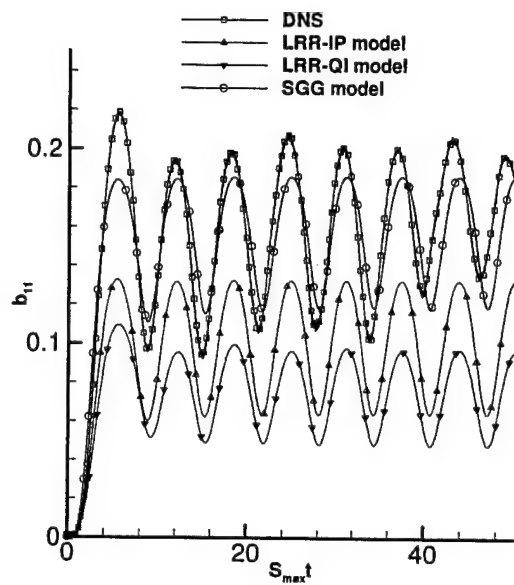


Figure F.25: Comparison of  $b_{11}$  obtained by DNS and Reynolds averaged Navier-Stokes turbulence models for  $\frac{\omega}{S} = 0.5$  case

## Bibliography

- [1] Rose, Results of an attempt to generate a homogeneous turbulent shear flow, *J. Fluid Mech.*, 25, 97-120, 1966.
- [2] Champagne, Harris, Corrsin, Experiments on nearly homogeneous turbulent shear flow, *J. Fluid Mech.*, 41, 81-139, 1970.
- [3] Tavoulris S. and Corrsin S. Experiments in nearly homogenous turbulent shear flow with a uniform mean temperature gradient. Part 1. *J. Fluid Mech.* 1981;104:311.
- [4] Tavoularis and Corrsin, Experiments in nearly homogeneous turbulent shear flow with a uniform mean temperature gradient. Part 2, the fine structure, *J. Fluid Mech.*, 104, 349-367, 1981.
- [5] Pumir and Sharaiman, Persistent small scale anisotropy in homogeneous shear flow, *Phys. Rev. Lett.*, 75(17), 3114-3117, 1995.
- [6] Pumir, Turbulence in homogeneous shear flow, *Phys. Fluids*, 8, 3112-3127, 1996.
- [7] Rogers MM, Moin P. The structure of the vorticity field in homogeneous turbulent flows. *J. Fluid Mech.* 1987;176:33-66
- [8] Lee, Kim, and Moin, Structure of turbulence at high shear rate, *J. Fluid Mech.*, 216, 561-583, 1990.
- [9] Kida and Tanaka, Dynamics of vortical structures in homogeneous shear flow, *J. Fluid Mech.*, 274, 43-68, 1994.
- [10] Jacobitz FG, Sarkar S, and Van Atta CW. Direct numerical simulations of turbulence evolution in a uniformly sheared and stably stratified flow. *J. Fluid Mech.* 1997; 342:231-261.

- 
- [11] Rogallo RS. Numerical experiments in homogeneous turbulence. *NASA TM-81315* 1981.
- [12] S. B. Pope, *Turbulent Flows* (Cambridge University Press, Cambridge, 2000).
- [13] D. Yu, R. Mei, L.-S. Luo, and W. Shyy, "Viscous flow computations with the method of lattice Boltzmann equation," *Prog. Aerospace Sci.* **39**(5), 329,2003.
- [14] Z. Guo and C. Zheng and B. Shi, "Discrete lattice effects on the forcing term in the lattice Boltzmann method ," *Phys. Eev. E* **65**, 046308,2002.

## Appendix G

# Lattice Boltzmann Models for Axisymmetric Flows in Cylindrical Coordinate

Nomenclature			
$c_s$	Speed of sound	$e_\alpha$	Discretized particle velocity
$f$	Distribution function	$f^{(eq)}$	Equilibrium distribution function
$u$	Fluid velocity	$\rho$	Fluid density
$\delta_t$	Time step	$\delta_x$	Grid size
$\tau$	Normalized relaxation time	$w_\alpha$	Weight function
$\rho_0$	Mean density	$\rho'$	Density fluctuation
$E_2$	L <sub>2</sub> norm error	$h$	Grid size
$\nu$	Viscosity		

### G.1 Introduction

LBM has demonstrated a significant potential and broad applicability with numerous advantages both physically and computationally, including the parallelism of algorithm, the simplicity of programming and the ability to incorporate microscopic interactions. Several

shortcomings, however, remained to be addressed. One of them, which is focused on partly in this Appendix, is the extension of LBM from the Cartesian coordinates to curvilinear coordinates to meet the needs of many practical flow problems. Several efforts have been made in this issue and achieved some successes. The finite volume version of LBM by Succi and his coworkers(1; 2) and the interpolation-supplemented lattice Boltzmann equation model by He et al(3; 4) extended LBM to curvilinear coordinate system. Yu and Zhao(5) applied LBM in paraboloidal coordinate system to simulate Rossby vortex. They specially introduced a scaling factor to re-scale all related physical quantities and to map non-uniform curvilinear mesh onto uniform flat mesh. All above methods focus on applying current lattice Boltzmann model in irregular mesh. Recently, Halliday et al(6) presented a model in cylindrical coordinate for pseudo-Cartesian flow. However, the implementation of this model is very complicated and not practical somehow.

In this Appendix, we present a lattice Boltzmann model in cylindrical coordinate system for both vector(momentum) field and scalar(temperature, concentration, etc.) field by introducing source-like term and body force-like term(6) in lattice Boltzmann equations. The model has the second order accuracy in space and is easy to be implemented.

The remainder of this Appendix is organized as follows. Lattice Boltzmann equations for axisymmetric flows in cylindrical coordinate system are given in Section G.2, in which macroscopic equations such as continuity equation, momentum equations, scalar equation for temperature or concentration are derived; Numerical evaluation are presented in Section G.3; Finally, we conclude in Section G.4 with a brief discussion.

## G.2 Lattice Boltzmann model for axisymmetric flows

### G.2.1 Hydrodynamic equations in cylindrical coordinate system

In cylindrical coordinate, continuity equation, Navier-stokes equations and scalar(temperature, mass concentration, etc.) equation for incompressible flow are expressed as following

$$\frac{\partial \rho}{\partial t} + \frac{1}{r} \frac{\partial(\rho r u_r)}{\partial r} + \frac{1}{r} \frac{\partial(\rho u_\theta)}{\partial \theta} + \frac{\partial(\rho u_z)}{\partial z} = 0, \quad (\text{G.1})$$

$$\frac{\partial u_r}{\partial t} + u_r \frac{\partial u_r}{\partial r} + \frac{u_\theta}{r} \frac{\partial u_r}{\partial \theta} + u_z \frac{\partial u_r}{\partial z} - \frac{v_\theta^2}{r} = -\frac{1}{\rho} \frac{\partial p}{\partial r} + \nu \left[ \frac{\partial^2 u_r}{\partial r^2} + \frac{1}{r} \frac{\partial u_r}{\partial r} + \frac{1}{r^2} \frac{\partial^2 u_r}{\partial \theta^2} + \frac{\partial^2 u_r}{\partial z^2} - \frac{u_r}{r^2} + \frac{2}{r^2} \frac{\partial u_\theta}{\partial \theta} \right] \quad (\text{G.2})$$

$$\frac{\partial u_\theta}{\partial t} + u_r \frac{\partial u_\theta}{\partial r} + \frac{u_\theta}{r} \frac{\partial u_\theta}{\partial \theta} + u_z \frac{\partial u_\theta}{\partial z} + \frac{u_\theta u_r}{r} = -\frac{1}{\rho r} \frac{\partial p}{\partial \theta} + \nu \left[ \frac{\partial^2 u_\theta}{\partial r^2} + \frac{1}{r} \frac{\partial u_\theta}{\partial r} + \frac{1}{r^2} \frac{\partial^2 u_\theta}{\partial \theta^2} + \frac{\partial^2 u_\theta}{\partial z^2} - \frac{u_\theta}{r^2} + \frac{2}{r^2} \frac{\partial u_r}{\partial \theta} \right] \quad (\text{G.3})$$

$$\frac{\partial u_z}{\partial t} + u_r \frac{\partial u_z}{\partial r} + \frac{u_\theta}{r} \frac{\partial u_z}{\partial \theta} + u_z \frac{\partial u_z}{\partial z} = -\frac{1}{\rho} \frac{\partial p}{\partial z} + \nu \left[ \frac{\partial^2 u_z}{\partial r^2} + \frac{1}{r} \frac{\partial u_z}{\partial r} + \frac{1}{r^2} \frac{\partial^2 u_z}{\partial \theta^2} + \frac{\partial^2 u_z}{\partial z^2} \right] \quad (\text{G.4})$$

$$\frac{\partial F}{\partial t} + u_r \frac{\partial F}{\partial r} + \frac{u_\theta}{r} \frac{\partial F}{\partial \theta} + u_z \frac{\partial F}{\partial z} = \mathcal{A}_F \left[ \frac{1}{r} \frac{\partial}{\partial r} (r \frac{\partial F}{\partial r}) + \frac{1}{r^2} \frac{\partial^2 F}{\partial \theta^2} + \frac{\partial^2 F}{\partial z^2} \right] + Q_F \quad (\text{G.5})$$

where  $\nu$  is the kinetic viscosity of the fluid,  $\mathcal{A}_F$  is the scalar related property such as the thermal diffusivity for temperature and diffusivity coefficient for concentration, and  $Q_F$  is a source term for the scalar field.

In an axisymmetric field with  $u_\theta = 0$ , above equations can be simplified as

$$\frac{\partial \rho}{\partial t} + \frac{\partial \rho u_r}{\partial r} + \frac{\partial \rho u_z}{\partial z} = -\frac{\rho u_r}{r}, \quad (\text{G.6})$$

$$\frac{\partial u_r}{\partial t} + \mathbf{u} \cdot \nabla u_r = -\frac{1}{\rho} \frac{\partial p}{\partial r} + \nu \nabla^2 u_r + \frac{\nu}{r} \left( \frac{\partial u_r}{\partial r} - \frac{u_r}{r} \right), \quad (\text{G.7})$$

$$\frac{\partial u_z}{\partial t} + \mathbf{u} \cdot \nabla u_z = -\frac{1}{\rho} \frac{\partial p}{\partial z} + \nu \nabla^2 u_z + \frac{\nu}{r} \frac{\partial u_z}{\partial r}, \quad (\text{G.8})$$

and

$$\frac{\partial F}{\partial t} + \mathbf{u} \cdot \nabla F = \mathcal{A}_F \nabla^2 F + s_F. \quad (\text{G.9})$$

respectively with  $\mathbf{u} = u_r \mathbf{e}_r + u_z \mathbf{e}_z$ ,  $\nabla = \partial_r \mathbf{e}_r + \partial_z \mathbf{e}_z$ ,  $\nabla^2 = \partial_r^2 + \partial_z^2$ , and  $s_F = \frac{\mathcal{A}_F}{r} \frac{\partial F}{\partial r} + Q_F$ .

### G.2.2 Lattice Boltzmann equation for vector(momentum) field

Comparing Eqs. (G.6) and (G.8) with 2D continuity equation and momentum equations in Cartesian coordinate respectively, we found there is an extra term of  $s = -\frac{\rho u_r}{r}$  in Eq. (G.6) and  $a_i = \frac{\nu}{r}(\partial_r u_i - \frac{u_r \delta_{ir}}{r})$ ,  $i = r, z$  in Eq. (G.8). This suggests us to introduce a term  $g_\alpha(\mathbf{r}, t)$  in lattice Boltzmann equation(7; 8)

$$f_\alpha(\mathbf{r} + \mathbf{e}_\alpha \delta_t, t + \delta_t) = f_\alpha(\mathbf{r}, t) - \frac{1}{\tau}[f_\alpha - f_\alpha^{(\text{eq})}] + \delta_t g_\alpha(\mathbf{r}, t), \quad (\text{G.10})$$

where  $f_\alpha$  is the density distribution function with discrete velocity  $\mathbf{e}_\alpha$  along  $\alpha$ th direction,  $f_\alpha^{(\text{eq})}$  is the equilibrium distribution function, and  $\tau$  is the relaxation time determining the viscosity  $\nu$  of the modeled fluid. We use the nine velocity model in two dimensions (D2Q9) in our analysis. The equilibria for incompressible flow(10) are

$$f_\alpha^{(\text{eq})} = w_\alpha \left\{ \rho' + \rho_0 \left[ \frac{3\mathbf{e}_\alpha \cdot \mathbf{u}}{c^2} + \frac{9(\mathbf{e}_\alpha \cdot \mathbf{u})^2}{2c^4} - \frac{3u^2}{2c^2} \right] \right\},$$

where  $\rho'$  is the density fluctuation, and  $\rho_0$  is the mean density in the system which is usually set to one. The total density is  $\rho = \rho_0 + \rho'$ . The mass and momentum conservations are enforced:

$$\begin{aligned} \rho' &= \sum_{\alpha} f_\alpha = \sum_{\alpha} f_\alpha^{(\text{eq})}, \\ \rho_0 \mathbf{u} &= \sum_{\alpha} \mathbf{e}_\alpha f_\alpha = \sum_{\alpha} \mathbf{e}_\alpha f_\alpha^{(\text{eq})}. \end{aligned}$$

The spatial and velocity dependent microscopic term  $g_\alpha(\mathbf{r}, t)$  is to reflect two extra terms mentioned above, source-like term  $s$  in Eq. (G.6) and body-force-like term  $\mathbf{a}$  in Eq. (G.8) simultaneously. We shall use Chapman-Enskog technique to determine it.

Chapman-Enskog expansions of  $f_\alpha$  and  $\partial t$  in the powers of  $\varepsilon$  are the same as Eq.(C.16). For purpose of extracting the dynamics of this model, we perform a chapman-Enskog type expansion with the  $g_\alpha$  as well as  $f_\alpha$ ,

$$f_\alpha = f_\alpha^{(0)} + \varepsilon f_\alpha^{(1)} + \varepsilon^2 f_\alpha^{(2)} + \dots, \quad (\text{G.11})$$



$$g_\alpha = \varepsilon g_\alpha^{(1)} + \varepsilon^2 g_\alpha^{(2)} + \dots, \quad (\text{G.12})$$

Here we have assumed that there is no zeroth term in the expansion(11).

Taylor expansion in  $\delta t$  to the second order and a substitution of chapman-Enskog expansions lead to

$$\begin{aligned} & f_\alpha(\mathbf{x} + \mathbf{e}_\alpha \delta t, t + \delta t) - f_\alpha(\mathbf{x}, t) \\ &= \delta t D_t f_\alpha + \frac{1}{2} \delta t^2 D_t D_t f_\alpha + o((\delta t)^3) \\ &= \varepsilon \delta t D_{t_0} f_\alpha^{(0)} + \varepsilon^2 \delta t (\partial_{t_1} f_\alpha^{(0)} + D_{t_0} f_\alpha^{(0)} + \frac{1}{2} \delta t D_{t_0}^2 f_\alpha^{(0)} + o(\varepsilon^3), \end{aligned}$$

where

$$D_t \equiv \partial_t + \mathbf{e}_\alpha \cdot \nabla, \quad D_{t_0} \equiv \partial_{t_0} + \mathbf{e}_\alpha \cdot \nabla.$$

The first few equations of a set of successive equations in the order of  $\varepsilon$  obtained from Eq. (G.10) are

$$\varepsilon^0 : f_\alpha^{(0)} = f_\alpha^{(eq)}, \quad (\text{G.13})$$

$$\varepsilon^1 : D_{t_0} f_\alpha^{(0)} = -\frac{1}{\Delta t \tau} f_\alpha^{(1)} + g_\alpha^{(1)}, \quad (\text{G.14})$$

$$\varepsilon^2 : \partial_{t_1} f_\alpha^{(0)} + \frac{(2\tau - 1) D_{t_0} f_\alpha^{(1)}}{2\tau} = -\frac{\delta t D_{t_0} g_\alpha^{(1)}}{2} - \frac{f_\alpha^{(2)}}{\Delta t \tau} + g_\alpha^{(2)}. \quad (\text{G.15})$$

The distribution function  $f_\alpha$  is the normal solution which is constrained by

$$\sum_\alpha f_\alpha^{(0)} \begin{bmatrix} 1 \\ \mathbf{e}_\alpha \end{bmatrix} = \begin{bmatrix} \rho' \\ \rho_0 \mathbf{u} \end{bmatrix}, \quad (\text{G.16})$$

$$\sum_\alpha f_\alpha^{(n)} \begin{bmatrix} 1 \\ \mathbf{e}_\alpha \end{bmatrix} = 0, \quad n > 0 \quad (\text{G.17})$$

For D2Q9 model, the tensor

$$E^{(n)} = \sum_\alpha w_\alpha e_{\alpha,1} e_{\alpha,2} \cdots e_{\alpha,n} \quad (\text{G.18})$$

where  $e_{\alpha,i}$  is the projection of  $\mathbf{e}_\alpha$  on  $i$ -axis ( $i = r$  or  $z$ ), has the following properties

$$E^{(2)} = \sum_{\alpha} w_{\alpha} e_{\alpha,i} e_{\alpha,j} = \frac{1}{3} \delta_{ij} \quad (\text{G.19})$$

$$E^{(4)} = \sum_{\alpha} w_{\alpha} e_{\alpha,i} e_{\alpha,j} e_{\alpha,k} e_{\alpha,l} = \frac{1}{9} c^4 \Delta_{ijkl} \quad (\text{G.20})$$

Also,  $E^{(2n+1)} = 0$  for  $n = 0, 1, \dots$ . As a result, we have

$$\sum_{\alpha} f_{\alpha}^{(0)} = \rho', \quad (\text{G.21})$$

$$\sum_{\alpha} \mathbf{e}_{\alpha} f_{\alpha}^{(0)} = \rho_0 \mathbf{u}, \quad (\text{G.22})$$

$$\sum_{\alpha} e_{\alpha i} e_{\alpha j} f_{\alpha}^{(0)} = \frac{1}{3} c^2 \rho' \delta_{ij} + \rho_0 u_i u_j, \quad (\text{G.23})$$

$$\sum_{\alpha} e_{\alpha i} e_{\alpha j} e_{\alpha k} f_{\alpha}^{(0)} = \frac{1}{3} c^2 \rho_0 (\delta_{ij} u_k + \delta_{ki} u_j + \delta_{jk} u_i). \quad (\text{G.24})$$

With the properties (G.21) and (G.22), the moments of Eqs. (G.14) and (G.15) lead to

$$\partial_{t_0} \rho' + \nabla \cdot (\rho_0 \mathbf{u}) = \sum_{\alpha} g_{\alpha}^{(1)}, \quad (\text{G.25})$$

$$\partial_{t_0} (\rho_0 u_i) + \partial_j \sum_{\alpha} e_{\alpha i} e_{\alpha j} f_{\alpha}^{(0)} = \sum_{\alpha} e_{\alpha i} g_{\alpha}^{(1)}, \quad (\text{G.26})$$

and

$$\partial_{t_1} \rho' = \sum_{\alpha} g_{\alpha}^{(2)} - \frac{1}{2} \delta_t \sum_{\alpha} D_{t_0} g_{\alpha}^{(1)} \quad (\text{G.27})$$

$$\begin{aligned} \partial_{t_1} (\rho_0 u_i) - \delta_t \left( \tau - \frac{1}{2} \right) \partial_j \sum_{\alpha} e_{\alpha i} e_{\alpha j} D_{t_0} f_{\alpha}^{(0)} &= \sum_{\alpha} e_{\alpha i} g_{\alpha}^{(2)} - \frac{\delta_t}{2} \left[ \sum_{\alpha} e_{\alpha i} D_{t_0} \right. \\ &\quad \left. + (2\tau - 1) \partial_j \sum_{\alpha} e_{\alpha i} e_{\alpha j} \right] g_{\alpha}^{(1)} \end{aligned} \quad (\text{G.28})$$

respectively. Eq. (G.14) motivates the selection

$$g_{\alpha}^{(1)} \equiv w_{\alpha} s \quad (\text{G.29})$$

such that Eqs. (G.25), (G.26) and (G.27), (G.28) become

$$\partial_{t_0} \rho' + \nabla \cdot (\rho_0 \mathbf{u}) = s \quad (\text{G.30})$$

$$\partial_{t_0} (\rho_0 u_i) + \frac{1}{3} c^2 \partial_i \rho' + \rho_0 \mathbf{u} \cdot \nabla u_i = 0 \quad (\text{G.31})$$

and

$$\partial_{t_1} \rho' = \sum_{\alpha} g_{\alpha}^{(2)} - \frac{1}{2} \delta_t \partial_{t_0} s \quad (\text{G.32})$$

$$\partial_{t_1} (\rho_0 u_i) - \frac{2\tau - 1}{6} \delta_t c^2 \rho_0 (\partial_x^2 + \partial_y^2) u_i = \sum_{\alpha} e_{\alpha i} g_{\alpha}^{(2)} - \frac{c^2}{3} \delta_t \tau \partial_i s. \quad (\text{G.33})$$

Combining the first and the second order of  $\varepsilon$  above, we obtain

$$\partial_t \rho' + \nabla \cdot (\rho_0 \mathbf{u}) = s + \sum_{\alpha} g_{\alpha}^{(2)} - \frac{1}{2} \delta_t \partial_{t_0} s, \quad (\text{G.34})$$

$$\partial_t u_i + \mathbf{u} \cdot \nabla u_i + \frac{1}{\rho_0} \partial_i p - \nu (\partial_x^2 + \partial_y^2) u_i = \frac{1}{\rho_0} \sum_{\alpha} e_{\alpha i} g_{\alpha}^{(2)} - \frac{c^2}{3\rho_0} \delta_t \tau \partial_i s, \quad (\text{G.35})$$

where  $p = c_s^2 \rho'$  and  $\nu = (2\tau - 1) c^2 \delta_t \rho_0 / 6$ .

For the purpose of recovering the macroscopic equations (G.6) and (G.8), we have the following constrains for  $g_{\alpha}^{(2)}$  by comparing Eq. (G.34) with Eq. (G.6) and Eq.(G.35) with Eq. (G.8) on the right-hand side respectively,

$$\sum_{\alpha} g_{\alpha}^{(2)} = \frac{1}{2} \delta_t \partial_{t_0} s = s', \quad (\text{G.36})$$

$$\sum_{\alpha} e_{\alpha i} g_{\alpha}^{(2)} = \rho_0 a_i + \frac{c^2}{3} \delta_t \tau \partial_i s = \rho_0 a_i + \frac{c^2}{3} a'_i,$$

where  $a'_i = \delta_t \tau \partial_i s$ . These equalities are achieved if we select

$$g_{\alpha}^{(2)} = \varepsilon(w_{\alpha} s) + \varepsilon^2 \left( \frac{3\rho_0}{c^2} w_{\alpha} \mathbf{e}_{\alpha} \cdot \mathbf{a} + w_{\alpha} \mathbf{e}_{\alpha} \cdot \mathbf{a}' \right) \quad (\text{G.37})$$

Notice from Eqs. (G.32) and (G.33) that

$$\partial_{t_0} s = \frac{c^2}{3y} \frac{\partial \rho'}{\partial y} + \frac{\rho_0}{y} (u_x \frac{\partial u_y}{\partial x} + u_y \frac{\partial u_x}{\partial y}).$$

Finally,  $g_\alpha$  can be expressed as

$$g_\alpha = w_\alpha s + \frac{3\rho_0}{c^2} w_\alpha \mathbf{e}_\alpha \cdot \mathbf{a} + \frac{1}{2} \frac{c^2}{3r} \frac{\partial \rho'}{\partial r} + \frac{\rho_0}{r} \mathbf{u} \cdot \nabla u_r + w_\alpha \mathbf{e}_\alpha \cdot \mathbf{a}' \quad (\text{G.38})$$

with

$$\begin{aligned} s &= -\frac{\rho_0 u_r}{r}, \\ a_z &= \frac{\nu}{r} \frac{\partial u_z}{\partial r}, \quad a_r = \frac{\nu}{r} \left( \frac{\partial u_r}{\partial r} - \frac{u_r}{r} \right), \\ a'_z &= \delta_t \tau \frac{\partial s}{\partial z}, \quad a'_r = \delta_t \tau \frac{\partial s}{\partial r} \end{aligned}$$

Substitute Eq. (G.37) into Eqs. (G.34) and (G.35), the continuity equation (G.6) and incompressible Navier-Stokes equation (G.8) are recovered.

### G.2.3 Lattice Boltzmann equation for scalar field

Following the same methodology as LBM to vector field, the lattice Boltzmann equation for scalar  $F$  is written as

$$F_\alpha(\mathbf{r} + \mathbf{e}_\alpha \delta_t, t + \delta_t) = F_\alpha(\mathbf{r}, t) - \frac{1}{\tau} [F_\alpha - F_\alpha^{(\text{eq})}] + \delta_t s_\alpha(\mathbf{r}, t), \quad (\text{G.39})$$

where  $s_\alpha = w_\alpha s_F$

The equilibria for D2Q9 mesh are

$$F_\alpha^{(\text{eq})} = w_\alpha F \left[ 1 + \frac{3\mathbf{e}_\alpha \cdot \mathbf{u}}{c^2} + \frac{9(\mathbf{e}_\alpha \cdot \mathbf{u})^2}{2c^4} - \frac{3u^2}{2c^2} \right]$$

Conservation law corresponding to the scalar considered is enforced

$$\sum_\alpha F_\alpha = \sum_\alpha F_\alpha^{(\text{eq})} = F \quad (\text{G.40})$$

Taylor expanding to the second order of  $\delta t$  yields

$$F_\alpha(\mathbf{r} + \mathbf{e}_\alpha \delta_t, t + \delta_t) - F_\alpha(\mathbf{r}, t) = \delta_t D_t F_\alpha + \frac{1}{2} \delta_t^2 D_t D_t F_\alpha + \dots \quad (\text{G.41})$$

Scalar transport (diffusion, thermal conduction, etc.) is a slow process on large spatial scales (12), which suggests the following Chapman-Enskog expansion

$$F_\alpha = F_\alpha^{(0)} + \varepsilon F_\alpha^{(1)} + \varepsilon^2 F_\alpha^{(2)} + o(\varepsilon^3) \quad (\text{G.42})$$

$$\partial_t = \varepsilon^2 \partial_{t_1} + o(\varepsilon^3) \quad (\text{G.43})$$

Substitutions of Taylor expansion (G.41) and Chapman-Enskog expansions (G.42) and (G.43) into Eq. (G.39) bring

$$\begin{aligned} & \varepsilon(\mathbf{e} \cdot \nabla) F_\alpha^{(0)} + \varepsilon^2 [\partial_{t_1} F_\alpha^{(0)} + (\frac{1}{2} - \tau) \delta_t (\mathbf{e} \cdot \nabla)^2 F_\alpha^{(0)}] + o(\varepsilon^3) \\ &= -\frac{1}{\tau \delta_t} (\varepsilon F_\alpha^{(1)} + \varepsilon^2 F_\alpha^{(2)} + o(\varepsilon^3)) + s_\alpha \end{aligned}$$

Summing over all  $\alpha$  of above equation, Eq. (G.9) is recovered by noticing  $F_\alpha^{(0)} = F_\alpha^{(eq)}$  (so that  $\sum_\alpha F_\alpha^{(1)} = \sum_\alpha F_\alpha^{(2)} = 0$ ) and  $F_\alpha^{(1)} = -\tau \delta_t (\mathbf{e} \cdot \nabla) F_\alpha^{(0)}$  with  $\mathcal{A}_F = \frac{(2\tau-1)c^2 \delta_t}{6}$

### G.3 Evaluation simulations

In order to evaluate the lattice Boltzmann models presented above, we perform simulations of two problems as following.

To discrete  $\nabla x^\sigma$  and  $\nabla \rho$  in the binary interaction term in Eq. (C.9) and  $\nabla u_r$  in Eq. (G.38), we use the following stencil for  $\partial_{x_1}$  and  $\partial_{x_2}$ :

$$\partial_{x_1} = \frac{1}{12} \begin{bmatrix} -1 & 0 & 1 \\ -4 & 0 & 4 \\ -1 & 0 & 1 \end{bmatrix}, \quad \partial_{x_2} = \frac{1}{12} \begin{bmatrix} 1 & 4 & 1 \\ 0 & 0 & 0 \\ -1 & -4 & -1 \end{bmatrix} \quad (\text{G.44})$$

That is

$$\begin{aligned} \partial_{x_1} f(\vec{x}) &\approx \frac{1}{12} [4f(\vec{x} + \vec{e}_1) + f(\vec{x} + \vec{e}_5) + f(\vec{x} + \vec{e}_8) \\ &\quad - f(\vec{x} + \vec{e}_6) - 4f(\vec{x} + \vec{e}_3) - f(\vec{x} + \vec{e}_7)] \end{aligned} \quad (\text{G.45})$$

$$\begin{aligned} \partial_{x_2} f(\vec{x}) &\approx \frac{1}{12} [4f(\vec{x} + \vec{e}_2) + f(\vec{x} + \vec{e}_5) + f(\vec{x} + \vec{e}_6) \\ &\quad - f(\vec{x} + \vec{e}_7) - 4f(\vec{x} + \vec{e}_4) - f(\vec{x} + \vec{e}_8)] \end{aligned} \quad (\text{G.46})$$

in which  $f$  can be  $\chi^\sigma$  and  $\rho^\sigma$  or  $u_r$  and  $u_z$ .

### G.3.1 Axisymmetric flows

In this part, our exercises are pipe flow and counter flow by using the model for vector field.

**Fully developed pipe flow:** In a pipe with the radius  $R$ , flow is driven by a constant pressure gradient  $G = -dp/dz$ . The geometric configuration of the pipe flow is shown in Fig. (G.1).

Assuming that the flow is a fully developed laminar flow, the analytical solution of velocity profile across the flow stream is

$$u_z(r) = -\frac{G}{4\nu\rho_0}(r^2 - R^2). \quad (\text{G.47})$$

Our simulation is carried out in the shadowed area of Fig. (G.1). Non-slip and symmetric boundary conditions are applied at the up and down parallel walls respectively and periodic boundary at inlet and outlet. The constant pressure gradient is treated as body force(13). The system size is  $N_z \times N_r = 250 \times 50$ . The initial condition is set as  $\mathbf{u} = 0$ ,  $\rho_0 = 1$ , and  $\rho' = 0$  everywhere in the domain. Two cases are run with  $G = 2.89351e - 05, \tau = 1.0$  and  $G = 1.73611e - 06, \tau = 0.8$  respectively.

The velocity profile comparisons between analytical solution from Eq. (G.47) and LBM simulation solution are shown in Fig. (G.2). Figures show that simulation solutions(symbols) are in excellent agreement with analytical solutions.

The  $L_2$  norm error between analytical solution and LBM simulation solution is defined as

$$E_2 = \sqrt{\frac{\sum_{j=1}^{Nr-0.5} (u_{zj}^{(s)} - u_{zj}^{(a)})^2}{\sum_{j=1}^{Nr-1} (u_{zj}^{(a)})^2}} \quad (\text{G.48})$$

In figure (G.3), the relation of  $E_2$  with the grid size  $h = 1/(Nr - 2)$  shows that current model has second order accuracy in space.

**Counterflow:** Counterflow field is established by impinging two symmetrical counterflowing streams from two identical nozzles facing up and down(see Fig.(G.4)).

The simulation is in shadowed area. Initially, we set  $\rho_0$ ,  $\rho'$ , and  $\mathbf{u}$  equal to zero everywhere. Symmetric boundary conditions are applied at left and bottom boundaries and fully developed boundary at outlet. A uniform velocity is given at inlet ( $z = -u_{in}$  and  $u_r = 0$ ). Grid resolution is:  $Nr \times Nz = 300 \times 180$ . We use  $\tau = 1.0$ ,  $u_{in} = 0.1$  in simulation.

Figure (G.5) shows velocity field after steady state is achieved. In Figure (G.6),  $M$  is the instant total mass while  $M_0$  is the initial total mass in the simulation domain. Figure (G.6) shows the mass conservation in the domain after a steady flow is achieved.

## G.4 Conclusions

We have presented a LBM model for axisymmetric flows in cylindrical coordinate system. Macroscopic equations governing the flows are derived in details by the Chapman-Enskog technique.

Simulations using this model are optimistic. The scheme has been proved in the second order of accuracy. In the fully developed pipe flow simulation, velocity profiles were in excellent agree with analytical predictions; while in the counterflow simulation, mass conservation was verified and stable velocity field was obtained.

## G.5 Figures

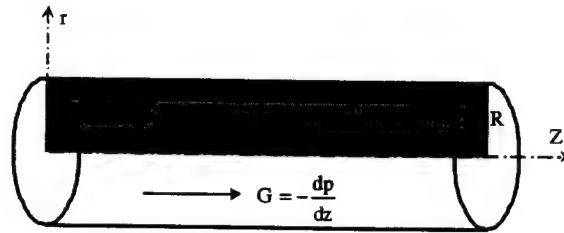


Figure G.1: A schematic illustration of pipe flow driven by a constant pressure gradient  $G$ . Only the shadowed region is simulated according to the symmetry feature.



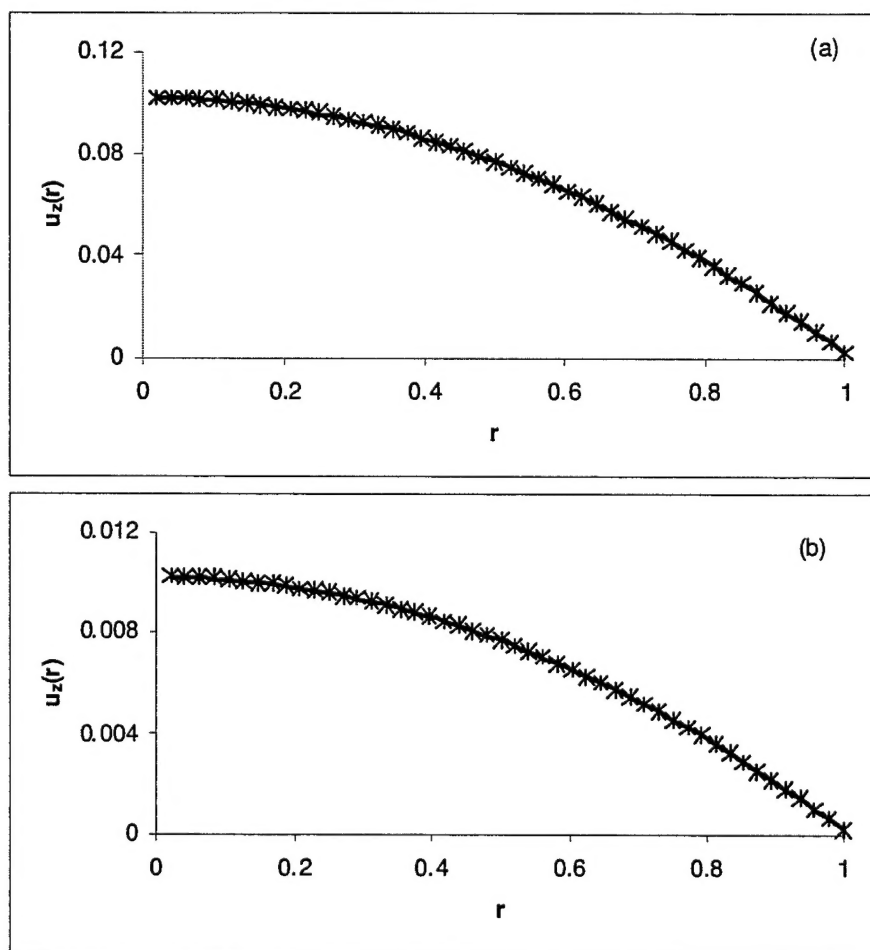


Figure G.2: Velocity profiles of a fully developed pipe flow. Lines: analytical solutions; Symbols: LBM simulation solutions. (a)  $G = 2.89351e - 05, \tau = 1.0$ ; (b)  $G = 1.73611e - 06, \tau = 0.8$

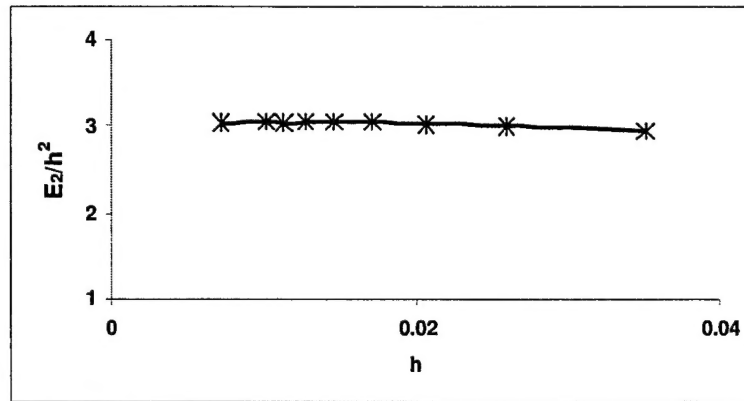


Figure G.3: Errors between numerical and analytical solutions computed by formula G.48.  
 $G = 2.89351e - 05$ ,  $\tau = 1.0$

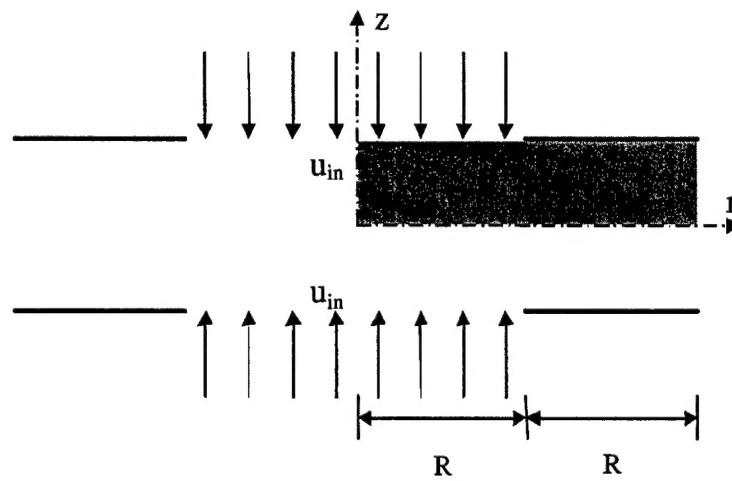


Figure G.4: A schematic illustration of counterflow

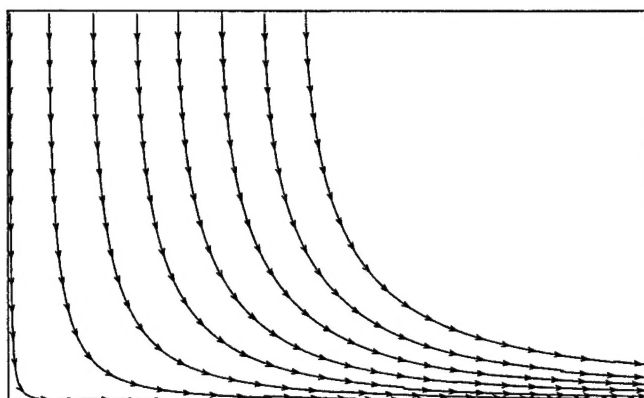


Figure G.5: A stable counterflow velocity field

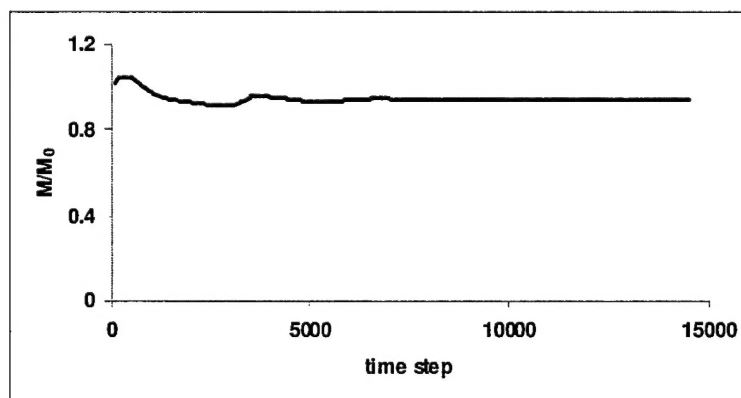


Figure G.6: Mass conservation test for counterflow

## Bibliography

- [1] F. Nannelli and S. Succi, The lattice Boltzmann equation on irregular lattices, *J. Stat. Phys.* **68**, 401(1992).
- [2] S. Succi, G. Amati, and R. Benzi, Challenges in lattice Boltzmann computing, *J. Stat. Phys.* **81**, 5(1995).
- [3] X. He, L.-S. Luo, and M. Dembo, Some progress in lattice Boltzmann method: Part I. Nonuniform mesh grids, *J. Comput. Phys.* **129**, 357(1996).
- [4] X. He and G. Doolen, Lattice Boltzmann Method on Curvilinear Coordinate System: Flow around a Circular Cylinder *J. Comput. Phys.* **134**, 306(1997).
- [5] H. Yu and K. Zhao, Rossby Vortex Simulation on Paraboloidal Coordinate System using Lattice Boltzmann Method, *Phys. Rev. E* **64** 056703(2001).
- [6] I. Halliday, L. A. Hammond, C. M. Care, K. Good, and A. Stevens, *Phys. Rev. E* **64** 011208(2001).
- [7] H. Chen, S. Chen, and H. W. Matthaeus, *Phys. Rev. A* **45**, R5339 (1992).
- [8] Y. Qian, D. d'Humières, and P. Lallemand, *Europhys. Lett.* **17**(6), 479 (1992).
- [9] P. L. Bhatnagar, E. P. Gross, and M. Krook, *Phys. Rev.* **94**, 511 (1954).
- [10] X. He and L.-S. Luo, *J. Stat. Phys.* **88**, 927 (1997).
- [11] L.-S. Luo and S. S. Girimaji, *Phys. Rev. E* **67**, 036302(R) (2003).
- [12] Dieter Wolf-Gladrow, *J Stat. Phys.* **79**, 1023 (1995)
- [13] L.-S Luo, *Phys. Rev. E* **62**, 4982 (2000).